UNIVERSITAT DE BARCELONA

How cosmology can help and benefit from other areas of physics

David Valcin

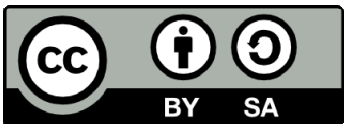

TESI DOCTORAL

How cosmology can help and benefit from other areas of physics

David VALCIN

UNIVERSITAT DE BARCELONA

TESI DOCTORAL

How cosmology can help and benefit from other areas of physics

Memòria presentada per optar al grau de doctor per la Universitat de Barcelona

Programa de doctorat en Física

Directora:	*Tutor:*	*Autor:*
Dra. Licia VERDE	Dr. Alberto MANRIQUE	David VALCIN

1 de Juliol de 2021

UNIVERSITAT DE BARCELONA

Declaration of Authorship

This thesis is presented following the regulations of the University of Barcelona (Approved by the CdG in the session of the 16th of March of 2012 and modified by the CdG on the 9th of May and 19th of July of 2012, 29th of May and 3rd of October of 2013, 17th of July of 2014, 16th of July of 2015, 15th of June and 21st of November of 2016, 5th of December of 2017, 4th of May of 2018, 15th of May and 22nd of July of 2019 and 7th of October of 2020). The listed regulations allow for the presentation of a PhD thesis as a "compendia of published articles". According to the regulations, the thesis must contain a minimum of three published or accepted articles. This thesis contains the published version of three articles. It also contains one additional article, submitted but not yet accepted for publication at the moment of thesis submission.

July 1, 2021

David VALCIN

Abstract

Context The current ΛCDM cosmological paradigm has seen remarkable success in recent decades (whether it is the discovery of the CMB, the formation of large-scale structures, the expansion of the universe etc.). Like any paradigm, there comes a point when the theory reaches its limits and the question arises as to whether it is simply due to the incompleteness of the theory or whether it should be questioned. In this thesis, I focused particularly on two aspects of the ΛCDM theory: how to effectively include massive neutrinos in the formation of structures and find a methodology to bring a new perspective in the tension surrounding the expansion of the universe.

Aims Our objective for this thesis is to show how cosmology can help and benefit from other areas of physics because there is a mutual interest in tackling problems at the interface between cosmology and other areas of physics.

Methods In the first part of the thesis, I devoted myself to the development of an emulator in order to be able to quickly and easily implement the effect of massive neutrinos on the clustering of dark matter halos. For that I used the `HADES` numerical simulations to calibrate the bias (a very useful quantity in cosmology which describes the relation between the clustering of dark matter and the different observables). By combining the result of these calibrations with a software which makes it possible to calculate the perturbative terms of the power spectrum, I was able to develop a competitive emulator up to non-linear scales.

Secondly, I devoted myself to the study of globular clusters in a cosmological context. I used a catalog of clusters provided by the HST telescope in the F606W and F814 filters. After removing the clusters with poor photometry, I performed a Bayesian analysis which allowed me to constrain the various parameters common to stars in the same cluster. Models that describe stellar evolution, like the ones I used for the analysis, are often defined for a given set of parameters that vary from model to model. Therefore to reduce the systematic errors due to the use of a specific stellar model, I studied the influence of the parameters governing the different evolutionary phases of stars with the `MESA` software.

Results The work carried out within the framework of the realization of an emulator, allowed us to highlight important results such as: even if the shape of the bias must be calibrated using numerical simulations, its amplitude can be simply rescaled by a factor proportional to the mass of the neutrinos or the combination of pre-computed coefficients with a software calculating the perturbative terms can be fast enough to be implemented in Monte Carlo sampling softwares.

On the other hand, the estimate of the age of the globular clusters that we obtained, coupled with some hypotheses on the time of galaxy formation makes it possible to put a lower limit on the age of the universe. After the reduction of the systematic errors, the age of the universe is thus compared to those obtained from the inference of cosmological parameters of various surveys. With our current precision it is not yet

possible to discard any of the measurements at odds (namely `Planck` or `SHOES`) in the H_0 tension but the results are very promising.

Conclusion Through this thesis I wanted to show that physics and more particularly cosmology could benefit from its interplay with other fields. With a better modeling of the effect of massive neutrinos it will be possible to both improve the inference of cosmological parameters and precisely constrain the mass of neutrinos (for the moment inaccessible to particle physics). A rigorous analysis of globular clusters also offers an estimate of the age of the universe almost independent of a cosmological model which is very valuable in this period of tension when the cosmological paradigm is questioned and challenged.

Resumen

El paradigma cosmológico actual LCDM ha tenido un éxito notable en las últimas décadas. Como cualquier paradigma, llega un momento en que la teoría alcanza sus límites y surge la pregunta de si se debe simplemente a que la teoría está incompleta o si debe ser cuestionada. En esta tesis, me enfoqué particularmente en dos aspectos de la teoría LCDM: cómo incluir efectivamente neutrinos masivos en la formación de estructuras y encontrar una metodología para traer una nueva perspectiva en la tensión que rodea la expansión del universo.

Nuestro objetivo para esta tesis es mostrar cómo la cosmología puede ayudar y beneficiarse de otras áreas de la física porque existe un interés mutuo en abordar problemas en la interfaz entre la cosmología y otras áreas de la física.

En la primera parte de la tesis me dediqué al desarrollo de un emulador para poder implementar rápida y fácilmente el efecto de neutrinos masivos sobre la agrupación de halos de materia oscura. Para eso utilicé simulaciones numéricas para calibrar el "bias". Combinando el resultado de estas calibraciones con un software que permite calcular los términos perturbativos del espectro de potencia, pude desarrollar un emulador competitivo hasta escalas no lineales. En segundo lugar, me dediqué al estudio de los cúmulos globulares en un contexto cosmológico. Usé un catálogo de grupos proporcionado por el telescopio HST. Después de eliminar los cúmulos con mala fotometría, realicé un análisis bayesiano que me permitió restringir los diversos parámetros comunes a las estrellas en el mismo cúmulo. Los modelos que describen la evolución estelar, como los que utilicé para el análisis, a menudo se definen para un conjunto dado de parámetros que varían de un modelo a otro. Por tanto, para reducir los errores sistemáticos debidos al uso de un modelo estelar específico, estudié la influencia de los parámetros que gobiernan las diferentes fases evolutivas de las estrellas.

El trabajo realizado en el marco de la realización de un emulador, permitió resaltar resultados importantes como: aunque la forma del bias deba calibrarse mediante simulaciones numéricas, su amplitud puede ser simplemente reescalada por un factor proporcional a la masa. de los neutrinos o la combinación de coeficientes precalculados con un software que calcula los términos perturbativos puede ser lo suficientemente rápido como para ser implementado en el software de "sampling" Monte Carlo.

Por otro lado, la estimación de la edad de los cúmulos globulares que obtuvimos, junto con algunas hipótesis sobre el tiempo de formación de las galaxias, permite poner un límite inferior a la edad del universo. Después de la reducción de los errores sistemáticos, se compara la edad del universo con las obtenidas a partir de la inferencia de parámetros cosmológicos de varios estudios. Con nuestra precisión actual, todavía no es posible descartar ninguna de las mediciones en desacuerdo en la tensión H0, pero los resultados son muy prometedores.

Un análisis riguroso de los cúmulos globulares también ofrece una estimación de la edad del universo casi independiente de un modelo cosmológico que es muy

valioso en este período de tensión cuando el paradigma cosmológico es cuestionado y desafiado.

Acknowledgements

First of all, I would like to start by thanking my thesis director Licia Verde, who gave me a chance and allowed me to become the researcher that I am today. Thank you for letting me stand on my own feet while providing me with valuable advice and a role model. Thank you for pushing and encouraging me to surpass myself. Thanks also to Raul who took me on his journey. Thank you for inspiring me, believing in me and offering such interesting projects while sharing your deep love of science.

Thank you to both of you for letting me be part of this wonderful group, which made the early morning wakes on Thursday bearable. Thanks to Jose, Nicola, Katie, Ali, Sam, Hector, Ben, Alex and my two Davides for the shared laughs, the discussions around a coffee, the scratching of heads in front of the blackboards and the precious advice. No thanks for cluttering up Aganice or Hipatia :), but thanks for killing your jobs when necessary. Thanks for the windowless time we spent in our office, thanks for letting me squat the postdoc office too.

Thank you to the collaborators whose paths I crossed, in particular Paco who showed me another face of science, invited me to his institute and helped me without any hesitation. Thank you also to Viviana who gave us machine learning courses and with whom I was able to have very enriching discussions.

Thank you to my companions from "planta 7", Alfred, Dani, Edgar, Friedrich, Laia, Lluís, Mar, Nuría, Oscar, Pau and sorry to those I could forget. Thank you for sharing the vicissitudes of the life of a doctoral student, for having always kindly agreed to go down to dunkin for a coffee or a boston mix. Thank you for the lunches on the terrace, the memorable defense after parties. Precious bowls of fresh air during the PhD.

Thank you to my family for their continued support. Thank you for encouraging me in my research even without having the slightest idea of what I am working on. Thank you for giving me a haven of peace where I could return and benefit from my mother's care.

Thank you to my second family, Simon, Alix, Ingrid, Baptiste, Renaud, Celine, Paul, Emilie, Samson, Martin that I get back to every vacation with enormous joy, to share a game of pétanque, cards or endless hikes through the woods. Thank you to my physicist friends Louis and Anna for sharing your successes with me and for always finding the time to go out for a drink.

Finally, thank you to my chérie Marie without whom nothing would have been possible. Thank you for being the best cheerleader, thank you for kicking me in the bottom when I needed to and putting up with my grumbles. Thanks for being my adventure partner, thanks for being lovely !!

Contents

Chapter 1

Introduction

Compared to other areas of physics, modern cosmology is a relatively new science. Even though knowing the origin and the properties of the universe has always been a subject of interest and fascination. It was more a matter reserved to philosophers or theologians. Throughout the centuries notable contributions were made towards a mathematical theory of the universe. We can cite as examples Aristotle, Ptolemy, Copernicus, Galileo or Newton but cosmology, in the modern sense, was born at the beginning of the 20^{th} century from two converging fronts.

On a more theoretical front General Relativity (GR), developed by Albert Einstein established new laws governing the movement of celestial bodies in the universe (Einstein, 1916). It provided a new framework to study distant and massive objects. The theory was quickly popularized by astronomers of the time (e.g. Schwarzschild) and shortly after confirmed by Arthur Eddington (cf. the solar eclipse expedition of 29 May 1919). "Cosmologists" soon realised that non only GR was good at describing astronomical phenomena but also that it was possible to make predictions about the universe. Ideas of a non static universe started to emerge and in 1922 Alexander Friedmann (Friedmann, 1922) introduced equations governing the dynamical evolution of the universe known today as the Friedmann equations. Before introducing formally the equations let's take a step back in our journey and go back in time. In the 17^{th} century Isaac Newton in his *Philosophiæ Naturalis Principia Mathematica* was the first to introduce the cosmological principle, along with his famous gravitation laws, which states that the universe is homogeneous and isotropic. Applied in General Relativity to a line element ds in a four dimensional space-time, given by the expression :

$$ds^2 = a(t)^2 dx^2 - c^2 dt^2, \tag{1.1}$$

where c is the speed of light, dt the time component and $a(t)$ and dx respectively represent the scale factor and the three dimensional metric. The cosmological principle only allows the metric to define three types of universe: closed (spherical with a positive curvature $k = 1$), flat ($k = 0$) and open (hyperbolic with negative curvature $k = -1$). Assuming the behavior of the universe's components as perfect fluids and using these metrics inside the Einstein's equations, Friedmann was able to derive two new equations describing the relative expansion of the universe as a function of the

scale parameter $a(t)$:

$$H^2(a) = \left(\frac{\dot{a}}{a}\right)^2 = \frac{8\pi G}{3}\rho - \frac{k}{a^2} + \frac{\Lambda}{3}$$
$$\frac{\ddot{a}}{a} = -\frac{4\pi G}{3}(\rho + 3p) + \frac{\Lambda}{3}, \tag{1.2}$$

where p is the pressure, ρ is the energy density, H is the Hubble parameter (named so later), G is Newton's gravitational constant and Λ is the cosmological constant. It is funny here to point out that the cosmological constant was introduced by Einstein, fervent opponent of the expanded universe, so that the universe remains static.

Parallel to the mathematical development of cosmology, observations of our nearby environment lead astronomers to question the nature of the universe, culminating with the organisation of the Great Debate in 1920. One group maintaining that spiral nebulae were stellar systems inside our own galaxy while the others argued that these nebulae were in fact very big systems outside the galaxy, an idea similar to the island universes championed by the like of Immanuel Kant. The latter group was proven to be right by further observations of the night sky, in particular the detection of Cepheid variables inside the spiral nebulae by Edwin Hubble at Mount Wilson Observatory. Cepheid variables are stars whose properties (brightness, diameter, temperature) vary periodically. Using the relationship between their period and luminosity discovered by Henrietta Swan Leavitt (Leavitt, 1908; Leavitt and Pickering, 1912) it is possible to infer their distance to the observer. Cepheids studied by Hubble had distances too big to belong to our galaxy (Hubble, 1929a) and proved the existence of stellar systems outside of the Milky way. Hubble went further and studied the relationship between distances and redshifts for his sample of Cepheids (Hubble, 1929b) and discovered what later became known as Hubble's law:

$$v = H_0 D, \tag{1.3}$$

where v is the recession velocity, D is the proper distance and H_0 is the Hubble constant. This law can be interpreted as the farther a galaxy is from the observer, the faster it moves away, which corresponds to an expanding universe.

As mentioned above the framework for this kind of universe was already laid out by Friedmann. Despite the fact that he began his observations after Friedmann's work, Hubble didn't make the connection with an expanding universe. Georges Lemaître (Lemaître, 1927) was the first to introduce an observational relationship between the distance and the recessional velocity based on Einstein's General relativity, which was confirmed later by Hubble's observations of the Cepheids. He also went further saying that if the universe was indeed expanding then there must have been a finite origin at the beginning of time and called it a "primeval atom" (Lemaître, 1931). Despite the quality and the accuracy of Lemaitre's pioneering work, it took several decades to others astronomers and cosmologist to accept this innovative idea. All these discoveries opened the door to a new universe. Modern cosmology was born.

1.1 Cosmological paradigm

More than 100 years after Einstein introduced to the world his theory of general relativity, the most complete, explanatory and accepted theory of the universe is the so-called ΛCDM model. Among its successes it is worth mentioning the detection (Penzias and Wilson, 1965), observation (Boggess et al., 1992; Hinshaw et al., 2007; Planck Collaboration et al., 2016) and measure of the polarization (Kovac et al., 2002) of the cosmic microwave background (CMB), successful tests of isotropy and homogeneity (Jimenez et al., 2019), the detection of gravitational waves (Abbott et al., 2016) etc. The ΛCDM model is based on several pillars, the most important being perhaps the cosmological principle. In its standard form, it only requires six independent parameters. In this section we are not going to make an exhaustive presentation of the model but rather introduce the aspect of the theory that will be useful for the rest of this thesis. We will focus in particular on two special points: the large scale structures and the expansion of the universe.

The large scale structures

The cosmic microwave background is a relic radiation coming from the "last scattering surface" around 380,000 years after the Big Bang. At this time the temperature of the universe dropped enough to allow the recombination of electrons and protons to form hydrogen atoms. The universe became transparent to the primordial photons that is they were free to travel with few interactions. As the universe expanded, their energy and so their temperature decreased. The Big Bang theory predicts that we should be surrounded by a bath of photons from this epoch. The detection of this cosmic radiation (Penzias and Wilson, 1965) was an extraordinary discovery for cosmology. It confirmed the prediction made by the Big Bang theory of a very hot and dense origin of the universe.

The cosmological principle states that the universe must be homogeneous and isotropic. A statement seemingly confirmed by the remarkable isotropy of the cosmic microwave background. However when we look at the night sky it is obvious that the matter is distributed in structures such as planets, stars, galaxies etc. How can we explain the origin of these structures ? The NASA Cosmic Background Explorer satellite COBE (Boggess et al., 1992) was the first to detect fluctuations in the temperature background of the order of one part in 100,000 (Smoot et al., 1992). At the time of the large scattering surface the CMB is "frozen" which implies that these anisotropies have to be either a result of an earlier mechanism or consequences of interactions at later times. The hypothesis of late time fluctuations is unlikely. First if these fluctuations are meant to be the seeds to all the structures we observe today they need time to grow and secondly because the density of radiation decreases rapidly after decoupling with interactions occurring at smaller scales. Several mechanisms have been postulated for the creation of these primordial density perturbations and we can classify them in two categories:

- Isocurvature or entropy perturbations. They don't require potential fluctuations and are created from stresses that move matter around inside the causal horizon. The perturbations affect the relative number densities of the different components.

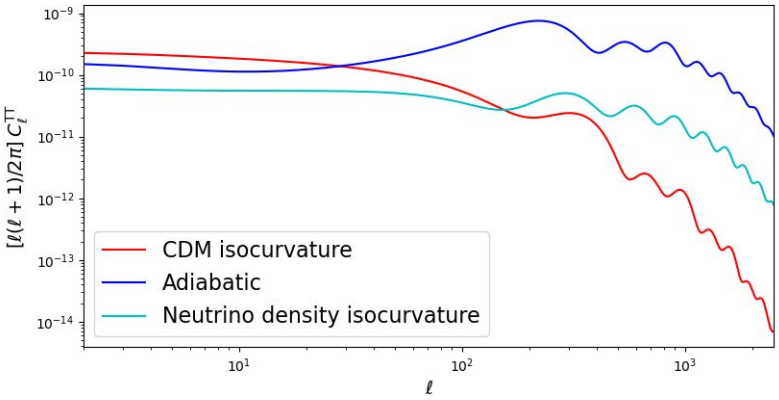

FIGURE 1.1: Angular power spectra of temperature anisotropies with different type of primordial perturbations. Figure made with CLASS (Lesgourgues, 2011).

- Adiabatic perturbations. They are present initially and arise from quantum fluctuations in the potential stretched by a period of inflation. The perturbations affect the relative energy densities of the different components.

Among the many interactions altering the angular distribution of the CMB, the baryonic acoustic oscillations (BAO) are of prime importance. BAO are the end product of two competing phenomena. In the early universe matter and radiation are mixed in a primordial plasma. Inside this plasma baryons around perturbations will undergo gravitational attraction to form over-densities while sound waves emitted by the radiation pressure will drag matter away from the over-densities creating spherical shells around every anisotropy. The cumulative effect of this pattern is visible as a series of peaks in the angular distribution of the cosmic microwave background. As the nature of the density perturbations greatly influences the signature of the peaks (the phase of the isocurvature perturbations is delayed compared to adiabatic models see Figure 1.1), it is important to measure them with accuracy. This was done by experiments like WMAP (Hinshaw et al., 2007), Planck (Planck Collaboration et al., 2016) etc. Their observations were consistent with the density perturbations being adiabatic.

The theory of cosmic inflation is one of the theories predicting an adiabatic origin of primordial density perturbations. It says that quantum fluctuations created during the very early universe will be stretched by a phase of exponential growth of the scale factor $a(t)$ (quantity introduced earlier see Equations 1.1 and 1.2). Many inflationary models make predictions about the modes of fluctuations (here we will only talk about the scalar modes as they are the only ones being observed so far) connecting their spatial scale to their distribution. Starting from the definition of fluctuations in energy density:

$$\delta(x) = \frac{\rho(x) - \bar{\rho}}{\bar{\rho}}, \tag{1.4}$$

where $\rho(x)$ represents the energy density at a given point and $\bar{\rho}$ the average energy density. The power spectrum $P(k)$ can be defined as the variation of power as a function of the spatial scale in Fourier space (here k is the wavenumber of the fluctuations):

$$\left\langle \delta_k \delta'_k \right\rangle \propto \delta(k - k')P(k) \tag{1.5}$$

Taking as an example a simple model of inflation, the power spectrum of primordial scalar perturbations can be expressed as a power law:

$$P_0(k) = A_s \frac{k}{k_0}^{n_s - 1}, \tag{1.6}$$

where A_s is the amplitude of the power spectrum of the perturbations at a pivot scale k_0, n_s is the scalar spectral index which describes how the fluctuations vary with scale. A value of $n_s = 1$ would mean scale invariant fluctuations. The latest estimation provided by the Planck survey (Planck Collaboration et al., 2020) gives a value of $n_s = 0.965 \pm 0.004$.

$P_0(k)$ describes the distribution of scalar perturbations in the very early universe but to compare the theory to current observations, perturbations need to be evolved through the history of the universe. The Einstein-Boltzmann equations are a set of differential equations designed to derive the evolution of these perturbations from initial conditions within the framework of general relativity. Each component of the early universe is treated as a fluid and density fluctuations inside these fluids are described by transfer functions $T(k, z)$ where k is the spatial scale and z is the redshift. Using these transfer functions, it is possible to relate the power spectrum of primordial fluctuations to the distribution of components at any time and scale and define the total matter power spectrum:

$$P_m(k, z) = \left(\sum_i T_i(k, z) \right)^2 P_0(k, z), \tag{1.7}$$

where the subscript i refers to any of the components considered in the computation of the power spectrum whether it is matter or radiation.

However an universe only composed of baryonic matter and radiation is not sufficient and several observations have pointed out the inconsistencies of the Big Bang model: the rotation curves of galaxies, the velocity dispersion of bound systems and later gravitational lensing. All indicating missing mass in the matter budget of the universe. Measurement of the CMB properties also highlighted some gaps in the theory of structure formation. Due to constant scattering and streaming of the photons, the matter over-densities are washed up or frozen in the early universe. After decoupling, since the density of radiation decreases faster than that of matter during the expansion of the universe ($\rho_\gamma \propto a^{-4}$ while $\rho_m \propto a^{-3}$), matter will be subject to fewer interactions with photons and will be free to collapse and form the structures that we observe today. The problem is that the temperature of the CMB was measured to be $T_{CMB} \simeq 2.7K$ placing the last scattering surface at some 380,000 years after the Big Bang which does not leave enough time for the matter over-densities to form sufficiently large structures. These observations led to the postulate of a new kind of non-luminous matter which only interacts in a gravitational manner. Thus immune to the constant

scattering of photons, this dark matter is able to form gravitational wells before decoupling acting as catalysts in the formation of structures. Numerical simulations in the 1980s showed that for a hierarchical formation model to accurately reproduce observations at $z = 0$, the velocity of this extra component must be much smaller than the speed of light at matter-radiation equality. All these properties are included under the name of Cold Dark Matter (CDM). Today's estimates say that it represents 27% of the energy budget of the universe while baryonic matter and radiation only accounts for 5% (Planck Collaboration et al., 2020).

The (accelerating) expansion of the universe

Large-scale structures bear witness to the interactions between the different components of the universe while the expansion is sensitive to the collective effect of all the components in the cosmos. As the constituents are embedded in an expanding universe, there is some interplay between the two. Measuring with precision the properties of the expansion provides a wealth of information about the history of the universe. In the first part of the introduction we mentioned that the expansion was postulated a long time ago by Friedmann and Lemaitre and observed experimentally by Hubble. Using the distance and redshift of Cepheid variable stars he obtained a linear relation, latter known as the Hubble law, with a slope of $H_0 = 500$ km/s/Mpc (Hubble, 1929b). This constant represents the value of the expansion flow today.

Even though it is possible to access the velocity of celestial objects by measuring their redshift, a direct measurement of the distance in the universe is only possible for objects close to the Earth. Unfortunately in the nearby sky the Hubble flow is dominated by peculiar motions induced by gravitational forces. Therefore we need "anchor" points to calibrate and measure the distances of celestial objects at high redshifts. Any desirable "anchor" points must possess three essential qualities. First they must be distinguishable from the foreground and background thanks to their special features, then they must be calibrated with well-known properties and finally they must be common enough or occur frequently enough to be used in most of the universe. In this regard some astrophysical objects are extremely valuable. An ensemble of techniques using these "anchor" points have been developed and regrouped under the denomination *Cosmic ladder* .

We can cite some of these methods here:

- Standard candles: a class of objects with known intrinsic luminosity or brightness L. Using their observed flux F we can compute their luminosity distance

$$d_L(z) = \sqrt{\frac{L}{4\pi F}} = (1+z)\, d_M(z)\,, \tag{1.8}$$

  where z is the redshift and d_M is the comoving transverse distance. Cepheid variable stars and type Ia supernovae are members of this class. They are very bright and luminous objects in the night sky which makes them easier to identify.

- Standard ruler: a class of objects with known physical size x. Using their observed angular size $\delta\theta$ we can compute their angular diameter distance

$$d_A(z) = \frac{x}{\delta\theta} = \frac{d_M(z)}{(1+z)}\,, \tag{1.9}$$

where z is the redshift and d_M is the comoving transverse distance. Baryonic acoustic oscillations are a good example of standard ruler. Indeed matter expelled by the acoustic waves created by the opposite effects of gravity and radiation pressure was allowed to travel up to some distance without scattering and defined a fixed scale predicted by theory.

- With the blossoming of gravitational waves cosmology, standard sirens are also worth mentioning. In this case the important quantity is the power (rate of energy emission) which is related to the orbital evolution of a binary system. It can be determined from the chirp mass:

$$M = \frac{(m_1 m_2)^{3/5}}{(m_1 + m_2)^{1/5}}\,, \tag{1.10}$$

where m_1 and m_2 refer to the masses of the binary system.

While some of the probes are located at high redshifts, these determinations of the Hubble constant remain "local" on the timescale of the universe. The cosmic microwave background offers an alternative to measure H_0 using a relic from the primordial universe. Assuming a cosmological model, we can infer the value of the Hubble parameter today from the size of the largest fluctuations in the CMB. A higher expansion rate would correspond to less time for the anisotropies to grow and inversely a smaller expansion rate would provide more time for the anisotropies to grow.

The term "Hubble constant" is a bit misleading because H_0 is not a constant *per se* but rather the actual value of the Hubble parameter (see Equation 1.2). Since the universe is evolving, its value must have been different in the past. Inside an homogeneous, isotropic and expanding universe (also known as FLRW universe) the deceleration parameter can be defined as:

$$q = -\frac{\ddot{a}a}{\dot{a}^2}\,, \tag{1.11}$$

where a is the scale factor and dotted quantities indicate time derivative. Since the Hubble parameter can also be defined as a function of the scale factor $H(t) = \dot{a}(t)/a(t)$, it is possible to express the derivative of the Hubble parameter as a function of the deceleration parameter:

$$\frac{dH}{dt} = -H^2(1+q) \tag{1.12}$$

For a long time cosmologists thought that the expansion should slow down (hence the name of the deceleration parameter) since gravity, the dominant force on large scales, should compensate its effect by bringing matter closer together. It came as a surprise when two teams simultaneously discovered that it was in fact the opposite (Riess et al., 1998; Perlmutter et al., 1999). They gathered a sample of supernovae at redshift high enough to measure the deviation from the linear Hubble law (indication of a different value of the Hubble parameter at earlier time). The latest estimate of q_0 (the value of q today) suggests a value $\simeq -0.55$ which means that:

1. the Hubble parameter will decrease with time (see Equation 1.12)

$$q > -1 \longrightarrow \frac{dH}{dt} < 0 \tag{1.13}$$

2. the expansion is accelerating (see Equation 1.11)

$$q < 0 \longrightarrow \ddot{a} > 0 \text{ since } a, \dot{a}^2 > 0 \tag{1.14}$$

The discovery of an accelerating expansion is another milestone of the cosmological paradigm. Rewriting the acceleration equation of Alexander Friedmann (see second line of Equation 1.2) in terms of the different component of the universe:

$$\frac{\ddot{a}}{a} = -\frac{4\pi G}{3}\sum_i(\rho_i + 3p_i) = -\frac{4\pi G}{3}\sum_i \rho_i(1 + 3w_i)\,, \tag{1.15}$$

where ρ is the mass-energy density, p is the pressure, w is the equation of state $w = p/\rho$ and the subscript i refers to each component. From equation 1.15 it can be inferred that for the expansion to accelerate ($\ddot{a} > 0$), the part of the right hand side between parenthesis $(1 + 3w_i)$ must be negative, which corresponds to an equation of state $w < -1/3$. This was problematic because of all the components of the universe postulated by the CDM model none satisfied this condition. For baryonic and cold dark matter $w = 0$ and for radiation $w = 1/3$. Just like large scale structures, there was a missing piece to the puzzle. Model universes entirely filled with cold dark matter, baryons and radiation are very good at reproducing the formation of galaxies and clusters but they require a lower value of the Hubble constant in tension with observations. Two of the most prominent models designed to fix this issue were 1) a mixture of cold and hot dark matter and 2) cold dark matter plus a cosmological constant known today as ΛCDM. Following the discovery of the accelerating expansion the latter was adopted by community as the correct one.

The cosmological constant Λ was created by Einstein to ensure that the universe predicted by the field equations of general relativity remained static but this solution is unstable and Friedmann showed that whatever the value of Λ, Einstein's equation can still be applied to a non static universe (see Equation 1.2). In fact in a dynamical universe the cosmological constant will increase the rate of expansion (or inversely the rate of contraction). Before the evidence of an expanding universe Einstein developed a new model of the cosmos based on Friedmann's equation with a null cosmological constant known today as the Einstein–de Sitter universe. Until the end of the 20^{th} century and the realisation that the expansion was accelerating, the cosmological constant was thought to be equal to zero but the discovery of the two supernovae teams (Riess et al., 1998; Perlmutter et al., 1999) implied a value of $\Lambda > 0$.

The origin and form of the energy driving the accelerating expansion is still unknown so it was called *Dark Energy* as a analogy to dark matter. While all dark energy models have different equation of state they must all respect the same constraint of $w < -1/3$ to ensure an accelerating expansion. They usually come in two forms either from scalar fields (Ratra and Peebles, 1988; Caldwell, Dave, and Steinhardt, 1998) or constant energy like Λ introduced above. The cosmological constant is one of the simplest explanation for dark energy. As mass and energy are intrinsically linked in general relativity, energy fluctuations created from the vacuum are expected to contribute to the dynamical evolution of the universe. The latest measurement from Planck CMB experiment (assuming a ΛCDM model) gives a value of $\Omega_\Lambda \simeq 0.6847$ (Planck Collaboration et al., 2020) which corresponds to $\simeq$ 68% of the mass-energy budget of the universe. Contrary to the predictions of quantum theories (a difference

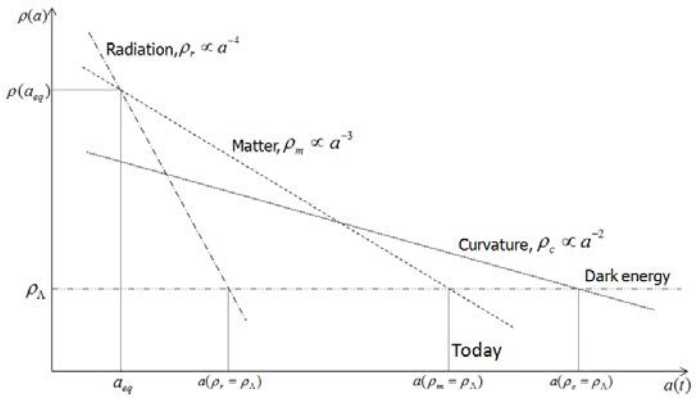

FIGURE 1.2: Evolution of the densities of the different elements of the universe by Muhammad under the CC BY-SA 3.0 licence.

of 120 orders of magnitude !), the density of dark energy is very low and the only reason why it is able to counterbalance the gravitational effect of matter is because it is uniformly spread across the universe. The energy densities of matter and radiation being inversely proportional to the scale factor $a(t)$, they decrease with time while Λ remains constant. We are now in the era of a universe dominated by dark energy (see Figure 1.2).

1.2 Tension and going beyond the model

Despite the many successes of the ΛCDM model, there are plenty of unknown within the cosmological paradigm whether it is about the nature of dark matter or dark energy or tensions in the measurement of some parameters. I will continue in the footsteps of the previous section and address some of the shortcomings of the two pillars of the ΛCDM model that I introduced i.e: large scales structures and the expansion of the universe.

Non linear scales

According to the accepted scenario, large scales structures are born from quantum fluctuations in the primordial plasma that underwent a phase of exponential inflation. The resulting over-densities induced the formation of potential wells of dark matter immune to interactions with radiation. After decoupling, baryonic matter was free to collapse inside the potential wells tracing the distribution of dark matter. This model is remarkable at predicting the large scale structure we observe today. The total matter power spectrum (see Equations 1.7), describing the distribution of matter as a function of scale, is derived from perturbation theory which predicts the effects of gravity upon perturbations in the framework of general relativity. As usual for this type of mathematical methods, perturbation theories tend to break when the perturbations become to big to be expanded. That is why the cosmological theory of perturbation is only considered to be valid when the universe is mostly homogeneous e.g. during the phase of cosmic inflation. As the wavelengths or Fourier modes of the

density perturbations are expected to evolve independently and the density field to be Gaussian on large scales, the total matter power spectrum is a good approximation on these scales. It is often referred to as the linear power spectrum.

On smaller scales where over-densities are much bigger than the average density of the universe, linear theory is not valid anymore. We must resort to N-body simulations or semi-analytic models to make predictions of the matter distribution. When observations were compared to predictions it was evident that the development of the ΛCDM model was incomplete at small scales. Among the issues:

- "*The cusp/core (CC) problem, designating the discrepancy between the flat density profiles of dwarf galaxies [...], Irregulars, and Low Surface Brightness galaxies [...], and the cuspy profile predicted by dissipationless N-body simulations, despite the fact that the observed galaxies are all of DM dominated types*" from Del Popolo and Le Delliou 2017;

- "*The "missing satellite problem" (MSP), coining the discrepancy between the number of predicted subhalos in N-body simulations and those actually observed, further complicated by the "Too Big To Fail" (TBTF) problem, arising from the ΛCDM prediction of satellites that are too massive and too dense, compared to those observed, to hope for their destruction in the history of mass assembly up to today*" from Del Popolo and Le Delliou 2017;

In order to solve theses issues cosmologists were tempted to go beyond the standard model of cosmology. E.g. a new type of dark matter called *warm dark matter* was theorized. It has the same properties as cold dark matter above the free-streaming scale leading to a bottom-up structure formation and similar to hot dark matter below the free streaming scale with a top-down formation. It is also thought that baryonic physics might alter the formation process of galaxies. However it is not obvious that these issues are coming from an incompleteness of the model. Indeed N-body simulations are very complex to implement because they require the modelization of interactions between millions or billions of particles. They are also limited by their resolution. As fluids are split into massive particles to speed up the computation a trade-off must be made between the smallest mass available and the resulting number of particles.

There is another reason to improve the treatment of the theory on non linear scales. This part of the power spectrum is sensitive to both the nature of the different components of the universe (peculiar velocity, streaming scale, mass etc.) and the interactions between themselves (self interacting particles, baryonic physics etc.). If they want to be seen as credible alternatives to ΛCDM, cosmological models must be able to perform as least as well on large scales while being free to make different predictions on small scales. Therefore an accurate modelling and description of the non linear scales will provides a wealth of information and will allow to disfavor and discriminate between cosmological models. Usually higher-order statistics are necessary to describe the distribution at small scales.

H_0 tension

For a long time after Lemaitre and Hubble first estimates of the rate of expansion it was thought that the value of H_0 was either close to 50 or 100 km/s/Mpc. As more

surveys became available it became possible to put tighter constraints on the constant, especially using cosmic microwave background experiments like WMAP or Planck (Hinshaw et al., 2007; Planck Collaboration et al., 2016). However CMB experiments provide an indirect determination of the Hubble constant because a cosmological model need to be assumed first. That is why CMB estimates must be compared against direct measurements, independent of a cosmological model. Direct measurements are based on Hubble's law which relates the distance of an object to its recessional velocity in an expanding universe. Of all the methods used to determine the distances of objects in the far universe (see *cosmic ladder* in the previous section 1.1) the most prominent one is the use of standard candles (Type Ia supernovae in combination with Cepheids (Riess et al., 2016)). This method is responsible for the discovery of the accelerating expansion of the universe. If the cosmological model assumed is correct then the direct and indirect measurements should agree but the CMB and supernovae measurements were at odd with a $\simeq 3\sigma$ tension (see Figure 1.3).

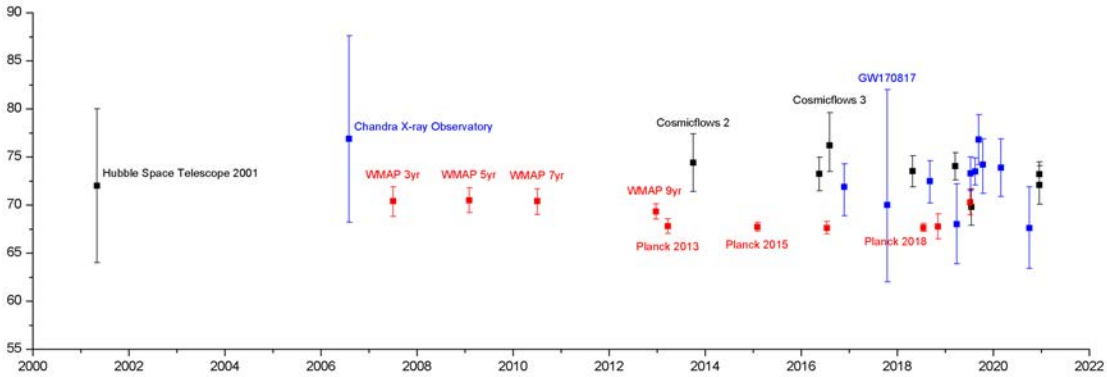

FIGURE 1.3: Estimated values of the Hubble constant, between 2001–2020, with cosmic ladder (black), CMB (red) and other techniques (blue). Created by Renerpho under the CC BY-SA 4.0 license.

The objects used for the cosmic ladder must be far from us ($D > 100$ Mpc) so that the Hubble flow dominates over the peculiar velocities, which makes it very difficult to measure the distances accurately. As the determination of the Hubble constant is heavily dependent of the assumptions made for the determination of the distances, the uncertainties of the different methods was a reasonable explanation for the spread of the estimates. With the increasing number of surveys and the improving precision of the measurements a convergence was expected, however not only was the tension not reduced but it increased reaching 4-5σ between direct and indirect measurements (Planck Collaboration et al., 2020; Riess et al., 2021).

If we assume that the measurements of the different experiments are valid (systematics under control, theoretical models are correct, universality of the tracers used in the cosmic ladder etc.) this result seems to point out that ΛCDM is incomplete and we need new physics beyond the standard model. Since the measurements at odds are sensitive to different epochs of the universe, several leads are worth considering and a lot of solutions have been proposed to alleviate the tension. They can be sorted in 4 categories according to (Efstathiou, 2021):

1. radical departures from conventional cosmology, including departures from General Relativity;
2. changes to the physics of the early universe (for example adding additional relativistic species or neutrino interactions);
3. new physics at matter-radiation equality, or recombination, that alters the value of the sound horizon;
4. changes to the physics at late times.

Solutions of types 3 and 4 seem to be favored nowadays, even if a modification of the physics at late time has to overcome more obstacles such as the fact that the origin of dark energy is still unknown or that some of the late time experiments agree well with the low value of H_0 inferred from Planck (Planck Collaboration et al., 2020).

1.3 Interplay between cosmology and other fields

Cosmology is a one of a kind in the realm of natural sciences. Indeed natural sciences are based on empirical observations of the environment and they try to establish general laws using scientific methods. Two very important notions for any scientific method are: *repeatability* (the ability to repeat an experiment by a same team of researchers) and *reproducibility* (the ability to reproduce the experiment by another team of researchers). Disregarding here the different theories of multiverse, let's assume that there is only one universe. The fact that it is only possible to observe a tiny fraction of it makes it difficult to achieve these standards. Beyond all the technical challenges that cosmologists had to overcome, this may explain why the status of cosmology as a real science was a subject of debate. Since the era of modern cosmology and despite some areas that still remain speculative (such as the origin of the universe), cosmology is a science in its own right. Even more it is a multidisciplinary science where mathematics are used to create a framework and make predictions, astronomy provide observations to invalidate and disfavour models and physics and chemistry theories help us explain the different phenomena. It is probably one of the most complete field of physics since it tries to conciliate the infinitely large with the infinitely small.

Nowadays the quantity of material to learn, necessary to contribute to the discipline as well as the variety of sub-fields studied, makes it possible to draw a delimitation between cosmology, astrophysics or other areas of physics. Even if the wall between astrophysics and cosmology remains quite porous (it is mainly a question of scale), it is rare that objects or phenomena are studied for the same reasons. Most of the time, astrophysics focuses on the nature of celestial objects while cosmology is more interested in their large-scale attributes (distribution of galaxies, distances of supernovae etc.). However in the history of cosmology there are various examples of astronomical discoveries which have revolutionized our knowledge of the universe. The importance of Cepheids and Type Ia supernovae was already mentioned for their role in the discovery that the universe was in a state of accelerating expansion, but it is also important to talk about the study of the Coma cluster of galaxies and the rotation curves of galaxies that have highlighted the existence of dark matter or the discovery by Walter Baade of several types of Cepheids (Baade, 1956) leading to an estimate

of the size of the universe twice as large as the previous one. For these reasons it is interesting to study celestial objects from a cosmological perspective.

In addition to astrophysics there is also a strong interplay between cosmology and particle physics. After its creation the universe was composed of a very hot and dense plasma of elementary particles and parallel to gravity and cosmic inflation, the interactions between particles (scattering, decay etc.) greatly contributed to its development. Through the theories of the cosmic microwave background and primordial nucleosynthesis of atoms (explaining the abundance of primordial elements observed today, cf. Alpher, Bethe, and Gamow 1948), particle physics was instrumental in establishing the Big Bang theory as a correct explanation for the singular origin of the universe, confirming the predictions of Lemaitre. It was later realized that the theory of Big Bang nucleosynthesis had two shortcomings: the heaviest elements couldn't be produced due to a bottleneck in the production mechanisms and the quantity of baryonic matter predicted by the model was not sufficient to match the observations of the rotation curves or the clusters of galaxies. The former can be solved by invoking astrophysical mechanisms such as the explosion of supernovae but the latter requires the introduction of a new kind of particles not predicted by the standard model, dark matter. The elusive nature of dark matter makes it difficult to study its properties in the laboratory. As particle physics studies the interaction between particles at high energies, creation and annihilation of more massive particles requires greater energy which in turn requires to build larger accelerators. In this sense the universe is an ideal laboratory because it allows both to observe phenomena occurring at gigantic energies and to study the overall effect of relic elementary particles and their signature in the current universe.

1.4 Computational methods

I would like to conclude this introduction by putting into perspective the work carried out in this thesis. Computational methods are omnipresent in natural sciences and cosmology is no exception to the rule. Nowadays cosmologists must, to some extent, possess some programming skills because it may be required at every step of the scientific process. Like all empirical sciences, it all starts with observations. Then the collected data need to be processed and reduced e.g. to infer cosmological parameters with software such as Monte Carlo samplers. It is probably during this phase that the majority of scientists are confronted with computational tools. Once the analysis is done theorists will explain the results obtained by creating new models or adjusting the existing ones. These models thus created will make it possible to make predictions whose robustness will be tested against new observations. This scientific cycle is shown schematically in Figure 1.4.

Research fields encompassed by the denominations computational cosmology or computational astrophysics mainly focus on the "theories" and "predictions" parts of the cycle. In some cases models and predictions can be established analytically but they are limited by the complexity of the phenomena studied. When the system is too complicated, it is usually necessary to resort to semi-analytical models or numerical simulations. This is the case, for example, for the formation of structures at small scales where the evolution of over-densities of matter is governed by non-linear physics.

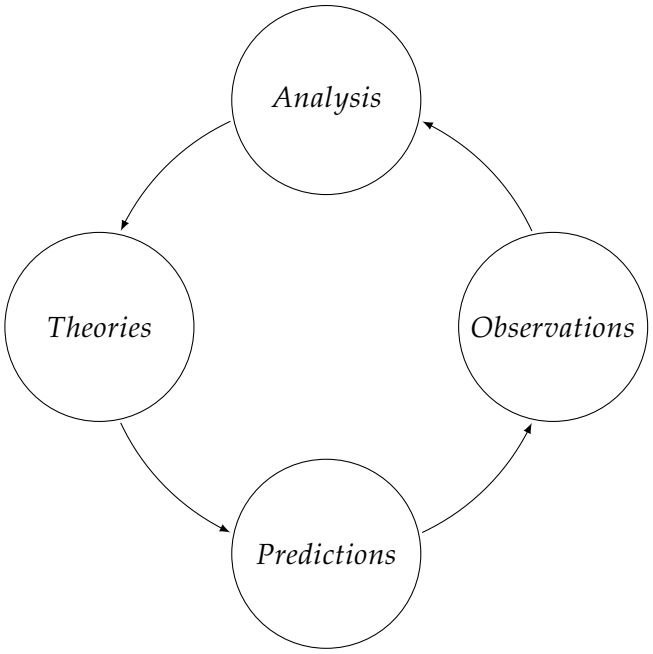

FIGURE 1.4: Scientific cycle

The predictive power of numerical simulation is a real asset in cosmology where only a single realization of the universe is accessible. More recently, machine learning has also made it possible to study areas where the underlying physics is not yet very well understood.

But there is also another aspect of computational cosmology, a little more "meta" in the sense that one uses computational methods to develop new computational methods. This is particularly the case for data analysis. As said previously, numerical simulations are excellent for making predictions but they can also be used to simulate future observations to create new analysis tools able to extract as much information as possible from the data that will be collected. The production of results makes science what it is, but it is important to continue to improve tools and methodologies in order to perpetuate the advancement of knowledge. It is a dimension that I wanted to bring to my work.

1.5 Objective and structure of the thesis

This thesis consists of a collection of my research published during my doctorate at the University of Barcelona. The objective of my work was to navigate at the interface between cosmology and other fields of physics in order to shed light on some of the properties of the components of the universe in the context of the ΛCDM cosmological paradigm. With this in mind my collaborators and I tried to bring new perspectives by developing new tools or by introducing new methodologies.

This thesis is organized as follows. In Chapter 2 we explain how the discovery of massive neutrinos alters not only the standard model of particle physics but also the theory of structure formation. In order to determine the mass of neutrinos with

precision, their effect on the clustering of matter should be adequately addressed. This chapter includes the publication (Valcin et al., 2019). In chapter 3 a sample of globular clusters, observed by the NASA HST telescope, is studied. In order to determine the attributes of these clusters, a Bayesian analysis is performed. I explain how the systematic errors can be reduced in order to make the results obtained more competitive. Finally, the age of the clusters is put in the context of the H_0 tension, where they can be used as standard clocks. This chapter includes the publications (Valcin et al., 2020; Bernal et al., 2021) and a manuscript under review (Valcin et al., 2021). Chapter 4 summarizes the conclusions and implications of the work presented as well as future prospects.

Chapter 2

Towards a determination of the absolute mass of neutrinos

2.1 Background

Neutrinos are fascinating objects, because of their nature, their impact on the universe and the mysteries they seem to conceal. Before explaining how cosmology can contribute to the study of neutrinos, I will start by giving a brief summary of their history. They were first postulated in 1930 by Wolfgang Pauli to explain the conservation of energy, momentum and angular momentum during the beta decay, i.e the decay of a neutron into a proton or vice versa.

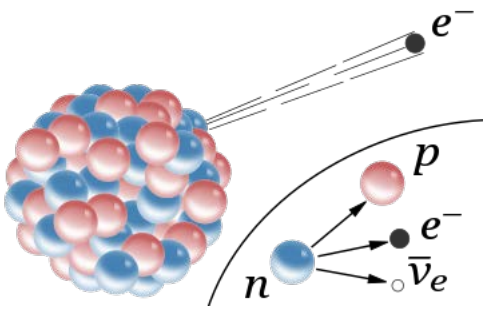

FIGURE 2.1: β decay inside an atomic nucleus by Inductiveload. Image from Public domain

The particle was first observed during the Cowan – Reines neutrino experiment (Cowan et al., 1956), where antineutrinos produced in a nuclear reactor interacted with protons to make neutrons and positrons. In the 1960s, the Homestake experiment (Davis, Harmer, and Hoffman, 1968) made the first measurement of the flux of electron neutrinos arriving from the core of the Sun and found a value that was between one third and one half of the number predicted by the Standard Solar Model (Bahcall and Davis, 1976). Even though scientists knew the existence of different neutrino flavors since the 1960s and 1970s, it was still several decades before a satisfactory explanation was found for this "Solar neutrino problem". In the 1950s Bruno Pontecorvo postulated the phenomenon of oscillation of neutrinos (Pontecorvo, 1957; Pontecorvo, 1967), analogous to muon oscillation, to answer the question but being limited by the technology of the time, it was not until the end of the 1990s that the first evidences for neutrino

oscillation (atmospheric from the Super-Kamiokande collaboration in Japan (Fukuda et al., 1998) and solar from the Sudbury Neutrino Observatory (SNO) in Canada) were obtained.

2.2 Neutrino Oscillation and consequences

The oscillation of neutrinos results from the mixing between the flavor and mass eigenstates. Neutrino states are the superposition of three quantum states of definite masses. When neutrinos travel through space, these different states of mass will travel at different rates, changing the superposition of the states. This modification of the superposition of the masses will lead to a change in flavor. Thus the neutrino flavor will be able to oscillate periodically, returning to its original flavor after a certain distance. Neutrino oscillation remains possible as long as the quantum states remain coherent along the path.

The fact that this phenomenon was observed had important consequences on particle physics. Indeed the standard model predicted that neutrinos were massless particles but neutrino oscillation is only possible if the three species have nonzero and slightly different masses. Subsequently a number of experiments were carried out to confirm this result and to learn more about the properties of neutrinos. A current limitation in the study of oscillations in laboratory is that experiments are only sensitive to the difference in the squares of the masses Δm^2. Recently new experiments have been designed to determine the absolute mass of neutrinos in the laboratory by analyzing the nuclear beta decay with spectrometers (KATRIN Weinheimer 2002) or calorimeters (MARE Monfardini et al. 2006).

2.3 Clustering of dark matter and neutrino sensitivity

This is where cosmology comes into play. As small as the mass of neutrinos is, their collective effect will modify the mass-energy budget of the universe. As relativistic particles in the early universe, they will also alter the formation history of structures. Assuming a ΛCDM cosmological model, the best explanation for all the large scales structures we observe today is a hierarchical bottom-up formation model where small structures grow due to gravitational pull and a succession of mergers (see Figure 2.2).

But what is the role of neutrinos in this picture ? According to the Big Bang theory neutrinos are expected to decouple early in the history of the universe (in the first few seconds) and as they rarely interact with matter (mainly via the weak interaction), they persisted as a cosmic neutrino background. Even after decoupling neutrinos remained in thermal equilibrium with the photons until the temperature dropped below the mass of the electron. Thus shaping the expansion of the early universe. The Big Bang nucleosynthesis predicts that the abundance of light elements will depend of the number of neutrino species N_ν. A prediction confirmed by the standard model of particle physics. Being a relativistic species, neutrinos will also contribute to the radiation budget of the universe and shift the epoch of matter-radiation equality which can impact the determination of the expansion rate at later times. E.g one solution considered to alleviate the H_0 tension is to modify the number of neutrino species (see section 1.2).

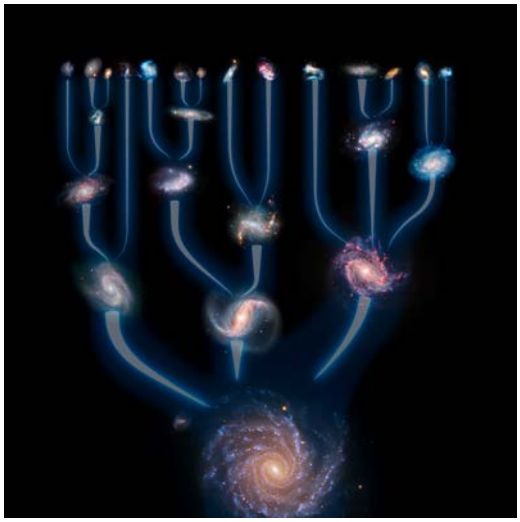

FIGURE 2.2: Hierarchical model of galaxy formation, by ESO/L. Calçada under the licence CC BY 4.0

Massive neutrinos are also of great interest in the study of the clustering of matter. Due to the fact that the are not luminous, that their existence has been proven and that they interact very little with their environment, massive neutrinos were ideal dark matter candidates. However the very small mass predicted by the oscillation mechanism suggests that neutrinos can travel at speeds comparable to that of light. This classifies neutrinos as hot dark matter, incompatible with a bottom-up formation model. In addition if dark matter was composed solely of neutrinos, the particles would have sufficient speed to escape galaxies, which does not agree with observations. The speed of neutrinos will also alter the clustering of matter at small scales. Indeed their thermal velocity will allow them to break and free stream outside of small over-densities. This effect will result in a suppression of the matter power spectra at small scales.

As can be seen in Figure 2.3 the matter power spectra are not only sensitive to massive neutrinos but also directly to the absolute mass of the neutrinos Σ_{m_ν}. This is both a blessing and a curse because it means that if we succeed to accurately model the power spectra we can put some constraints on the total neutrino mass and even disfavour one of the neutrino hierarchy models. It also means that if we want to extract the wealth of information encapsulated in the power spectra (especially at small scales where the modes are more abundant) we must be able to recreate accurately the impact of massive neutrinos on the clustering of matter.

2.4 Bias and redshift space distortion

One of the main obstacle in cosmology is that we are trying to learn more about the universe while we are able to only access a small part of it. Whether it is because of distance, insufficient luminosity, foreground, detector sensitivity etc. The usual workarounds are to search for interactions between the objects studied and their environment. For the clustering of matter, since we can not directly observe dark matter, we study

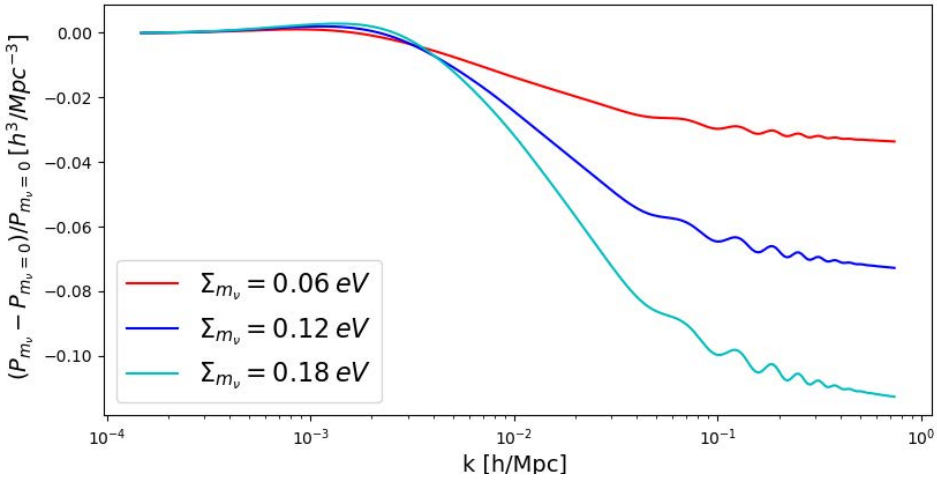

FIGURE 2.3: Ratio of the total matter power spectra for different neutrino masses. Figure made with CLASS (Lesgourgues, 2011).

the distribution of tracers in the universe (these could be galaxies, clusters of galaxies, dark matter halos etc.). The problem is that these tracers do not perfectly reproduce the distribution of dark matter and we need to correct this effect by introducing a new quantity called *bias* and usually denoted by the letter b. The bias will link the distribution of dark matter predicted by theory to the distribution of the observed tracers.

$$\begin{aligned} \delta_{\text{tracers}} &= b \times \delta_{\text{theory}} \\ P_{\text{tracers}} &= b^2 \times P_{\text{theory}} \end{aligned} \tag{2.1}$$

where δ represents over-densities and $P = <\delta|\delta>$ the power spectra. The bias is a complex quantity and will depend on several parameters according to the nature of the tracers and the surrounding environment. In a ideal universe, rescaling the dark matter power spectra by a constant value would be enough to match the observed distribution of tracers and it is usually the assumption made on linear scales where the phenomena happening in the universe are governed and best described by linear physics. However in this era of precision cosmology it is crucial to extract the information contained in smaller scales. At these scales the approximation of a constant bias is not valid because the clustering properties will depend on the portion of the sky selected. This can be translated as a scale dependent bias $b \longrightarrow b(k)$.

Beyond the bias, other effects will prevent the measurement of the tracers distribution with accuracy. Among the most dominant are the Redshift Space Distortions (RSD). As it is very difficult to directly access the distance to sources, in almost all the analyses in cosmology the redshift is used as a proxy. The problem is that experimentally the shift measured is the combination of two movements: the expansion of the universe and the peculiar velocity of tracers with respect to the expansion. This deviation of the Hubble law will lead to inaccurate determination of distances if not corrected. The

Redshit space distortions will modify the power spectra in two particular ways that can be distinguished by the scales impacted:

- The Kaiser effect (Kaiser, 1987) at large scales: caused by the coherent motions of galaxies as they fall towards the center of clusters leading to a flattening of the structure (see left panel of Figure 2.4).
- The Fingers of God (Jackson, 1972) at small scales: virial motion associated with the random peculiar velocities of galaxies bound in clusters (see right panel of Figure 2.4).

Both the bias and the redshift space distortions have been extensively studied. It can be difficult to model them accurately, especially in the non linear scales because it requires mathematical artefacts such as perturbations theory, effective field theory etc. which are computationally expensive.

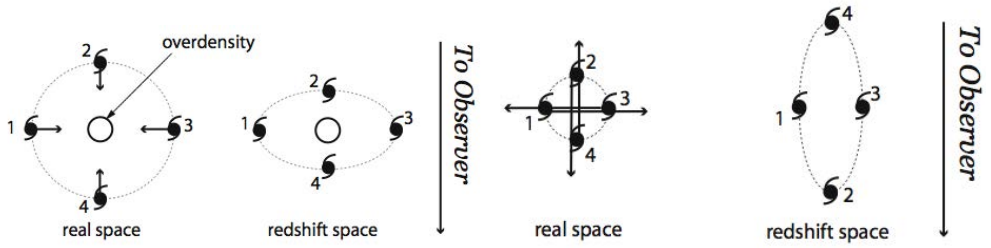

FIGURE 2.4: (Left) Kaiser effect, (Right) Fingers of God, credit: Eiichiro Komatsu, UTAP Seminar, University of Tokyo, Tokyo, Japan. December 18, 2007

2.5 BE-HaPPY: bias emulator for halo power spectrum including massive neutrinos

The impact of massive neutrinos on the linear clustering is pretty well understood but the non linear scales effect remains a subject of investigation. On one side analytical formulas tend to be unaccurate or break on non linear scales. On the other side, semi-analytic models or N-body simulations, best suited to follow the structure formation, did not give the same detailed treatment to neutrinos as to baryons, stars, cold dark matter etc. This was not a first order problem given the precision of the past surveys but it needs to be addressed to extract the most of the data for this new era of "precision" cosmology.

As we have seen in the previous section the power spectra will be dominated by effects such as the bias and redshift space distortions. That is why the idea behind our project was to study the impact of massive neutrinos on these effects. The first part was to model them accurately using N-body simulations and then create an emulator able to quickly implement our calibration for clustering analyses.

Journal of Cosmology and Astroparticle Physics
An IOP and SISSA journal

BE-HaPPY: bias emulator for halo power spectrum including massive neutrinos

David Valcin,[a,1] **Francisco Villaescusa-Navarro,**[b] **Licia Verde**[c,a] **and Alvise Raccanelli**[d,a]

[a]ICC, University of Barcelona, IEEC-UB,
Marti i Franques, 1, E08028 Barcelona, Spain
[b]Center for Computational Astrophysics, Flatiron Institute,
162 5th Avenue, 10010, New York, NY, U.S.A.
[c]ICREA, Pg. Lluis Companys 23, 08010 Barcelona, Spain
[d]Theoretical Physics Department, CERN,
1 Esplanade des Particules, CH-1211 Geneva 23, Switzerland
E-mail: d.valcin@icc.ub.edu, fvillaescusa@flatironinstitute.org,
liciaverde@icc.ub.edu, alvise.raccanelli@cern.ch

Received February 6, 2019
Revised October 10, 2019
Accepted October 25, 2019
Published December 18, 2019

Abstract. We study the clustering properties of dark matter haloes in real- and redshift-space in cosmologies with massless and massive neutrinos through a large set of state-of-the-art N-body simulations. We provide quick and easy-to-use prescriptions for the halo bias on linear and mildly non-linear scales, both in real and redshift-space, which are valid also for massive neutrinos cosmologies. Finally we present a halo bias emulator, **BE-HaPPY**, calibrated on the N-body simulations, which is fast enough to be used in the standard Markov Chain Monte Carlo approach to cosmological inference. For a fiducial standard ΛCDM cosmology **BE-HaPPY** reproduces the simulation inputs with percent or sub-percent accuracy for the halo mass cuts it is calibrated on ($M > \{5 \times 10^{11}, 10^{12}, 3 \times 10^{12}, 10^{13}\} h^{-1} M_{\odot}$) on the scales of interest (linear and well into the mildly non-linear regime). The approach presented here represents a well defined route to meeting the halo-bias accuracy requirements for the analysis of next-generation large-scale structure surveys. The software **BE-HaPPY** can run both in emulator mode and in calibration mode, on user-supplied simulations outputs, and is made publicly available.

Keywords: cosmological parameters from LSS, cosmological simulations, neutrino masses from cosmology, power spectrum

ArXiv ePrint: 1901.06045

[1]Corresponding author.

https://doi.org/10.1088/1475-7516/2019/12/057

JCAP12(2019)057

Contents

JCAP12(2019)057

1 Introduction

To fully take advantage of next generation surveys such as Euclid,[1] DESI,[2] WFIRST,[3] SKA[4] EMU,[5] PSF,[6] and LSST[7] we must improve our modelling of clustering of the tracers of the dark matter density field. The amplitude and scale dependence of the matter power spectrum carry important cosmological informations about e.g., the primordial Universe or the absolute neutrino mass scale, highly complementary to that provided by cosmic microwave background observations. Galaxy or halo bias, which is the relation between these tracers and the underlying matter field, is one of the main source of uncertainty preventing us from achieving this goal. Since galaxies are hosted in dark matter halos, the first step is to model correctly the bias of the halo field or halo bias. Hereafter when we refer to bias we mean the halo bias. Accurate modelling of the halo bias is a necessary (although not sufficient) step to achieve accurate modelling of the observable dark matter tracers. The (halo) bias is usually approximated by a constant on linear scales and then marginalized over. However the approximation of scale independence may be insufficient, even on linear scales. This is all the more true in a cosmological model with massive neutrinos. Indeed, because of their thermal velocities, neutrinos act as relativistic species during the growth of cosmological perturbations and therefore can escape region of higher density fluctuations. This phenomenon, known as the "neutrino streaming" effect, results in suppression of power at small scales. Massive neutrinos also have an additional effect on the growth of structures. As tiny as their mass could be, neutrinos modify the shape of the power spectrum and thus the halo bias. Neutrinos are one of the most mysterious fundamental particles of nature. The value of their masses remains a mystery today. Constraining their masses is among the goals of upcoming surveys. In order to achieve this, accurate theoretical predictions are needed. The purpose of this work is to investigate in detail the shape and amplitude of the halo bias, as a proxy and a preliminary step for galaxy bias, in cosmologies with massive neutrinos into the mildly non-linear[8] and non-linear regime, and offer a fast way to model it.

While not an issue for present-day surveys, Raccanelli et al. [1] (see also Vagnozzi et al. [2]), showed that an inaccurate model for the bias in cosmologies with massive neutrinos will induce a systematic and statistically significant shift in the inferred cosmological parameters for forthcoming surveys.

A solution proposed by e.g., [1, 3–6] to account for this massive neutrinos effect is to use the power spectrum of the cold dark matter plus baryons, $P_{\rm cc}$, instead of that of the total matter, $P_{\rm mm}$, as the relevant theoretical input. It is therefore $P_{\rm cc}$ the quantity to be modelled and thus the one to be used in the definition the tracers bias. On large-scales, in cosmologies with massive neutrinos, the halo bias defined in this way become effectively scale-independent and on smaller scales, its scale-dependence, has been found to be neutrino-mass independent [4–6] (at least to current precision); a small scale dependence even on linear scales is expected [7], but it does not affect the results presented here.

[1] European Space Agency — Euclid, http://sci.esa.int/euclid.
[2] The Dark Energy Spectroscopic Instrument, https://www.desi.lbl.gov.
[3] Wide Field Infrared Survey Telescope, https://wfirst.gsfc.nasa.gov.
[4] Square Kilometre Array, https://www.skatelescope.org.
[5] Australia Telescope National Facility, https://www.atnf.csiro.au/people/Ray.Norris/emu/index.html.
[6] Prime Focus Spectrograph, https://pfs.ipmu.jp.
[7] Large Synoptic Survey Telescope, https://www.lsst.org.
[8] Here mildly non-linear scales refers to scales where non linear effects arise but low order perturbation-theory approximations are still valid.

JCAP12(2019)057

In this work, we use a large set of state-of-the-art N-body simulations with massive and massless neutrinos to study and model the effects induced by massive neutrinos on halo bias. We establish a simple link between the halo bias in models with massive and massless neutrinos. The results of this investigation are summarised in a software package which computes halo bias including its scale dependence, also in the presence of massive neutrinos, **BE-HaPPy**: Bias Emulator for Halo Power spectrum in Python. **BE-HaPPy** provides a bias emulator, fast enough to be used as a plug-in for standard Markov Chain Monte Carlo (MCMC) cosmological analyses, which is accurate, easy to implement and signifies only a small additional computational cost. With **BE-HaPPy** a standard Boltzmann-MCMC can quickly compute also the halo power spectrum into the mildly non-linear regime. While strictly we have calibrated the bias emulator for a fixed set of cosmological parameters, those of a standard concordance LCDM model, we will argue that current data already constrain cosmological parameters enough that the **BE-HaPPy** approach can be used beyond the specific cosmology used here. Nevertheless **BE-HaPPy** can also be run in calibration mode with a user-supplied set of power spectra for arbitrary cosmologies.

Calibration on simulations is not the only approach that has been proposed in the literature. Recently, Muñoz and Dvorkin [3] also studied the impact of massive neutrinos in the galaxy bias and, as [1], reached the conclusion that their effect should be included in any future survey analysis. They developed a code **RelicFast**, [3] which computes the large, linear scales Lagrangian and Eulerian biases in the presence of relics that are non-relativistic today (see [6, 7] for some background on this topic). **RelicFast** and **BE-HaPPy** offer two complementary codes to compute the halo bias in the presence of massive neutrinos. **RelicFast** offers quasi-analytical approach to compute the large-scales scale-dependence of the linear bias through spherical collapse and peak-background split, where **BE-HaPPy** uses fitting and interpolating functions calibrated on N-body simulations on linear-to-mildly non-linear scales. Simulations are less versatile (only a finite set of cosmologies can be explored) but remain one of the best method to obtain the bias especially in the (mildly)non-linear regime. The analytical approach offers valuable physics insights but is valid only on fully linear scales; hence the two approaches are highly complementary. This paper is structured as follows. After an introduction to notation, definitions and set up in section 2, we briefly present the tools we used to study and model the halo bias. In section 3 we introduce the methodology and the choices made towards the development of the emulator, which is designed for both cosmologies with massive and massless neutrinos. Our emulator works both in real- and redshift-space. We discuss in detail the extension of our emulator in redshift-space in section 4. In section 5 we summarize the main properties and features of our emulator and conclude in section 6.

2 Definitions, set up and methodology

The key idea we build upon is that, in presence of massive neutrinos, halo bias should not be defined with respect to total matter $P_{\rm mm}(k)$, but with respect to the cold dark matter (CDM)+baryons field, $P_{\rm cc}(k)$:

$$b_{\rm mm}(k) = \sqrt{\frac{P_{\rm hh}(k)}{P_{\rm mm}(k)}} \;\Rightarrow\; b_{\rm cc}(k) = \sqrt{\frac{P_{\rm hh}(k)}{P_{\rm cc}(k)}}\,. \tag{2.1}$$

The reason behind this idea is that neutrinos barely cluster on small scales [8], so both the abundance and clustering of haloes and galaxies will be characterized by the CDM+baryon

JCAP12(2019)057

density field instead of the total matter field [1, 4, 5]. We note however that it is expected that the scale-dependent growth rate produced by neutrinos will induce a small linear scale-dependent bias [6, 7]. We have neglected this small effect because here we are interested in studying the theoretical templates needed to describe halo clustering on mildly to fully non-linear scales. This effect can be included a posteriori and on larger scales, since it affects $k \lesssim 10^{-2}$ h/Mpc (see [7, 9] for details).

At linear order, the two halo bias definitions can simply be related through the linear transfer functions

$$b_{\rm mm}(k) = \frac{T_{\rm cc}(k)}{T_{\rm mm}(k)}\, b_{\rm cc}(k) \tag{2.2}$$

where

$$T_{\rm cc}(k) = \frac{\Omega_{\rm c} T_{\rm cc}(k) + \Omega_{\rm bb} T_{\rm b}(k)}{\Omega_{\rm c} + \Omega_{\rm b}}\,, \tag{2.3}$$

and the subscripts c, b and m stand for CDM, baryons and total matter (i.e. CDM plus baryons plus neutrinos) respectively. Ω_i represents the energy fraction of each component i at $z = 0$. We note that the total matter power spectrum and the different transfer functions can be easily obtained from Boltzmann solvers such as CLASS and CAMB [10, 11]. Raccanelli et al. [1] showed that the validity of the above equation extends well into the (mildly) non-linear regime.

In this paper we will be working under one important assumption: neutrinos only affect the overall amplitude of the bias ($b_{\rm cc}$), not its scale-dependence

$$b_{\rm cc}(k, M_\nu) \simeq \alpha\, b_{\rm cc}(k, M_\nu = 0) = \frac{b_{\rm cc}^{\rm LS}(M_\nu)}{b_{\rm cc}^{\rm LS}(M_\nu = 0)} b_{\rm cc}(k, M_\nu = 0)\,, \tag{2.4}$$

where we have followed the notation of ref. [1] and $b_{\rm cc}^{\rm LS}$ denotes the large-scale bias for CDM+baryons; $b_{\rm cc}^{\rm LS}$ is computed on linear scales where $b_{\rm cc}$ becomes scale-independent ($b_{\rm cc}^{\rm LS}$ can be interpreted as the limit[9] of $b_{\rm cc}(k)$ for $k \longrightarrow 0$).

The above equation relates the halo bias between two models that have the same values for the parameters h, n_s, $\Omega_{\rm m}$, $\Omega_{\rm b}$ and A_s, but different values of $\Omega_{\rm c}$ and neutrino mass, where $\Omega_{\rm c} = \Omega_{\rm m} - \Omega_{\rm b} - \Omega_\nu$. Conveniently, the scale dependence of $b_{\rm cc}$ can be computed for massless neutrino cosmology. This has two immediately obvious advantages: it can be calibrated on massless neutrino simulations, which are easier to run, and it can be modelled, for example, by resorting to a perturbation theory description of the power spectrum, which validity has been studied extensively for massless neutrinos cosmologies and which can be computed given a set of cosmological parameters.

Equation (2.4) is an approximation that is expected to break down if the neutrino masses are large and/or if the halo bias is high, see ref. [1]. Below we will test the performance and exploit the potential of the above equation.

While we will be focusing our attention on modelling $b_{\rm cc}(k)$ in cosmologies with massive and massless neutrinos, if, in models with massive neutrinos, the desired quantity is the halo bias with respect to the total matter density field, it can easily be obtained from eqs. (2.2) and (2.4) as

$$b_{\rm mm}(k, M_\nu) = \frac{T_{\rm cc}(k)}{T_{\rm mm}(k)} \frac{b_{\rm cc}^{\rm LS}(M_\nu)}{b_{\rm cc}^{\rm LS}(M_\nu = 0)} b_{\rm cc}(k, M_\nu = 0)\,. \tag{2.5}$$

[9] If the small effect –evident on scales larger than $k \simeq 10^{-2}$h/Mpc– of a scale dependence of the linear bias of ref. [6] is to be included in the modelling, then $b_{\rm cc}^{\rm LS}$ should be computed on large linear scales where the bias "plateau" is [6, 7, 9].

JCAP12(2019)057

Below we will present two approaches to model $b_{\rm cc}$: one phenomenological polynomial model (as in [1]) and one perturbation theory-based; each will be calibrated on simulations.

2.1 N-body simulations

The N-body simulations analyzed in this paper belong to the HADES suite (initially presented in [12] but extended since). They were run using the TreePM+SPH code GADGET-III, (see [13] for a description of GADGET-II). The simulations follow the evolution of 1600^3 CDM and 1600^3 neutrino particles in a box of size 1000 comoving h^{-1}Mpc. The gravitational softening of both CDM and neutrinos is set to 15 h^{-1}kpc. All simulations share the value of the following cosmological parameters, that are in excellent agreement with the latest constraints from Planck [14]: $\Omega_{\rm m} = \Omega_{\rm c} + \Omega_{\rm b} + \Omega_\nu = 0.3175$, $\Omega_{\rm b} = 0.049$, $\Omega_\Lambda = 0.6825$, $\Omega_{\rm k} = 0$, $h = 0.6711$, $n_s = 0.9624$ and $A_s = 2.13 \times 10^{-9}$. In models with massive neutrinos we set $\Omega_\nu h^2 = M_\nu/93.14\,{\rm eV}$, where $M_\nu = \sum_i m_{\nu_i}$. We assume three degenerate neutrino masses in our simulations, as neutrino mass hierarchy is not relevant to our approach.

We use the classical particle-based method [8, 15] to simulate the evolution of massive neutrinos in the fully non-linear regime. The initial conditions were generated at $z = 99$ through the method illustrated in [16], i.e., by rescaling the $z = 0$ power spectrum and transfer functions while accounting for the scale-dependent growth factor and growth rate present in cosmologies with massive neutrinos. We have run simulations for two different models. A model with massless neutrinos and a model with $M_\nu = 0.15\,{\rm eV}$. For each model, we have run 10 paired fixed simulations[10] [17, 18]. As shown in [18], this set up improves the statistics of all clustering measurements considered in this work. While we do not expect improvements for the halo bias, a significant reduction on the sample variance of quantities such as the matter or halo power spectrum can be achieved through this setup (see discussion in ref. [17]).

For each simulation we have saved snapshots at redshifts 0, 0.5, 1 and 2. Dark matter haloes are identified through the Friends-of-Friends algorithm [19] with a value of the linking length parameter equal to $b_l = 0.2$. Our halo catalogues consists of all haloes with masses above $5 \times 10^{11}\ h^{-1} M_\odot$. Smaller halos would not have a sufficient number of particle to provide a sufficiently converged halo power spectrum. In reality to study the halo-halo correlation properties at mildly non-linear scales it is customary to consider a minimum number of particles per halo around few tens because at this level the halo correlation function at large scales is expected to be sufficiently converged. We are consistent with this convention.

2.2 Halo mass bins and $k_{\rm max}$

Since the halo bias depends on halo mass, we consider four different halo mass bins. Instead of focusing on narrow mass bins, where our statistics will be limited, we consider all haloes above a certain mass. We work with haloes with masses above $5 \times 10^{11}\ h^{-1} M_\odot$ (M1), $1 \times 10^{12}\ h^{-1} M_\odot$ (M2), $3 \times 10^{12}\ h^{-1} M_\odot$ (M3) and $1 \times 10^{13}\ h^{-1} M_\odot$ (M4). The different mass bins are also shown in table 1. We do not consider mass bins with a higher mass cut given their very low number density in both simulations and data.

Another important parameter in our analysis is the minimum scale — maximum wavenumber — used, $k_{\rm max}$. The amount of information that can be extracted from galaxy surveys depends critically on $k_{\rm max}$, however modelling becomes increasingly complicated and less accurate with increasing k. We explore the performance of our approach as a function of $k_{\rm max}$.

[10] Note that each pair of fixed simulations consists of two simulations.

JCAP12(2019)057

bin name	M1	M2	M3	M4
mass range ($h^{-1}M_\odot$)	$>5\times10^{11}$	$>1\times10^{12}$	$>3\times10^{12}$	$>1\times10^{13}$

Table 1. This table shows the different mass bins we have considered in our analysis.

case	I	II	III
$k_{\rm max}$	$\triangle^2(k_{\rm max},z)=\triangle^2(0.16\,h{\rm Mpc}^{-1},z)$	$\triangle^2(k_{\rm max},z)=\triangle^2(0.12$ h Mpc$^{-1},z)$ & $k_{\rm max}<0.2$ h/Mpc	0.15 h/Mpc at all z

Table 2. This table shows different criteria used to set $k_{\rm max}$.

In particular, following [1], we also consider the three different cases (I, II and III) for $k_{\rm max}$. For case I the maximum k increases in redshift so that the r.m.s of the density fluctuations is constant in redshift and has the same value as the one for $k_{\rm max}=0.16$ h/Mpc at z = 0. Case II is more conservative, having $k_{\rm max}=0.12$ h/Mpc at z = 0; $k_{\rm max}$ initially grows in redshift to keep Δ^2 ($k_{\rm max}$) constant but then it saturates at $k_{\rm max}=0.2$ h/Mpc. Case III is simpler and conservative, as it keeps $k_{\rm max}=0.15$ h/Mpc, constant in redshift. Table 2 summarizes the different cases.

2.3 Shot-noise correction

The discreteness of haloes affects their measured clustering. To model the cosmological clustering of these tracers, we need to separate halo discreteness effects from the cosmic signal in our measurements.

A simple way to do this is by subtracting a Poisson shot-noise $1/n$, where n is the tracer mean number density, from the measured halo auto-power spectrum. In the left panel of figure 1 we show the halo power spectrum for the model with massless neutrinos at $z=0$ for different mass bins. In the same panel we display with dashed lines the expected amplitude of the shot-noise. As can be seen, on small scales, the halo power spectrum is dominated by shot-noise, whose amplitude matches well with the expected $1/n$ value.

In the right panel of figure 1 we plot the halo bias; the amplitude of the halo auto-power spectrum is corrected for shot-noise as explained above. The shot-noise contribution to the halo power spectrum can become sub-Poissonian for the most massive haloes [20–22]. This effect can be explained by the fact that the more massive haloes occupy a larger volume, implying a halo exclusion mechanism that leads to a sub-Poissonian shot-noise. Under these circumstances, the simple Poissonian shot-noise removal will result in unphysical, negative values for the halo power spectrum.

In what follows we still subtract a Poisson contribution to correct for the shot-noise,[11] but to make sure that sub-Poisson effects do not severely impact our results, we restrict our analysis to scales where the amplitude of the shot-noise is less than 80% of the total halo power spectrum. In terms of the widely used nP quantity, where n is the average tracers number density and P the shot-noise subtracted power spectrum, we impose $nP>0.25$. The vertical dotted lines in figure 1 indicate the corresponding scale.

This criteria sets a limit on the smallest scale (largest wavenumber $k_{\rm lim}$) we can consider, which is well into the non-linear regime in all cases: e.g., $k_{\rm lim}\sim0.55$ h/Mpc for the most

[11] As it will be clearer later when performing parameters fit the shot noise amplitude will be corrected by a nuisance parameter to be marginalised over, see appendix A.

JCAP12(2019)057

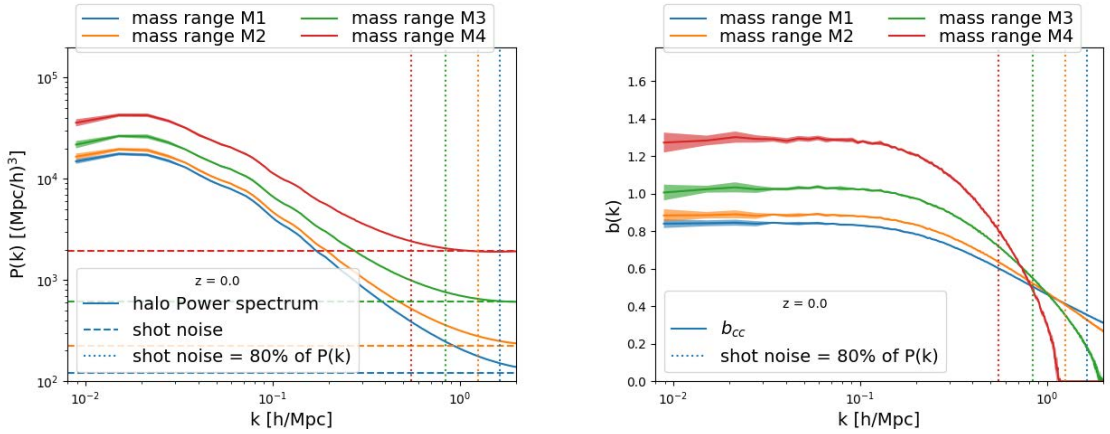

Figure 1. *Left*: halo power spectrum for the massless neutrino model for different mass ranges at $z = 0$. We show the mean and the standard deviation of the 10 pairs of different realizations. The expected Poissonian shot-noise contribution, $1/n$ is shown with horizontal dashed lines for the different mass bins. *Right*: halo bias after subtracting the haloes shot-noise from their auto-power spectrum. On small scales the shot-noise becomes sub-Poissonian for the most massive halos. In this work we restrict our analysis to scales where the amplitude of the shot-noise is smaller than 80% of the total halo power spectrum (i.e., $nP > 0.25$, vertical dotted lines).

stringent case of mass bin M4 at $z = 0$. As it will be clear below, the scales of interest for our emulator satisfy $k < k_{\rm lim}$.

2.4 Perturbation theory

For a given cosmological model our emulator also computes and provides the perturbation-theory prediction of the halo power spectrum. For this we use FAST-PT [23, 24].

FAST-PT offers a computationally efficient way to compute the power spectrum (both of dark matter in real and redshift-space and of biased tracers) through perturbation theory and includes bias up to second order. In our analysis we will also consider third order bias, so we modified FAST-PT to achieve this. The use of a perturbation theory approach such as FAST-PT ensures that **BE-HaPPy** can be used beyond the specific cosmology adopted here.

We note that care must be taken when comparing predictions from FAST-PT versus simulation outputs. The FAST-PT input power spectrum must be precisely sampled; uneven sampling due to a finite number of significant digits will appear as numerical noise [23]. We apply the same k-binning to both the output of FAST-PT and the simulations. This provides a fair comparison among the two results and avoid artificial differences due to binning, that can be important on large-scales.

2.5 Fitting procedure

We calibrate out theoretical model by fitting the model parameters to the outputs of the N-body simulations. For each halo mass range and redshift the simulations provide the halo and the CDM+baryons power spectra; we compute the halo bias as

$$b_{\rm cc}(k) = \left[\frac{(P_{\rm hh}(k) - P_{\rm SN})}{P_{\rm cc}(k)}\right]^{1/2} \tag{2.6}$$

and estimate its errors from the dispersion of the 10 realizations of each cosmology. We then fit our results using any of the two bias models we consider: a phenomenological polynomial

JCAP12(2019)057

model and perturbation theory. The best-fit (i.e., the multi-dimensional maximum of the posterior) and error bars (actually full posterior distribution) of the theoretical model parameters are found by using a Markov Chain Monte Carlo (MCMC) method. The procedure is detailed in appendix A.

While to reduce the impact of shot noise it is customary to define the bias as the ratio between the halo-matter cross power spectrum and the matter auto power spectrum, here we stick to eq. (2.6). This is motivated by the fact that beyond a simple linear bias model the two bias definitions may not coincide. We argue here that the bias obtained from eq. (2.6) is closer to the quantity that will be useful to interpret clustering observations. In doing so we pay the price of a higher shot noise.

Due to the limited number of simulations we have access to, our fits do not account for the correlation between different k-bins, i.e., our likelihood only accounts for the diagonal part of covariance matrix. Therefore, the absolute values of the χ^2 should be taken as a mere guide of the quality of the model.

3 Halo clustering in configuration space

We begin by studying in detail the clustering of haloes in real space. We compare and calibrate with massless neutrino simulations the two bias models adopted and then we quantify the accuracy of our rescaling eq. (2.4) to obtain $b_{\rm cc}(k, M_\nu)$ for the massive neutrinos case from $b_{\rm cc}(k, M_\nu = 0)$.

3.1 Halo bias model I: polynomial

It is well known that the linear, scale independent bias approximation is accurate only on very large-scales [25–28]. On smaller scales, the bias becomes scale-dependent. Following [1], we use a simple phenomenological model and parameterize the halo bias as:

$$b_{\rm cc}(k, z) = b_1(z) + b_2(z)k^2 + b_3(z)k^3 + b_4(z)k^4\,, \tag{3.1}$$

where the coefficients b_1, b_2, b_3 and b_4 are free-parameters whose values depend on redshift, halo mass, M_ν and cosmology. Eq. (3.1) is however unphysical, as isotropy constraints require the bias to have even powers of k [29]. Nevertheless, we expect that the inclusion of the k^3 term improves the quality of the fit. We also use a more physically motivated model with only even powers of k:

$$b_{\rm cc}(k, z) = b_1(z) + b_2(z)k^2 + b_4(z)k^4\,. \tag{3.2}$$

In both models, the value of the linear (large scale) bias is simply given by $b_{\rm cc}^{\rm LS}(z) = b_1(z)$. We fit the halo bias from the massless neutrinos simulations with the above two models at different redshifts and for the different mass bins. Because of $k_{\rm lim}$ considerations (see section 2.3) we set $k_{\rm max} = \{0.55, 0.54, 0.53, 0.42\}$ h/Mpc at $z = \{0, 0.5, 1, 2\}$, respectively. We show our results in figure 2.

Both approaches yield a very good fit (under $\sim 1\%$ until $k_{\rm max}$); the presence of the extra parameter, b_3, slightly improves the quality of the fit on large scales. The best-fit values of the coefficients for all mass bins and redshifts are reported in appendix D. Because of its slightly better fit at the largest scales, and for direct comparison with ref. [1], unless otherwise stated in what follows our reference "polynomial" bias model is that of eq. (3.1). The values of the coefficients for the odd-powers polynomial model are provided by **Be-HaPPy**. This polynomial bias model as calibrated here might not perform as well for different cosmologies.

JCAP12(2019)057

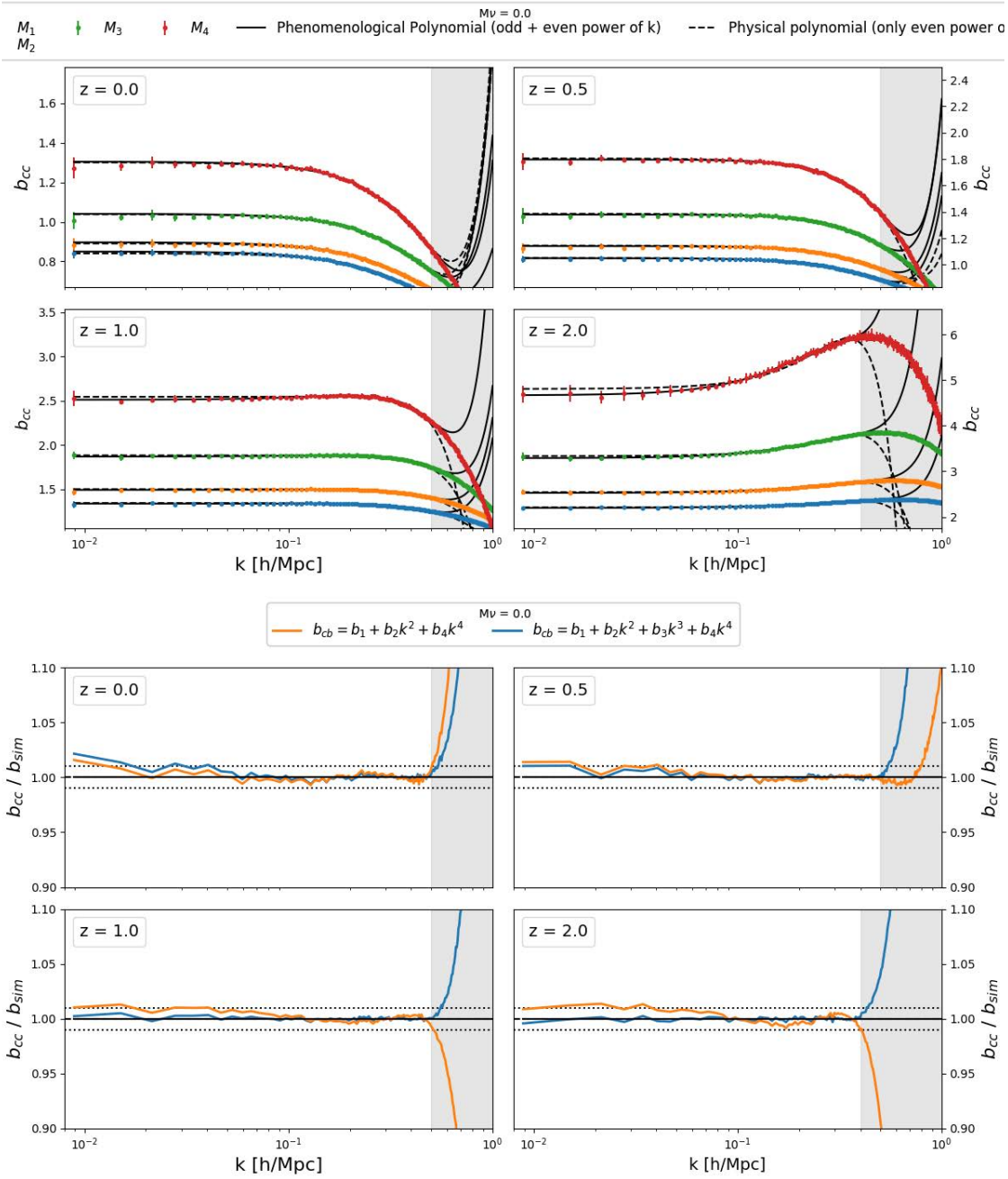

Figure 2. The top four panels show the halo bias for the four different mass bins (color lines) at four different redshifts (different panels) for the model with massless neutrinos. The fits for the phenomenological models of eqs. (3.1) (black solid lines) and (3.2) (black dashed lines) only include $k < k_{\rm lim}$ (excluded scales shown as a grey region). The bottom four panels show the ratio between the halo bias obtained from the simulations and the fit. For clarity we only show the average ratio of the four different mass ranges. (Individual mass bins are shown in appendix B, figure 12, in the fitting range were is not much difference hence justifying showing the mean behaviour). Both models reproduce the halo bias within $\simeq 1\%$ in the relevant k range at all redshifts for all mass bins.

JCAP12(2019)057

For this reason we introduce below a more flexible bias model that can easily account for varying cosmological parameters.

3.2 Halo bias model II: perturbation theory

A more physically motivated model is the perturbation theory-based, non-linear bias expansion [30–33]. This approach has the advantage that the dependence on cosmology is naturally included. Saito et al. [33] showed that a good model to describe the (shot-noise subtracted) halo power spectrum in N-body simulations in the mildly non-linear regime can be obtained by including up to third-order nonlocal bias terms:

$$\begin{aligned} P_{\rm hh}(k) = & \, b_1^2 P_{\rm cc}(k) + 2b_2 b_1 P_{b2,{\rm cc}}(k) \\ & + 2b_{s2} b_1 P_{bs2,{\rm cc}}(k) + 2b_{3nl} b_1 \sigma_3^2 P_{\rm cc}^{\rm lin}(k) \\ & + b_2^2 P_{b22}(k) + 2b_2 b_{s2} P_{b2s2}(k) + b_{s2}^2 P_{bs22}(k) \end{aligned} \tag{3.3}$$

where $P_{\rm cc}(k)$ is the non-linear CDM+baryons power spectrum, $P_{\rm cc}^{\rm lin}$ is the linear CDM+baryons power spectrum, b_1 is the linear bias, b_2 2nd-order local bias, b_{s2} 2nd-order non-local bias and b_{3nl} 3rd-order non-local bias.[12] All other terms represent n-loop power spectra (always for CDM+baryons) whose exact expressions can be found in the appendix C or in [31]. The second-order bias expansion consists of all the terms involving the first and second order coefficients b_1, b_2 and b_{s2}, while the third order expansion also includes the b_{3nl} term whose explicit expression is reported in appendix E. Since FAST-PT does not incorporate this term, we have modified it to account for it.

If the bias is assumed to be local in Lagrangian space, then the Eulerian bias is non-local but the values of b_{s2} and b_{3nl} are related to b_1: $b_{s2} = -4/7(b_1 - 1)$ and $b_{3nl} = 32/315(b_1 - 1)$ [30–34]. Without this constraint, with both b_{s2} and b_{3nl} as free parameters, one accounts for a more general case of a non-local Eulerian bias model. In this work we keep b_1 and b_2 as free parameters, and consider two possibilities for b_{s2} and b_{3nl}: 1) set them to $-4/7(b_1 - 1)$ and $\frac{32}{315}(b_1 - 1)$ (local bias in Lagrangian space), respectively, and 2) leave them as free parameters.

Eq. (3.3), either at second or third order, represents thus our model for the halo power spectrum in configuration space. Note that thanks to eq. (2.4), this perturbation theory-based model is only used for the massless neutrinos cases, which is where its validity and performance has been extensively tested. The halo bias $b_{\rm cc}$ is then obtained from the ratio between $P_{\rm hh}(k)$ and $P_{\rm cc}(k)$, which we fit to the N-body simulations with massless neutrinos for the different mass ranges and redshifts. We show the results in figure 3 where we have set $k_{\rm max} = 0.15$ h/Mpc at all redshifts (case III).

The different perturbation theory models reproduce, within $\simeq 1\%$, the results of the simulations in all cases. As predicted by Saito et al. [33], we also find that (although not easily apparent from the figures) the model where b_{s2} and b_{3nl} are left as a free parameters performs slightly better than the model where they are fixed, in particular on large-scales.

For comparison we also show the polynomial bias model fitted to the same $k_{\rm max}$. The models based on perturbation theory work as well as the polynomial model (within 1% for the fitted k-range) but perform better on extrapolation beyond $k_{\rm max}$.

The best-fit values of the bias coefficients for the different perturbation theory models of this section, for all the mass bins and redshift snapshots are reported in appendix F.

[12] This term encompasses various non-local third-order terms. Since it results in a k-dependent factor that multiplies the linear power spectrum, its contribution become relevant at "large" scales [34] and is therefore considered here. See also appendix E.

JCAP12(2019)057

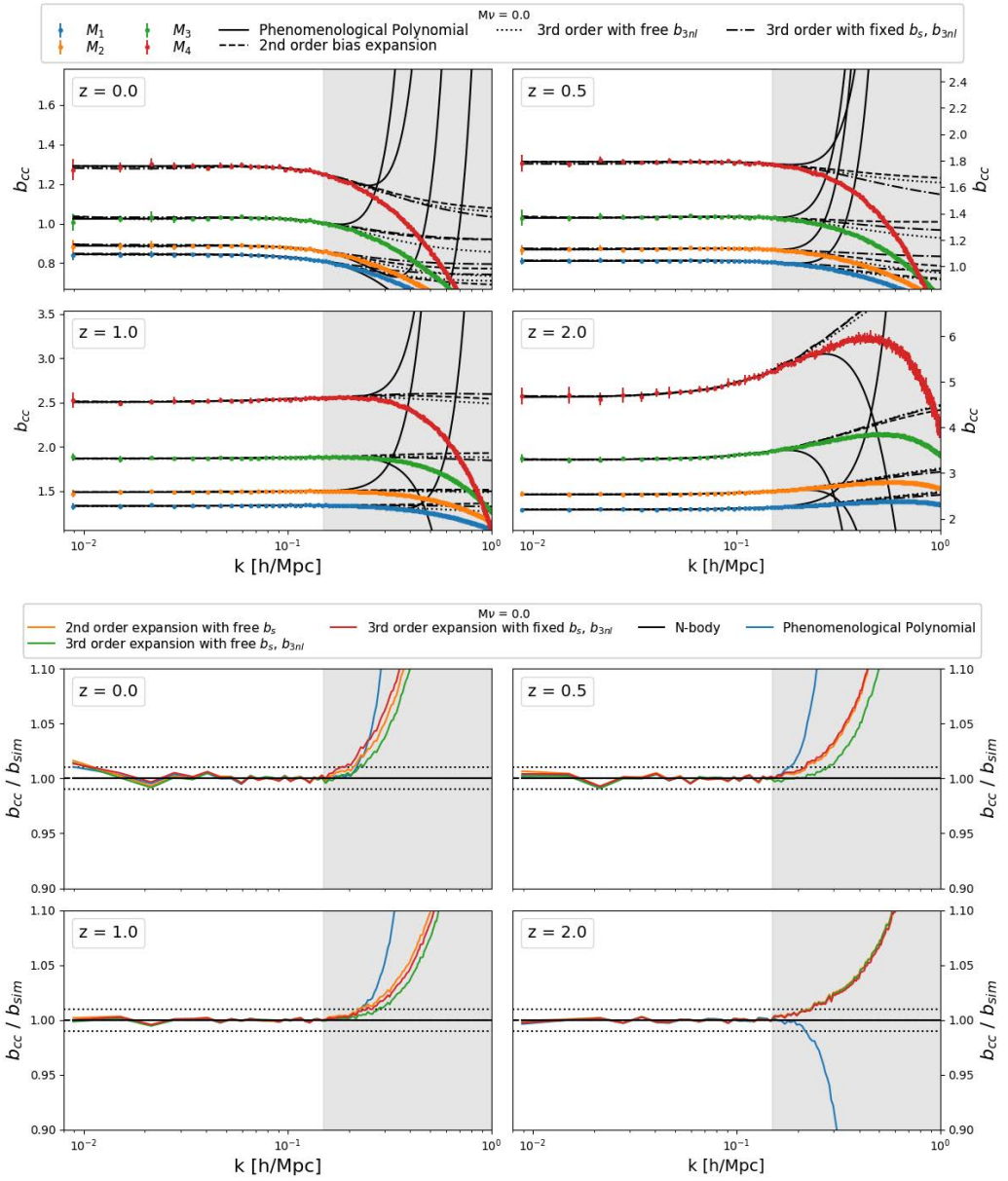

Figure 3. The top panels show the halo bias from the simulations with massless neutrinos for different mass ranges (colored lines) at different redshifts (different panels). We fit these results with the perturbation theory-base model for halo bias (see eq. (3.3)) up to $k_{\rm max} = 0.15$ h/Mpc. We show the best-fits for the models with second-order bias (dashed), third order bias with b_{s2} and b_{3nl} as free parameters (dotted) and third order bias with b_{s2} and b_{3nl} fixed (dot-dashed). The black solid lines correspond to the polynomial model fit up to the same $k_{\rm max}$. The bottom four panels show the ratio between the best-fit models and the results of the simulations. For clarity, we only show the average ratio of the four mass ranges. The models based on perturbation theory work as well as the polynomial model eq. 3.1 (within 1% for the fitted k-range) but perform better on extrapolation beyond $k_{\rm max}$.

JCAP12(2019)057

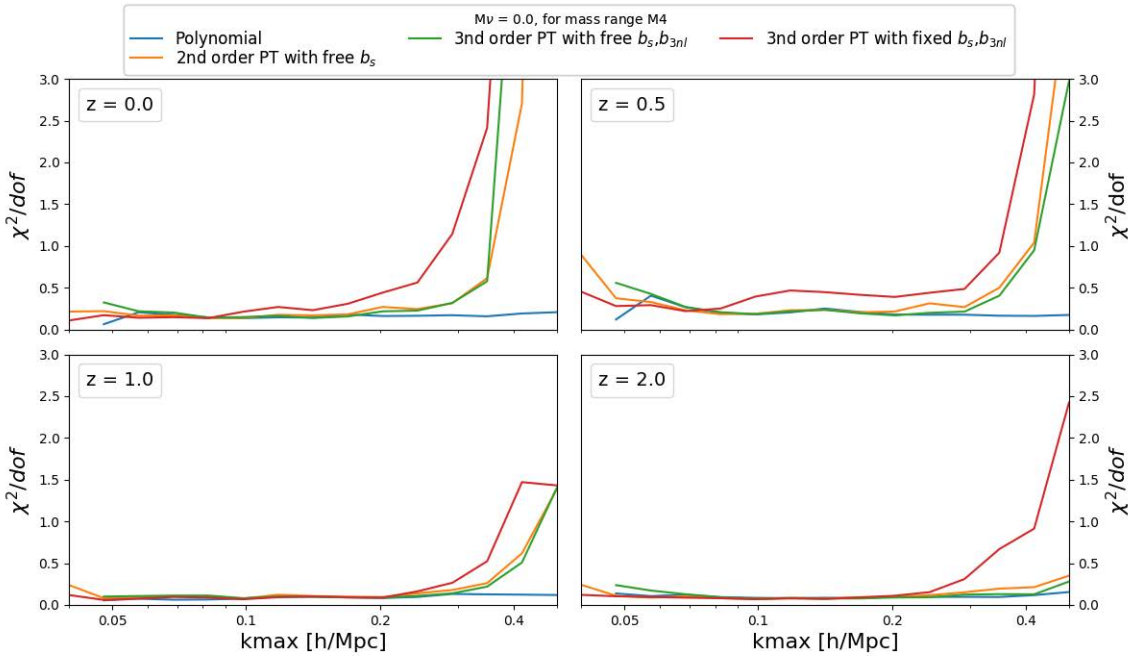

Figure 4. Reduced chi square, χ^2/dof, as a function of $k_{\rm max}$ for the halo bias fit for the mass range M4 (similar results hold for the other mass ranges) from the massless neutrino simulations: polynomial model (blue line) and the different perturbation theory models (orange, green and red; see legend) at different redshifts. While the absolute χ^2 amplitude is not meaningful, a sharp increase in χ^2 with $k_{\rm max}$ denotes breakdown of the model. In general, the perturbation theory model that performs better is the third order bias with free b_{s2} and b_{3nl}.

3.3 Performance as a function of $k_{\rm max}$ and discussion

Above we adopted $k_{\rm max} = 0.15$ h/Mpc when fitting the perturbation theory models to the results of the simulations, finding excellent agreement. This is not surprising since these are mildly-non linear scales. Given the extra information present on smaller scales we explore performance of the model as a function of $k_{\rm max}$.

In figure 4 we show the value of the reduced chi square, χ^2/dof, as a function of $k_{\rm max}$ at different redshifts for the massless neutrino case and for mass bin M4. Since in the fit we do not account for the correlations between k-bins, the absolute value of the χ^2 is not meaningful, but relative values can be used to compare models. As expected, perturbation theory works very well on large scales, but it fails on small scales: perturbation theory-based halo bias models breaks down at $k \sim \{0.15, 0.2, 0.25, 0.3\}$ h/Mpc at redshifts $z = \{0, 0.5, 1, 2\}$. Of the perturbation theory based models, the one with more free parameters, 3rd order bias with free b_{s2} and b_{3nl}, always performs better. For comparison we also show the performance of the polynomial model. Very similar results hold for the other mass ranges.

BE-HaPPy implements both the polynomial and the perturbation theory models. The polynomial model is very accurate on small scales and very fast to evaluate, but its cosmology-dependent part is very approximate and the model itself is not physically well motivated. The perturbation theory models are on the other hand well motivated theoretically, correctly incorporate the dependence on cosmology but its range of validity is smaller than the polynomial model and is more computationally expensive to evaluate. Depending

JCAP12(2019)057

on the requirement of the problem, the user has the freedom to choose between the two approaches.

Inspection of the reported errors on the best fit bias parameters in appendix D and F, indicates that the perturbative expansion coefficients are much better constrained than the polynomial fit coefficients. Not surprisingly, the bias coefficient that more closely determines the large-scale bias is the best constrained parameter, with similar errors across the different models.

This is in large part because we report marginalised errors, and in the polynomial model the parameters are much more correlated than in the perturbation theory-based approach. The parameters of the perturbation theory-based approach are reasonably well constrained, even the third order bias. Our interpretation is that the parameters in the perturbative expansion are "physical" parameters and as such have well defined and roughly independent effects on the observables. While the coefficients in the polynomial expansion are effective parameters, which, taken individually, do not correspond to a specific physical effect. As a result they are more correlated. We thus conclude that the perturbation theory approach represent a better "basis" to retrieve information on bias and cosmology.

We envision that these considerations may be useful even for application beyond the scope of this paper.

3.4 Massive neutrinos

We now discuss how to connect the real-space halo-bias for the massless neutrino case to that in the massive neutrino case; in other words we estimate the performance of eq. (2.4). In analyses where the overall bias amplitude is a nuisance parameter, the correct calibration of $b_{\rm cc}^{\rm LS}$ becomes unimportant.

The approach of eq. (2.4) requires the value of the linear bias in the massive neutrinos case. We will assume that analytical bias models, while not accurate enough to reproduce the linear bias from simulations at percent-level, can reproduce the *ratio* of the linear bias to the required accuracy:

$$\frac{b_{\rm cc}^{\rm LS}(M_\nu \neq 0)}{b_{\rm cc}^{\rm LS}(M_\nu = 0)} = \frac{b_{\rm cc,model}^{\rm LS}, M_\nu \neq 0)}{b_{\rm cc,model}^{\rm LS}(M_\nu = 0)}\,, \tag{3.4}$$

where $b_{\rm cc}$ refers to the value of the simulations' bias (i.e., the square root of the ratio between $P_{\rm hh}$ and $P_{\rm cc}$) while $b_{\rm cc,model}$ stands for the analytic value of the large-scale bias, which can be calculated as:

$$b_{\rm cc,model}^{\rm LS}(z, M_{\rm bin}) = \frac{\int_{M_{\rm min}}^{M_{\rm max}} n(M,z)\, b(M,z) dM}{\int_{M_{\rm min}}^{M_{\rm max}} n(M,z) dM}\,, \tag{3.5}$$

where $n(M,z)$ and $b(M,z)$ are the analytic halo mass function and linear (scale-independent) halo bias at redshift z for haloes of mass M. The right-hand side of eq. (3.4) can then be computed numerically without running expensive simulations. In our calculations we have made use of the Crocce et al. halo mass function [35] while we use the fitting formula of Tinker et al. [36] to estimate the halo bias.[13] We emphasize that in order to compute $b_{\rm cc,model}^{\rm LS}(M_\nu)$

[13]The use of the Crocce mass function is motivated by the fact that we find halos in our simulations with the friends-of-friends algorithm. The Tinker mass function is accurate for halos found via the spherical overdensities method. Note that we use the Tinker halo bias fitting formula, not the peak background-split halo bias derived from the Tinker mass function. While in principle one could have derived the peak background-split halo bias from the Crocce mass function, this has not been presented in the literature and it goes beyond the scope of this paper.

JCAP12(2019)057

we have used the CDM+baryons power spectrum and not the total matter power spectrum. We show below that the above formula works very well.

We can finally express the halo bias in models with massive neutrinos as a simple function of the halo bias in the model with massless neutrinos (see eq. (2.4)):

$$b_{\rm cc}(k, M_\nu) = b_{\rm cc}(k, M_\nu = 0)\alpha_{\rm model} = b_{\rm cc}(k, M_\nu = 0)\frac{b^{\rm LS}_{\rm cc,model}(M_\nu)}{b^{\rm LS}_{\rm cc,model}(M_\nu = 0)} \ . \tag{3.6}$$

As discussed around eq. (2.4), supported by refs. [1, 2, 4–6] here we assume that the definition of the bias with respect to cold dark matter + baryons removes all scale dependence due to neutrino mass on linear and mildly non-linear scales. As a consequence the only effect of massive neutrino is a change of overall amplitude. Values of the α coefficients as a function of mass bin and redshift are shown in appendix J. In practice this means that all the bias coefficients (b_1, b_2, b_{s2} and b_{3nl}) must be rescaled by $\alpha_{\rm model}$ to achieve eq. (3.6) for $b_{\rm cc}$. The above equation is expected to hold when the models with massive and massless neutrinos share the value of $\Omega_{\rm m}$, $\Omega_{\rm b}$, h, n_s and A_s. In the top panels of figure 5 we show with solid lines the halo bias of the massive neutrino model at different redshifts for different halo masses. The dashed lines in the top panels display our prediction using eq. (3.6). As can be seen, the agreement is excellent in all cases; under 1% for the scales of interest and below 5% all the way to $k = 1$ h/Mpc at $z = 2$.

On small scales, for very massive haloes and at high-redshift some differences appear between the simulations and our rescaling procedure. This is somewhat expected (see discussion after eq. (2.4)) since massive haloes are highly biased (see appendix B for a figure with mass-bin dependence of the fit residuals.) Note that most deviations happen beyond the interesting k-range used for the fit, making this issue not too crucial. However it is expected that σ_8 will affect the bias coefficients. The massive and massless neutrinos simulations despite having the same A_s have different σ_8. Interestingly, appendix I shows that large part of the effect is due to the different σ_8 between the massless and massive simulations, indicating that eq. (2.4) holds when σ_8 is kept constant and not the primordial amplitude A_s. A detailed discussion on this point has been presented in refs. [37–39], therefore a more thorough discussion goes beyond the scope of this paper.

To highlight the accuracy of the fitting and rescaling procedure, we compare the massive neutrinos simulations' bias with our bias models in the bottom panels of figure 5 (see caption for details). We find that these models are able to describe very accurately, $\simeq 1\%$ level, the massive neutrinos simulations' outputs. Similarly to what is shown in figure 4, in figure 6 we show the value of the reduced chi square, χ^2, as a function of $k_{\rm max}$ for the massive neutrinos case. The sharp increase in χ^2 with $k_{\rm max}$ denoting breakdown of the model happens at very similar scales as in figure 4 for the massless neutrinos case.

4 Halo clustering in redshift-space

Peculiar velocities induce clustering anisotropies along the line of sight called redshift-space distortions (RSD). RSD if accurately modelled, can be used to retrieve cosmological information, such as the growth rate of matter perturbations. Here we build on [12, 40] to model the effects of massive neutrinos on halo bias in redshift-space.

Below we present the four different models we consider to describe redshift-space distortions before quantifying the accuracy of our models against the simulations' results.

JCAP12(2019)057

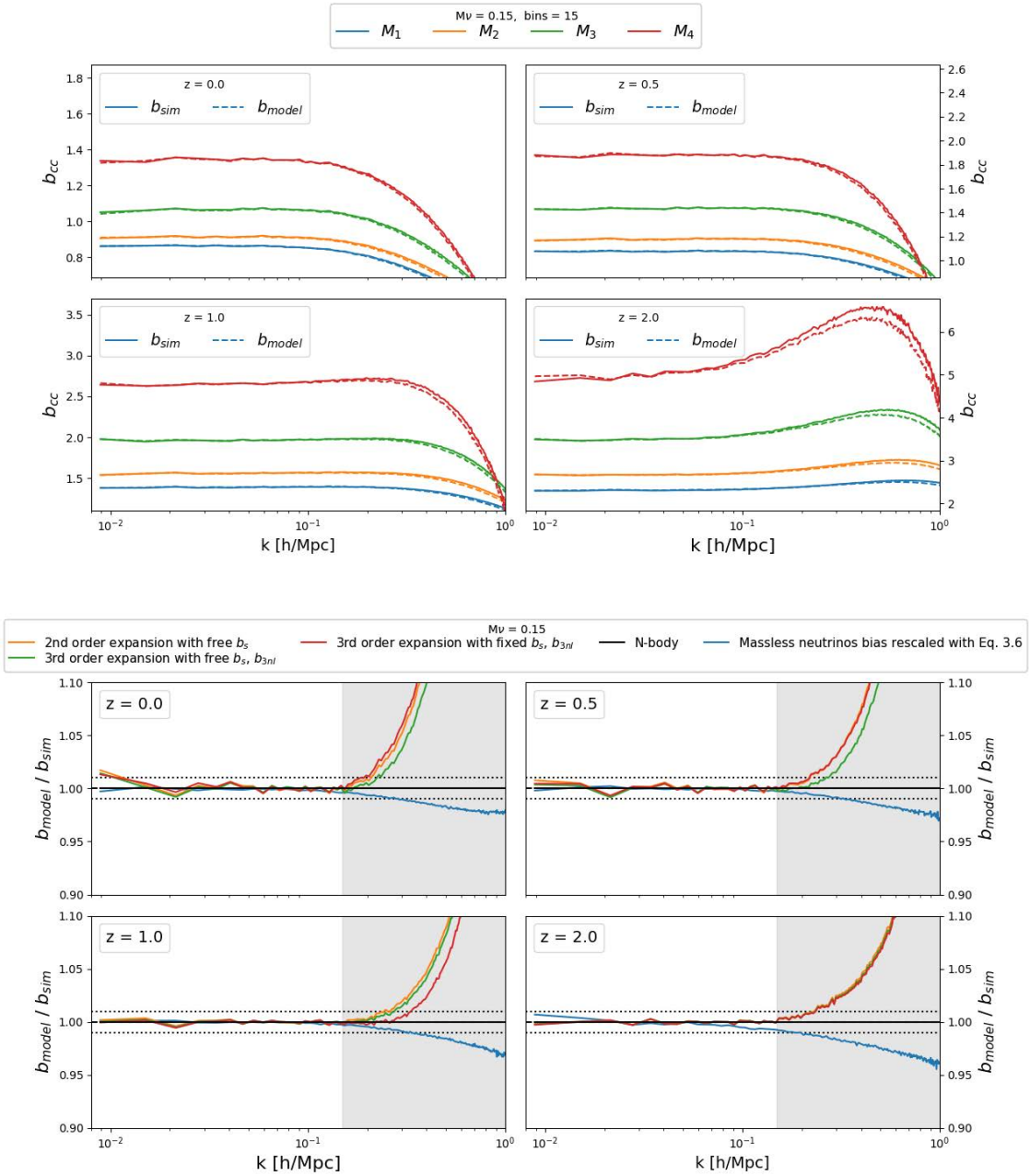

Figure 5. The top panels show the halo bias of the massive neutrino model for different mass ranges at different redshifts. The solid lines represent the results of the N-body simulations, while the dashed lines correspond to our prediction through eq. (3.6). For clarity we do not show the scatter of the simulations results (they are very similar to those of the massless neutrino model). The bottom panels show the ratio between simulations outputs and the model fit. In all cases, we only fit up to $k_{\rm max} = 0.15$ h/Mpc. The lines show the mean among the four different mass ranges. Individual mass bins are shown in appendix B, figure 13. We find that our model to relate the bias of massive neutrino models to massless neutrinos models works very well down to the smallest scale we consider. Our perturbation theory model is also able to accurately describe the results of the simulations up to $k_{\rm max}$.

JCAP12(2019)057

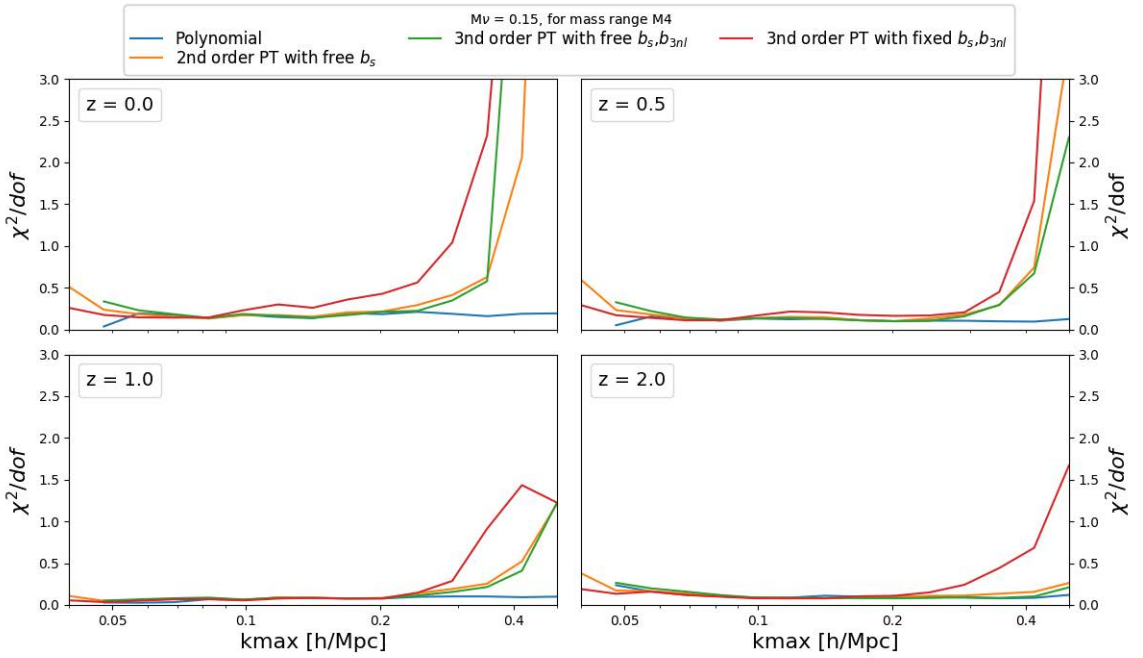

Figure 6. Reduced chi square, χ^2/dof, as a function of $k_{\rm max}$ for the halo bias fit for the mass range M4 (similar results hold for the other mass ranges) from the massive neutrino simulations: polynomial model (blue line) and the different perturbation theory models (orange, green and red; see legend) at different redshifts. While the absolute χ^2 normalisation is not meaningful, a sharp increase in χ^2 with $k_{\rm max}$ denotes breakdown of the model. In general, the perturbation theory model that performs better is the third order bias with free b_{s2} and b_{3nl}.

4.1 RSD model I: linear theory, Kaiser

Villaescusa-Navarro et al. 2018 [12] showed that, at linear level — Kaiser RSD [41] —, the (shot-noise subtracted) halo power spectrum in redshift-space (indicated by the s superscript) in models with massive and massless neutrinos is given by

$$P^s_{\rm hh}(k,\mu) = (b_{\rm cc} + f_{\rm cc}\,\mu^2)^2 P_{\rm cc}(k)\,, \tag{4.1}$$

where $P_{\rm cc}(k)$ is the CDM+baryons power spectrum, μ the cosine of the angle with respect to the line of sight and $f_{\rm cc}$ is the linear CDM+baryons growth rate ($d\ln\sqrt{P_{\rm cc}(k,a)}/d\ln a$, with a the scale factor) of the CDM+baryons component. While in the original Kaiser [41] formulation the configuration space power spectrum should be the linear one, in what follows we will use a non-linear $P_{\rm cc}(k)$ in eq. (4.1) as well as the full scale-dependent $b_{\rm cc}(k)$. In the figures below we will use $P_{\delta\delta}$ computed with FAST-PT (see appendix G) from a CDM + baryons linear power spectrum for $P_{\rm cc}(k)$ and our model (see captions) for $b_{\rm cc}(k)$.

4.2 RSD model II: Scoccimarro

Scoccimarro [42] was among the firsts to propose a non-linear extension of the large-scale, linear Kaiser model for RSD:

$$P^s(k,\mu) = P_{\delta\delta}(k) + 2f\mu^2 P_{\delta\theta}(k) + f^2\mu^4 P_{\theta\theta}(k) \tag{4.2}$$

JCAP12(2019)057

where $P^s(k,\mu)$ is the matter power spectrum in redshift-space,[14] $P_{\delta\delta}(k)$, $P_{\delta\theta}(k)$ and $P_{\theta\theta}(k)$ are the density, density-velocity and velocity power spectrum, respectively.

For our purposes, in models with massive neutrinos, the density and velocities and therefore the power spectra are the ones of the CDM+baryons field, not of the total matter field. $P_{\delta\theta}$ and $P_{\theta\theta}$ have the same shape as $P_{\delta\delta}$, and thus can be computed with FAST-PT in the same fashion. As an example we take eq. 64 of [42]:

$$P_{\theta\theta}(k) = \underbrace{P(k)}_{\text{linear part}} + \underbrace{2\int [G_2(p,q)]^2 P(p)P(q)d^3q}_{P_{22}(\mathrm{k})} + \underbrace{6P(k)\int G_3(k,q)P(q)d^3q}_{P_{33}(\mathrm{k})} \tag{4.3}$$

where $G_2(p,q)$ and $G_3(k,q)$ are perturbation theory kernels. The P_{22} convolution integrals are computed using spherical harmonics after the kernel is expanded in Legendre polynomials (cf. section 2.2 of [23]). The P_{13} integrals are more difficult because the wavenumber structure is different and the kernels are more complicated. It also requires regularization to correct for IR divergence (see section 2.3 and 2.4 of [23]). As a cross check of our implementation, we compare the results of Scoccimarro et al. [42] with our calculations, obtained using similar cosmological parameters to theirs, finding a good agreement (see figure 15 in appendix G). To generalise eq. (4.2) to haloes we use

$$P^s_{\rm hh}(k,\mu) = b^2_{\rm cc}(k)P_{\delta\delta}(k) + 2b_{\rm cc}(k)f\mu^2 P_{\delta\theta}(k) + f^2\mu^4 P_{\theta\theta}(k)\,. \tag{4.4}$$

4.3 RSD model III: TNS

The above model is the basis for one of the most popular models of redshift-space distortions: the Taruya, Nishimichi and Saito (TNS) model [43] where several coefficients were added to the Scoccimarro model to account for the mode coupling between the density and velocity fields. In summary TNS adds two "coefficients", A and B, that depend on k, μ and f to eq. (4.2).

FAST-PT incorporates routines to compute these coefficients for the matter power spectrum. If we apply a linear bias to the matter fluctuation $\delta_g \longrightarrow b_1\delta(x)$, it is easy to show that expressions for the A and B coefficients for the halo power spectrum become:[15]

$$A(k,\mu,f) \Rightarrow b_1^3 A(k,\mu,\beta) \tag{4.5}$$

$$B(k,\mu,f) \Rightarrow b_1^4 B(k,\mu,\beta) \tag{4.6}$$

where b_1 is the linear bias, $\beta = f/b_1$. While a linear bias approximation is not sufficient for this model, as indicated in [31, 33, 43] the bias coefficient in front of the A and B functions, which are higher-order corrections, is the linear one i.e., b_1.

4.4 RSD model IV: eTNS

To go beyond linear bias, we consider the so-called eTNS bias model [31, 33].

$$P^s_{\rm hh}(k,\mu) = P_{\rm hh}(k) + 2f\mu^2 P_{h,\delta\theta}(k) + f^2\mu^4 P_{\theta\theta}(k) + b_1^3 A(k,\mu,\beta) + b_1^4 B(k,\mu,\beta) \tag{4.7}$$

[14] In what follows in order not to carry too many subscripts when in redshift space and when not ambiguous we will drop the mm subscript from the matter power spectrum symbol.

[15] A and B are in fact proportional to b^2, the other powers of b come from the $k\mu f$ factor in the integrals of $A(k,\mu,f)$ and $B(k,\mu,f)$.

JCAP12(2019)057

where b_1 is the linear bias, $\beta = f/b_1$ and it is assumed that there is no velocity bias. $P_{\rm hh}(k)$ is given by eq. 3.3 and the expression of $P_{{\rm h},\delta\theta}(k)$ is given by [31]

$$P_{{\rm h},\delta\theta}(k) = b_1 P_{\delta\theta}(k) + b_2 P_{b2,\delta}(k) + b_{s2} P_{bs2,\delta}(k) + b_{3nl}\, \sigma_3^2\, P^{\rm lin}(k)\,. \tag{4.8}$$

We limit ourselves to the linear bias term when computing the A and B correction terms in eq. 4.7. Of course, for models with massive neutrinos, the above quantities need to be computed by using the CDM+baryons power spectrum, not the total matter power spectrum.

4.5 Fingers of God

The motions of particles/galaxies inside haloes induce a characteristic feature in redshift-space: the so-called Fingers-of-God (FoG). When modeling redshift-space distortions, it is important to account for this effect, as it dominates the amplitude and shape of the power spectrum on small scales but can also propagate to large scales.

Here we characterize the FoG as:

$$F(k,\mu) = \exp\left[-k^2 f(z)\sigma_v(z)^2\mu^2\right] \tag{4.9}$$

where $\sigma_v(z) = D(z)\sigma_0$, $D(z)$ is the linear growth rate of perturbations normalised to unite at $z = 0$ and σ_0 is a free parameter representing the effective velocity dispersion of particles/galaxies inside halos. This approach goes under the "streaming" models category i.e., the FoG term is treated independently of the linear and mildly non-linear effects. The effect of FoG on the clustering of haloes should be small if not negligible, but **BE-HaPPy** allows the user to optionally include it.[16]

4.6 Comparison to massless neutrinos simulations

From the massless neutrino simulations, we computed the monopole of the halo redshift-space power spectrum for different mass ranges at different redshifts. To improve the statistics, we have taken the average of RSD along the three cartesian axes. The simulation outputs are used to study the accuracy of our theoretical models: the Kaiser (section 4.1, with non-linear rather than linear power spectrum — hereafter non-linear Kaiser), Scoccimarro (section 4.2), TNS (section 4.3) and eTNS (section 4.7).

For each of the above models, we fit the massless neutrinos simulations' redshift-space power spectrum monopole at different redshifts and for different mass ranges and $k_{\rm max} = 0.15$ h/Mpc. In this case we do not fit for the value of the bias parameters, but use the values we obtained from the real space fit. Thus, the only free parameter is σ_0. We show the results in figure 7. The best fit σ_0 is in the range 6–8 Mpc/h which is consistent with the findings of e.g., [44].

All models are able to describe the clustering of haloes in redshift-space as observed in the HADES simulations up to $k_{\rm max}$, with percent accuracy. As expected, the model that performs better is eTNS, with sub-percent accuracy on a wide k-range. The deviations of the model at the largest scales (top left panel of the bottom half of figure 7) are probably due to sample variance. In fact, to reproduce more closely a realistic analysis, we have used the FAST-PT non-linear $P_{\rm cc}(k)$, instead of the simulations outputs. We have checked that using the simulations outputs for $P_{\rm cc}(k)$ instead, the deviation effectively disappears.

[16] A small but possibly non-negligible value for σ_0 for halos has been found in the literature before [44]. It can be argued that this extra degree of freedom absorbs high k residuals in the fit arising from limitations of the modelling.

JCAP12(2019)057

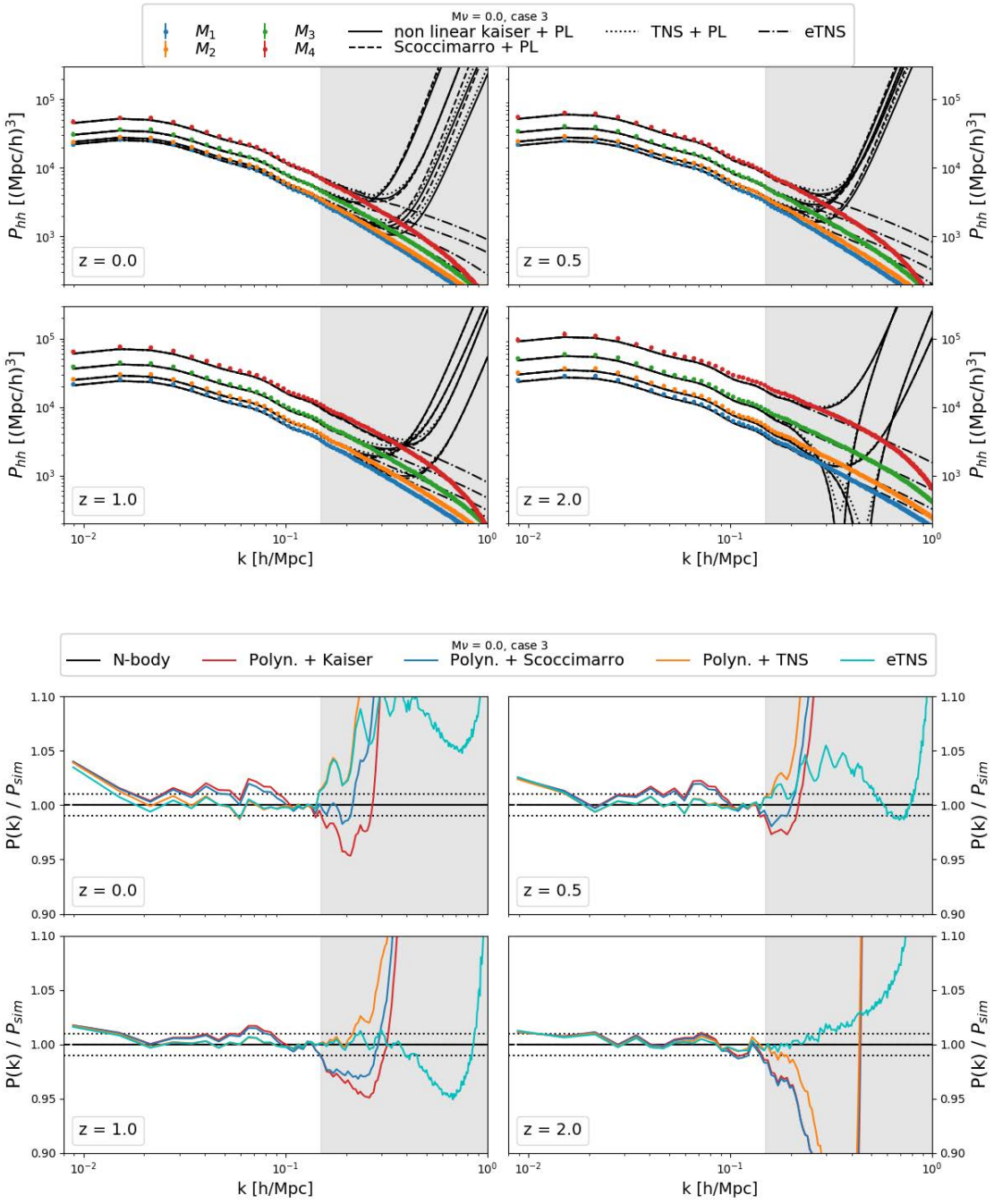

Figure 7. The top panels show the massless neutrinos N-body simulations' redshift-space power spectrum monopole for different mass ranges at different redshifts. We then fit these results using our four different theoretical models: non-linear Kaiser (4.1) with polynomial bias (solid black), Scoccimarro (4.2) with polynomial bias (dashed black), TNS (4.3) with polynomial bias (dotted black) and eTNS (4.7) (dot-dashed black). In all cases we set $k_{\rm max} = 0.15$ h/Mpc for the fit (case III). The bottom panels display the ratio between the fits and the simulations outputs. For clarity, we show the average results of the four different mass ranges. The models reproduce accurately the results of the simulations, with the eTNS performing better in all cases.

JCAP12(2019)057

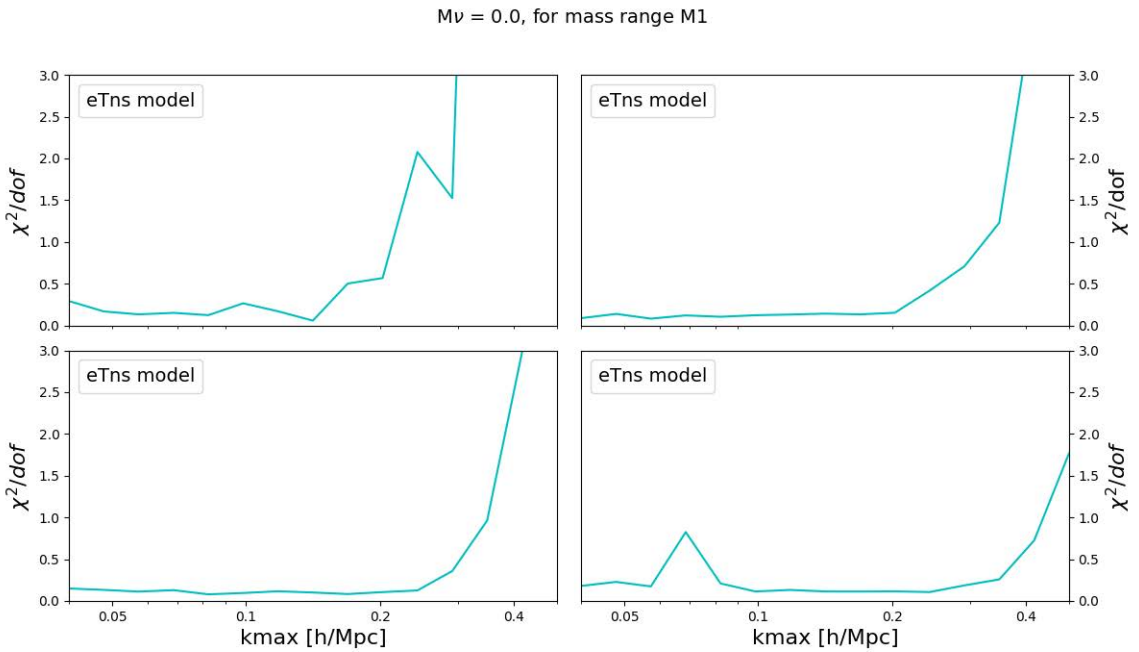

Figure 8. Reduced chi square, χ^2/dof, as a function of $k_{\rm max}$ for the halo power spectrum fit for the mass range M1 (similar results hold for the other mass ranges) from the massless neutrino simulations in redshift-space: eTNS model at different redshifts. While the absolute χ^2 normalisation is not meaningful, a sharp increase in χ^2 with $k_{\rm max}$ denotes breakdown of the model.

To qualitatively assess the (small scales) breakdown of the modelling in redshift-space, in figure 8 we show the reduced chi square, χ^2/dof, as a function of $k_{\rm max}$ for the eTNS model. The behaviour (the χ^2 dependence on the redshift and different bias models but weak dependence on the mass bins is expected from perturbation theory.).

4.7 Comparison to massive neutrinos simulations

We finally quantify the performance of our approach for the redshift-space massive neutrinos case. The massless to massive neutrinos models re-scaling eqs. (2.4) and (3.4) for the Kaiser eq. (4.1) and Scoccimaro eq. (4.2) models is straightforward, since the full expression of the bias $b_{\rm cc}(k)$ appear explicitly in the equations. For the other models, all the perturbation theory bias coefficients b_1, b_2, b_{s2} etc. (calibrated in real space and for massless neutrinos) must be rescaled according to eq. (3.6) and related discussion.

We use the halo bias $b_{\rm cc}$ model (or alternatively the $\alpha_{\rm model}$ for the bias parameters in TNS and eTNS) calibrated in real space for massless neutrinos, leave σ_0 as a free parameter (in the spirit that in any analysis it will be a nuisance parameter to be marginalised over) re-scale the bias coefficients in the presence of massive neutrinos (eq. (3.6)) and apply the redshift-space mapping of section 4.1, 4.2, 4.3, 4.4 with the FoG modelling of section 4.5. To quantify the performance of this approach (calibration on massless neutrino simulations and rescaling) we compare this (benchmark) to a fit to $b_{\rm cc}$ (or the perturbation theory bias parameters) done directly on the massive neutrino simulations outputs (in real space). A summary is reported in table 3. The comparison is shown in figure 9.

JCAP12(2019)057

	fit of $M_\nu \neq 0$ sims	**BE-HaPPy**
bias coefficients	fitted on $b_{\rm cc}(k, M_\nu = 0.15)$	fitted on $b_{\rm cc}(k, M_\nu = 0.0)$
linear bias b_1 input for A (4.5) and B (4.6) coefficients	fitted on $b_{\rm cc}(k, M_\nu = 0.15)$	fitted on $b_{\rm cc}(k, M_\nu = 0.0)$
velocity dispersion	free parameter	free parameter
rescaling	no	yes

Table 3. Benchmark of Be-HaPPY performance in figure 9. BE-HaPPy (third column) uses only massless neutrino simulations to calibrate the fit and obtains $b_{\rm cc}$ via rescaling. The performance of this is quantified by comparing it to a $b_{\rm cc}$ fit done on massive neutrino simulations (second column).

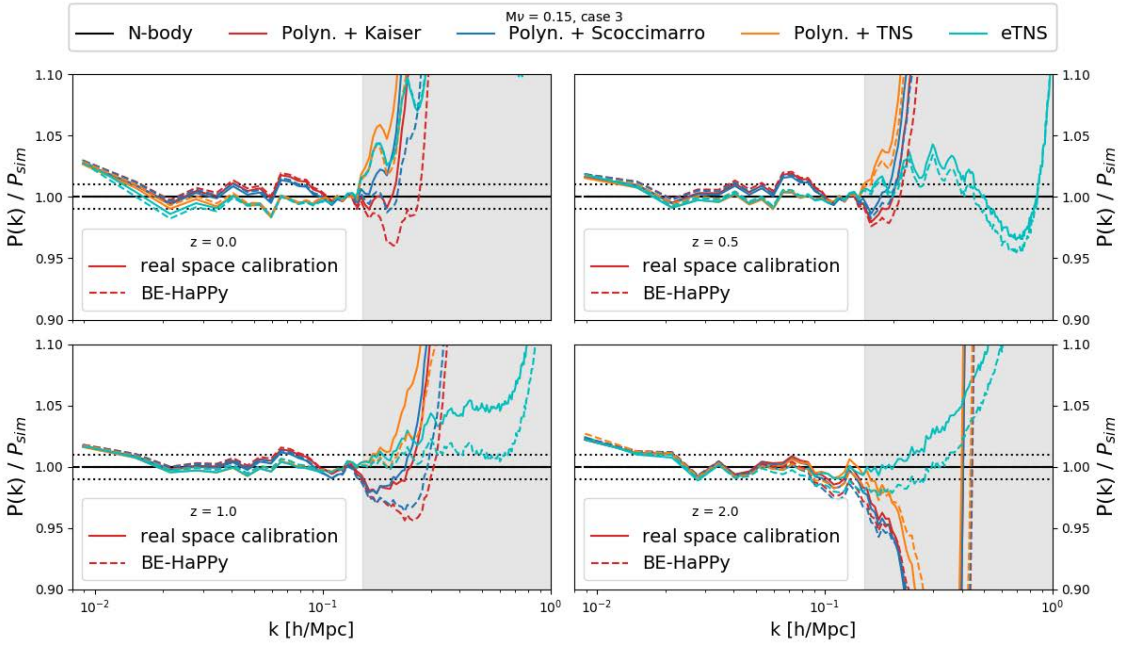

Figure 9. Residuals between $b_{\rm cc}(k)$ in redshift-space from **BE-HaPPy** and $b_{\rm cc}(k)$ calibration done for (configuration space) massive neutrinos simulations. See table 3 for details. The $> 1\%$ deviations at high k and high z arise from the σ_8 mis match, see appendix I.

The performance is qualitatively similar to that of the massless neutrinos case except for the highest redshift panel. The $> 1\%$ mis match at high k and high z arises from the σ_8 mis match (See discussion below eq. (3.6) and appendix I).

5 BE-HaPPy

BE-HaPPY, that stands for Bias Emulator for Halo Power spectrum Python is a plug-in designed to be implemented in MCMC softwares.[17] The primary goal of **BE-HaPPY** is to accurately predict the halo power spectrum in real- and redshift-space in a very compu-

[17] Our current implement supports only MontePython [45].

JCAP12(2019)057

tationally efficient manner. Explanations on the installation of the code, its usage and its various components are available on the author github account.[18]

BE-HaPPY as a plug-in for MontePython [45] can be ran in two modes: *calibration mode* and *emulator mode*.

In the *calibration mode* the code goes through all the calibration steps described in this paper. It provides our modified FAST-PT and the calibration procedure. The user must supply the necessary simulations outputs. In this way cosmologies different from the fiducial one used here (and different mass ranges, redshifts snapshots etc.) can be explored. While we expect that for cosmologies consistent with current data, and for the expected precision of forthcoming surveys the provided calibration is good enough , it may be of interest to explore detailed dependence of calibration for other cosmological models to adjust to the required precision of next generation surveys.

The good performance of the rescaling eq. (3.6) implies that only calibration on massless neutrinos simulations is really necessary, provided that the corresponding massive neutrinos case of interest has the same values for the other cosmological parameters and in particular the same value for the σ_8 parameter. Of course, if the user envisions marginalising over the overall bias amplitude, calibration is also only necessary on massless neutrinos simulations. However, as long as the other cosmological parameters do not vary much, we expect our modelling to still perform well.

In the *emulator mode*, **BE-HaPPY** uses the templates, bias coefficients and RSD modelling calibrated for our fiducial cosmology (or user supplied as a result of a previous *calibration mode* run) to provide an emulator for the halo bias. This is then used in the standard MCMC run. The implicit approximation done here is that in the MCMC exploration of parameter space, the cosmology does not deviates too drastically from the fiducial one as to invalidate the calibration. This is more of a concern for the polynomial bias modelling than for the perturbation theory-based one. Note that marginalisation over bias parameters (with user-supplied priors) is also an option of the code, thus making this mode (emulator+ bias parameters marginalisation) very robust to the choice of cosmology. Although beyond the scope of this paper, one could envision sampling the (cosmological) parameter space also for other parameters than neutrino mass and use techniques such as Gaussian processes to extend our modelling beyond the fiducial cosmology adopted here. **BE-HaPPY** would still provide the workhorse for such an effort. It could provide calibration in several regions in parameter space around specific sets of cosmological parameters. The the Gaussian processes approach (or similar) would smoothly interpolate across these regions.

Below we summarise the features of **BE-HaPPY**, more info can be found in the code repository.

1. Four cumulative mass bins are available (see table 1).
2. Results for four different $k_{\rm max}$ values; cases I, II and III (see table 2).
3. Outputs between $z = 0$ and $z = 2$; calibrations at redshifts 0, 0.5, 1 and 2 and interpolations in between.
4. Three models of bias are available: 1) linear, 2) polynomial (section 3.1), and 3) perturbation theory expansion up to third order (section 3.3).

[18]The code in emulator mode and calibration mode will be made available on the same repository. In this modality the code relies on our extension of the FAST-PT software, so any public release must be coordinated across different collaborations.

JCAP12(2019)057

5. Four RSD models are available: (non-linear) Kaiser (section 4.1), Scoccimarro (section 4.2), TNS (section 4.3) and eTNS (section 4.4).

6. The user has the option to include the Fingers of God term (section 4.9) with σ_0 as a free parameter.

7. Text files of bias coefficients and PT terms. User has the option to substitute these with those for a different model/calibration.

BE-HaPPy is designed to work with both models with massless and massive neutrinos. Importantly, the output for the massive neutrinos models is obtained through our proposed rescaling of the bias for massless neutrinos. This reduces the dimensionality of the parameter space, enabling a faster calculation. **BE-HaPPy** allows the user to output halo bias results with respect to CDM+baryons or total matter (eq. (2.5)).

We calibrated the emulator so **BE-HaPPy** achieves percent or sub-percent precision on the scales of interest (see figures 3, 5 (bottom panel), 7 and 9 (bottom panel)). This is the precision level achieved in fitting the relevant quantities from the HADES simulations. This is not necessarily the accuracy level achieved in fitting the relevant quantities in the real Universe. Moreover this calibration may not work as well for cosmologies that differ significantly from our fiducial one and used in the simulations.

We designed the code to be as modular as possible, providing text files for the required quantities (bias and perturbation theory coefficients). While we use FAST-PT to compute the non linear density spectrum $P_{\rm cc}(k)$ this can be substituted by another cosmic emulator (e.g., [46]) or Halofit [47]. It is also possible to use softwares like **RelicFast** to include large-scales linear effects not included here. **BE-HaPPy** may also be used with a different cosmological model as a test. To keep track of the impact of any deviations from our settings, we added an "error" feature in the code where the user can access the relative error (value and percentage) at each k of the selected arrays between the power spectra computed by **BE-HaPPy** and those obtained from the original suite of N-body simulations we used for the calibration. This feature is only available for the cosmology and neutrino masses ($M_\nu = 0$ and $M_\nu = 0.15\,\mathrm{eV}$) models of the simulations considered here.

6 Conclusions

We have presented fast and accurate modelling of the halo bias in Fourier space which includes the effect of massive neutrinos and applies to both real and redshift-space. The modelling has been calibrated on a suite of state-of-the-art N-body simulations (the HADES simulations).

Our approach relies on the fact that, unlike that defined with respect to the total matter, the halo bias with respect to the CDM+baryons, $b_{\rm cc}$, does not show extra scale dependence induced by –and dependent on– neutrino masses. Hence we have provided a detailed calibration and analytic expression of $b_{\rm cc}(k)$ which holds into the mildly non-linear and even non-linear regime. We have used two approaches: one phenomenological, where the halo bias takes a polynomial form in k, and a perturbation-theory based.

The $b_{\rm cc}(k)$ model so calibrated on massless neutrinos simulations can then be converted to that for massive neutrinos models by a simple (analytic) amplitude rescaling. While we have carefully quantified how this rescaling works, and tested its performance with massive neutrinos N-body simulations, it is important to keep in mind that in most cosmological analyses the (scale-independent) bias amplitude is treated as a nuisance parameter and

JCAP12(2019)057

marginalised over. The scale dependence of the halo bias however is important and must be accurately modelled as it has been shown that if neglected can induce statistically significant systematic shifts in the recovered cosmological parameters from forthcoming surveys.

The polynomial bias model reaches percent to sub-percent accuracy into the non-linear regime, the perturbation theory based model achieves the same accuracy only in the mildly non-linear regime. The modelling of redshift-space distortions, being also perturbation theory-based, reaches percent to sub-percent accuracy in the mildly non-linear regime. This is the accuracy level at which the relevant quantities of the input simulations are being recovered by **BE-HaPPy**. This reported accuracy level does not take into account that the input simulations may not be a sub-percent description of the Universe. For example only specific halo mass bins were considered, the mass resolution of the simulations is set as well as the fiducial cosmology. With the advent of more accurate simulations **BE-HaPPy** should be re-calibrated.

Observable tracers such galaxies are likely to reside in dark matter halos, so while the model we provide here for the halo bias might not be sufficient to interpret future galaxy surveys, it is a necessary preliminary ingredient.

We provide a fast emulator for the halo bias (**BE-HaPPy**). **BE-HaPPy** returns the halo bias as function of scale, redshift and halo mass, in real or redshift-space for both massless and massive neutrino cosmologies, as well as the perturbation theory-based non-linear redshift-space halo power spectrum. The user can select which modelling to use, the scales of interest and other option about e.g., redshift-space distortions implementation. **BE-HaPPy** is fast enough to be included in standard Markov chain Monte Carlo runs at only small additional computational cost. Since we have calibrated **BE-HaPPy** on a concordance ΛCDM set of cosmological parameters, the polynomial bias model might be less robust to change of cosmology than the perturbation theory approach. For cosmological models significantly different from the concordance ΛCDM we recommend the users to check the **BE-HaPPy** performance and if needed to re-calibrate it.

The next-generation large-scale structure surveys will provide unprecedented wealth of information about the clustering properties of the Universe provided that the modelling tools used reach the required accuracy. **BE-HaPPy** aspires to be one of them. It provides an easy solution to compute the halo power spectrum in massive and massless neutrinos cosmologies taking into account crucial effects such as scale-dependent bias, neutrino bias or redshift-space distortions. It can be easily re-calibrated on user-supplied simulation outputs which accuracy should match the required accuracy of the model, set, in turn, by the expected precision achievable from the data set of interest. The design of the code makes it possible to use as a complement to other cosmological codes or even to add other cosmological phenomena like Alcock-Paczynski, wide-angle or GR corrections. We envision it will be useful for the analysis of next-generation surveys such as Euclid, DESI, WFIRST, SKA, PFS, EMU and LSST.

Acknowledgments

We acknowledge support by the Spanish MINECO under projects AYA2014-58747-P AEI/FEDER UE; MDM-2014-0369 of ICCUB (Unidad de Excelencia Maria de Maeztu) and European Union's Horizon 2020 research and innovation programme ERC (BePreSySe, grant agreement 725327). Simulations were run at the **Rusty** cluster of the Center for Computational Astrophysics. The work of FVN is supported by the Simons Foundation. AR has received funding from the People Programme (Marie Curie Actions) of the European Union

JCAP12(2019)057

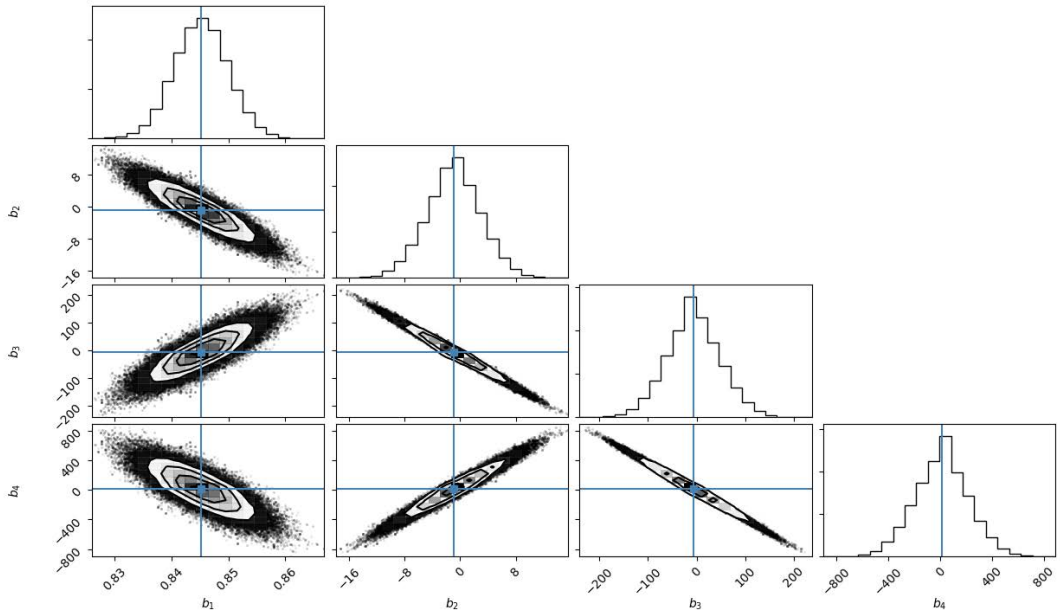

Figure 10. Posteriors for the bias coefficients for the polynomial model, mass bin M1, z =0, $k_{\rm max}$ = 0.12 h/Mpc, case II

H2020 Programme under REA grant agreement number 706896 (COSMOFLAGS). A special thank you to Cora Dvorkin, Shun Saito and Marko Simonovic for their precious insights. We acknowledge Alexander mead and Emiliano Sefusatti for feedback and comments on the draft. DV would like to thank his fellow PhD students (Katie, Jose, Nicolas, Ali and Sam) at ICC for their patience and support.

A MCMC fitting

We used the MCMC ensemble sampler *emcee* [48] to fit the bias coefficients and quantify their error using least squares results as initial guesses. This is shown in figures 16 and 17.

The errors on the bias as a function of wavenumber k is given by the standard deviation of the 10 pairs of realizations. Covariance between different k-bins is ignored, given the limited number of available simulations. This is justified by simplicity and by the fact that we work in the linear and mildly-non-linear regime. The likelihood is taken to be Gaussian. This is a standard assumption widely used in the literature. In reality, even if the over-density field is Gaussian (which is not because of bias and gravitational instability), its power spectrum does not follow a Gaussian probability distribution. However for band powers, especially those populated by many modes and therefore with better signal to noise, the central limit theorem ensures that the Gaussian approximation holds well. The parameters to fit are the set of the bias parameters of the model, for each of the four redshift snapshots (n_z) and each of the four mass bins (n_M) . Hence the total number of parameters n_{params} is $n_z \times n_M \times n_{\rm model}$ where $n_{\rm model}$ is 4 for the polynomial model, 3 for the polynomial model with only even powers of k, and 4 or 5 in the perturbation theory-based fits. We use uniform improper priors for all the parameters.

JCAP12(2019)057

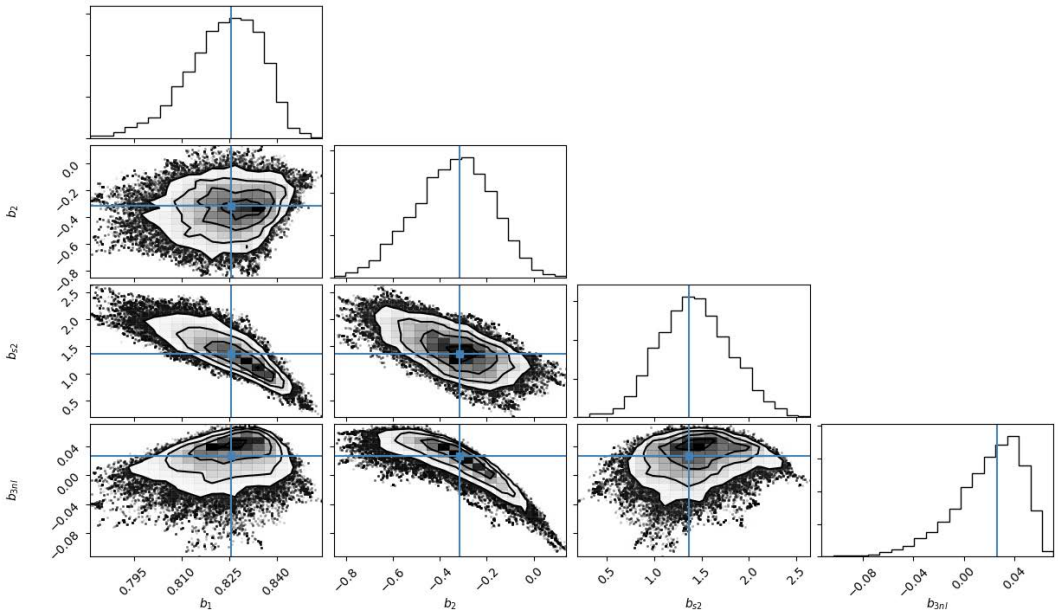

Figure 11. Posteriors for the bias coefficients for the perturbation theory-based 2nd order expansion model. Mass bin M1, z =0, kmax = 0.12 h/Mpc, case II.

Emcee used 300 walkers and 1000 steps for each walker. Illustrative cases for the posteriors for the bias parameters of the models considered are shown in figures 10–11 (see figure caption for details).

The best fits of each bias parameter, and errors marginalised over all other parameters, as function of the mass bins and redshift snapshots are reported in tables appendix D and F. We introduced a shot noise correction parameter, to account for non-Poisson behaviour of shot noise, which is marginalised over. The value of this parameter is not reported here because it is kept as a nuisance parameter in BE-HaPPy.

B Fit to the halo bias, dependence on mass bin

For completeness we report the ratio between the halo bias obtained from the simulations and the fit (figure 2) for each mass bin. We also report the mass deendenve of the residuals to the bias fit for (figure 5), only for $z = 1$ which is where the effect we discuss becomes evident.

C PT terms

For completeness we report here the expression for the perturbation theory terms used the main text.

$$P_{b2,\delta}(k) = \int \frac{d^3q}{(2\pi)^3} P^{lin}(q) P^{lin}(|k-q|) F_s^{(2)}(q, k-q) \tag{C.1}$$

$$P_{b2,\theta}(k) = \int \frac{d^3q}{(2\pi)^3} P^{lin}(q) P^{lin}(|k-q|) G_s^{(2)}(q, k-q) \tag{C.2}$$

JCAP12(2019)057

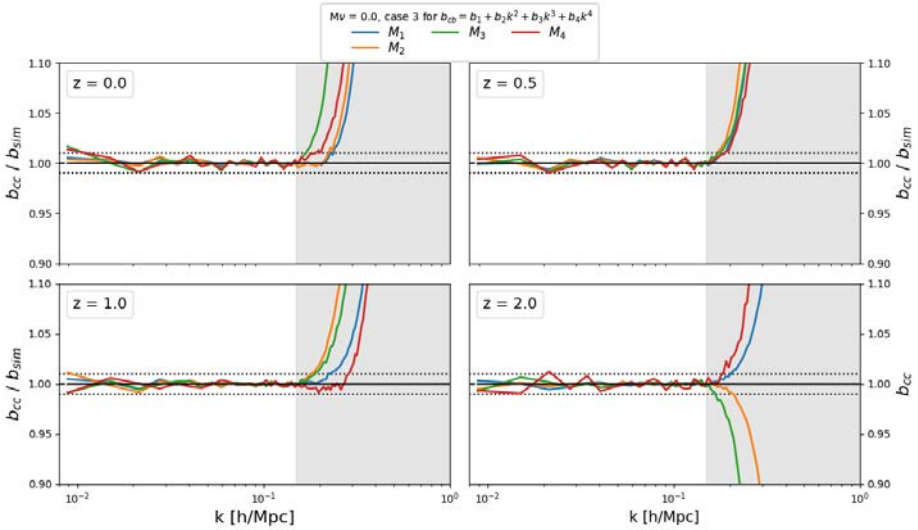

Figure 12. Ratio between the halo bias obtained from the simulations and the fit split by mass bin, see figure 2.

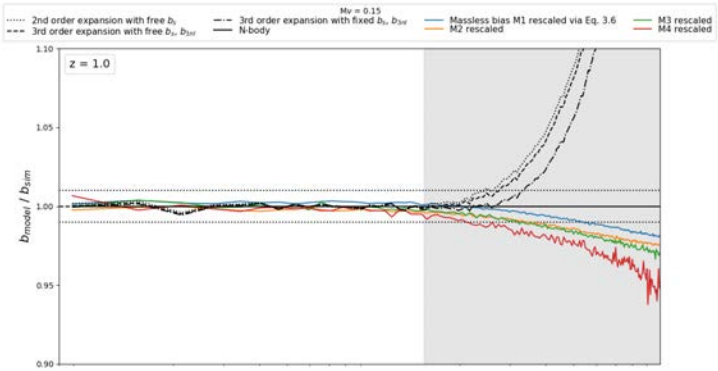

Figure 13. Figure 5, bottom panel at $z = 1$ but now also showing the dependence on the mass bin.

$$P_{bs2,\delta}(k) = \int \frac{d^3q}{(2\pi)^3} P^{lin}(q) P^{lin}(|k-q|) F_s^{(2)}(q, k-q) S_s^{(2)}(q, k-q) \tag{C.3}$$

$$P_{bs2,\theta}(k) = \int \frac{d^3q}{(2\pi)^3} P^{lin}(q) P^{lin}(|k-q|) G_s^{(2)}(q, k-q) S_s^{(2)}(q, k-q) \tag{C.4}$$

$$P_{b22}(k) = \frac{1}{2} \int \frac{d^3q}{(2\pi)^3} P^{lin}(q) \left[P^{lin}(|k-q|) - P^{lin}(q) \right] \tag{C.5}$$

$$P_{b2s2}(k) = -\frac{1}{2} \int \frac{d^3q}{(2\pi)^3} P^{lin}(q) \left[\frac{2}{3} P^{lin}(q) - P^{lin}(|k-q|) S_s^{(2)}(q, k-q) \right] \tag{C.6}$$

$$P_{bs22}(k) = -\frac{1}{2} \int \frac{d^3q}{(2\pi)^3} P^{lin}(q) \left[\frac{4}{9} P^{lin}(q) - P^{lin}(|k-q|) S_s^{(2)}(q, k-q)^2 \right] \tag{C.7}$$

where $F_s^{(2)}$, $G_s^{(2)}$ and $S_s^{(2)}$ are 2nd order perturbation theory kernels.

JCAP12(2019)057

Mass bins	b_1	$-$err b_1	$+$err b_1	b_2	$-$err b_2	$+$err b_2	b_3	$-$err b_3	$+$err b_3	b_4	$-$err b_4	$+$err b_4
M1	*0.845*	0.005	0.005	*-0.898*	3.833	3.81	*-6.75*	53.83	54.688	*12.125*	205.818	203.14
M2	*0.888*	0.006	0.006	*0.893*	4.916	4.924	*-21.222*	69.02	68.804	*42.956*	254.91	256.332
M3	*1.023*	0.008	0.008	*5.545*	6.222	6.225	*-79.71*	86.735	87.672	*245.958*	326.821	322.981
M4	*1.29*	0.012	0.012	*1.655*	10.178	10.163	*-38.373*	145.538	144.508	*102.042*	545.552	555.432

Table 4. Polynomial model coefficients of $b_{\rm cc}$; $k_{\rm max} = 0.15$ h/Mpc, z = 0.0.

Mass bins	b_1	$-$err b_1	$+$err b_1	b_2	$-$err b_2	$+$err b_2	b_3	$-$err b_3	$+$err b_3	b_4	$-$err b_4	$+$err b_4
M1	*1.04*	0.006	0.006	*2.919*	4.711	4.682	*-38.52*	65.679	67.014	*108.898*	253.156	245.006
M2	*1.127*	0.008	0.008	*6.157*	6.454	6.554	*-77.288*	91.978	91.83	*242.857*	347.767	346.377
M3	*1.366*	0.009	0.009	*6.914*	7.61	7.686	*-86.903*	108.453	109.369	*279.133*	415.68	410.437
M4	*1.792*	0.013	0.013	*1.792*	10.659	10.54	*-32.749*	155.715	156.452	*106.696*	612.877	616.677

Table 5. Polynomial model coefficients of $b_{\rm cc}$; $k_{\rm max} = 0.15$ h/Mpc, z = 0.5.

Mass bins	b_1	$-$err b_1	$+$err b_1	b_2	$-$err b_2	$+$err b_2	b_3	$-$err b_3	$+$err b_3	b_4	$-$err b_4	$+$err b_4
M1	*1.332*	0.007	0.007	*2.15*	5.736	5.676	*-15.717*	78.401	79.434	*24.882*	293.963	287.496
M1	*1.487*	0.008	0.008	*3.348*	6.889	6.695	*-34.19*	93.048	97.687	*107.953*	367.823	346.865
M1	*1.868*	0.012	0.012	*1.282*	9.469	9.532	*-1.931*	136.007	134.97	*-13.002*	512.986	517.966
M1	*2.503*	0.019	0.019	*8.383*	17.182	17.466	*-61.065*	260.602	254.053	*131.255*	990.305	1022.662

Table 6. Polynomial model coefficients of $b_{\rm cc}$; $k_{\rm max} = 0.15$ h/Mpc, z = 1.0.

Mass bins	b_1	$-$err b_1	$+$err b_1	b_2	$-$err b_2	$+$err b_2	b_3	$-$err b_3	$+$err b_3	b_4	$-$err b_4	$+$err b_4
M1	*2.199*	0.009	0.009	*3.825*	7.197	7.158	*-21.639*	101.805	102.2	*77.61*	388.068	387.347
M2	*2.531*	0.013	0.012	*2.094*	9.894	9.993	*25.194*	141.411	141.223	*-113.229*	539.035	535.428
M3	*3.297*	0.029	0.029	*7.211*	22.679	22.397	*67.113*	317.97	324.107	*-398.872*	1244.717	1206.446
M4	*4.664*	0.086	0.085	*45.85*	70.202	70.9	*-147.646*	1025.801	1017.184	*96.813*	3901.527	3973.001

Table 7. Polynomial model coefficients of $b_{\rm cc}$; $k_{\rm max} = 0.15$ h/Mpc, z = 2.0.

D Bias coefficients: polynomial fit

In table 4, 5, 6 and 7 we report the best fit bias coefficients and their marginal errors for the polynomial model of section 3.1.

E Third-order bias

We compute the coefficient of the 3rd-order non local bias term using eq. 53 of [31]. As introduced and explained in McDonald & Roy [34], in the expansion of the power spectrum, the three integrals involving the third-order nonlocal terms are exactly proportional to each other after renormalization, and can be encompassed in a single third order bias term b_{3nl}, simplifying significantly the resulting expressions. Thus we just need to compute the quantity σ_3^2:

$$\sigma_3^2 = \frac{105}{16}\int \frac{d^3q}{(2\pi)^3} P^{lin}(q)\left[D^{(2)}(-q,k)S^{(2)}(q,k-q)+\frac{8}{63}\right] \tag{E.1}$$

JCAP12(2019)057

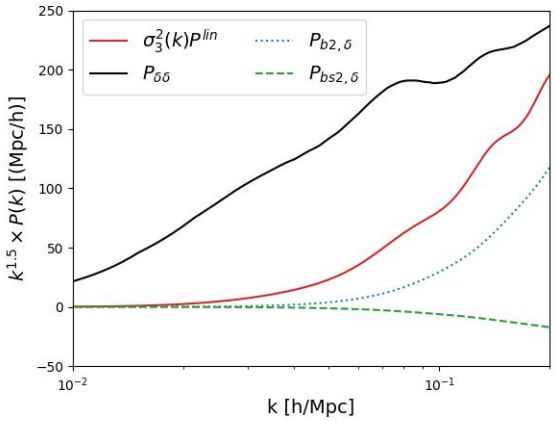

Figure 14. Comparison of terms in the 3rd order expansion. This figure can be compared directly with figure 1 of ref. [32], bearing in mind that here the power spectra are in units of Mpc/h.

Through a change of variable we can rewrite the expression $\sigma_3^2 \times P^{lin}(k)$ as

$$\begin{aligned}\sigma_3^2 P^{lin}(k) &= \frac{105}{16} P^{lin}(k) \int \frac{d^3q}{(2\pi)^3} P^{lin}(q) \left[D^{(2)}(-q,k) S^{(2)}(q,k-q) + \frac{8}{63} \right] \\ &= \frac{105\, k^3}{16\,(2\pi)^2} P^{lin}(k) \int dr\, r^2 P^{lin}(kr) I_R(r)\end{aligned} \tag{E.2}$$

where

$$I_R = \int_{-1}^{1} \left[D^{(2)}(-q,k) S^{(2)}(q,k-q) + \frac{8}{63} \right] d\mu$$

and $r = q/k$; $\mu = \vec{k} \,.\, \vec{q}/(kq)$.

The second line of eq. (E.2) is very similar to a P_{13} convolution integral (see section 2.3 of [23]) simplifying the implementation in FAST-PT.

The relevant terms appearing in eq. (3.3) $-\sigma_3^2 P^{\rm lin}(k)$, the non linear matter power spectrum from simulation $P_{\delta\delta}$, the second-order local bias term $P_{b2,\delta}$ and the second-order nonlocal bias term $P_{bs2,\delta}$– are shown in figure 14. Like ref. [33] we see that the third-order nonlocal term dominate over the second-order local and nonlocal terms, as long as the b_2 term is sufficiently small.

F Bias coefficients: perturbation theory-based fit

In tables 8, 9, 10, 11, 12, 13, 14, 15 we report the best fit bias coefficients and their marginal errors for the perturbation theory-based model of section 3.2.

G redshift-space checks

We have performed a cross check of our implementation of redshift-space distortions in FAST-PT with the original results by Scoccimarro et al. [42].

Figure 15 shows excellent agreement with only a little residual discrepancy at small scales, which is probably due to the fact that we do not know exactly (and therefore may not have matched perfectly) all the cosmological parameters used in [42] to initialize the input linear power spectrum.

JCAP12(2019)057

Mass bins	b_1	$-$err b_1	$+$err b_1	b_2	$-$err b_2	$+$err b_2	b_{s2}	$-$err b_{s2}	$+$err b_{s2}
M1	*0.838*	0.006	0.008	*-0.328*	0.086	0.095	*0.038*	0.143	0.08
M2	*0.849*	0.019	0.018	*-0.227*	0.084	0.158	*1.696*	0.481	0.436
M3	*0.98*	0.024	0.024	*-0.198*	0.082	0.141	*1.907*	0.531	0.493
M4	*1.277*	0.017	0.02	*-0.474*	0.196	0.253	*-0.175*	0.295	0.171

Table 8. Coefficients of $b_{\rm cc}$, 2nd order expansion model, $k_{\rm max} = 0.15$ h/Mpc, z= 0.

Mass bins	b_1	$-$err b_1	$+$err b_1	b_2	$-$err b_2	$+$err b_2	b_{s2}	$-$err b_{s2}	$+$err b_{s2}
M1	*1.032*	0.01	0.012	*-0.362*	0.152	0.19	*-0.374*	0.221	0.124
M2	*1.118*	0.015	0.016	*-0.37*	0.22	0.279	*-0.577*	0.297	0.153
M3	*1.344*	0.024	0.03	*-0.044*	0.083	0.171	*1.948*	0.992	1.058
M4	*1.79*	0.01	0.022	*-0.302*	0.235	0.439	*-0.286*	0.884	0.44

Table 9. Coefficients of $b_{\rm cc}$, second order expansion model, $k_{\rm max} = 0.15$ h/Mpc, z= 0.5

Mass bins	b_1	$-$err b_1	$+$err b_1	b_2	$-$err b_2	$+$err b_2	b_{s2}	$-$err b_{s2}	$+$err b_{s2}
M1	*1.321*	0.012	0.019	*0.093*	0.058	0.096	*1.455*	0.966	1.012
M2	*1.488*	0.005	0.012	*0.001*	0.158	0.27	*-0.753*	0.837	0.483
M3	*1.869*	0.007	0.014	*0.094*	0.164	0.317	*-0.696*	1.39	0.808
M4	*2.481*	0.03	0.041	*-0.231*	0.653	0.968	*-2.719*	1.334	0.61

Table 10. Coefficients of $b_{\rm cc}$, second order expansion model, $k_{\rm max} = 0.15$ h/Mpc, z= 1.0.

Mass bins	b_1	$-$err b_1	$+$err b_1	b_2	$-$err b_2	$+$err b_2	b_{s2}	$-$err b_{s2}	$+$err b_{s2}
M1	*2.201*	0.005	0.011	*0.983*	0.137	0.283	*-1.45*	2.049	1.674
M2	*2.532*	0.007	0.013	*1.4*	0.204	0.424	*-2.437*	2.557	1.91
M3	*3.264*	0.029	0.067	*1.995*	0.794	1.364	*-9.241*	3.797	1.872
M4	*4.611*	0.093	0.236	*7.502*	0.759	1.452	*-1.539*	12.318	10.691

Table 11. Coefficients of $b_{\rm cc}$, second order expansion model, $k_{\rm max} = 0.15$ h/Mpc, z= 2.0.

Mass bins	b_1	$-$err b_1	$+$err b_1	b_2	$-$err b_2	$+$err b_2	b_{s2}	$-$err b_{s2}	$+$err b_{s2}	b_{3nl}	$-$err b_{3nl}	$+$err b_{3nl}
M1	*0.826*	0.009	0.013	*-0.315*	0.158	0.183	*1.368*	0.352	0.353	*0.026*	0.02	0.03
M2	*0.855*	0.015	0.016	*-0.444*	0.222	0.206	*1.879*	0.462	0.403	*0.041*	0.026	0.033
M3	*0.989*	0.017	0.022	*-0.552*	0.26	0.273	*2.211*	0.541	0.535	*0.068*	0.028	0.037
M4	*1.266*	0.015	0.025	*-0.698*	0.368	0.361	*2.211*	0.759	0.78	*0.093*	0.027	0.047

Table 12. Coefficients of $b_{\rm cc}$, third expansion model with b_{3nl} kept as free parameter, $k_{\rm max} = 0.15$ h/Mpc, z = 0.

JCAP12(2019)057

Mass bins	b_1	$-$err b_1	$+$err b_1	b_2	$-$err b_2	$+$err b_2	b_{s2}	$-$err b_{s2}	$+$err b_{s2}	b_{3nl}	$-$err b_{3nl}	$+$err b_{3nl}
M1	*1.029*	0.007	0.011	*-0.562*	0.284	0.293	*1.848*	0.556	0.585	*0.097*	0.023	0.041
M2	*1.118*	0.007	0.014	*-0.925*	0.407	0.396	*2.339*	0.851	0.773	*0.136*	0.03	0.051
M3	*1.358*	0.008	0.014	*-0.634*	0.388	0.439	*1.907*	1.011	1.011	*0.155*	0.035	0.067
M4	*1.788*	0.012	0.012	*-0.466*	0.544	0.59	*1.061*	1.337	1.345	*0.094*	0.074	0.138

Table 13. Coefficients of $b_{\rm cc}$, third order expansion model with b_{3nl} kept as free parameter, $k_{\rm max}$ = 0.15 h/Mpc, z = 0.5.

Mass bins	b_1	$-$err b_1	$+$err b_1	b_2	$-$err b_2	$+$err b_2	b_{s2}	$-$err b_{s2}	$+$err b_{s2}	b_{3nl}	$-$err b_{3nl}	$+$err b_{3nl}
M1	*1.329*	0.006	0.006	*-0.354*	0.382	0.417	*0.799*	1.008	0.927	*0.136*	0.06	0.11
M2	*1.488*	0.008	0.008	*-0.116*	0.397	0.442	*0.218*	1.105	1.141	*0.087*	0.116	0.152
M3	*1.866*	0.011	0.011	*-0.091*	0.56	0.591	*0.367*	1.588	1.591	*0.105*	0.169	0.21
M4	*2.5*	0.017	0.017	*-0.551*	1.146	1.286	*1.261*	2.919	2.685	*0.358*	0.167	0.323

Table 14. Coefficients of $b_{\rm cc}$, third order expansion model with b_{3nl} kept as free parameter, $k_{\rm max}$ = 0.15 h/Mpc, z = 1.0.

Mass bins	b_1	$-$err b_1	$+$err b_1	b_2	$-$err b_2	$+$err b_2	b_{s2}	$-$err b_{s2}	$+$err b_{s2}	b_{3nl}	$-$err b_{3nl}	$+$err b_{3nl}
M1	*2.202*	0.009	0.009	*1.085*	0.738	0.728	*-1.57*	1.898	1.818	*-0.054*	0.338	0.419
M2	*2.533*	0.013	0.013	*1.516*	0.863	0.984	*-2.665*	2.566	2.254	*-0.074*	0.513	0.556
M3	*3.273*	0.036	0.05	*3.175*	1.781	2.094	*0.042*	4.611	4.333	*-0.006*	1.158	1.347
M4	*4.624*	0.085	0.123	*6.026*	4.376	5.034	*-1.637*	11.736	9.845	*1.528*	2.591	3.921

Table 15. Coefficient of $b_{\rm cc}$, third order expansion model with b_{3nl} kept as free parameter, $k_{\rm max}$ = 0.15 h/Mpc, z = 2.0.

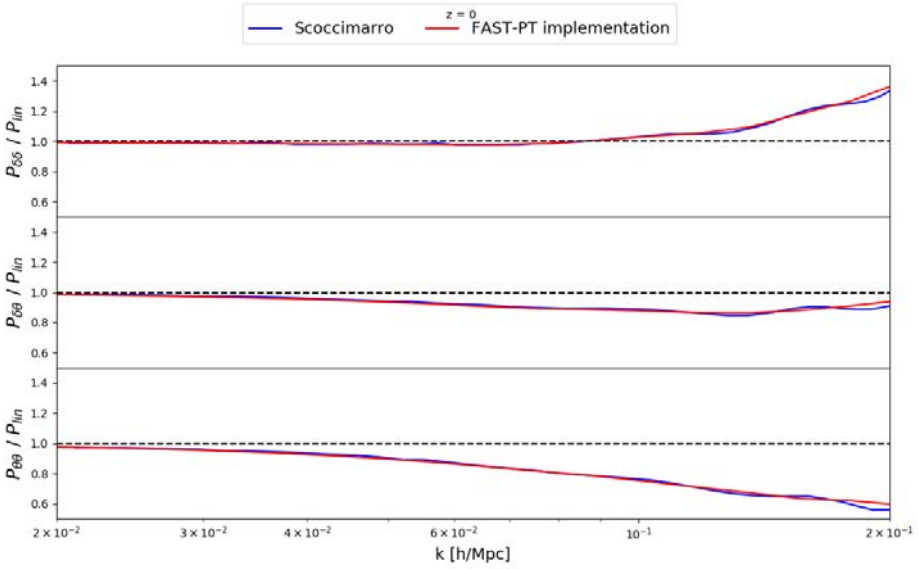

Figure 15. Comparison of FAST-PT modifications (red) vs Scoccimarro [42] (blue) at z = 0. For this figure we use a flat ΛCDM model with $\Omega_m = 0.26$, $\sigma_8 = 0.9$, $\Omega_b = 0.04$ and $h = 0.7$ as in [42].

H Multipole expansion

Redshift-space power spectra are often plotted in terms of their so-called multipoles. Both eqs. (4.2) and (4.7) depend on k and μ. Instead of working with these 2-dimensional functions,

JCAP12(2019)057

we expand them into Legendre polynomials, L_ℓ, following the traditional approach:

$$P_l^s(k) = \frac{2l+1}{2}\int_{-1}^{1} d\mu\, P^s(k,\mu)L_l(\mu) \tag{H.1}$$

In order to isolate the μ dependence of the A and B coefficients of the TNS and eTNS models, we write

$$A(k,\mu,f) = \bar{A}(k,\mu,f) \times k\mu f$$
$$B(k,\mu,f) = \bar{B}(k,\mu,f) \times (k\mu f)^2$$

The $\bar{A}$ and $\bar{B}$ integrals can be decomposed as a summation of convolution integrals (see appendix C of [23]) which in turn can be written as Legendre expansions.

$$\bar{A}(k,\mu,f) = \sum_{i=0} A_i(k,f)\mu^i$$
$$\bar{B}(k,\mu,f) = \sum_{i=0} B_i(k,f)\mu^i$$

We can this finally express A and B as

$$A(k,\mu,f) = kf \times \sum_{i=0} A_i(k,f)\mu^{i+1}$$
$$B(k,\mu,f) = (kf)^2 \times \sum_{i=0} B_i(k,f)\mu^{i+2}.$$

For biased tracers in the above equations $f \longrightarrow \beta$. In **BE-HaPPy** the integration of μ is split in the same way as Cole et al. [49]:

$$\begin{aligned} P_l^s(k) &= \frac{2l+1}{2}\int_{-1}^{1} d\mu\, P_g^s(k,\mu)L_l(\mu) \\ &= \frac{2l+1}{2}\int_{-1}^{1} d\mu\, K(k,\mu)F(k,\mu^2)L_l(\mu)\,, \end{aligned} \tag{H.2}$$

where $L_l(\mu)$ are the first even Legendre polynomials, and $K(k,\mu)$ can be the Kaiser, Scoccimarro or TNS models, and $F(k,\mu^2)$ is the FoG term. **BE-HaPPy** allows the user to choose among all these different models.

I σ_8 scale-dependence

In figure 5 we rescaled the amplitude of the bias calibrated with a massless neutrinos simulation and compare with the bias of a massive neutrinos simulation (M_ν =0.15 eV). If the bias is calibrated with respect to CDM + baryons $b_{\rm cc}$, we expect that all the scale dependence is encompassed in the massless case and that the only effect of massive neutrinos would be on the amplitude of the bias. However in figure 5, we observe an extra scale dependence. This scale dependence becomes more pronounced with increasing linear bias. Because of the degeneracy between M_ν and σ_8, we argue that this scale dependence is not due neutrinos but to a difference of σ_8 between the massless and massive simulation. To test this we compared our rescaling procedure with another simulation (with massless neutrinos) where σ_8 is closer to that of the massive neutrinos simulation. All other parameters (Ω_m, Ω_b, Ω_Λ, n_s, h) are identical. This is shown in figure 17. One can appreciate that the extra scale dependence decreases for a better matched σ_8 (blue line). The blue line is only plotted to larger scale (smaller k) because of the different (lower) resolution of the simulation. Unfortunately we are limited by the simulations available at this time and this could not be investigated further.

JCAP12(2019)057

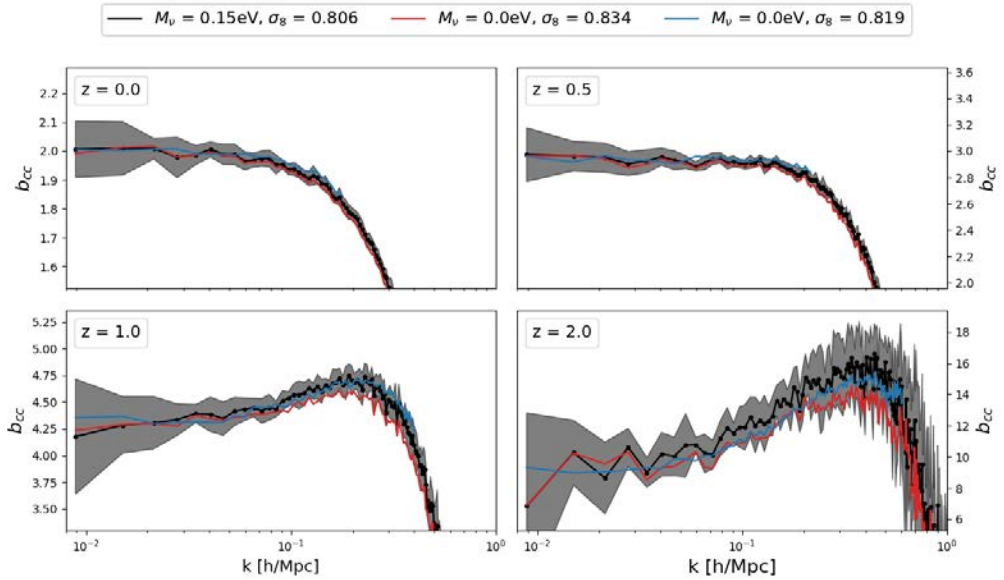

Figure 16. Influence of σ_8 in the performance of the rescaling of equation (3.4). To enhance the effect, the figure corresponds to haloes with masses $> 5 \times 10^{13} M_\odot$. We applied the rescaling method of eq. 3.4 to simulations with the same cosmological parameters $\Omega_\mathrm{m} = \Omega_\mathrm{c} + \Omega_\mathrm{b} + \Omega_\nu = 0.3175$, $\Omega_\mathrm{b} = 0.049$, $\Omega_\Lambda = 0.6825$, $\Omega_\mathrm{k} = 0$, $h = 0.6711$, $n_s = 0.9624$ and $M_\nu = 0.0\,\mathrm{eV}$ but with different σ_8 (0.819 for the blue curve and 0.834 for the red one). The improvement at small scales for the lower σ_8 confirms our hypothesis about the scale dependence seen in figure 5.

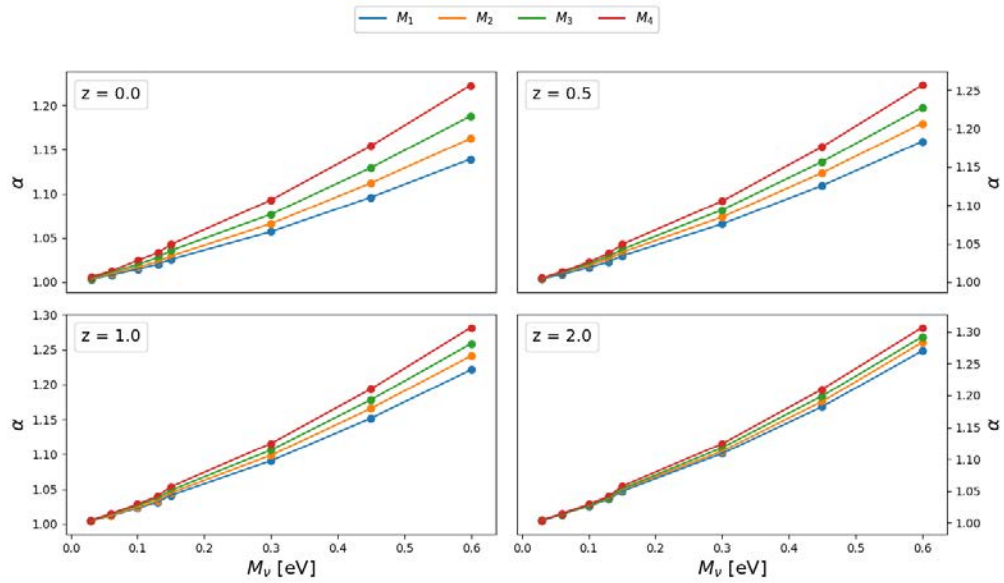

Figure 17. Value of the rescaling coefficients α as a function of mass bins and redshift. We can see here that the relation between the rescaling and the mass of the neutrinos is quasi linear.

J Rescaling coefficient α

For completeness here we show the dependence of α values (eq. (3.6)) on neutrino mass and redshift.

JCAP12(2019)057

References

[1] A. Raccanelli, L. Verde and F. Villaescusa-Navarro, *Biases from neutrino bias: to worry or not to worry?*, *Mon. Not. Roy. Astron. Soc.* **483** (2019) 734 [arXiv:1704.07837] [INSPIRE].

[2] S. Vagnozzi et al., *Bias due to neutrinos must not uncorrect'd go*, *JCAP* **09** (2018) 001 [arXiv:1807.04672] [INSPIRE].

[3] J.B. Muñoz and C. Dvorkin, *Efficient computation of galaxy bias with neutrinos and other relics*, *Phys. Rev.* **D 98** (2018) 043503 [arXiv:1805.11623] [INSPIRE].

[4] F. Villaescusa-Navarro et al., *Cosmology with massive neutrinos I: towards a realistic modeling of the relation between matter, haloes and galaxies*, *JCAP* **03** (2014) 011 [arXiv:1311.0866] [INSPIRE].

[5] E. Castorina, E. Sefusatti, R.K. Sheth, F. Villaescusa-Navarro and M. Viel, *Cosmology with massive neutrinos II: on the universality of the halo mass function and bias*, *JCAP* **02** (2014) 049 [arXiv:1311.1212] [INSPIRE].

[6] M. LoVerde, *Halo bias in mixed dark matter cosmologies*, *Phys. Rev.* **D 90** (2014) 083530 [arXiv:1405.4855] [INSPIRE].

[7] C.-T. Chiang, W. Hu, Y. Li and M. Loverde, *Scale-dependent bias and bispectrum in neutrino separate universe simulations*, *Phys. Rev.* **D 97** (2018) 123526 [arXiv:1710.01310] [INSPIRE].

[8] F. Villaescusa-Navarro, S. Bird, C. Pena-Garay and M. Viel, *Non-linear evolution of the cosmic neutrino background*, *JCAP* **03** (2013) 019 [arXiv:1212.4855] [INSPIRE].

[9] C.-T. Chiang, M. LoVerde and F. Villaescusa-Navarro, *First detection of scale-dependent linear halo bias in N-body simulations with massive neutrinos*, *Phys. Rev. Lett.* **122** (2019) 041302 [arXiv:1811.12412] [INSPIRE].

[10] D. Blas, J. Lesgourgues and T. Tram, *The cosmic linear anisotropy solving system (CLASS) II: approximation schemes*, *JCAP* **07** (2011) 034 [arXiv:1104.2933] [INSPIRE].

[11] A. Lewis, *Efficient sampling of fast and slow cosmological parameters*, *Phys. Rev.* **D 87** (2013) 103529 [arXiv:1304.4473] [INSPIRE].

[12] F. Villaescusa-Navarro et al., *The imprint of neutrinos on clustering in redshift-space*, *Astrophys. J.* **861** (2018) 53 [arXiv:1708.01154] [INSPIRE].

[13] V. Springel, *The Cosmological simulation code GADGET-2*, *Mon. Not. Roy. Astron. Soc.* **364** (2005) 1105 [astro-ph/0505010] [INSPIRE].

[14] PLANCK collaboration, *Planck 2015 results. XIII. Cosmological parameters*, *Astron. Astrophys.* **594** (2016) A13 [arXiv:1502.01589] [INSPIRE].

[15] M. Viel, M.G. Haehnelt and V. Springel, *The effect of neutrinos on the matter distribution as probed by the Intergalactic Medium*, *JCAP* **06** (2010) 015 [arXiv:1003.2422] [INSPIRE].

[16] M. Zennaro, J. Bel, F. Villaescusa-Navarro, C. Carbone, E. Sefusatti and L. Guzzo, *Initial conditions for accurate n-body simulations of massive neutrino cosmologies*, *Mon. Not. Roy. Astron. Soc.* **466** (2017) 3244 [arXiv:1605.05283] [INSPIRE].

[17] R.E. Angulo and A. Pontzen, *Cosmological N-body simulations with suppressed variance*, *Mon. Not. Roy. Astron. Soc.* **462** (2016) L1 [arXiv:1603.05253] [INSPIRE].

[18] F. Villaescusa-Navarro et al., *Statistical properties of paired fixed fields*, *Astrophys. J.* **867** (2018) 137 [arXiv:1806.01871] [INSPIRE].

[19] M. Davis, G. Efstathiou, C.S. Frenk and S.D.M. White, *The evolution of large scale structure in a universe dominated by cold dark matter*, *Astrophys. J.* **292** (1985) 371 [INSPIRE].

JCAP12(2019)057

[20] T. Baldauf, U. Seljak, R.E. Smith, N. Hamaus and V. Desjacques, *Halo stochasticity from exclusion and nonlinear clustering*, *Phys. Rev.* **D 88** (2013) 083507 [arXiv:1305.2917] [INSPIRE].

[21] N. Hamaus, U. Seljak, V. Desjacques, R.E. Smith and T. Baldauf, *Minimizing the stochasticity of halos in large-scale structure surveys*, *Phys. Rev.* **D 82** (2010) 043515 [arXiv:1004.5377] [INSPIRE].

[22] R.E. Smith, R. Scoccimarro and R.K. Sheth, *The scale dependence of halo and galaxy bias: effects in real space*, *Phys. Rev.* **D 75** (2007) 063512 [astro-ph/0609547] [INSPIRE].

[23] J.E. McEwen, X. Fang, C.M. Hirata and J.A. Blazek, *FAST-PT: a novel algorithm to calculate convolution integrals in cosmological perturbation theory*, *JCAP* **09** (2016) 015 [arXiv:1603.04826] [INSPIRE].

[24] X. Fang, J.A. Blazek, J.E. McEwen and C.M. Hirata, *FAST-PT II: an algorithm to calculate convolution integrals of general tensor quantities in cosmological perturbation theory*, *JCAP* **02** (2017) 030 [arXiv:1609.05978] [INSPIRE].

[25] 2DFGRS collaboration, *The 2dF galaxy redshift survey: power-spectrum analysis of the final dataset and cosmological implications*, *Mon. Not. Roy. Astron. Soc.* **362** (2005) 505 [astro-ph/0501174] [INSPIRE].

[26] H.-J. Seo and D.J. Eisenstein, *Baryonic acoustic oscillations in simulated galaxy redshift surveys*, *Astrophys. J.* **633** (2005) 575 [astro-ph/0507338] [INSPIRE].

[27] U. Seljak, *Redshift space bias and beta from the halo model*, *Mon. Not. Roy. Astron. Soc.* **325** (2001) 1359 [astro-ph/0009016] [INSPIRE].

[28] E. Huff, A.E. Schulz, M.J. White, D.J. Schlegel and M.S. Warren, *Simulations of baryon oscillations*, *Astropart. Phys.* **26** (2007) 351 [astro-ph/0607061] [INSPIRE].

[29] T. Matsubara, *Nonlinear perturbation theory integrated with nonlocal bias, redshift-space distortions and primordial non-gaussianity*, *Phys. Rev.* **D 83** (2011) 083518 [arXiv:1102.4619] [INSPIRE].

[30] T. Baldauf, U. Seljak, V. Desjacques and P. McDonald, *Evidence for quadratic tidal tensor bias from the halo bispectrum*, *Phys. Rev.* **D 86** (2012) 083540 [arXiv:1201.4827] [INSPIRE].

[31] BOSS collaboration, *The clustering of galaxies in the SDSS-III baryon oscillation spectroscopic survey: testing gravity with redshift-space distortions using the power spectrum multipoles*, *Mon. Not. Roy. Astron. Soc.* **443** (2014) 1065 [arXiv:1312.4611] [INSPIRE].

[32] M. Biagetti, V. Desjacques, A. Kehagias and A. Riotto, *Nonlocal halo bias with and without massive neutrinos*, *Phys. Rev.* **D 90** (2014) 045022 [arXiv:1405.1435] [INSPIRE].

[33] S. Saito, T. Baldauf, Z. Vlah, U. Seljak, T. Okumura and P. McDonald, *Understanding higher-order nonlocal halo bias at large scales by combining the power spectrum with the bispectrum*, *Phys. Rev.* **D 90** (2014) 123522 [arXiv:1405.1447] [INSPIRE].

[34] P. McDonald and A. Roy, *Clustering of dark matter tracers: generalizing bias for the coming era of precision LSS*, *JCAP* **08** (2009) 020 [arXiv:0902.0991] [INSPIRE].

[35] M. Crocce, P. Fosalba, F.J. Castander and E. Gaztanaga, *Simulating the Universe with MICE: the abundance of massive clusters*, *Mon. Not. Roy. Astron. Soc.* **403** (2010) 1353 [arXiv:0907.0019] [INSPIRE].

[36] J.L. Tinker et al., *The large scale bias of dark matter halos: numerical calibration and model tests*, *Astrophys. J.* **724** (2010) 878 [arXiv:1001.3162] [INSPIRE].

[37] E. Castorina, E. Sefusatti, R.K. Sheth, F. Villaescusa-Navarro and M. Viel, *Cosmology with massive neutrinos II: on the universality of the halo mass function and bias*, *JCAP* **02** (2014) 049 [arXiv:1311.1212] [INSPIRE].

JCAP12(2019)057

[38] F. Villaescusa-Navarro et al., *Cosmology with massive neutrinos I: towards a realistic modeling of the relation between matter, haloes and galaxies*, *JCAP* **03** (2014) 011 [arXiv:1311.0866] [INSPIRE].

[39] F. Villaescusa-Navarro, A. Banerjee, N. Dalal, E. Castorina, R. Scoccimarro, R. Angulo et al., *The imprint of neutrinos on clustering in redshift-space*, *Astrophys. J.* **861** (2018) 53 [arXiv:1708.01154] [INSPIRE].

[40] E. Castorina, C. Carbone, J. Bel, E. Sefusatti and K. Dolag, *DEMNUni: the clustering of large-scale structures in the presence of massive neutrinos*, *JCAP* **07** (2015) 043 [arXiv:1505.07148] [INSPIRE].

[41] N. Kaiser, *Clustering in real space and in redshift space*, *Mon. Not. Roy. Astron. Soc.* **227** (1987) 1 [INSPIRE].

[42] R. Scoccimarro, *Redshift-space distortions, pairwise velocities and nonlinearities*, *Phys. Rev.* **D 70** (2004) 083007 [astro-ph/0407214] [INSPIRE].

[43] A. Taruya, T. Nishimichi and S. Saito, *Baryon acoustic oscillations in 2D: modeling redshift-space power spectrum from perturbation theory*, *Phys. Rev.* **D 82** (2010) 063522 [arXiv:1006.0699] [INSPIRE].

[44] H. Gil-Marin, C. Wagner, L. Verde, C. Porciani and R. Jimenez, *Perturbation theory approach for the power spectrum: from dark matter in real space to haloes in redshift space*, *JCAP* **11** (2012) 029 [arXiv:1209.3771] [INSPIRE].

[45] B. Audren, J. Lesgourgues, K. Benabed and S. Prunet, *Conservative constraints on early cosmology: an illustration of the Monte Python cosmological parameter inference code*, *JCAP* **02** (2013) 001 [arXiv:1210.7183] [INSPIRE].

[46] J. Kwan et al., *Cosmic emulation: fast predictions for the galaxy power spectrum*, *Astrophys. J.* **810** (2015) 35 [arXiv:1311.6444] [INSPIRE].

[47] J.A. Peacock and R.E. Smith, *HALOFIT: nonlinear distribution of cosmological mass and galaxies*, Astrophysics source code library (2014).

[48] D. Foreman-Mackey, D.W. Hogg, D. Lang and J. Goodman, *emcee: The MCMC Hammer*, *Publ. Astron. Soc. Pac.* **125** (2013) 306 [arXiv:1202.3665] [INSPIRE].

[49] S. Cole, K.B. Fisher and D.H. Weinberg, *Constraints on Omega from the IRAS redshift surveys*, *Mon. Not. Roy. Astron. Soc.* **275** (1995) 515 [astro-ph/9412062] [INSPIRE].

JCAP12(2019)057

Chapter 3

Globular clusters as standard clocks

In the introduction and in section 1.3 in particular, I talked about the tight relation between cosmology and astronomy and how learning more about the nature of celestial objects can provide valuable information about the universe. In a bottom-up hierarchical formation of structures, the small pieces of the puzzle provide complementary information to large-scale structures. In the first place because they are often easier to observe than the effects at large scales and also because they are the witnesses of earlier times in the universe.

3.1 Globular clusters

According to Walter Baade's stellar classification (Baade, 1956), type III stars are believed to be the oldest in the universe. The theory predicts that these extremely massive stars use up all their fuel and eventually explode. This is why population II stars are often considered to be the oldest stars that can be observed. Population II consists of stars very poor in metal, formed during the early days of the universe. They are usually found near the central galactic bulge, in the galactic halo or in globular clusters. Population II stars are relics of a younger universe and in sense are good estimators of the age of the universe, however it would be very difficult to use a random collection of these stars in order to estimate the parameters of the universe given all the factors that can influence their evolution.

Globular clusters (GC) are made up of tens or even hundreds of thousands of old, low-metal population II stars very tightly bound which gives them their globular shapes (see Figure 3.1). Their formation mechanism is not yet fully understood but the theory predicts that all stars within a globular cluster were formed from the same molecular cloud which provides a sample of stars in a "controlled" environment with approximately the same age and metallicity. However, recent observations have shown that most globular clusters have multiple populations. It is therefore important to treat adequately this multiplicity to infer the properties of GCs. Another advantage of globular clusters is the fact that they are very common. Every sufficiently large galaxy is expected to host at least hundreds of them, which makes them ideal candidates for studies. For these reasons they have often played a major role in cosmology.

3.2 Color-magnitude diagram and stellar codes

The Color-magnitude diagram (or the Hertzsprung-Russell diagram) is an important tool in astronomy because it allows to visualize the different evolutionary phases of a star's life as a function of some of its properties: magnitude vs color (or luminosity vs temperature). When plotted on a color-magnitude diagram (CMD) all the stars within a globular clusters seem to follow a well-defined curve (see figure 3.2), which seems to be an indication that all stars were formed at the same period with similar physical properties. As the position of the curve is dependent on the initial mass of the stars or equivalently of the age of the stars, the shape of the CMD of globular clusters can be a good estimator of the age of the stellar population.

In reality it is not that simple because the shape of the CMD does not depend only on the age but also on several parameters such as the distance, the metallicity, the extinction etc. With the help of observational surveys and theoretical background, the astronomical community was able to design stellar evolutionary codes (e.g `MESA` Paxton et al. 2011) that can be used to make predictions. These codes are able to evolve stars across all the evolutionary phases of the CMD for a whole range of astrophysical parameters. Stellar evolutionary codes output evolutionary tracks which are a set of stellar parameters at different timesteps. However these tracks are best suited to study the evolution of a single star. If we want to study stellar populations, as it is the case for globular clusters, instead it is better to use isochrones [1] where input masses have been replaced by input ages assuming a common time of formation. Several isochrones software are already publicly available (`DSED` Dotter et al. 2008, `MIST` Dotter 2016, `BASTI` Pietrinferni et al. 2004, `PARSEC` Bressan et al. 2012 etc.) each with different sets of independent parameters. They provide the positions of stars in the CMD given a chosen set of parameters, among others the age. These isochrone software are therefore ideal to constrain the properties of globular clusters.

[1] Isochrones are derived from a set of tracks with a given range of initial masses but with the same initial chemical composition

3.3 Inferring the Age of the Universe with Globular Clusters

Determining the age of globular clusters makes it possible to put a lower limit on the age of the universe since obviously the universe must be older than its components. However, this determination depends heavily on the quality of the stellar model and the methodology used. For a long time, estimates of the age of the universe obtained from H_0 and the oldest stars in the universe left astronomers perplexed because the stars appeared to be older than the universe. With the improvement of measurements on both sides (Planck Collaboration et al., 2020; O'Malley, Gilligan, and Chaboyer, 2017), this crisis seems to be resolved. The errors of the previous estimates of the age of the clusters were too large to be able to make any precise statement on the age of the universe and a fortiori on the cosmological model. That is why obtaining a measurement with sufficiently small errors would make it possible to directly relate the age of the clusters to that of the universe by making some assumptions about the time of galaxies formation.

Journal of Cosmology and Astroparticle Physics

Inferring the age of the universe with globular clusters

Journal of Cosmology and Astroparticle Physics
An IOP and SISSA journal

Inferring the age of the universe with globular clusters

David Valcin,[a,b] **José Luis Bernal,**[c,a,b] **Raul Jimenez,**[a,d] **Licia Verde**[a,d] **and Benjamin D. Wandelt**[e,f,g]

[a]ICC, University of Barcelona, IEEC-UB,
Martí i Franquès, 1, E08028 Barcelona, Spain
[b]Dept. de Física Quàntica i Astrofísica, Universitat de Barcelona,
Martí i Franquès 1, E08028 Barcelona, Spain
[c]Department of Physics and Astronomy, Johns Hopkins University,
3400 North Charles Street, Baltimore, Maryland 21218, U.S.A.
[d]ICREA,
Pg. Lluis Companys 23, Barcelona, 08010, Spain
[e]Sorbonne Université, CNRS, UMR 7095, Institut d'Astrophysique de Paris,
98 bis bd Arago, 75014 Paris, France
[f]Sorbonne Université, Institut Lagrange de Paris (ILP),
98 bis bd Arago, 75014 Paris, France
[g]Center for Computational Astrophysics, Flatiron Institute,
162 5th Avenue, 10010, New York, NY, U.S.A.

E-mail: d.valcin@icc.ub.edu, jbernal2@jhu.edu, raul.jimenez@icc.ub.edu, liciaverde@icc.ub.edu, bwandelt@iap.fr

Received July 20, 2020
Revised October 13, 2020
Accepted October 15, 2020
Published December 1, 2020

JCAP12(2020)002

 https://doi.org/10.1088/1475-7516/2020/12/002

Abstract. We present an estimate of the absolute age of 68 galactic globular clusters obtained by exploiting the distribution of stars in the full color-magnitude diagram. In particular, we jointly estimate the absolute age, distance, reddening, metallicity ([Fe/H]) and [α/Fe] of each cluster, imposing priors motivated by independent observations; we also estimate possible systematics from stellar modeling. Our derived distances for the globular cluster sample are in agreement with those obtained from GAIA using main-sequence dwarf stars (where available), and the inferred ages are in good agreement with those previously published. The novelty of our approach is that, with the adopted priors, we are able to estimate robustly these parameters from the globular cluster color-magnitude diagram. We find that the average age of the oldest globular clusters is $t_{\rm GC} = 13.32 \pm 0.1({\rm stat.}) \pm 0.5({\rm sys.})$, at 68% confidence level, including systematic uncertainties from stellar modeling. These measurements can be used to infer the age of the Universe, largely independently of the cosmological parameters: we find an age of the Universe $t_{\rm U} = 13.5^{+0.16}_{-0.14}({\rm stat.}) \pm 0.5({\rm sys.})$ at 68% confidence level, accounting for the formation time of globular clusters and its uncertainty. This value is compatible with $13.8 \pm 0.02\,{\rm Gyr}$, the cosmological model-dependent value inferred by the Planck mission assuming the ΛCDM model.

Keywords: cosmological parameters from CMBR, stars

ArXiv ePrint: 2007.06594

JCAP12(2020)002

Contents

JCAP12(2020)002

1 Introduction

The color magnitude diagram of co-eval stellar populations in the Milky Way can be used to infer the age of its oldest stars. The age can also be estimated for individual stars if their metallicity and the distance to them are known. For resolved stellar populations, however, an independent measurement of the distance is not strictly necessary as the full morphology of the color-magnitude diagram can, in principle, provide a determination of the absolute age. There is extensive literature on this subject; reviews can be found in e.g., refs. [1–3].

Historically, the age of the oldest stellar populations in the Milky Way has been measured using the luminosity of the main-sequence turn off point (MSTOP) in the color-magnitude diagram of globular clusters (GCs). Globular clusters are (almost — more on this below) single stellar populations of stars (see e.g., ref. [3]). It has long been recognized

that they are among the most metal poor ($\sim 1\%$ of the solar metallicity) stellar systems in the Milky Way, and exhibit color-magnitude diagrams characteristic of old ($> 10\,\mathrm{Gyr}$) stellar populations [1, 3, 4].

In fact, the first quantitative attempt to compute the age of the globular cluster M3 was made by Haselgrove and Hoyle more than 60 years ago [5]. In this work, stellar models were computed on the early Cambridge mainframe computer and its results compared "by eye" to the observed color-magnitude diagram. A few stellar phases were computed by solving the equations of stellar structure; this output was compared to observations. Their estimated age for M3 is only 50% off from its current value.[1] This was the first true attempt to use computer models to fit resolved stellar populations and thus obtain cosmological parameters: the age of the Universe in this case. Previous estimates of the ages of GCs involved just analytic calculations, which significantly impacted the accuracy of the results, given the complexity of the stellar structure equations (see e.g., ref. [6]).

The absolute age of a GC inferred using only the MSTOP luminosity is degenerate with other properties of the GC. As already shown in the pioneering work of ref. [5], the distance uncertainty to the GC entails the largest contribution to the error budget: a given % level of relative uncertainty in the distance determination involves roughly the same level of uncertainty in the inference of the age. Other sources of uncertainty are: the metallicity content, the Helium fraction, the dust absorption [3] and theoretical systematics regarding the physics and modeling of stellar evolution.

However, there is more information enclosed in the full-color magnitude diagram of a GC than that enclosed in its MSTOP. As first pointed out in refs. [7, 8], the full color-magnitude diagram has features that allow for a joint fit of the distance scale and the age (see appendix A for a visual rendering of this). On the one hand, figure 2 in ref. [9] shows how the different portions of the color-magnitude diagram constrain the corresponding physical quantities. On the other, figure 1 in ref. [8] and figure 3 in ref. [9] show how the luminosity function is not a pure power law but has features that contain information about the different physical parameters of the GC. This technique enabled the estimation of the ages of the GCs M68 [7], M5 and M55 [9]. Moreover, in principle, exploiting the morphology of the horizontal branch makes it possible to determine the ages of GCs independently of the distance [10].

Further, on the observational front, the gathering of Hubble Space Telescope (HST) photometry for a significant sample of galactic GCs has been a game changer. HST has provided very accurate photometry with a very compact point spread function, thus easing the problems of crowding when attempting to extract the color-magnitude diagram for a GC and making it much easier to control contamination from foreground and background field stars.

For these reasons, a precise and robust determination of the age of a GC requires a global fit of all these quantities from the full color-magnitude diagram of the cluster. In order to exploit this information, and due to degeneracies among GC parameters, we need a suitable statistical approach. Bayesian techniques, which have recently become the workhorse of cosmological parameter inference, are of particular interest. In the perspective of possibly using the estimated age of the oldest stellar populations in a cosmological context as a route to constrain the age of the Universe, it is of value to adopt Bayesian techniques in this context too.

[1] Their low age estimate is due to the use of an incorrect distance to M3, since the stellar model used deviated just $\sim 10\%$ from current models' prediction of the effective temperature and gravity of stars, with their same, correct assumptions [3].

JCAP12(2020)002

There are only a few recent attempts at using Bayesian techniques to fit GCs' color-magnitude diagrams, albeit only using some of their features (see e.g., ref. [11]). Other attempts to use Bayesian techniques to age-date individual stars from the GAIA catalog can be found in ref. [12]. A limitation with the methodology presented in ref. [11] is the large number of parameters needed in their likelihood. Actually, for a GC of $N_{\rm stars}$ there are, in principle, $4 \times N_{\rm stars} + 5$ model's parameters (effectively $3 \times N_{\rm stars} + 5$), where the variables for each star are: initial stellar mass, photometry, ratio of secondary to primary initial stellar masses (fixed to 0 in ref. [11]) and cluster membership indicator. In addition, there are 5 (4) additional GC variables, namely: age, metallicity (fixed in the analysis of ref. [11]), distance modulus, absorption and Helium fraction. For a cluster of 10,000 or more stars, the computational cost of this approach is very high. To overcome this issue ref. [11] randomly selected a subsample of 3000 stars, half above and half below the MSTOP of the cluster, "to ensure a reasonable sample of stars on the sub-giant and red-giant branches". Another difficulty arises from the fact that the cluster membership indicator variable can take only the value of 0 or 1 (i.e., whether a star belongs to the cluster or not). This creates a sample of two populations referred to as a *finite mixture distributions* [11].

Capitalizing on the wide availability and potential of current observations, the aim of this paper is to present a Bayesian approach to exploit features in the color-magnitude diagram beyond the MSTOP and determine robustly the absolute age, jointly with all other relevant quantities such as metallicity, distance, dust absorption and abundance of α-enhanced elements, of each GC. In addition to statistical errors, we estimate systematic theoretical uncertainties regarding the stellar model. We bypass the computational challenge of the approach explored in ref. [11] by introducing some simplifications and by coarse-graining the information in the GC color-magnitude diagram, which greatly reduces the dimensionality of the problem without significant loss of information.

Our paper is organized as follows. In § 2 we describe the HST GC data; the stellar model used to fit the data and the calibration of the GC data is shown in § 3. The approach developed to obtain the parameters of GCs is introduced in § 4 where we describe the likelihood adopted and how we explore the posterior with Monte Carlo Markov chains. Results, the age of the oldest GCs and the corresponding inferred age of the Universe are presented in § 5. We expose our conclusions in § 6. A series of appendices cover the technical details of our method.

2 Data and stellar model

2.1 Globular cluster catalogs: defining our sample

We use the HST-ACS catalog of 65 globular clusters [13] plus 6 additional ones from ref. [14]. Out of 71 clusters, two were removed because of high differential reddening and a lack of red giant branch stars [11], one more was removed because of a lack of reasonable extinction prior from the literature, leaving 68 clusters in total. The data are available in two different Vega filters: F606W and F814W.

In order to clean the data of stars with poorly determined photometry, we use the same prescriptions as in ref. [11]. First, we remove stars for which photometric errors,[2] in both filters, fall into the outer 5% tail of the distribution. Then, we also remove stars in the outer

[2]Each photometric error has been rescaled depending on the number of observations according to the catalog instructions in the `readme` file.

JCAP12(2020)002

2.5% tails of the distributions of X and Y pixel location errors. Indeed, large pixel location errors indicate a non-reliable measurement of the properties of the star.

Similarly, we also expect measurements to be less robust at very low magnitudes. Moreover, the photometric error corresponding to these stars becomes very large, reducing drastically the information content of this part of the color-magnitude diagram.

Hence, for each cluster we define a "functional" magnitude interval between the lowest apparent magnitude of the brightest stars and a magnitude cut arbitrarily defined at $m_{F606W} = 26$, to include most of the main sequence stars for every cluster.

Only stars that satisfy all the conditions listed above and belong to the defined functional magnitude interval are considered further.[3] For readers interested in the number and percentage of stars retained, details are reported in table 2 of appendix B.

2.2 Software and stellar models

For the theoretical modeling of the data, we choose to work with a modified version of the software package `isochrones`[4] [15]. This software reads synthetic photometry files provided by stellar models and then interpolates magnitudes along isochrones (points in the stellar evolutionary track at same age) correcting for absorption, given the input parameters. Even though a new version is currently under development (`isochrones`2.0), and that in the main text of this paper we only use one model, we decided to use a modified version of the previous release as it enables us to consider different stellar models. The two stellar models already implemented are `MIST` [16, 17] and `DSED` [18]. Each stellar model comprises a set of *photometry files* that correspond to (discretized) isochrones in a color magnitude diagram. However, it is important to note that only in the photometry files of `DSED` several different abundances (parameterised by [α/Fe]) of α-enhanced elements, other than the solar abundance, are provided. These are elements like O, Ne, Mg, Si, S, Ca and Ti that are created via α-particle (helium nucleus) capture; [α/Fe] is fixed to 0 in the photometry files corresponding to the `MIST` model. This is important as GCs do have non-solar-scaled abundances. As we will show below (see appendix A) the abundance [α/Fe] is partially (but only partially) degenerate with variations of the GC's age and metallicity, so that it must be considered as a free parameter in the analysis to avoid biasing the results and to infer the correct statistical uncertainties. Therefore, we consider [α/Fe] as an independent parameter and limit our analysis to the `DSED` model; the ranges in parameter space covered by the `DSED` model photometry files in `isochrones` are specified in table 1.

The modifications we made to the code include:

- change of the cubic interpolation process, going from (Mass, Age, Metallicity) to (EEP, Age, Metallicity) where EEPs are equivalent isochrone evolutionary points.[5] EEPs are provided by `isochrones`, we only modify the interpolation interface, following the implementation of `isochrones`2.0,
- implementation of a standard magnitude correction to account for extinction in the selected filters according to the Fitzpatrick extinction curve (see e.g., ref. [22]) in the selected (here HST F_{606W} and F_{814W}) and V band filter,
- interpolation on the [α/Fe] parameter.

[3] A further cut at low magnitudes is introduced in section 3. The cut described here is motivated by the survey limitations; the cut in section 3 is to speed up the analysis without removing significant signal.

[4] https://github.com/timothydmorton/isochrones, version 1.1-dev.

[5] EEPs were introduced in refs. [19–21]. EEPs are a uniform basis which simplifies greatly the interpolation among evolutionary tracks. Each phase of stellar evolution is represented by a given number of points, each point in one track has a comparable interpretation in another track.

JCAP12(2020)002

Stellar model	DSED
initial rotation rate v/v_{crit}	0.0
Age range	0.250-15 Gyr
Age sampling	0.5 Gyr
number of EEPs per isochrone	$\simeq$ 270
Metallicity range [Fe/H]	-2.5 to 0.5 dex
Helium fraction configuration	$Y_{\rm init}$ = 0.245†, 0.33, 0.40 ‡
[α/Fe]	-0.2 to 0.8^{+}

† The varying Helium fraction configurations, Y, are defined in photometry files as $Y = Y_{\rm init} + 1.5Z$ where Z is the metal mass fraction and $Y_{\rm init}$ is the starting value.

‡ Fixed Helium fraction configurations Y = 0.33 and 0.40 are only available for [Fe/H] $\leq$ 0.

$^{+}$ For the fixed Helium fraction configurations, only two options [α/Fe]= 0 or +0.4 are available.

Table 1. Properties of the `DSED` stellar models available in the `isochrones` package. We refer the reader to original ref. [18] for more details.

The set of fitted parameters for each GC are age, distance modulus, metallicity, [α/Fe] and absorption. Note that there are different photometry files corresponding to different values of metallicity [Fe/H] and Helium fraction, Y.[6] These, however, are not two fully independent quantities: both quantities are a function of the stellar and (proto)-solar metal mass fraction, denoted by Z and $Z_{\odot}$, respectively. Consequently, they are highly correlated. We are interested in the Age-Metallicity relation, hence for our purposes we can use only one of them, the [Fe/H] fraction[7] in our case, as the independent variable. We vary [α/Fe] independently of [Fe/H] and Y.

3 Color-magnitude diagram-based likelihood for globular clusters

As mentioned in section 1, the traditional Bayesian analysis of this kind of data sets attempts to model each star independently, which implies a significant computational cost due to the large number of parameters to explore. A common approach is to fit the initial mass of each of the $N_{\rm stars}$ stars in the color-magnitude diagram as an independent parameter (along all other stellar parameters). Then, the posterior is marginalized over all individual star parameters to infer the parameters describing the GC.

Here we attempt to reduce the high dimensionality of the parameter space using a different approach. While the large number of stars can be a liability in terms of computational cost for traditional Bayesian approaches, we turn it to our advantage, especially in the most populated part of the color-magnitude diagram. For each isochrone of the stellar model, there are a number of equivalent evolutionary points (EEPs) (see line 5 of table 1) associated with an initial stellar mass. Each EEP has a counterpart in every isochrone, making it possible to identify specific points in the color-magnitude diagram across different isochrones,

[6] The Helium fraction Y of a GC is not necessarily identical to the cosmological one. If Population III stars have enriched the medium with Helium, it is the resulting Helium fraction that matters here. Hence, in principle there could be object by object (GC) variations of Y.

[7] The metallicity Z is related to [Fe/H] fraction in the usual way: [Fe/H] = 1.024 log(Z) + 1.739, see ref. [21].

JCAP12(2020)002

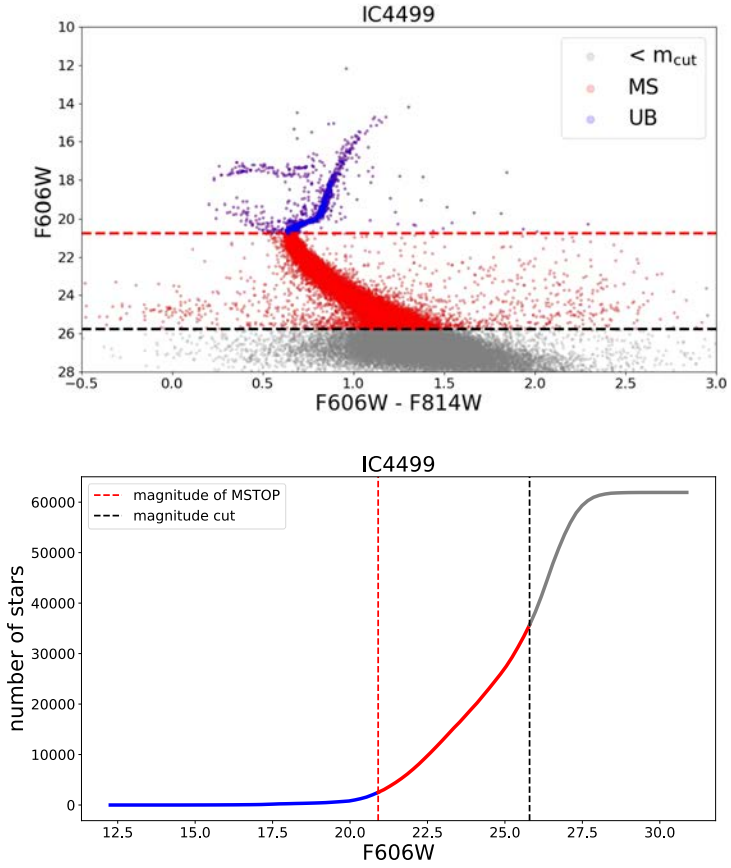

Figure 1. Top Panel: illustration, for a typical GC (IC4499), of the initial split of the "functional" magnitude interval in two parts (MS below the MSTOP and UB above the MSTOP). The red line corresponds to $m_{\rm MSTOP}$, and the black line marks $m_{\rm cut}$. Points below $m_{\rm cut}$ do not add significant additional information, but significantly slow down and complicate our analysis. This is why they are not considered here. Bottom panel: cumulative distribution of stars and adopted magnitude cuts for the same cluster.

e.g., the MSTOP. In other words, the isochrone profile in the color-magnitude diagram is sampled by EEPs (which are "universal" across different isochrones) obtained for different adopted values of the parameters of interest. This is the reason why, as it is well known, the interpolation between evolution tracks is greatly simplified by interpolating instead directly between EEPs. Since we are not interested in the initial mass of stars, we do not model each star independently and exploit the benefits of the EEPs working directly with them, as provided by the relevant photometry files. This reduces the dimensionality of our analysis to just the five GC parameters described in the previous section.

We divide the "functional" magnitude interval into two parts as illustrated in figure 1: the part below the MSTOP, which we refer to as MS for main sequence, and the part above, which we refer to as UB for upper branch. The large spread of colors at low magnitudes introduces a lot of noise, which slows down significantly the convergence of our algorithm without adding, in practice, any useful additional signal. For this reason, on top of the selection cuts described in section 2, we apply a potentially more stringent upper magnitude

JCAP12(2020)002

cut. In practice, for the 68 clusters in our catalog we choose an upper cut magnitude value

$$m_{\rm cut} = \min(m_{\rm MSTOP} + 5\,, 26), \tag{3.1}$$

where $m_{\rm MSTOP}$ is the magnitude corresponding to the MSTOP. In fact, for some GCs going 5 magnitudes below the MSTOP would cause to include noisy data. With this choice we limit the cut for those GCs to $m_{\rm cut} = 26$. Our findings are not sensitive to the details of this cut as long as the noisy, dim part of the color-magnitude diagram is removed, and enough EEPs in the main sequence are retained, which is what we ensure here.

3.1 Main sequence

We proceed to bin in magnitude the sample of stars belonging to the main sequence; these bins should be thin enough so that the isochrone can be approximated as linear in each bin, yet with number of stars per bin large enough to satisfy the central limit theorem. Given the large number of stars in the MS (as illustrated in the bottom panel of figure 1), these two conditions are fulfilled for all GCs. In practice, we use bins in the F_{606W} magnitude interval for the MS with constant width of 0.2 mag, which yields a maximum of 25 bins and a minimum of 20 for the GCs in our catalog. The number of stars per bin is proportional to the number of stars in the GC and ranges from several hundreds to several thousands. It is then justified to assume that the scatter in color of stars inside each magnitude bin follows a Gaussian distribution centered on the true underlying isochrone. This simplification (akin to a coarse-graining in the color-magnitude diagram, and thus to a data-compression) alone allows us to decrease the effective size of the data set, and thus, compared to previous approaches, to reduce the number of model parameters for this part of the analysis: we have 5 parameters, and $N_{\rm bins}$ number of data points. The main peak of the distribution of star positions along the color axis in each bin, indexed by i, should be, and is, well approximated by a Gaussian distribution (see figure 9 in appendix C for an illustration). Bins where the distribution cannot be fit by a unimodal Gaussian — a possible sign of multiple populations — are removed from the analysis. This always happens at the faint end of the main sequence (except for three clusters for which one to two bins are removed), even after the cut from equation (3.1). For this reason we use instead the median of the distribution. It allows us to keep the maximum of 25 bins while taking into account the effect of the multiple population. The median value is almost identical to the Gaussian mean and larger error bars are a reasonable trade-off for outliers. More details are presented in appendix C. The color at bin center for each magnitude bin $C_i^{\rm data}$ is defined by the median. Since the main sequence in the color-magnitude diagram is not perfectly vertical, we rescale the error by $\sigma_i^{\rm data} \approx 1.253\sigma_{{\rm EEP},i} \times \cos(\phi_i)$ where $1.253\sigma_{{\rm EEP},i}$ is the standard error of the median and ϕ_i is the angle between the data orientation and the vertical axis inside bin i as detailed in appendix C (in particular see figure 10 in the appendix). This correction is very small and always well below 4%. Figure 2 shows an example of this binning for GC IC4499, along with the corresponding $C^{\rm data}$ and $\sigma^{\rm data}$.

Assuming that bins are uncorrelated (which given the small observational errors in the star magnitudes is a fair assumption), the logarithm of the likelihood is defined as

$$\mathcal{L}_{MS} = \ln\, L = -\frac{1}{2}\sum_{i=1}^{N_{\rm bins}} \left(\frac{C_i^{\rm data} - C_i^{\rm th}}{\sigma_i^{\rm data}}\right)^2 \tag{3.2}$$

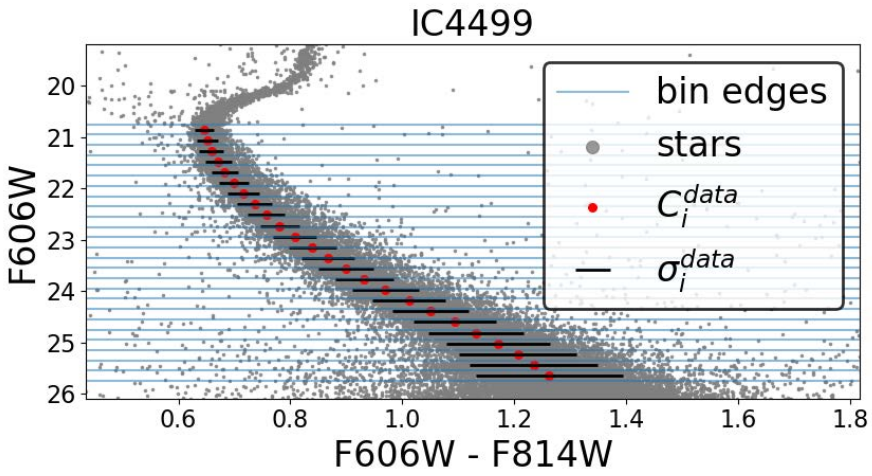

Figure 2. Binning of the main sequence, illustrated for the GC IC4499. The red dots and black lines represent the central value and standard deviation of the color distribution in each bin, respectively.

where $C_i^{\rm th}$ is the theoretical isochrone color interpolated at the center of bin i, and $N_{\rm bins}$ is the number of bins considered in the analysis (i.e., after removing the bins with bimodal color distributions).

3.2 Upper branch

In addition to the main sequence, we consider stars belonging to the Upper Branch (UB) i.e., stars brighter than the MSTOP. We bin the magnitude interval as we did for the main sequence. However, in this case, the number of stars is not large enough to support the central limit theorem for small magnitude bins; in addition we expect that the measurement will be highly sensitive to outliers. Therefore, we cannot fit the color distribution to a Gaussian function as done for the MS. Instead, we apply these three prescriptions:

- Since `DSED` isochrones do not include stages beyond the tip of the red giant branch — i.e., do not include EEPs belonging to the Horizontal branch and the asymptotic giant branch — we mask out all the bins which correspond to stars (and EEP) that do not belong to either the sub-giant branch or the red giants.

- Since the estimation of the mean is easily contaminated by outliers, we use the median color instead in each bin as an estimate for $C_i^{\rm data}$. In fact, we expect that the color errors follow a Gaussian distribution, and that the outliers are stars that are not part of the GC main sequence of upper branch (our target sample). If we could select only stars that belong to our target sample, they would follow a Gaussian distribution. In practice, using the median down weights the contribution of outliers on the estimate of the central value of the distribution. Therefore, it provides a good estimate of the mean value of the distribution of the target sample; here we *assume* that the resulting distribution matches the target distribution and can be assumed to be Gaussian.

- We use the error of the median for normal distributions $\sigma_{{\rm med},i} = 1.253\sigma_{{\rm EEP},i}$, where $\sigma_{{\rm EEP},i}$ is the regular standard deviation in bin i.

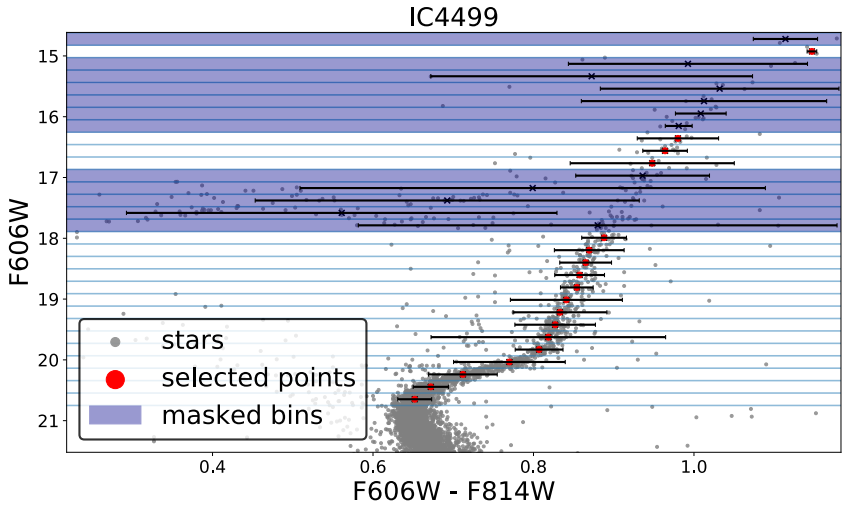

Figure 3. Binning of the upper branch for a representative GC IC4499. The grey points are the stars, the horizontal blue lines show the adopted binning. The masked bins are shaded. Each red point represents the median value at bin center. The error bars correspond to $\sigma_{\mathrm{med},i}$.

This is illustrated in figure 3. In this figure, for a representative GC, IC4999, the stars in the color-magnitude diagram are shown as grey points, the excluded bins are shaded, the red points show the C_i^{data}, and the error bars show the $\sigma_{\mathrm{med},i}$.

Finally the likelihood is also taken to be Gaussian as in eq. (3.2), with the only differences of C_i^{data} being the median value at bin center, and $\sigma_{\mathrm{med},i}$ the associated error for bin i. We are aware that this choice of Gaussian likelihood is not as well motivated as for the MS. Nevertheless we note here that other systematic uncertainties (see section 4.1) are likely larger than the one introduced by this approximation.

3.3 Multiple populations and magnitude cut

For the sake of simplicity in the analysis, we assume that parameters such as age, metallicity and distance are common to all stars belonging to the GC. Nonetheless, GCs can be more complex and host distinct populations. Multiple populations in GCs is an active research area (see e.g., [23] for a review). It is important to note that multiple populations do not necessarily have different ages, they may have e.g., different element abundances. Moreover, the effects of multiple populations are minimized for the filters used to create the catalog (F_{606W} and F_{814W}; see ref. [23] and references therein). When we apply our analysis to GCs known to host multiple populations to quantify the effect that this might have in the inferred constraints, we find that having multiple populations introduces an additional widening in the marginalized inferred age, as well as multiple peaks for the metallicities. GCs with multiple populations have a manifestly multi-modal posterior distribution where additional *local* maxima may appear. We find that the magnitude cut m_{cut} (see equation 3.1) we impose helps to reduce the sensitivity to secondary populations, i.e., it suppresses the secondary local maxima, but leave the global maximum unaffected. This is because it is easier to see multiple population in the faint end of the MS; at brighter magnitudes, the two populations blend. Nevertheless, the posterior distributions obtained for some GCs are still multi-modal. Masking out bins where the distribution is markedly multimodal further minimize this effect. Any residual multi-

JCAP12(2020)002

modality is blended with the main maximum and thus effectively contributes to growing the errors. The way we deal in practice with the multi-modality of these secondary local maxima is developed further in section 4.

4 Parameter inference

We assume that the two parts (MS and UB) of the "functional" magnitude interval considered are independent. The total log-likelihood, $\mathcal{L} = \ln L$, is then $\mathcal{L} = \mathcal{L}_{\rm MS} + \mathcal{L}_{\rm UB}$.

The parameters that we vary are: age, metallicity [Fe/H], absorption, distance and α enhancement [α/Fe]. In order to ensure that we remain inside the interpolation domain of the stellar model, we use uniform priors corresponding to the intersection of the parameter-space volumes of the stellar model (in our case this corresponds to the prior region of `DSED` see table 1). These are: [1,15] Gyr for the age, [−2.5,0.5] dex for metallicity, (0,3] for absorption, (0,∞) for distance and [−0.2,0.8] for [α/Fe].

In addition, we adopt gaussian priors on the metallicity, distance modulus, absorption and [α/Fe] as follows. For the metallicity, α enhancement and distance the priors are centered around estimates from the literature for each globular cluster (see ref. [14]). For 65 clusters the extinction estimates are based on the two catalogs of refs. [24, 25]; however, for three globular clusters (NGC 6121, NGC 6144, NGC 6723) we use instead values from more recent literature (refs. [26–28] respectively) since the quality of the fit and the posterior were unacceptable when using the catalogs estimates.

We adopt $\sigma_{\rm [Fe/H]} = 0.2$ dex for the width of the Gaussian priors for the metallicity, based on spectroscopic measurements, corresponding to twice the typical errors reported in ref. [3]).[8] The width adopted for the distance modulus prior is $\sigma_{\rm dm} = 0.5$ from Gaia/Hipparcos indirect distances, 2–3 times the typical errors reported in refs. [3, 4]. We assume a dispersion on the reddening $\sigma_{E(B-V)} = 0.02$, in agreement with ref. [4], which translates into Gaussian priors on absorption with $\sigma_{\rm abs} = 0.06$ following the Cardelli et al. [30] relation. For [α/Fe] we adopt a prior of $\sigma_\alpha = 0.2$ which is equivalent to the sampling step of the DSED stellar grid.

Unlike the priors on metallicity or distance which are conservative compared to recent literature, the prior on absorption needs to be restrictive to reduce the degeneracy between age and absorption. Even though it may appear narrow, one should bear in mind that this parameter is usually kept fixed in other analyses in the literature.[9]

For some clusters, the posterior distribution is cut by the 15 Gyr age limit imposed by the grid of the stellar models, but even in these cases the peak of the distribution is always well determined and the cut happens at the $\sim 2\sigma$ level, hence the effect on the results can be kept under control.

Given the nature of the problem (degeneracy between the age, distance and the metallicity), the nature of the data (possible presence of multiple populations), and the nature of the likelihood calibration (we fit, at the same time, the MS and the UB, where, in principle, each might favor a different region of the parameter space and be affected by different degeneracies), we expect that the posterior distribution might be multi-modal. In this case, the standard `emcee` sampler may be inefficient.

[8] In principle, this prior could be more stringent, following ref. [29]. However we decide not to do this here, and explore a wider range in metallicy.

[9] We have also explored relaxing the metallicity prior by increasing the width of the gaussian by a factor few. We find that this more conservative choice does not affect the final results of the inferred age ($t_{\rm GC}$, $t_{\rm U}$) as statistical errors remain below the systematic ones.

JCAP12(2020)002

Existing methodologies to handle multi-modal distributions include slicing the parameter space and combining the results afterwards, or techniques like parallel-tempering Monte Carlo Markov chains where the chains are run at different temperatures, which makes it easier to the chains to communicate and thus "move" between peaks and low likelihood regions. The first approach is expensive in terms of computational cost and we found the second one not efficient in our case. Parallel tempering MCMC will move the "coldest" chains to a formal global maximum which is however in a non-physical region of parameter space (ages $\gtrsim 15\,\mathrm{Gyr}$ and very low metallicities $[\mathrm{Fe/H}] < -2.3$ dex). We explain this tendency as follows. At high ages and low metallicities the evolutionary tracks in the color magnitude diagram become very similar to each other (as shown in figure 8 in appendix A). In other words, there is a lot of prior volume to explore, and therefore the chains tend to spend a lot of time there. This is an artifact of the prior probability distribution chosen.

One of the consequences of having multi-modal posterior distributions with several local maxima of the likelihood and one global maximum, and using the standard affine invariant `emcee` sampler, is a low acceptance fraction. This is especially significant if the modes are well separated, i.e., if the separation between modes is much larger than the width of the distribution around the maxima. Indeed, only a small fraction of MCMC steps, close to the likelihoods peaks are accepted. One possibility to bypass this technical difficulty may involve re-parametrization [31] or non-uniform priors, in addition to using stronger Gaussian priors on the metallicity.

We decided to stick to the standard `emcee` sampler and increased the number of chains to improve the number of accepted steps. We run 100 chains (or walkers for `emcee`) for 5000 steps (several times the autocorrelation length) with a burn-in phase of 500 steps. This set up returns a suitable and stable acceptance rate. For multimodal distribution, the initialization of the chains can be a important factor. We tested two configurations (a tiny Gaussian ball centered on estimates from the literature see ref. [14] and a uniform distribution with boundaries matching the uniform priors. Both gave consistent results and we kept the second configurations as it is more objective. We have also made several convergence tests on a subset of clusters varying the number of walkers and increasing the steps of each of them (from 100 to 700 walkers for up to 100,000 steps) and found that this does not change the results.

We report the error on the parameters as the highest posterior density interval (also sometimes referred to as minimum credible interval) at a given confidence level. Note that for non-symmetric distributions (such as those we have here) these errors are not necessarily symmetric.

4.1 Systematic uncertainties

In our approach, all the parameters that describe the GCs (age, distance, metallicity, $[\alpha/\mathrm{Fe}]$ and extinction) are determined directly from the data. While HST photometry does have some remaining systematic uncertainty, this is minute compared to the uncertainty associated with the theoretical stellar model (see below). We estimate the systematic uncertainties in the ages of GCs induced by the theoretical stellar model using the recipe in table 2 of ref. [4]. To our knowledge, this is the most rigorous approach among stellar model-building to estimate the systematic uncertainties using the "known-unknowns". Inspection of table 2 in ref. [4] shows that the main systematic uncertainty is due to the use of mixing length theory to model convection in the 1D stellar models. The other dominant systematic uncertainty is

JCAP12(2020)002

related to reaction rates and opacities.[10] Everything else is subdominant, thus the combined effect these two components captures well the extent of systematic errors.

Mixing-length theory[11] has two parameters: the mixing-length parameter (i.e., roughly how much the convection cells travel before they break up), and the overshoot parameter (how much the convective cell travels beyond the equilibrium condition). Of these two, the second one is unimportant for low-mass stars such as those in GCs. These two parameters dominate the uncertainty in stellar model building; the uncertainties in nuclear reactions are at the % level.

In principle, changes in the mixing length do not alter the lifetime of the star, see discussion in page 725, of ref. [32]. The effect on the inferred age arises from degeneracies with metallicity. In this work the metallicity is strongly constrained so that, in principle, the effect of mixing length uncertainties could be reduced significantly.

In fact, the mixing length parameter is usually calibrated from fits to the Sun, but astro-seismology from other stars at different evolutionary stages indicates a spread of values between 1.0 and 1.7. Thus, the results from observations of the Sun are extrapolated to stars belonging to GCs, but adopting the full spread of mixing length parameter values to quantify the systematic uncertainties. However, a better estimation of systematic uncertainties related with the mixing length parameter is possible. As shown in ref. [10], not only the morphology of the red giant branch can be used to constrain the value of the mixing length, but also all the GCs analysed in ref. [10], had the same value for the mixing length and showed no star-to-star variation of the mixing length parameter. Therefore, the morphology of the red giant branch is sufficient to constrain the mixing length, once the metallicity is constrained, without the need to rely on the solar calibration. Thus, potentially, for the present study, as the metallicity can be constrained from the lower main sequence as well as the sub-giant branch (see figure 8), the upper giant branch could be used to determine the value of the mixing length as done in ref. [10]. This approach would require adding the mixing length parameter as an extra free parameter in our analysis; we leave this for future work.

Here instead we prefer to be conservative and use the full range for the mixing length considered in ref. [4] (i.e., between 1.0 and 1.7), which is conservative because the study of ref. [10] showed that fits to the position of the red giant branch with known metallicity indicate no significant spread in mixing length parameter. These fits recover a value of 1.6, well in agreement with results from calibration to the Sun. To estimate the error in ages due to mixing length variations over the full conservative interval, we use the stellar models of ref. [32], and in particular the fitting formulas therein. This yields a 0.3 Gyr age uncertainty.

In addition to this we add an extra 0.2 Gyr to account for uncertainties in reaction rates and opacities, as from table 2 of ref. [4]. In total, we have a 0.5 Gyr uncertainty budget due to systematic effects in stellar modeling.

Note that in the standard MSTOP approach, another systematic uncertainty to account for would be the value of [α/Fe], which in general is not known and is assumed to be between 0.2–0.4. However, in our approach, this is not the case as this is a parameter of the model: its value is directly constrained by the analysis and its uncertainty is therefore already included in our marginalized errors.

[10] Rotation is another source of systematic uncertainty, as the rotation speed of stars in GCs is unknown. However, the main effect of rotation is to alter the depth of the convection zone. Given that we have explored a wide range of values of the mixing length parameters, the effect of rotation is effectively included in our systematic budget estimation.

[11] In appendix D we give a brief description of mixing-length theory.

JCAP12(2020)002

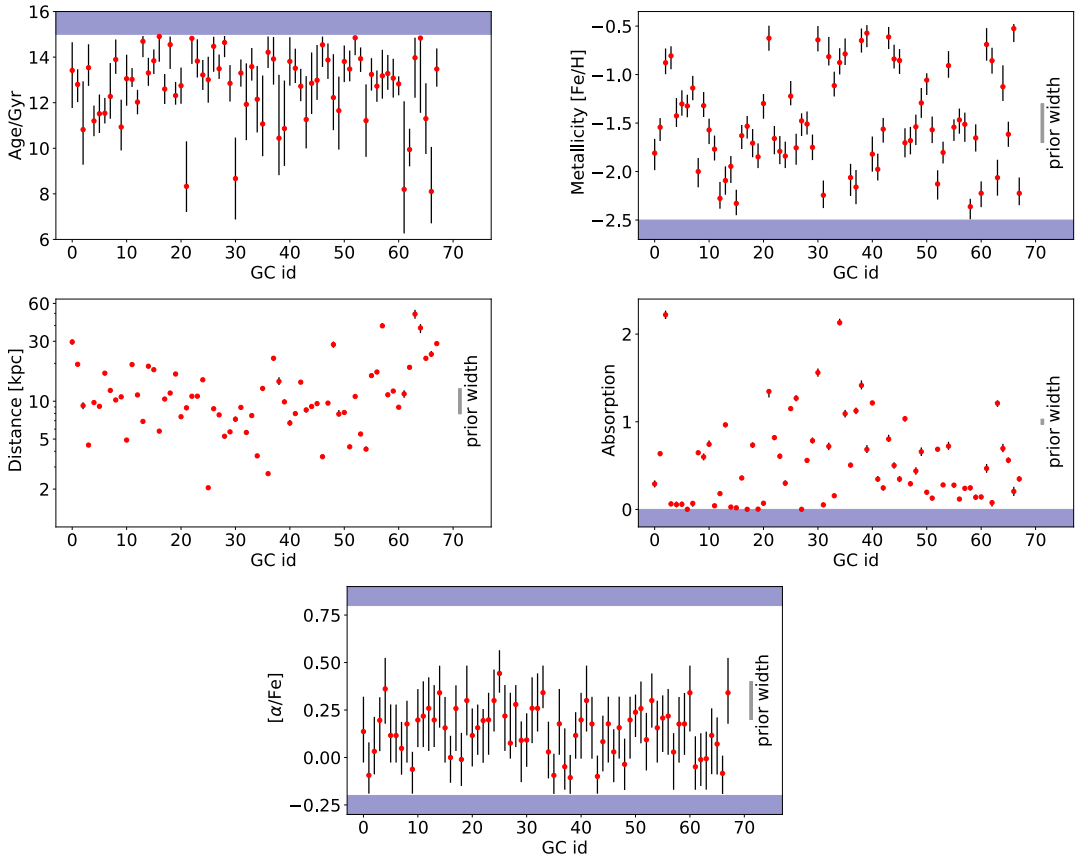

Figure 4. 68% confidence level marginalised constraints for the five parameters of interest for each of the GC in the sample (CG id, in the x-axis, corresponds to the ordering of table 3). The shaded blue regions represent boundaries of the uniform prior. There are additional gaussian priors of $\sigma_{[Fe/H]} = 0.2$ dex for metallicity, $\sigma_{\rm dm} = 0.5$ on the distance modulus, $\sigma_{[\alpha]} = 0.2$ for alpha enhancement and $\sigma_{\rm abs} = 0.06$ in the absorption centered around values from the literature (see text for details).

5 Results

We apply the methodology presented in previous sections to our catalog of 68 GCs. Two-dimensional marginalized posteriors for all pairs of parameters can be found for a representative GC in appendix F. Figure 4 shows our main results (see also appendix E and tables 3 and 4). We present marginalized constraints on the absolute age, metallicity, distance, absorption and [α/Fe] of each GC assuming the `DSED` model. The x-axis in each panel shows the cluster id following the same order as in table 3. The gray horizontal areas show the hard priors imposed by the stellar models domain in parameter space and the gray vertical band (when reported) illustrates the width the gaussian prior adopted (see section 4). We find no correlation between age and distances, absorption or [α/Fe]. In particular the absorption values are low and the distribution presents a scatter that is not correlated with the age. On an individual cluster-basis the constraints on [α/Fe] are very weak, however values of [α/Fe]> 0.6 are typically disfavored. A comparison with Dotter et al. [14] spectroscopic measurements can be found in figure 11 in appendix F.

In figure 5 we compare our inferred constraints with the findings of ref. [4] for the 22 GCs in common. It is interesting to note the good agreement obtained for the metallicity estimates

JCAP12(2020)002

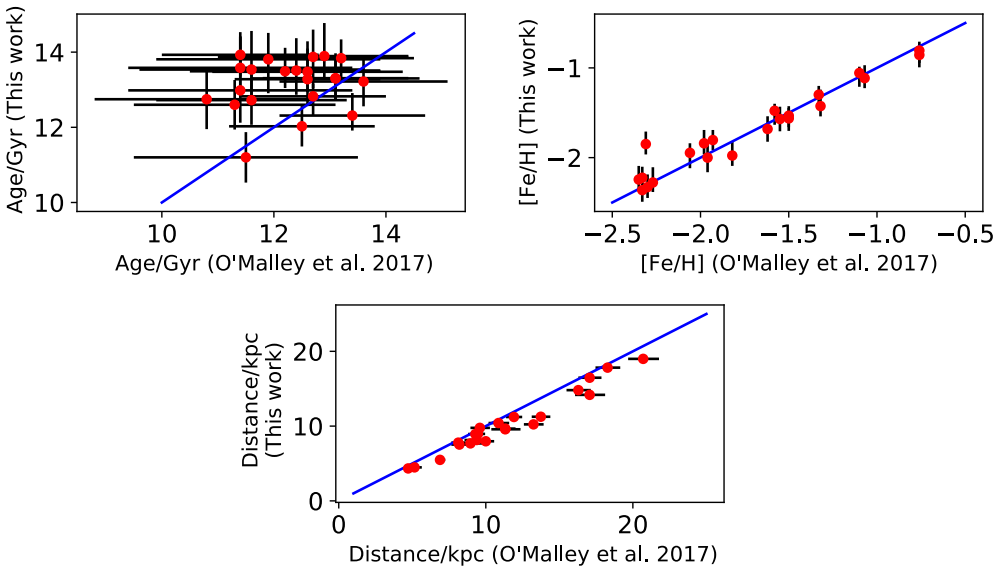

Figure 5. Direct comparison between our marginalized constraints on the age, distance and metallicity of GCs with results from ref. [4] for the 22 GCs in common. The blue lines indicate the identity. We plot uncertainty bars for both determinations when available. There is excellent agreement for the metallicity determination and reasonable agreement for the distance determinations, although our distances (with error bars so small that are behind the red dots) are on average somewhat shorter than those of ref. [4] by about 200 pc. The age agreement is within the uncertainties, but our ages are slightly older on average. See text for more details.

of [Fe/H]. Our distances, using information from the color-magnitude diagram and only very weak priors, are in reasonable agreement with those obtained ref. [4], which rely on external information (GAIA parallaxes and accurate distance to nearby dwarf stars). However, we find a small shift as our determination of distances is ~ 200 pc smaller on average. This small discrepancy arises because the analysis in ref. [4] assumes a fixed extinction value, while we treat extinction as a free parameter to be constrained by the data and marginalized over. For the ages determination the agreement is within 68% confidence level uncertainties. From the first panel of figure 5 it is possible to appreciate that the errors from this study are smaller that those of ref. [4] even when ref. [4] uses additional external information, not used here. This illustrates the advantage of considering regions of the color-magnitude diagram beyond the main sequence.

The use of the full color-magnitude diagram, along with the adoption of the priors motivated in section 4, enables us to break the age-distance-metallicity degeneracy. In particular, the breaking of the age-metallicity degeneracy is visualized in appendix A where we show how the isochrones and the color magnitude diagram change in response to variations of these parameters.

5.1 The age of the oldest GCs

On average, the oldest GCs are those expected to be more metal poor. Here we consider two metallicity cuts as a way to select the oldest GCs: [Fe/H]< -2 as adopted in ref. [33] — leaving 11 clusters — and [Fe/H]< -1.5 — leaving 38 clusters. We estimate the age distribution $t_{\rm GC}$ for these two samples by multiplying the individual bayesian posteriors (see figure 6).

JCAP12(2020)002

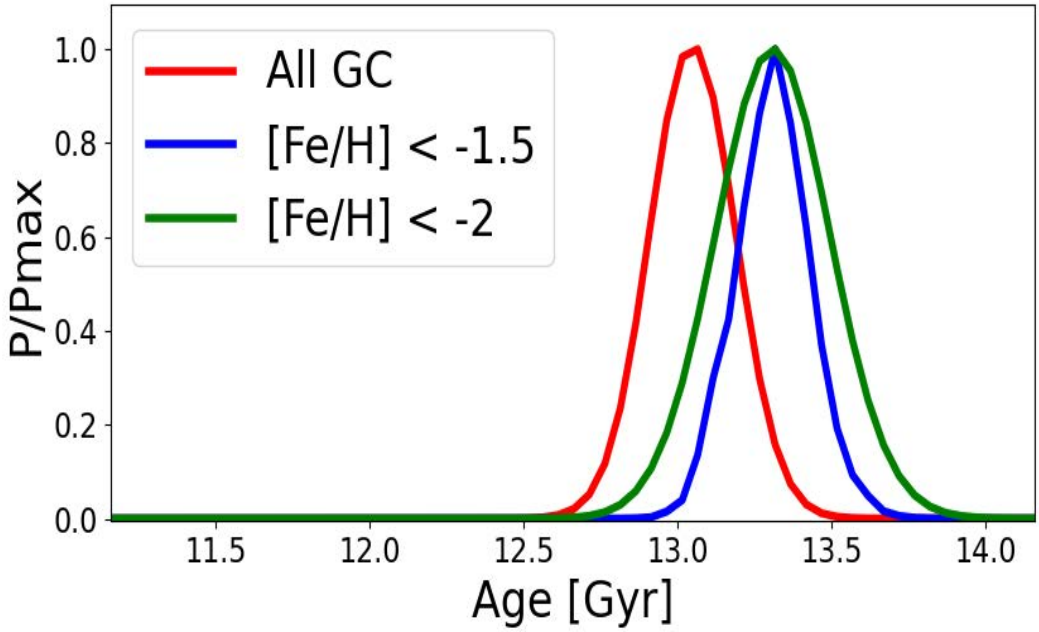

Figure 6. Age distribution for globular clusters with different metallicity cuts ([Fe/H] < 2 (dot-dashed); [Fe/H] < 1.5 (solid); no cut (dashed)). The behavior is consistent with the expected age-metallicity relation. We only display the statistical uncertainty. An additional uncertainty of 0.5 Gyr at 68% confidence level needs to be added to account for the systematic uncertainty.

For [Fe/H]< -2 this yields $t_{\rm GC} = 13.32^{+0.15}_{-0.20}({\rm stat.}) \pm 0.5({\rm sys.})$, while for [Fe/H]$< -1.5$ we obtain $t_{\rm GC} = 13.32 \pm 0.1({\rm stat.}) \pm 0.5({\rm sys.})$. The first uncertainty is the statistical uncertainty while the second uncertainty is the systematic one, as calculated in section 4.1. The results for the two cuts are very consistent; as expected, the additional 27 clusters in the [Fe/H]< -1.5 cut reduce the statistical error significantly; here we therefore adopt the [Fe/H]< -1.5 cut due to the increased statistical power.

5.2 From globular cluster ages to the age of the Universe

The age of the oldest stars sets a lower limit for the age of the Universe. These stars and the oldest GCs formed at a redshift $z_{\rm f}$. Hence, it is possible to estimate the age $t_{\rm U}$ of the Universe from the age $t_{\rm GC}$ of the oldest GCs adding a formation time Δt, corresponding to the look back time at $z_{\rm f}$.

As argued in ref. [33], it is possible to estimate the probability distribution of Δt by considering that the first galaxies are found at $z \sim 11$ and a significant number of galaxies are found at $z > 8$. Many of these galaxies contain stellar populations that indicate that star formation started at $z \sim 15$–40 [34–36]; $z_{\rm f}$ is thus assumed to be $z_{\rm f} \geq 11$. Both theoretically [37–41] and observationally [42] GC seem to form at $z_f > 10$. On the other hand, GCs could not have formed before the start of reionization which is estimated to happen around $z_{\rm f,max} \sim 30$. Ref. [33] includes a computation of the probability distribution of Δt marginalizing over H_0, $\Omega_{m,0}$ and $z_{\rm f}$, with $z_{\rm f}$ varying between $z_{\rm f,min} = 11$ and $z_{\rm f,max}$. The resulting distribution depends very weakly on cosmology for reasonable values of the cosmological parameters, and very weakly on the choice of $z_{\rm f,max}$ provided $z_{\rm f,max} > 20$. Here

JCAP12(2020)002

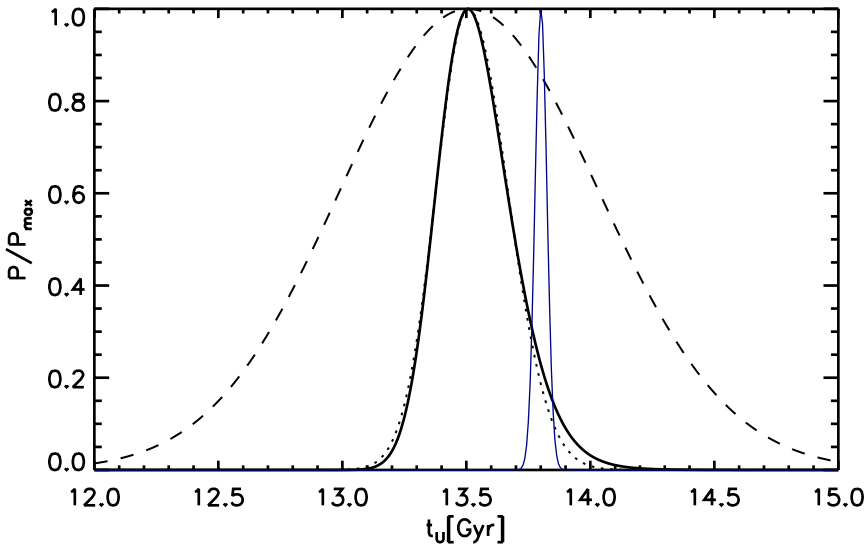

Figure 7. Estimate of the age of the Universe from the age of the oldest globular clusters (solid thick black line) including systematic uncertainties (dashed line) added in quadrature to a gaussian fit (with asymmetric variances) of the statistical distribution (dotted line). The thin blue line shows the Planck 2018 posterior for the age of the Universe.

we estimate the full probability distribution of $t_{\rm U} = t_{\rm GC} + \Delta_t$ by performing a convolution of the posterior probability distribution for $t_{\rm GC}$ as provided in § 5.1 and the probability distribution of Δ_t from ref. [33] for which we provide a fitting formula in appendix G.

We find $t_{\rm U} = 13.5^{+0.16}_{-0.14}({\rm stat.}) \pm 0.5({\rm sys.})$ at 68% confidence level. The resulting posterior distribution for the age of the Universe $t_{\rm U}$ is presented in figure 7. The solid black line is the result including only statistical errors, the dashed line is obtained by fitting this distribution with two gaussians with the same maximum but independent variances for the two sides (dotted line), and then adding the systematic error in quadrature (dashed line). For reference the blue thin line shows the constraint inferred from CMB observations from Planck, assuming the ΛCDM model [43].

6 Summary and conclusions

Resolved stellar populations of GCs provide an excellent data set to constrain the age of the Universe, which in turn is a key parameter in cosmology governing the background expansion history of the Universe. Since the mid 90's, estimates of the ages of GCs have been in the range 12–14 Gyr consistently (see e.g. ref. [10]). With current improvements in observational data and stellar modeling, it is possible to decrease the uncertainty on the ages by a factor 4. Given the high-quality of data obtained by HST and the improvement in the accuracy of stellar models, we have attempted to estimate the physical parameters of GCs including their age, using as many features as possible in their color-magnitude diagrams.

It is well known that the MSTOP is very sensitive to the GC's age; however, it is also sensitive to distance, metallicity, and other parameters, due to significant degeneracies in parameter space. However, degeneracies can be in large part lifted if other features of

JCAP12(2020)002

the color-magnitude diagram are exploited (see appendix A). In this paper, we have analyzed a sample of 68 ACS/HST globular clusters using most of the information in the color-magnitude diagram: specifically, the main sequence and red giant branch. We have developed a Bayesian approach to perform an analysis of each GC, varying simultaneously their age, distance, metallicity, [α/Fe] and reddening adopting physically-motivated priors based on independent measurements of distances, metallicities and extinctions found in recent literature. Our obtained posteriors yield constraints that are fully compatible with previous, and independent, values in the literature.

The average age of the oldest (and most metal poor) GCs is $t_{\rm GC} = 13.32 \pm 0.1(\text{stat.}) \pm 0.5(\text{sys.})$ Gyr. The systematic errors are due to theoretical stellar model uncertainties and in particular uncertainties in the mixing length, reaction rates and opacities. Systematic errors are now bigger than the statistical error, once constraints from several objects are combined. Hence, to make further progress, uncertainties in stellar model-building should be addressed.

This determination can be used to estimate the Universe absolute age by taking into account the look back time at the likely redshift of formation of these objects. We find the age of the Universe as determined from stellar objects to be $t_{\rm U} = 13.5^{+0.16}_{-0.14}(\text{stat.}) \pm 0.5(\text{sys.})$ at 68% confidence level. The statistical error is 1.2%; the error budget is dominated by systematic uncertainties on the stellar modeling. The prospect of determining the age of the Universe with an accuracy competitive with current cosmology standards, may serve to motivate an effort to reduce uncertainties in stellar-model building. This will be addressed in future work. The statistical uncertainty in t_U is now sufficiently small to warrant comparison to the CMB model-dependent inferred age, which is one of the most accurately quantities inferred from the CMB [44]. Thus comparing the CMB derived value to independent astrophysical estimates can yield precious insights into possible new physics, or support the ΛCDM model. Our determined value of $t_{\rm U}$ is fully compatible with the inferred value from the Planck mission observations assuming the ΛCDM model.

Acknowledgments

We thank the stellar modelers for making their stellar models publicly available. We thank the anonymous referee for an useful and constructive report. We also thank David Nataf for very useful feedback. This work is supported by MINECO grant PGC2018-098866-B-I00 FEDER, UE. JLB is supported by the Allan C. and Dorothy H. Davis Fellowship. JLB has been supported by the Spanish MINECO under grant BES-2015-071307, co-funded by the ESF, during part of the development of this project. LV acknowledges support by European Union's Horizon 2020 research and innovation program ERC (BePreSySe, grant agreement 725327). The work of BDW is supported by the Labex ILP (reference ANR-10-LABX-63) part of the Idex SUPER, received financial state aid managed by the Agence Nationale de la Recherche, as part of the programme Investissements d'avenir under the reference ANR-11-IDEX-0004-02; and by the ANR BIG4 project, grant ANR-16-CE23-0002 of the French Agence Nationale de la Recherche. The Center for Computational Astrophysics is supported by the Simons Foundation.

JCAP12(2020)002

A Test of sensitivity of the color-magnitude diagram to model parameters

In this appendix we explore the dependence of the isochrones in the color-magnitude diagram of a GC on the model parameters. On top of illustrating the sensitivity of different sections of the evolutionary track to these parameters, this exercise will allow us to convey how parameter degeneracies can be lifted by considering regions above the main sequence. We start from a common set of parameters (based on estimates from literature, see ref. [14]) and vary one parameter at a time, while we keep the others fixed. As we vary the parameter of interest, we compare the color at the interpolated magnitudes for each isochrone.

We show the corresponding comparison as function of age, metallicity, and [α/Fe] in figure 8. The figure clearly shows that most of the sensitivity to age is around the MSTOP, but if only this point is used, age is degenerate with metallicity. However, both the red giant branch and the lower main sequence are sensitive to metallicity, significantly more than to age. This explains why using more features of the color-magnitude diagram breaks the degeneracy. Further, the whole color-magnitude diagram has a different sensitivity to [α/Fe] than to [Fe/H]. Thus, with enough signal-to-noise, both quantities can be constrained in a joint analysis.

JCAP12(2020)002

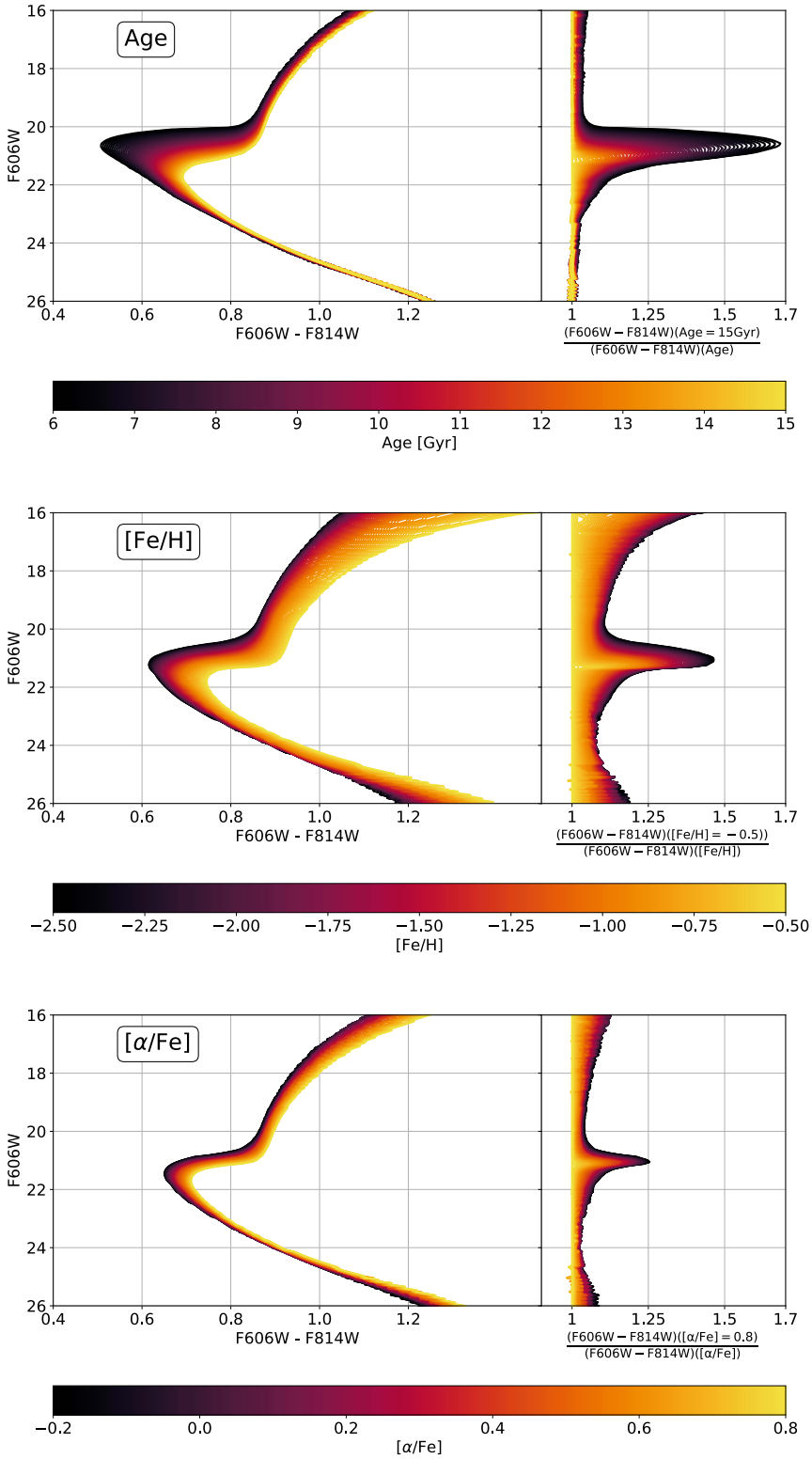

Figure 8. Dependence of the stellar isochrone on variations of age, metallicity and [α/Fe] of the GC with all other parameters fixed. Right panels show the relative difference in color.

JCAP12(2020)002

B Globular clusters properties after the cuts

Cluster name	Total number of stars	Stars with magnitude $< m_{cut}$	percentage of remaining stars
arp2	23010	10611	46
ic4499	61931	33938	54
lynga7	44927	27496	61
ngc0104	140016	113700	81
ngc0288	26814	14465	53
ngc0362	111393	71978	64
ngc1261	97780	61767	63
ngc1851	130655	82732	63
ngc2298	20288	13453	66
ngc2808	277727	214443	77
ngc3201	31908	17056	53
ngc4147	19717	13977	70
ngc4590	60058	33182	55
ngc4833	60889	41720	68
ngc5024	222899	132605	59
ngc5053	23957	11104	46
ngc5139	300622	206535	68
ngc5272	161342	106494	66
ngc5286	190379	131490	69
ngc5466	29776	13660	45
ngc5904	108602	73235	67
ngc5927	96349	69333	71
ngc5986	148963	100314	67
ngc6093	125128	88784	70
ngc6101	67032	33715	50
ngc6121	11975	7070	59
ngc6144	22485	15612	69
ngc6205	138295	97673	70
ngc6218	29767	20840	70
ngc6254	54662	38462	70
ngc6304	100830	58706	58
ngc6341	129969	83376	64
ngc6352	25779	14784	57
ngc6362	30541	17724	58
ngc6366	10567	4427	41
ngc6388	310630	257049	82
ngc6397	14277	9404	65
ngc6426	57321	30576	53
ngc6441	340872	299187	87
ngc6496	22938	14486	63
ngc6535	9590	3640	37
ngc6541	111010	71816	64
ngc6584	62694	35346	56
ngc6624	62637	40960	65
ngc6637	61801	44484	71
ngc6652	29936	16586	55
ngc6656	92090	57379	62
ngc6681	48442	32417	66
ngc6715	345989	270157	78
ngc6717	15209	8235	54
ngc6723	60289	42353	70
ngc6752	47657	31250	65
ngc6779	79381	47224	59
ngc6809	42870	24095	56
ngc6838	14504	7582	52
ngc6934	81104	47218	58
ngc6981	44154	29154	66
ngc7006	72056	46216	64
ngc7078	243929	152629	62
ngc7089	227533	159739	70
ngc7099	67053	37756	56
palomar1	9330	685	7
palomar12	7915	1981	25
palomar15	22790	6648	29
pyxis	11311	6281	55
ruprecht106	23800	13285	55
terzan7	21637	7752	35
terzan8	39847	16477	41

Table 2. Impact of the magnitude cut on the number of stars; all numbers are given after the photometry cleaning

JCAP12(2020)002

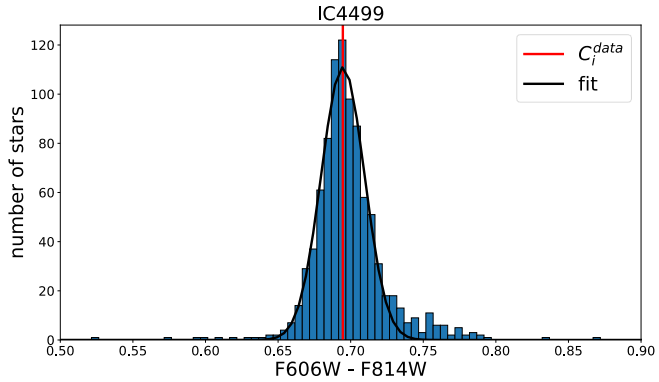

Figure 9. Distribution of color inside a typical MS magnitude bin (at the dim end of the MS) showing secondary population contamination. The black solid line shows how the algorithm isolates and fits the distribution of the main population.

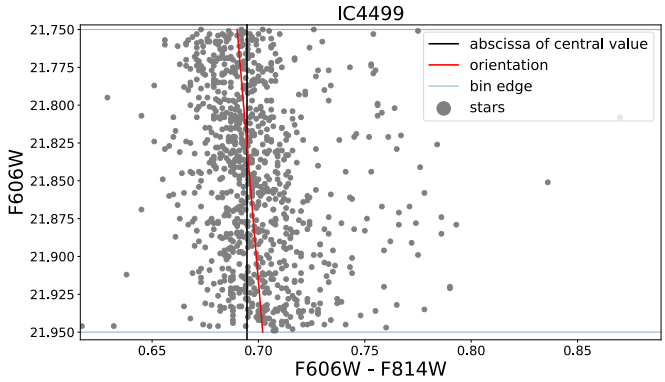

Figure 10. Orientation of the data compared to the vertical axis inside a typical MS magnitude bin (far away from the dim end cut).

C Main sequence calibration

We fit the histogram of the color distribution within each magnitude bin with a unimodal Gaussian with the `curve_fit` routine of `Scipy`, for a `maxfev`=950000.[12] If the routine cannot find a fit to the color distribution, the bin is ignored. Otherwise, the bin is retained and the resulting Gaussian distribution is adopted. A typical example of a small contamination is shown in figure 9: the fitting procedure captures the distribution of the main "population".

Once the central value of the distribution is obtained (see figure 9), we rescale the error on the distribution due to the inclination of the observed stars in the color-magnitude diagram. The orientation of the data in a MS magnitude bin i is obtained by linear regression the median of the data in sub-bins, and is compared to a vertical line passing through the color of the central value (see figure 10). The resulting angle is referred to as ϕ_i and it ranges between [$\simeq$ 0–10°].

[12] `maxfev` is set to a very large value to make sure of the non convergence of the unimodal fit.

D Mixing length theory

Uncertainties in the modeling of convection in the envelopes of low mass stars are the main contributor to systematic uncertainties in determining stellar parameters (see table 2 in ref. [4]). Given the broad audience which this paper (hopefully) reaches, it is worth to briefly review mixing length theory (MLT), to understand the origin of these uncertainties.

The envelopes (about the outer 30% radius) of low mass (< 2 M$_\odot$) stars are fully convective and turbulent, with Reynolds number $\approx 10^{10}$. Modeling these systems is highly challenging: in principle, a full hydro-dynamical solution should be obtained. Instead, the standard solution is to model the gradient of convective transport by the so-called MLT. Conceptually, it is a very simple approach: it assumes that a blob of gas starts at a point and continues moving until it dissolves after a certain length, the mixing length l_m.

Consider a sphere of radius r and an element e of the envelope (a blob of gas) located there. After e has traveled a mixing length l_m, its increase in temperature T will be

$$\frac{\Delta T}{T} = \frac{1}{T}\frac{\partial(\Delta T)}{\partial r} l_m = (\nabla - \nabla_e) l_m \frac{1}{H_P} \tag{D.1}$$

where the scale height is $H_P = -dr/d\ln P$, P is the pressure, ∇ denotes the gradient in the environment and ∇_e is the gradient in the blob. Now, combining this with the equations of stellar structure, it is possible to obtain a system of five differential equations for five independent variables, namely: pressure, temperature, density, and the advective and radiative gradients. Then l_m is an extra free parameter which needs to be determined from observations. The usual parameter that stellar modelers fit is $\alpha_{\rm MLT} = l_m/H_P$; this has a typical value of 1.6 from fits to the Sun and to the position of red giant branch in the color-magnitude diagram of GCs [10]. The interested reader can consult the textbook by Kippenhahn & Weigert for a detailed account of all equations of stellar structure [45]. Changes for this parameter from the typical value would propagate into systematic shifts in the metallicity and age determinations.

JCAP12(2020)002

E Parameter constraints: globular clusters

The table shows the best-fit parameters for the GC sample considered in this paper and the one-dimensional marginalized statistical uncertainties at 68% confidence level.

Cluster name	Age [Gyr]	[Fe/H]	Distance [kpc]	A_V	[α/Fe]
arp2	$13.42^{+1.24}_{-1.65}$	$-1.81^{+0.15}_{-0.18}$	$29.61^{+1.46}_{-1.46}$	$0.29^{+0.04}_{-0.04}$	$0.14^{+0.18}_{-0.16}$
ic4499	$12.80^{+0.66}_{-0.78}$	$-1.54^{+0.09}_{-0.14}$	$19.68^{+0.45}_{-0.45}$	$0.64^{+0.03}_{-0.03}$	$-0.09^{+0.17}_{-0.10}$
lynga7	$10.82^{+2.12}_{-1.54}$	$-0.88^{+0.15}_{-0.12}$	$9.23^{+0.58}_{-0.58}$	$2.22^{+0.05}_{-0.05}$	$0.03^{+0.18}_{-0.12}$
ngc0104	$13.54^{+1.03}_{-0.80}$	$-0.81^{+0.10}_{-0.14}$	$4.48^{+0.08}_{-0.11}$	$0.06^{+0.03}_{-0.03}$	$0.20^{+0.12}_{-0.16}$
ngc0288	$11.20^{+0.67}_{-0.67}$	$-1.43^{+0.18}_{-0.11}$	$9.77^{+0.20}_{-0.20}$	$0.05^{+0.04}_{-0.03}$	$0.36^{+0.16}_{-0.18}$
ngc0362	$11.52^{+0.84}_{-0.84}$	$-1.30^{+0.14}_{-0.12}$	$9.12^{+0.21}_{-0.21}$	$0.06^{+0.03}_{-0.03}$	$0.12^{+0.16}_{-0.14}$
ngc1261	$11.54^{+0.67}_{-0.45}$	$-1.32^{+0.12}_{-0.12}$	$16.72^{+0.38}_{-0.25}$	$0.00^{+0.03}_{0.00}$	$0.12^{+0.16}_{-0.14}$
ngc1851	$12.27^{+1.47}_{-0.98}$	$-1.14^{+0.13}_{-0.13}$	$12.19^{+0.32}_{-0.32}$	$0.07^{+0.03}_{-0.04}$	$0.05^{+0.14}_{-0.14}$
ngc2298	$13.89^{+0.88}_{-0.63}$	$-2.00^{+0.14}_{-0.16}$	$10.23^{+0.22}_{-0.22}$	$0.65^{+0.03}_{-0.03}$	$0.18^{+0.12}_{-0.20}$
ngc2808	$10.93^{+1.20}_{-1.03}$	$-1.32^{+0.14}_{-0.12}$	$10.84^{+0.38}_{-0.38}$	$0.60^{+0.04}_{-0.04}$	$-0.06^{+0.09}_{-0.13}$
ngc3201	$13.05^{+1.05}_{-1.19}$	$-1.57^{+0.12}_{-0.15}$	$4.91^{+0.15}_{-0.08}$	$0.74^{+0.04}_{-0.03}$	$0.20^{+0.16}_{-0.14}$
ngc4147	$13.02^{+0.50}_{-0.33}$	$-1.77^{+0.14}_{-0.12}$	$19.58^{+0.34}_{-0.34}$	$0.04^{+0.02}_{-0.02}$	$0.22^{+0.18}_{-0.16}$
ngc4590	$12.03^{+0.54}_{-0.54}$	$-2.28^{+0.17}_{-0.11}$	$11.22^{+0.17}_{-0.25}$	$0.18^{+0.02}_{-0.02}$	$0.26^{+0.16}_{-0.22}$
ngc4833	$14.69^{+0.23}_{-0.70}$	$-2.09^{+0.15}_{-0.15}$	$6.91^{+0.18}_{-0.12}$	$0.97^{+0.02}_{-0.03}$	$0.20^{+0.18}_{-0.14}$
ngc5024	$13.31^{+0.66}_{-0.57}$	$-1.95^{+0.11}_{-0.17}$	$18.99^{+0.55}_{-0.37}$	$0.03^{+0.01}_{-0.02}$	$0.34^{+0.14}_{-0.18}$
ngc5053	$13.84^{+0.50}_{-0.58}$	$-2.33^{+0.14}_{-0.12}$	$17.82^{+0.29}_{-0.29}$	$0.02^{+0.01}_{-0.01}$	$0.16^{+0.16}_{-0.18}$
ngc5139	$14.91^{+0.00}_{-1.11}$	$-1.63^{+0.11}_{-0.14}$	$5.78^{+0.16}_{-0.16}$	$0.36^{+0.03}_{-0.02}$	$-0.00^{+0.11}_{-0.13}$
ngc5272	$12.60^{+0.66}_{-0.66}$	$-1.53^{+0.11}_{-0.13}$	$10.41^{+0.18}_{-0.28}$	$0.00^{+0.02}_{0.00}$	$0.26^{+0.12}_{-0.22}$
ngc5286	$14.55^{+0.36}_{-1.07}$	$-1.71^{+0.15}_{-0.15}$	$11.62^{+0.40}_{-0.27}$	$0.73^{+0.03}_{-0.03}$	$-0.01^{+0.14}_{-0.14}$
ngc5466	$12.31^{+0.60}_{-0.40}$	$-1.85^{+0.14}_{-0.12}$	$16.47^{+0.39}_{-0.17}$	$0.00^{+0.02}_{-0.00}$	$0.30^{+0.18}_{-0.18}$
ngc5904	$12.75^{+0.80}_{-0.80}$	$-1.30^{+0.10}_{-0.16}$	$7.53^{+0.11}_{-0.17}$	$0.07^{+0.02}_{-0.03}$	$0.12^{+0.14}_{-0.16}$
ngc5927	$8.33^{+1.98}_{-1.13}$	$-0.62^{+0.13}_{-0.13}$	$8.87^{+0.20}_{-0.39}$	$1.35^{+0.03}_{-0.07}$	$0.16^{+0.12}_{-0.14}$
ngc5986	$14.82^{+0.00}_{-1.12}$	$-1.66^{+0.13}_{-0.16}$	$10.95^{+0.40}_{0.00}$	$0.82^{+0.03}_{-0.03}$	$0.19^{+0.06}_{-0.22}$
ngc6093	$13.83^{+0.96}_{-0.72}$	$-1.79^{+0.16}_{-0.13}$	$10.97^{+0.26}_{-0.26}$	$0.61^{+0.03}_{-0.03}$	$0.20^{+0.14}_{-0.18}$
ngc6101	$13.22^{+0.66}_{-0.66}$	$-1.84^{+0.15}_{-0.12}$	$14.81^{+0.37}_{-0.25}$	$0.30^{+0.03}_{-0.03}$	$0.30^{+0.16}_{-0.16}$
ngc6121	$13.01^{+1.01}_{-1.01}$	$-1.22^{+0.16}_{-0.09}$	$2.05^{+0.03}_{-0.05}$	$1.15^{+0.02}_{-0.02}$	$0.44^{+0.12}_{-0.10}$
ngc6144	$14.47^{+0.42}_{-1.12}$	$-1.76^{+0.15}_{-0.17}$	$8.72^{+0.23}_{-0.23}$	$1.27^{+0.03}_{-0.03}$	$0.22^{+0.16}_{-0.18}$
ngc6205	$13.49^{+0.62}_{-0.45}$	$-1.48^{+0.08}_{-0.16}$	$7.79^{+0.09}_{-0.12}$	$0.00^{+0.02}_{0.00}$	$0.08^{+0.27}_{-0.08}$
ngc6218	$14.64^{+0.29}_{-0.64}$	$-1.51^{+0.13}_{-0.11}$	$5.27^{+0.12}_{-0.04}$	$0.56^{+0.03}_{-0.03}$	$0.28^{+0.10}_{-0.22}$
ngc6254	$12.85^{+0.80}_{-0.80}$	$-1.75^{+0.13}_{-0.13}$	$5.71^{+0.14}_{-0.12}$	$0.78^{+0.04}_{-0.03}$	$0.09^{+0.10}_{-0.22}$
ngc6304	$8.67^{+1.80}_{-1.80}$	$-0.64^{+0.14}_{-0.12}$	$7.20^{+0.35}_{-0.35}$	$1.56^{+0.05}_{-0.05}$	$0.09^{+0.14}_{-0.14}$

Table 3.

JCAP12(2020)002

Cluster name	Age [Gyr]	[Fe/H]	Distance [kpc]	A_V	[α/Fe]
ngc6341	$13.30^{+0.60}_{-0.60}$	$-2.24^{+0.15}_{-0.13}$	$8.94^{+0.20}_{-0.17}$	$0.05^{+0.03}_{-0.03}$	$0.26^{+0.16}_{-0.18}$
ngc6352	$11.93^{+1.80}_{-1.57}$	$-0.82^{+0.20}_{-0.09}$	$5.64^{+0.23}_{-0.18}$	$0.72^{+0.04}_{-0.04}$	$0.26^{+0.18}_{-0.12}$
ngc6362	$13.58^{+0.82}_{-0.61}$	$-1.11^{+0.14}_{-0.11}$	$7.69^{+0.18}_{-0.08}$	$0.16^{+0.02}_{-0.02}$	$0.34^{+0.14}_{-0.08}$
ngc6366	$12.15^{+1.46}_{-1.46}$	$-0.88^{+0.15}_{-0.12}$	$3.68^{+0.11}_{-0.11}$	$2.13^{+0.05}_{-0.03}$	$0.03^{+0.16}_{-0.14}$
ngc6388	$11.07^{+2.12}_{-1.42}$	$-0.79^{+0.16}_{-0.11}$	$12.65^{+0.49}_{-0.61}$	$1.09^{+0.04}_{-0.04}$	$-0.09^{+0.11}_{-0.10}$
ngc6397	$14.21^{+0.69}_{-0.69}$	$-2.06^{+0.14}_{-0.19}$	$2.65^{+0.05}_{-0.05}$	$0.51^{+0.03}_{-0.02}$	$0.18^{+0.18}_{-0.16}$
ngc6426	$13.92^{+0.96}_{-1.12}$	$-2.16^{+0.18}_{-0.18}$	$21.99^{+0.85}_{-1.02}$	$1.12^{+0.04}_{-0.04}$	$-0.05^{+0.20}_{-0.12}$
ngc6441	$10.44^{+2.78}_{-1.62}$	$-0.65^{+0.12}_{-0.12}$	$14.38^{+1.15}_{-0.92}$	$1.42^{+0.06}_{-0.05}$	$-0.11^{+0.12}_{-0.09}$
ngc6496	$10.86^{+2.11}_{-1.64}$	$-0.57^{+0.08}_{-0.14}$	$9.88^{+0.44}_{-0.29}$	$0.68^{+0.05}_{-0.04}$	$0.12^{+0.12}_{-0.12}$
ngc6535	$13.81^{+1.06}_{-1.06}$	$-1.82^{+0.18}_{-0.18}$	$6.71^{+0.38}_{-0.31}$	$1.22^{+0.02}_{-0.03}$	$0.20^{+0.14}_{-0.20}$
ngc6541	$13.51^{+0.86}_{-0.65}$	$-1.98^{+0.16}_{-0.12}$	$7.97^{+0.18}_{-0.18}$	$0.35^{+0.04}_{-0.03}$	$0.30^{+0.18}_{-0.16}$
ngc6584	$12.72^{+0.76}_{-0.66}$	$-1.56^{+0.12}_{-0.14}$	$14.18^{+0.24}_{-0.37}$	$0.25^{+0.03}_{-0.03}$	$0.18^{+0.14}_{-0.18}$
ngc6624	$11.26^{+1.90}_{-1.27}$	$-0.61^{+0.10}_{-0.12}$	$8.53^{+0.33}_{-0.41}$	$0.80^{+0.05}_{-0.03}$	$-0.10^{+0.11}_{-0.09}$
ngc6637	$12.85^{+1.35}_{-1.35}$	$-0.84^{+0.15}_{-0.10}$	$9.09^{+0.29}_{-0.29}$	$0.50^{+0.04}_{-0.04}$	$0.08^{+0.14}_{-0.16}$
ngc6652	$12.98^{+1.55}_{-0.86}$	$-0.86^{+0.12}_{-0.14}$	$9.57^{+0.39}_{-0.39}$	$0.35^{+0.03}_{-0.03}$	$0.18^{+0.14}_{-0.20}$
ngc6656	$14.54^{+0.36}_{-0.97}$	$-1.70^{+0.15}_{-0.15}$	$3.62^{+0.09}_{-0.09}$	$1.04^{+0.03}_{-0.03}$	$0.03^{+0.12}_{-0.16}$
ngc6681	$13.87^{+0.73}_{-0.83}$	$-1.68^{+0.14}_{-0.14}$	$9.66^{+0.22}_{-0.27}$	$0.29^{+0.03}_{-0.03}$	$0.16^{+0.16}_{-0.16}$
ngc6715	$12.22^{+1.91}_{-1.43}$	$-1.54^{+0.13}_{-0.19}$	$28.25^{+1.58}_{-1.58}$	$0.44^{+0.04}_{-0.04}$	$-0.04^{+0.14}_{-0.14}$
ngc6717	$11.65^{+1.50}_{-1.71}$	$-1.29^{+0.15}_{-0.15}$	$7.91^{+0.60}_{-0.34}$	$0.66^{+0.05}_{-0.05}$	$0.20^{+0.12}_{-0.20}$
ngc6723	$13.81^{+0.70}_{-0.90}$	$-1.06^{+0.07}_{-0.15}$	$8.14^{+0.16}_{-0.16}$	$0.20^{+0.03}_{-0.03}$	$0.24^{+0.09}_{-0.13}$
ngc6752	$13.48^{+0.81}_{-0.54}$	$-1.57^{+0.14}_{-0.14}$	$4.34^{+0.09}_{-0.06}$	$0.13^{+0.03}_{-0.03}$	$0.26^{+0.14}_{-0.18}$
ngc6779	$14.85^{+0.08}_{-0.76}$	$-2.13^{+0.14}_{-0.16}$	$10.92^{+0.27}_{-0.18}$	$0.69^{+0.02}_{-0.02}$	$0.09^{+0.14}_{-0.16}$
ngc6809	$13.93^{+0.50}_{-0.58}$	$-1.80^{+0.11}_{-0.11}$	$5.49^{+0.09}_{-0.07}$	$0.28^{+0.02}_{-0.02}$	$0.30^{+0.14}_{-0.14}$
ngc6838	$11.21^{+1.59}_{-1.59}$	$-0.91^{+0.15}_{-0.13}$	$4.16^{+0.21}_{-0.14}$	$0.72^{+0.05}_{-0.04}$	$0.16^{+0.14}_{-0.18}$
ngc6934	$13.24^{+0.71}_{-0.71}$	$-1.54^{+0.08}_{-0.14}$	$15.99^{+0.39}_{-0.29}$	$0.28^{+0.02}_{-0.03}$	$0.21^{+0.12}_{-0.18}$
ngc6981	$12.72^{+0.69}_{-0.69}$	$-1.47^{+0.12}_{-0.14}$	$17.08^{+0.49}_{-0.32}$	$0.12^{+0.02}_{-0.02}$	$0.22^{+0.14}_{-0.20}$
ngc7006	$13.18^{+1.14}_{-1.00}$	$-1.51^{+0.12}_{-0.18}$	$39.78^{+2.11}_{-1.41}$	$0.24^{+0.03}_{-0.03}$	$0.03^{+0.10}_{-0.20}$
ngc7078	$13.28^{+0.82}_{-0.71}$	$-2.36^{+0.08}_{-0.13}$	$11.25^{+0.22}_{-0.33}$	$0.25^{+0.02}_{-0.03}$	$0.18^{+0.14}_{-0.20}$
ngc7089	$13.08^{+0.85}_{-0.85}$	$-1.65^{+0.14}_{-0.14}$	$12.05^{+0.35}_{-0.29}$	$0.14^{+0.03}_{-0.03}$	$0.18^{+0.16}_{-0.16}$
ngc7099	$12.82^{+0.33}_{-0.50}$	$-2.22^{+0.12}_{-0.14}$	$8.96^{+0.16}_{-0.13}$	$0.14^{+0.02}_{-0.03}$	$0.34^{+0.14}_{-0.20}$
palomar1	$8.20^{+3.87}_{-1.93}$	$-0.69^{+0.17}_{-0.17}$	$11.44^{+0.78}_{-0.78}$	$0.47^{+0.05}_{-0.05}$	$-0.05^{+0.16}_{-0.12}$
palomar12	$9.94^{+0.92}_{-0.73}$	$-0.86^{+0.13}_{-0.13}$	$18.62^{+0.63}_{-0.42}$	$0.08^{+0.03}_{-0.04}$	$-0.01^{+0.14}_{-0.14}$
palomar15	$13.97^{+0.88}_{-1.76}$	$-2.06^{+0.19}_{-0.19}$	$49.35^{+4.04}_{-4.04}$	$1.21^{+0.03}_{-0.04}$	$-0.01^{+0.14}_{-0.16}$
pyxis	$14.84^{+0.00}_{-3.28}$	$-1.13^{+0.22}_{-0.15}$	$38.29^{+2.77}_{-3.46}$	$0.70^{+0.05}_{-0.04}$	$0.12^{+0.14}_{-0.20}$
ruprecht106	$11.30^{+1.55}_{-1.55}$	$-1.62^{+0.13}_{-0.13}$	$21.95^{+0.73}_{-0.73}$	$0.56^{+0.03}_{-0.03}$	$0.07^{+0.14}_{-0.16}$
terzan7	$8.10^{+1.96}_{-1.40}$	$-0.53^{+0.05}_{-0.14}$	$23.65^{+1.42}_{-1.13}$	$0.21^{+0.05}_{-0.05}$	$-0.08^{+0.09}_{-0.11}$
terzan8	$13.48^{+0.90}_{-0.77}$	$-2.22^{+0.16}_{-0.12}$	$28.74^{+0.99}_{-0.79}$	$0.35^{+0.03}_{-0.03}$	$0.34^{+0.18}_{-0.16}$

Table 4.

JCAP12(2020)002

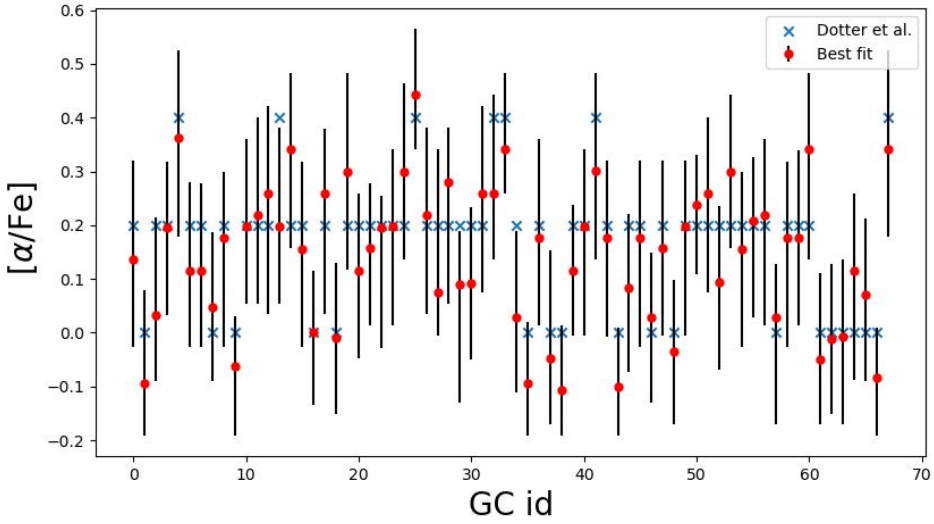

Figure 11. Comparison of [α/Fe] best fits and 1-σ errors with spectroscopic measurements from Dotter et al. [14].

F Fits to ACS globular clusters

In this appendix we show fits for typical Globular clusters in the ACS sample as an illustration of the adopted methodology. For each GC the upper row of figure 12 shows the color-magnitude diagram for the globular cluster. The gray points correspond to the individual stars, the red points show the best fit isochrone for the `DSED` model. The bottom row shows the marginalized posteriors of the model parameters obtained applying our analysis. The contours indicate the two-dimensional 68%, 95% and 99.7% confidence levels constraints, while the panels in the diagonal show the one-dimensional marginalized posteriors.

We also show the comparison between the best fit of the 68 Globular clusters and spectroscopic values from Dotter et al. catalog [14]. We find a very good agreement. For alsmost all the clusters, the spectroscopic value is within the 1-σ range of the best fit.

G Fitting formula for the distribution of Δ_t

The distribution of Δ_t shown in the right panel of figure 1 of ref. [33] can be well approximated by the following fitting formula (see figure 13). Let x indicate Δ_t, $l = \log_{10}(\Delta_t)$ and $l_1 \equiv \log_{10}(0.1155)$, $l_2 \equiv \log_{10}(0.255)$, $\sigma_1 = 0.15$, $\sigma_1' = 0.17$, $\sigma_2 = 0.155$ then

$$F_1(x) = \exp\left(-\frac{1}{2}\frac{(l-l_1)^2}{\sigma_1^2}\right) \quad \text{if } x \leq 0.1155 \tag{G.1}$$

$$F_1(x) = \exp\left(-\frac{1}{2}\frac{(l-l_1)^2}{\sigma_1'^2}\right) \quad \text{if } x \geq 0.1155 \tag{G.2}$$

$$F_2(x) = \exp\left(-\frac{1}{2}\frac{(l-l_2)^2}{\sigma_2^2}\right) \tag{G.3}$$

$$P_{\Delta_t}(x) \propto 0.95\, F_1(x) + 0.45\, F_2(x) \tag{G.4}$$

JCAP12(2020)002

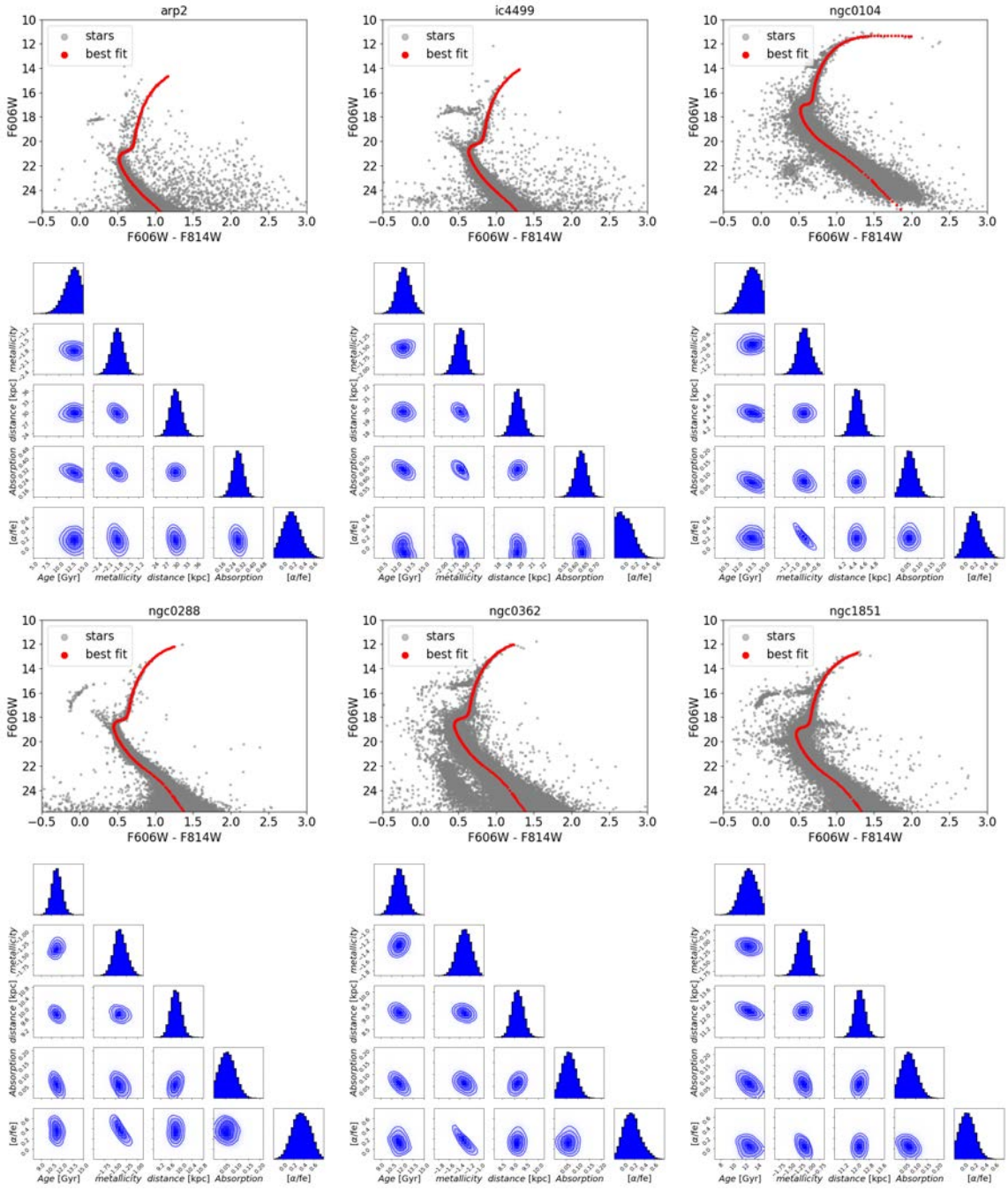

Figure 12. Fit to 6 Globular clusters and the corresponding join Bayesian posterior for the corresponding parameters. The contour levels are confidence, 2D join, intervals for $1, 2$ and $3-\sigma$.

JCAP12(2020)002

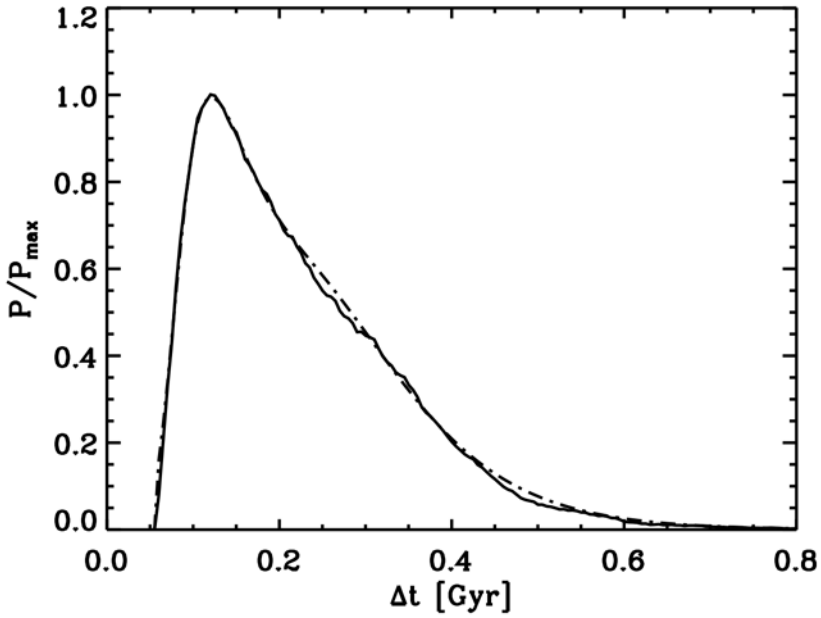

Figure 13. Distribution of the Δ_t taken from the right panel of figure 1 of ref. [33] (solid line) and fitting formula used here (dot-dashed line).

References

[1] M. Catelan, *The ages of (the oldest) stars*, in *Rediscovering Our Galaxy*, C. Chiappini, I. Minchev, E. Starkenburg and M. Valentini, eds., vol. 334 of *IAU Symposium*, pp. 11–20, 2018 [1709.08656].

[2] D.R. Soderblom, *The ages of stars*, *Ann. Rev. Astron. Astrophys.* **48** (2010) 581 [arXiv:1003.6074] [INSPIRE].

[3] D.A. VandenBerg, M. Bolte and P.B. Stetson, *The age of the galactic globular cluster system*, *Ann. Rev. Astron. Astrophys.* **34** (1996) 461 [INSPIRE].

[4] E.M. O'Malley, C. Gilligan and B. Chaboyer, *Absolute ages and distances of 22 GCs using monte carlo main-sequence fitting*, *Astrophys. J.* **838** (2017) 162 [1703.01915].

[5] C.B. Haselgrove and F. Hoyle, *A preliminary determination of the age of type II stars*, *Mon. Not. Roy. Astron. Soc.* **116** (1956) 527.

[6] A.R. Sandage and M. Schwarzschild, *Inhomogeneous stellar models. II. Models with exhausted cores in gravitational contraction*, *Astrophys. J.* **116** (1952) 463.

[7] R. Jimenez and P. Padoan, *A new self-consistency check on the ages of globular clusters*, *Astrophys. J. Lett.* **463** (1996) L17.

[8] P. Padoan and R. Jimenez, *Ages of globular clusters: breaking the age-distance degeneracy with the luminosity function*, *Astrophys. J.* **475** (1997) 580 [astro-ph/9603060] [INSPIRE].

[9] R. Jimenez and P. Padoan, *The ages and distances of globular clusters with the luminosity function method: the case of m5 and m55*, *Astrophys. J.* **498** (1998) 704 [astro-ph/9701141] [INSPIRE].

[10] R. Jimenez, P. Thejll, U. Jorgensen, J. MacDonald and B. Pagel, *Ages of globular clusters: a new approach*, *Mon. Not. Roy. Astron. Soc.* **282** (1996) 926 [astro-ph/9602132] [INSPIRE].

[11] R. Wagner-Kaiser et al., *The ACS survey of Galactic globular clusters - XIV. Bayesian single-population analysis of 69 globular clusters*, *Mon. Not. Roy. Astron. Soc.* **468** (2017) 1038 [1702.08856].

[12] C.L. Sahlholdt, S. Feltzing, L. Lindegren and R.P. Church, *Benchmark ages for the Gaia benchmark stars*, *Mon. Not. Roy. Astron. Soc.* **482** (2019) 895 [1810.02829].

[13] A. Sarajedini et al., *The ACS survey of galactic globular clusters. 1. Overview and clusters without previous HST photometry*, *Astron. J.* **133** (2007) 1658 [astro-ph/0612598] [INSPIRE].

[14] A. Dotter et al., *The ACS survey of galactic globular clusters. IX. Horizontal branch morphology and the second parameter phenomenon*, *Astrophys. J.* **708** (2010) 698 [arXiv:0911.2469] [INSPIRE].

[15] T.D. Morton, *isochrones: stellar model grid package*, Astrophysics Source Code Library (2015).

[16] A. Dotter, *MESA isochrones and stellar tracks (MIST) 0: methods for the construction of stellar isochrones*, *Astrophys. J. Suppl.* **222** (2016) 8 [1601.05144].

[17] J. Choi, A. Dotter, C. Conroy, M. Cantiello, B. Paxton and B.D. Johnson, *Mesa isochrones and stellar tracks (MIST). I. Solar-scaled models*, *Astrophys. J.* **823** (2016) 102 [1604.08592].

[18] A. Dotter, B. Chaboyer, D. Jevremovic, V. Kostov, E. Baron and J.W. Ferguson, *The Dartmouth stellar evolution database*, *Astrophys. J. Suppl.* **178** (2008) 89 [arXiv:0804.4473] [INSPIRE].

[19] E. Simpson et al., *Studies in stellar evolution.IX. Theoretical isochrones for early-type clusters*, *Astrophys. J.* **159** (1970) 895.

[20] G. Bertelli, R. Betto, A. Bressan, C. Chiosi, E. Nasi and A. Vallenari, *Theoretical isochrones with convective overshoot*, *Astron. Astrophys. Suppl. Series* **85** (1990) 845.

JCAP12(2020)002

[21] G. Bertelli, A. Bressan, C. Chiosi, F. Fagotto and E. Nasi, *Theoretical isochrones from models with new radiative opacities*, *Astron. Astrophys. Suppl. Series* **106** (1994) 275.

[22] E.L. Fitzpatrick, *Correcting for the effects of interstellar extinction*, *Publ. Astron. Soc. Pac.* **111** (1999) 63 [astro-ph/9809387] [INSPIRE].

[23] N. Bastian and C. Lardo, *Multiple stellar populations in globular clusters*, *Annu. Rev. Astron. Astrophys.* **56** (2018) 83 [1712.01286].

[24] W.E. Harris, *A catalog of parameters for globular clusters in the milky way*, *Astron. J.* **112** (1996) 1487 [INSPIRE].

[25] C.M. Dutra and E. Bica, *Foreground and background dust in star cluster directions*, *Astron. Astrophys.* **359** (2000) 347 [astro-ph/0005108] [INSPIRE].

[26] B. Hendricks, P.B. Stetson, D.A. VandenBerg and M. Dall'Ora, *A new reddening law for M4*, *Astron. J.* **144** (2012) 25 [arXiv:1204.5719] [INSPIRE].

[27] R.K. Neely, A. Sarajedini and D.H. Martins, *CCD Photometry of the Galactic Globular Cluster NGC 6144*, *Astron. J.* **119** (2000) 1793.

[28] J.-W. Lee, M. López-Morales, K. Hong, Y.-W. Kang, B. L. Pohl and A. Walker, *Toward a better understanding of the distance scale from RR Lyrae variable stars: a case study for the inner halo globular cluster NGC 6723*, *Astrophys. J. Suppl* **210** (2014) 6 [1311.2054].

[29] E. Carretta, A. Bragaglia, R. Gratton, V. D'Orazi and S. Lucatello, *Intrinsic iron spread and a new metallicity scale for globular clusters*, *Astron. Astrophys.* **508** (2009) 695 [arXiv:0910.0675] [INSPIRE].

[30] J.A. Cardelli, G.C. Clayton and J.S. Mathis, *The relationship between infrared, optical, and ultraviolet extinction*, *Astrophys. J.* **345** (1989) 245 [INSPIRE].

[31] A. Kosowsky, M. Milosavljevic and R. Jimenez, *Efficient cosmological parameter estimation from microwave background anisotropies*, *Phys. Rev. D* **66** (2002) 063007 [astro-ph/0206014] [INSPIRE].

[32] R. Jimenez and J. MacDonald, *Stellar evolutionary tracks for low-mass stars*, *Mon. Not. Roy. Astron. Soc.* **283** (1996) 721.

[33] R. Jimenez, A. Cimatti, L. Verde, M. Moresco and B. Wandelt, *The local and distant Universe: stellar ages and H_0*, *JCAP* **03** (2019) 043 [arXiv:1902.07081] [INSPIRE].

[34] T. Hashimoto et al., *The onset of star formation 250 million years after the Big Bang*, *Nature* **557** (2018) 392 [1805.05966].

[35] V. Strait et al., *Stellar properties of $z \gtrsim 8$ galaxies in the reionization lensing cluster survey*, *Astrophys. J.* **888** (2020) 124 [1905.09295].

[36] C. Binggeli et al., *Balmer breaks in simulated galaxies at $z > 6$*, *Mon. Not. Roy. Astron. Soc.* **489** (2019) 3827 [1908.11393].

[37] P. Padoan, R. Jimenez and B. Jones, *On star formation in primordial protoglobular clouds*, *Mon. Not. Roy. Astron. Soc.* **285** (1997) 711 [astro-ph/9604055] [INSPIRE].

[38] M. Trenti, P. Padoan and R. Jimenez, *The relative and absolute ages of old globular clusters in the Lcdm framework*, *Astrophys. J. Lett.* **808** (2015) L35 [arXiv:1502.02670] [INSPIRE].

[39] N. Choksi, O. Gnedin and H. Li, *Formation of globular cluster systems: from dwarf galaxies to giants*, *Mon. Not. Roy. Astron. Soc.* **480** (2018) 2343 [1801.03515].

[40] L. Knox, N. Christensen and C. Skordis, *The age of the universe and the cosmological constant determined from cosmic microwave background anisotropy measurements*, *Astrophys. J. Lett.* **563** (2001) L95 [astro-ph/0109232] [INSPIRE].

JCAP12(2020)002

[41] J.M.D. Kruijssen, *The minimum metallicity of globular clusters and its physical origin — implications for the galaxy mass-metallicity relation and observations of proto-globular clusters at high redshift*, *Mon. Not. Roy. Astron. Soc. Lett.* **486** (2019) L20 [1904.09987].

[42] D.A. Forbes, N. Pastorello, A.J. Romanowsky, C. Usher, J.P. Brodie, J. Strader, *SLUGGS survey: inferring the formation epochs of metal-poor and metal-rich globular clusters*,*Mon. Not. Roy. Astron. Soc. Lett.* **452** (2015) 1045 [1506.06820]

[43] Planck collaboration, *Planck 2018 results. VI. Cosmological parameters*, *Astron. Astrophys.* **641** (2020) A6 [arXiv:1807.06209] [INSPIRE].

[44] L. Knox, N. Christensen and C. Skordis, *The age of the universe and the cosmological constant determined from cosmic microwave background anisotropy measurements*, *Astrophys. J. Lett.* **563** (2001) L95 [astro-ph/0109232] [INSPIRE].

[45] R. Kippenhahn and A. Weigert, *Stellar structure and evolution*, Springer-Verlag Berlin Heidelberg (1990).

JCAP12(2020)002

3.4 The Age of the Universe with Globular Clusters: reducing systematic uncertainties

Compared to Planck's value for the age of the universe (13.8 ± 0.02 Gyr Planck Collaboration et al. 2020), our estimate of $t_{\rm U} = 13.5^{+0.16}_{-0.14}(\text{stat.}) \pm 0.5(\text{sys.})$ at 68% confidence level is in good agreement. In order to make this result more competitive, it is necessary to reduce the various errors which affect the measurement. In particular systematic errors.

Prepared for submission to JCAP

The Age of the Universe with Globular Clusters: reducing systematic uncertainties

David Valcin,[a,b] **Raul Jimenez,**[a,c] **Licia Verde,**[a,c] **José Luis Bernal,**[d] **Benjamin D. Wandelt**[e,f,g]

[a]ICC, University of Barcelona, Martí i Franquès, 1, E08028 Barcelona, Spain
[b]Dept. de Física Quàntica i Astrofísica, University of Barcelona, Martí i Franquès 1, E08028 Barcelona, Spain
[c]ICREA, Pg. Lluis Companys 23, Barcelona, 08010, Spain.
[d]Department of Physics and Astronomy, Johns Hopkins University, 3400 North Charles Street, Baltimore, Maryland 21218, USA
[e]Sorbonne Université, CNRS, UMR 7095, Institut d'Astrophysique de Paris, 98 bis bd Arago, 75014 Paris, France.
[f]Sorbonne Université, Institut Lagrange de Paris (ILP), 98 bis bd Arago, 75014 Paris, France.
[g]Center for Computational Astrophysics, Flatiron Institute, 162 5th Avenue, 10010, New York, NY, USA.
E-mail: d.valcin@icc.ub.edu, jbernal2@jhu.edu, raul.jimenez@icc.ub.edu, liciaverde@icc.ub.edu, bwandelt@iap.fr

Abstract. The dominant systematic uncertainty in the age determination of galactic globular clusters is the depth of the convection envelope of the stars. This parameter is partially degenerate with metallicity which is in turn degenerate with age. However, if the metal content, distance and extinction are known, the position and morphology of the red giant branch in a color-magnitude diagram are mostly sensitive to the value of the depth of the convective envelope. Therefore, using external, precise metallicity determinations this degeneracy and thus the systematic error in age, can be reduced. Alternatively, the morphology of the red giant branch of globular clusters color magnitude diagram can also be used to achieve the same. We demonstrate that globular cluster red giant branches are well fitted by values of the depth of the convection envelope consistent with those obtained for the Sun and this finding is robust to the adopted treatment of the stellar physics. With these findings, the uncertainty in the depth of the convection envelope is no longer the dominant contribution to the systematic error in the age determination of the oldest globular clusters, reducing it from 0.5 to 0.23 or 0.33 Gyr, depending on the methodology adopted: i.e., whether resorting to external data (spectroscopic metallicity determinations) or relying solely on the morphology of the clusters's color-magnitude diagrams. This results in an age of the Universe $t_{\rm U} = 13.5^{+0.16}_{-0.14}({\rm stat.}) \pm 0.23(0.33)({\rm sys.})$ at 68% confidence level, accounting for the formation time of globular clusters and its uncertainty. An uncertainty of 0.27(0.36) Gyr if added in quadrature. This agrees well with 13.8 ± 0.02 Gyr, the cosmological model-dependent value inferred by the Planck mission assuming the ΛCDM model.

Contents

1 Introduction

A Bayesian analysis to estimate, as precisely and accurately as possible, the absolute ages of galactic globular clusters (GCs) with resolved stellar populations was presented in a recent paper [1]. The objective of the work in Ref. [1] was to use the age of the oldest GCs to obtain an estimate of the age of the Universe insensitive to cosmology and, in turn, constrain cosmological models. By using the morphology of the color-magnitude diagram (CMD) and not just the luminosity of the main sequence turn off, we showed that the age, distance and metal content could be determined without relying on external data sets. By using the extensive set of GC CMDs from the ACS-HST survey, an age for the oldest GCs of $t_{\rm GC} = 13.32 \pm 0.1({\rm stat.}) \pm 0.5({\rm sys.})$, at 68% confidence level, was obtained. As it is apparent, the uncertainty in the age is dominated by the systematic uncertainty, which in turn dominates the estimate of the age of the Universe (see also [2–4]).

The most important "known unknown" contributing to the systematic uncertainty budget is the value of the depth of the convection envelope in low mass stars (those around solar mass). This by itself contributes to 60% of the systematic uncertainty (see Table 2 in Ref. [2], the rest of the systematic error budget being due to reaction rates and opacities). The problem is at follows: low mass stars have fully convective and turbulent envelopes (Reynolds number $\simeq 10^{10}$) and because of this, a full hydro-dynamical solution is prohibitive for a large grid of stellar models varying parameters like mass, metallicity and age (this can be done

for a single star, and it is done when modelling the Sun, but cannot -yet- be extended to a full library of stellar models). Instead, one models the gradient of the convective transport by assuming 1D geometry and following a convective cell as it dissolves into the envelope. With this approach, the equations of stellar structure contain five independent differential equations for five variables and an extra parameter: the mixing length ($\alpha_{\rm MLT}$). The value of the mixing length parameter has to be obtained from fits to observations. While there is some recent theoretical progress on matching 3D to 1D models for low mass stars (see e.g., Ref. [13]) which could open the possibility to eliminate the need to empirically calibrate $\alpha_{\rm MLT}$, this step cannot be avoided at the moment.

The standard way to determine the free mixing length parameter is to fit it to the Sun and assume this value applies to all stars. This, of course, is an assumption that is not guaranteed to hold for stars in GCs which have very different metallicity than the Sun.[1] While the adopted value for the mixing length parameter does not affect the age determination directly, it indirectly does so via degeneracies with other parameters, most notably metallicity. The approach of Ref. [1] is to propagate a variation of the mixing length parameter over a wide range into the systematic error budget for the age, as adopted and motivated by e.g., Ref. [2]. However, as anticipated in Refs. [1, 8] this does not need to be the case as the mixing length can, at least in principle, be constrained from the morphology of the CMD of GCs. We address this methodology in this article.

The rationale behind this approach is simple. As a first step, let us assume that the metallicity of the GC has been determined (for example, via spectroscopic observations). For a fixed metallicity, the color of the red giant branch (RGB) in a theoretical CMD depends mostly on the value of $\alpha_{\rm MLT}$ (see Fig. 1). As we will show below, other parameters affecting stellar structure do not modify the color of the RGB as much as $\alpha_{\rm MLT}$. Hence the spread in color of the RGB in the CMD of a single GC yields an upper limit to the star-to-star variations in $\alpha_{\rm MLT}$ (assuming the scatter is solely due to spread in $\alpha_{\rm MLT}$ values). Without resorting to external constraints on the GC metallicity, the metallicity determination for each GC of Ref. [1], obtained assuming a fixed fiducial mixing length parameter value, should be affected by an (unknown) shift induced by the $\alpha_{\rm MLT}$ choice. Now, if the distance is known, GCs of similar estimated metallicity can be suitably aligned on the theoretical CMD (or an HR diagram). In this case, the dispersion in color of the RGB can be used to constrain the $\alpha_{\rm MLT}$ range, in particular if one assumes that the full scatter is solely induced by $\alpha_{\rm MLT}$.

In this paper we quantify this dispersion and constrain the range of $\alpha_{\rm MLT}$ values. This significantly reduces the systematic uncertainty in the age estimation of GCs, making the mixing length contribution to the statistical error budget now subdominant to other systematics, and propagates into a determination of the age of the Universe with systematic errors reduced by $\sim 50\%$.

2 Data

Following Ref. [1], we consider the globular clusters from the HST-ACS catalog which we group into three metallicity samples (according to the best fit metallicity value): 12 clusters with [Fe/H] < 2.0, 11 clusters with $-2 <$ [Fe/H] $<$ -1.75 and 15 with $-1.75 <$ [Fe/H] $<$ -1.5. One of the clusters in Ref. [1], (NGC6715) shows clear signs of multiple populations in the RGB, its metallicity is just at the high edge of the range considered in this work and its age determination has a very large error-bar. We exclude this cluster from the present

[1] See the discussion in section 2.2 in Ref. [2] and references therein.

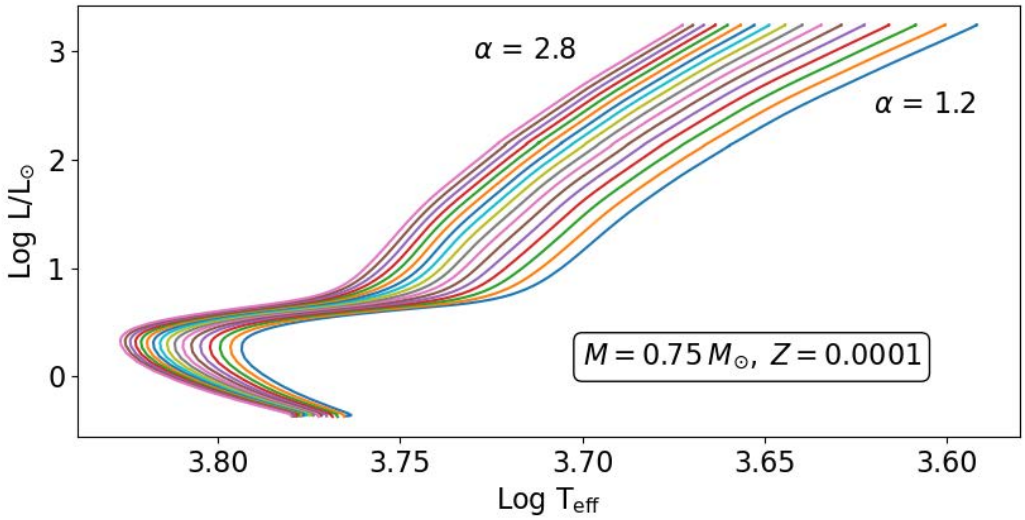

Figure 1. Variation of the HR diagram due to changes in the mixing length parameter $\alpha_{\rm MLT}$ ($\Delta_\alpha = 0.1$) for a star with a fixed initial mass and metallicity. As we can see, the color (effective temperature) of the RGB is the most sensitive region to the mixing length value, while the sub-giant branch is the least sensitive part of the HR diagram.

analysis, leaving us with a sample of 38 clusters (including it does not change the results in any significant way, due to the large uncertainties on its age).

These clusters also have spectroscopically-determined metallicities from Ref. [2] (for only 16 of the 38 clusters) and [14, 15] (for all 38); the latter determination is complete for our purposes, then it is the main one we use here. The comparison between spectroscopic metallicity and the metallicities estimated by Ref. [1] is shown in Fig. 2. The comparison with Ref. [2] metallicities can be found in Fig. 5, of Ref. [1].

In order to compare the clusters with each other and with the stellar tracks, it is necessary to convert the apparent magnitudes of each star into absolute magnitudes. To do this we use the best fits obtained in Ref. [1] (see their Table 3, Appendix E) for the absorption and the distance modulus. In the three panels of Fig. 3, we show the (absolute) CMD of all the clusters, as if they were all at the same distance (i.e., 10 pc), subdividing the sample in the three metallicity ranges listed above. Clearly, the RGBs of the different clusters appear nicely aligned in each metallicity interval. When considering the combined distribution of all the stars from all the GC in each sample, there are many possible contributions to the resulting width of the RGB: photometric errors, errors in the best-fit parameter values (e.g., distance, absorption) used to generate the plots, errors in metallicity determinations and the spread in metallicity within the selected sample, and the effects of variations in $\alpha_{\rm MLT}$ (which is the quantity we are interested in).

3 Method

Several parameters affect the color of the RGB in low-mass stars ($< 2M_\odot$). The most important one is the metallicity content, as can be seen from Fig. 8 in Ref. [1], where one can appreciate that the color of the RGB is quite insensitive to age, but sensitive to

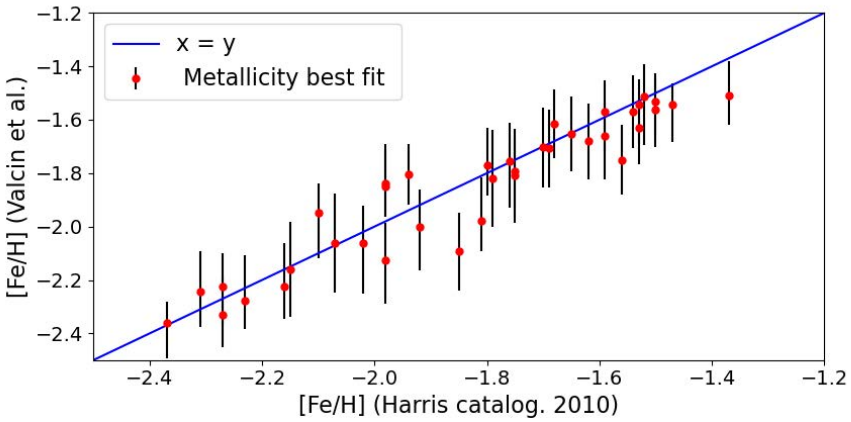

Figure 2. Metallicity determination of Ref. [1] vs spectroscopic metallicity determination of Ref. [15] of the 38 clusters in our sample. The 1:1 line guides the eye. The scatter around this relation is $\sigma_{[\mathrm{Fe/H}]} = 0.09$, with no indication of a dependence on metallicity or systematic bias (i.e., a systematic deviation from the 1:1 line).

metallicity. The next leading parameter determining the color of the RGB is the mixing length (α_{MLT}), as we will show below by varying the parameters of the microphysics in the star and comparing the resulting stellar tracks (see Fig. 1). As recognized by Ref. [2], this parameter dominates the systematic uncertainty when obtaining ages of GCs using the luminosity of the main sequence turn off.

Here we explore two approaches to reduce this uncertainty. The first one is based on external metallicity determinations, the second one uses only internal information from the morphology of the CMDs of each GC.

3.1 Resorting to Spectroscopic metallicity determination

We can appreciate in Fig. 2 that there is a good agreement between spectroscopic and CMD-estimated metallicities, with no indication of a dependence on metallicity and no indication of a systematic bias (i.e., a systematic deviation from the 1:1 line). When a linear fit is performed, the best-fit line has a slope of 0.89 ± 0.15 and an intercept of -0.21 ± 0.28. When forcing the line to have a slope of 1 a possible systematic normalization shift in the metallicity determination is -0.023 ± 0.093. We find similar results when limiting this comparison to each of the subsamples in metallicity. Hence, we quantify the scatter in the relation i.e., a possible difference between spectroscopic and CMD-estimated metallicity to be $\sigma_{[\mathrm{Fe/H}]} = 0.093$.

These results are obtained using the metallicities from Ref. [15]; results obtained using Ref. [2] instead are consistent, but more uncertain because of the smaller number of objects included. Since the metallicity determination of Ref. [1] is obtained for a value of $\alpha_{\mathrm{MLT}} = 1.938$ fixed a priori,[2] and there is an expected degeneracy between α_{MLT} and metallicity, a systematically incorrect choice of α_{MLT} would have biased the metallicity determination,

[2]The value of the α_{MLT} parameter assumed depends on the stellar code used. In Ref. [1], the values reported were according to the convention of the codes used there i.e., `DSED`. Here we convert to the convention of the `MESA` (and `JimMacD`) codes, see below. For reference the solar value for α_{MLT} are 1.938, 2, 1.4, respectively. This change, however, only amounts to a shift; the relevant quantity for our argument is the interval or range adopted, which does not depend on the convention.

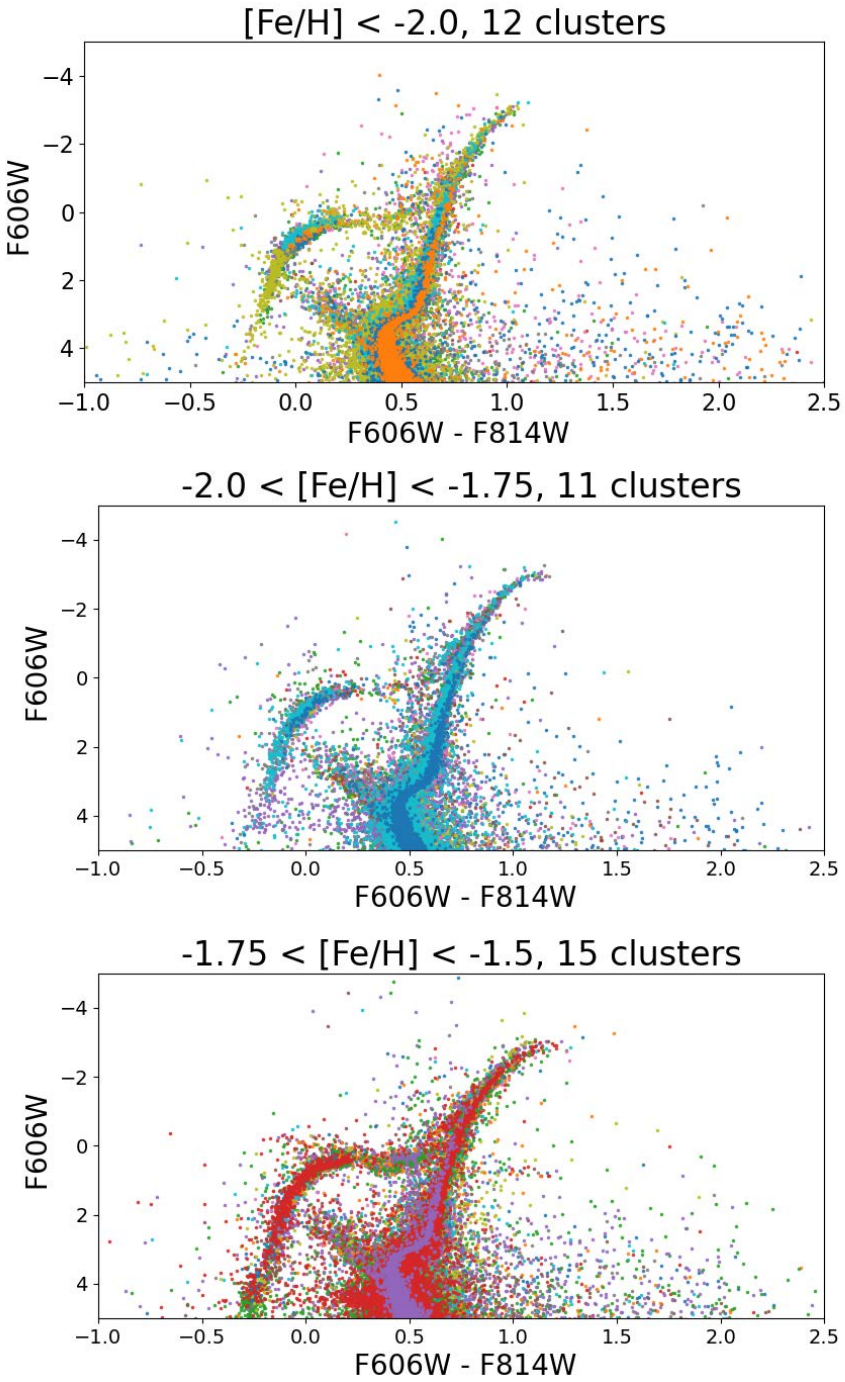

Figure 3. Top panel: Combined CMD of the GCs with metallicities below [Fe/H] < -2, shifted to be at the same distance using the best fit distances and absorption from Ref. [1]. Middle and bottom panels: same as top panel but for metallicity ranges as indicated.

and hence the age. On the other hand, an incorrect value of $\alpha_{\rm MLT}$ with a cluster-to-cluster variation would induce a scatter in the comparison of Fig. 2, which we estimate to be $\sigma_{\rm [Fe/H]} = 0.093$. Below, we will estimate the allowed range of $\alpha_{\rm MLT}$ by attributing the full scatter of

this relation to variations in the mixing length parameter.

3.2 Using only internal information

When using the full morphology of the CMD, it should be possible to treat $\alpha_{\rm MLT}$ as an additional model parameter to be constrained by the data, as mentioned in Ref. [1]. Here we develop this idea. We start by illustrating the sensitivity of the RGB to stellar parameters and in particular to $\alpha_{\rm MLT}$ using the publicly available 1D stellar structure and evolution codes `MESA` [5] and the `JimMacD` code [6]. These codes compute the 1D equations of stellar structures and evolve them in time, thus providing the structure of a star and its position and evolution in time in the theoretical CMD for given initial mass and chemical composition. The numerical solution of the stellar structure equations of both codes are the same. The main difference between the two codes is that `MESA` is a modern 1D stellar code that employs new updates in opacities and nuclear reaction rates. On the other hand, the older version of `JimMacD` that we use adopts different values for opacities and nuclear reaction rates and a different formulation of the mixing length formulation. We use these two different codes to illustrate that recent updates in nuclear reaction rates and opacities do not affect our results. We then proceed to constrain the mixing length parameter from the color of the RGB and quantify its spread for the oldest GCs.

3.2.1 Color transformation

The output of `MESA` allows us to plot directly the evolution of a star in the theoretical HR diagram (effective temperature vs log luminosity), but if we want to compare our tracks with the GCs observations we must transform the luminosity into the magnitudes corresponding to the filters of the HST-ACS catalog (F606W and F814W). The transformation is carried out in 4 stages:

1. convert luminosity to bolometric magnitude using the formula

$$\mathcal{M}_{\rm bol} = -2.5 \log_{10} \frac{\rm L_\star}{\rm L_0}$$

   where $L_\star$ is the star's bolometric luminosity in watts and L_0 is the zero point luminosity $= 3.0128 \times 10^{28}$ W ,

2. produce bolometric correction tables using the Vega calibration (Calspec Alpha Lyrae)[3] and the atmospheric models of Castelli & Kurucz [9] for various metallicity values, or the `Bolometric Corrections` code from Casagrande & VandenBerg [10][4] . This is further discussed in Appendix A, where we show that the choice of bolometric correction is unimportant for our purpose,

3. interpolate bolometric corrections (BC) using effective temperature, surface gravity, and extinction where we assume to have corrected the data for extinction and therefore take E(B - V) = 0 ,

4. transform bolometric magnitude into absolute magnitude

$$\mathcal{M}_{\rm filter} = \mathcal{M}_{\rm bol} - {\rm BC}_{\rm filter}$$

   where $\mathcal{M}_{\rm filter}$ and ${\rm BC}_{\rm filter}$ are respectively the absolute magnitude and the bolometric correction in the desired filter.

[3] https://ssb.stsci.edu/cdbs/current_calspec/

[4] For the rest of the paper we choose to work with bolometric corrections from Ref. [10].

3.2.2 Stellar tracks

The CMD of a GC is an isochrone which covers a range of initial masses for the stars. Isochrones are generally more complicated to model than stellar tracks and are usually available for more limited choices of parameters (such as $\alpha_{\rm MLT}$, opacities, reaction rates, etc.) than stellar tracks. However, it is well known that a stellar track for a fixed mass, corresponding to the mass of the main sequence turn off, will approximate very well the parts of CMD of the GC which we consider here, in particular the upper part of the RGB (where the dependence on the mass is very small). The RGB for an isochrone of a fixed age can always be approximated by a stellar track for a suitable choice of the initial mass. We fix the age for the isochrone to be 13.32 Gyr and find that $M = 0.75\,M_{\odot}$ yields the best fit for our purposes. A variation of the value of the initial mass has an effect on an isochrone very similar to changing the age, and mainly affects the main sequence and its turn off. This is further discussed in Appendix A, especially Fig. 7, but see also Figure 8 in Ref. [1].

The isochrone-track agreement is illustrated in Fig. 4. In both panels, the dotted lines correspond to isochrones, and the solid lines, to stellar tracks for representative values of metallicity and mixing length parameter. For the magnitude range ($\mathcal{M} \gtrsim 0$), and the combination of parameters we are interested in, the differences between isochrones and stellar tracks are very small and completely negligible compared to the differences induced by changes in metallicity and $\alpha_{\rm MLT}$ considered here. In our analysis, we also include a cut for magnitudes $\mathcal{M} \gtrsim -2$; for $\mathcal{M} < 0$ the differences between isochrones and tracks as obtained according to our procedure of sec. 3.2.1, are slightly more pronounced. For this reason, the $\mathcal{M} > -2$ cut is only reported in the appendices and serve to check for possible effects of outliers and to cap the effect of such mismatch.

We begin by computing stellar tracks using the `MESA` software package [5], evolving a star from pre main-sequence to a luminosity limit of $\log_{10}(\mathrm{L_{max}}) = 3.25$, sufficient to compare the tip of the RGB for different values of the mixing length parameter. Among the various parameters needed to configure the tracks, the initial mass and metallicity are the two most important.

We calculate the stellar tracks for 8 initial values of metallicity spanning a range from $Z = 0.00005$ to $Z = 0.0004$ (equivalent to $-2.45 < [\mathrm{Fe/H}] < -1.55$)[5] to sample the [Fe/H] range of the 38 GCs in our sample (see Table 3 in Ref. [1]). Except for its tip, the RGB varies only slightly with changes in the metallicity. This is why we argue that, for a metallicity range comparable to current uncertainties from CMD studies, the scatter around the the RGB may be used to constrain the maximum range of $\alpha_{\rm MLT}$. The impact of the choice of mass, metallicity and the stellar model on the stellar tracks and the CMD is explored in more detail in Appendix A (see Figure 8).

Besides adopting the solar abundance scale, we use the same configuration parameters as those presented in Ref. [7] (see table 1 and section 3 for further explanations). All other parameters have been used with their default values. Table 1 summarizes the value of the relevant parameters used in our study. We also compute stellar tracks with the old stellar code `JimMacD` [6] in order to show the robustness of the position of the RGB to input physics and how a different modelling of stellar structure doesn't affect our conclusions. While the inital mass value adopted using the `MESA` code is $M = 0.75\,M_{\odot}$, this exact value is not available for `JimMacD`. Hence, when comparing the two codes directly, we also consider the closest available value in `JimMacD` which is $M = 0.80\,M_{\odot}$, and use initial metallicity

[5] Recall that $[\mathrm{Fe/H}] = \log_{10}(Z/Z_{\odot})$ where $Z_{\odot} = 0.02$ for `JimMacD` and $Z_{\odot} = 0.0142$ for `MESA` .

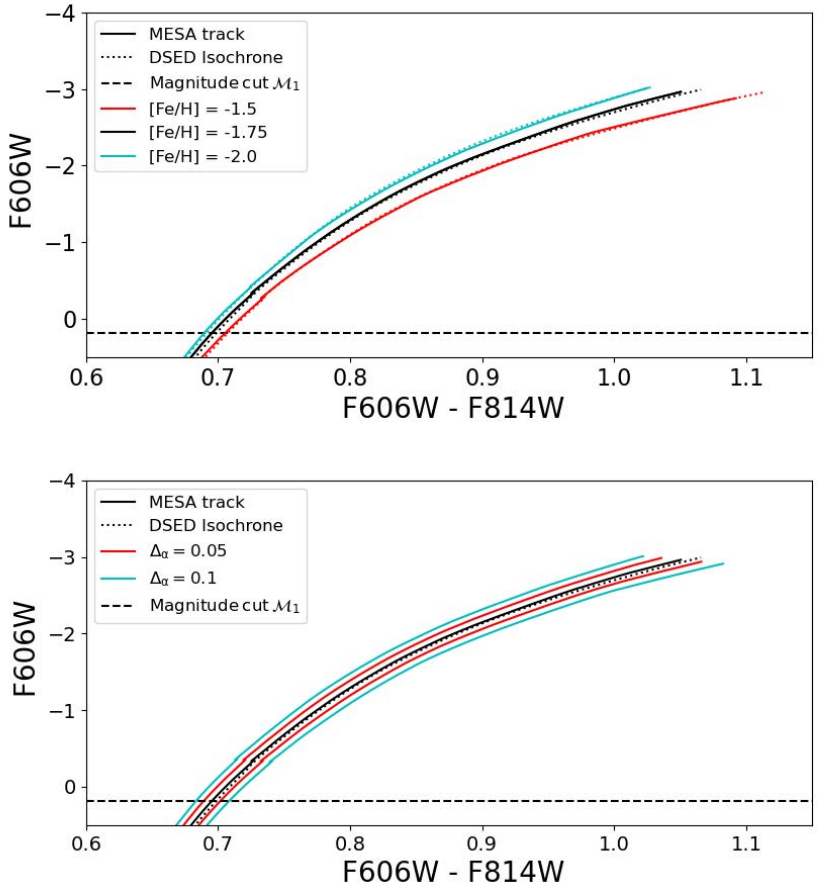

Figure 4. The upper part of the RGB of an isochrone is very well approximated by the stellar track for a suitable choice of mass (and age, but the sensitivity to age is small). For each isochrone the age is equal to 13.32 Gyr and for each track the mass is equal to $0.75 M_\odot$. In this figure the dotted lines correspond to isochrones, the solid lines to stellar tracks. The top panel shows the agreement for few representative values of metallicity; the bottom panel shows that the differences between isochrones and tracks are much smaller than those induced by a change in $\alpha_{\rm MLT}$ of the magnitude of interest.

$Z = 0.0002$ ([Fe/H]$= -2$). As discussed above, the RGB is very insensitive to the choice of mass. The detailed comparison of the two codes is presented in Appendix B where also the corresponding stellar tracks are shown. Since the impact of differences between the two codes in our results is negligible, in what follows the main text only report results for the `MESA` code.

3.3 Response of the color of the RGB to changes in metallicity and $\alpha_{\rm MLT}$

The grid of stellar tracks enables us to estimate how changes in key parameters (metallicity and $\alpha_{\rm MLT}$) affect the color of the RGB. For relatively small changes around fiducial values we can linearize this dependence and report an estimate of $d{\rm C}/d\alpha_{\rm MLT}$ (where C denotes the color of the RGB at a given magnitude) and $d{\rm C}/d{\rm Z}$ or $d{\rm C}/d[{\rm Fe/H}]$, obtained as finite differences for few representative magnitudes. These quantites are only indicative, but can help build physical intuition about the effect we want to describe. We find that these quantities, as expected, depend on the magnitude; results are reported in table 2. The color response to

Parameter	Value
Initial mass M	0.75, 0.80
Initial metallicity Z	[0.00005, 0.004] $\Delta_Z = 0.00005$
Initial Helium mass fraction	0.24 + 2 × Initial metallicity Z (default)
Mixing length $\alpha_{\rm MLT}$	[1.2, 2.8], $\Delta_\alpha = 0.1$
Atmosphere boundary conditions	model atmosphere tables for photosphere constructed using the PHOENIX model atmospheres [21, 22] and the models in Ref. [9].

Table 1. Values for the stellar parameters used when computing the `MESA` stellar tracks.

metallicity (Z) is linear to a very good approximation, the response does not depend on the ΔZ adopted to compute the derivative, but it shows some dependence on the fiducial choice of $\alpha_{\rm MLT}$. We find that we can approximately rescale the derivative to different fiducial values as $(\alpha_{\rm MLT}/\alpha_{\rm fid})^3 dC/dZ|_{\alpha_{\rm fid}} = $ const. if $\alpha_{\rm fid}$ is around the solar value ($\alpha_{\rm MLT\odot} \sim 2$). The relation between Z and [Fe/H] is not linear hence we report $\frac{\Delta C}{\Delta[{\rm Fe/H}]} = Z\frac{\Delta C}{\Delta Z}$ for two represenative metallicities; using the linearized relation for [Fe/H] is valid only for small shifts. The $\alpha_{\rm MLT}$ dependence on the other hand is not linear, so the linearized approximation is only valid for small changes $\Delta_\alpha < 0.1$, which is what we adopt here.

	$\mathcal{M} = 0$	$\mathcal{M} = -2$
$\frac{\Delta C}{\Delta Z}\|_{Z=0.00015}$	115	285
$\frac{\Delta C}{\Delta Z}\|_{Z=0.00025}$	106	297
$\frac{\Delta C}{\Delta[{\rm Fe/H}]}\|_{[{\rm Fe/H}]=-2.0}$	0.017	0.043
$\frac{\Delta C}{\Delta[{\rm Fe/H}]}\|_{[{\rm Fe/H}]=-1.75}$	0.027	0.074
$\frac{\Delta C}{\Delta\alpha_{\rm MLT}}(Z = 1.5\times10^{-4})$	0.116	0.202
$\frac{\Delta C}{\Delta\alpha_{\rm MLT}}(Z = 2.5\times10^{-4})$	0.125	0.225

Table 2. Response of the RGB color to changes in metallicity and mixing length parameter around a fiducial model for the stellar track of $\alpha = 2$. Here $\mathcal{M}$ denotes the magnitude in F606W filter and color, C, denotes the difference F606W-F814W. The response to $\alpha_{\rm MLT}$ show some dependence on the fiducial metallicity so we report several representative values.

We can then proceed to estimate (approximately, given the linearization assumption implicitly made when computing derivatives by finite differences) what change $\Delta\alpha$ is needed to keep the color of the RGB unchanged under a change in metallicity $\Delta_{\rm [Fe/H]}$. This is visualized in Fig. 5 where one can directly appreciate that a change in metallicity of $\pm\Delta_{\rm [Fe/H]} = 0.09$ (which is close to the value of the scatter found in sec. 3.1) is compensated by a change $\pm\Delta_\alpha \lesssim 0.04$. This upper limit in the required shift in $\alpha_{\rm MLT}$ provides a conservative estimate of the uncertainty in this parameter introduced by its degeneracy with [Fe/H]. This is in broad agreement with the values reported in Tab. 2 if one keeps in mind that the results in the table are approximated because evaluated at a fixed magnitude value implicitly assuming linear dependence of the color on the parameters and that in practice the overall effect should be seen as a suitably weighted average shift over the magnitude range $\mathcal{M} > 0$. In section 4

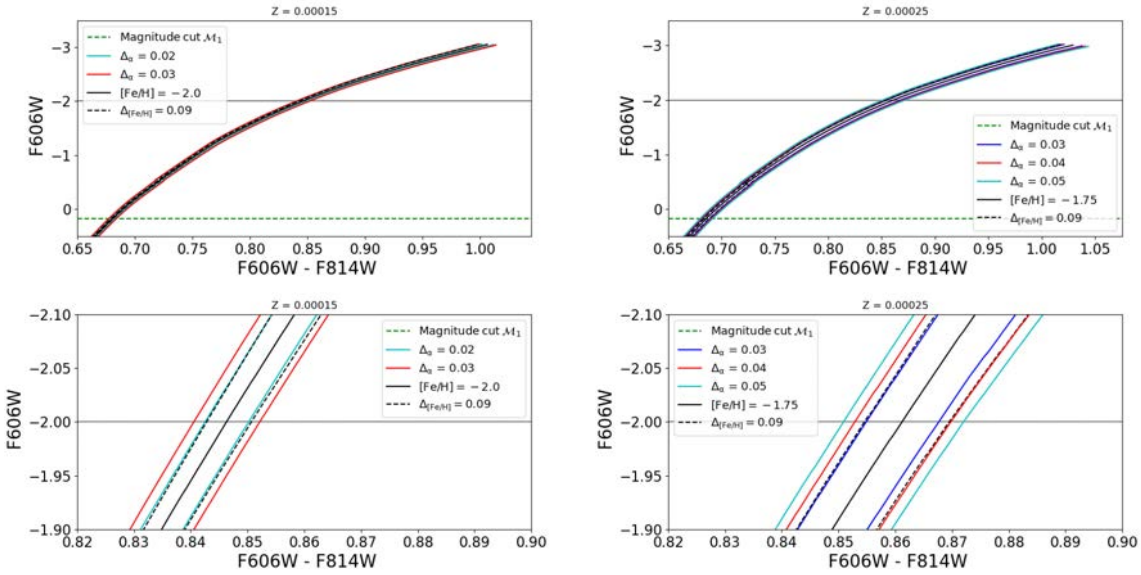

Figure 5. Response of the color of the RGB to a change in metallicity and a change in $\alpha_{\rm MLT}$ for discrete representative values. The top panels show the full RGB range while the bottom panels are a zoom in around magnitude M_1 (solid horizontal line). This illustrates that to keep the color of the RGB unchanged for a small change in metallicity $\Delta_{\rm [Fe/H]} = 0.09$, (very close to the scatter evaluated in sec. 3.1, Fig. 2) around the fiducial ([Fe/H] $= -1.75$ and $\alpha_{\rm MLT} = 2$), the corresponding change in $\alpha_{\rm MLT}$ is given by $\Delta_\alpha/\Delta_{\rm [Fe/H]} \simeq -0.4$. This is the value we adopt, as it corresponds to that of the effective metallicity of our GC sample.

we conservatively adopt $d\alpha_{\rm MLT}/d{\rm [Fe/H]} = -0.4$ when converting the measured metallicity scatter into an estimate fo the scatter in $\alpha_{\rm MLT}$.

3.3.1 Selecting the RGB

In order to select only stars in the RGB for each cluster we define a band of color around the best fit obtained in Ref. [1]. We choose a value of ΔC = 0.06 large enough to include all the stars in the red giant branch and narrow enough to remove most of the stars belonging to the horizontal branch. We also define a magnitude cut, $\mathcal{M}_0$, corresponding to the start of the RGB. The collection of stars selected for all clusters in the low metallicity sample is shown in Figure 6 where the 12 low metallicity GCs are plotted on top of each other. Indeed the best fit $\alpha_{\rm MLT}$ can be biased and the dispersion σ_α can be increased by the dispersion in color induced either by outliers or by misclassified stars belonging to the horizontal or asymptotic branch. As the number of stars decreases when we move towards the brightest magnitudes, we define two additional magnitudes cuts to study the dispersion in $\alpha_{\rm MLT}$. The first one $\mathcal{M}_1 = \mathcal{M}_0 - 2.0$ and the second one $\mathcal{M}_2 = \mathcal{M}_1 - 2.0 = \mathcal{M}_0 - 4.0$. A value of the scatter in the color of the RGB changing across different magnitude cuts would indicate outlier contamination. Because the correspondence isochrone-stellar tracks is less precise for $\mathcal{M} > 0$, we adopt results using the $\mathcal{M}_1$ cut and report the $\mathcal{M}_0$ cut results only in the Appendices.

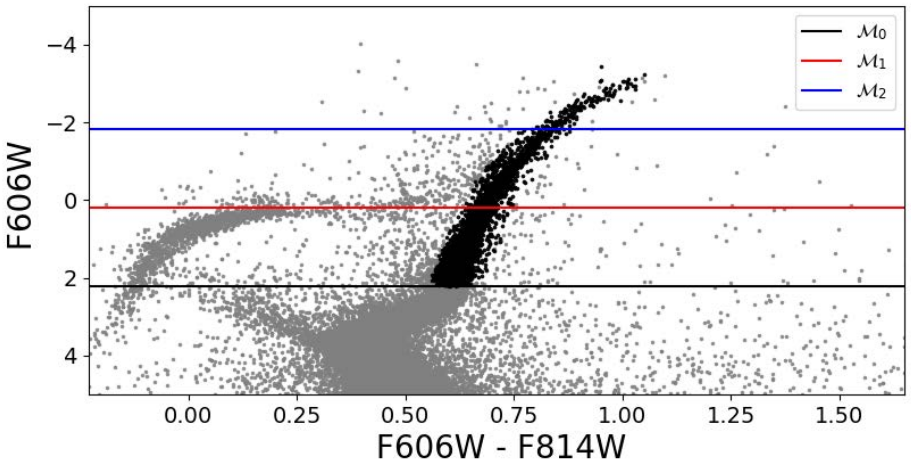

Figure 6. The different cuts in luminosity used to define the spread computed in Table 3 and Table 4. The gray points represents all the stars in the CMD of the combined 12 GCs of the [Fe/H] < 2 sample, the black points show those passing the color selection of the RGB.

3.3.2 Computing RGB dispersion

We compute the RGB dispersion for each individual cluster and the combination of all the GC in each of the three metallicity samples. If we assume that the photometric dispersion is Gaussian around the isochrone (as argued in Ref. [1]), we can define the dispersion of color by measuring the color distance to the fit:

$$\sigma_{\rm color} = \sqrt{\frac{1}{\rm N}\sum_{\rm i=1}^{\rm N}({\rm C}^{\rm i}_{\rm star} - {\rm C}^{\rm i}_{\rm fit})^2} \tag{3.1}$$

where $\rm C^i_{star}$ and $\rm C^i_{fit}$ respectively correspond to the color of a given star (index i) and the color of the track at the same magnitude, and N is the number of stars in the magnitude interval considered. As we compute the dispersion for brighter magnitude cuts ($\mathcal{M}_1$ and $\mathcal{M}_2$), the number of stars N decreases and the distribution becomes sometimes dominated by Poisson noise for individual clusters. Therefore, we set a limit of N = 10 under which the dispersion is not computed. To estimate the scatter in the mixing length the ideal approach would be to perform a Bayesian analysis with the mixing length as a free parameter (akin to the approach of Ref. [1]). However stellar grids are defined only for a specific value of $\alpha_{\rm MLT}$; recomputing full grids of different mixing lengths and would be very computationally expensive and is beyond the scope of this paper. We proceed instead as follows. We start by mapping the response of the RGB track to discrete changes in $\alpha_{\rm MLT}$ (see Appendix B).

A (small) shift in the $\alpha_{\rm MLT}$ value might happen when matching tracks with isochrones. We then perform a least square fit between stellar tracks for different values of the mixing length parameter and the isochrone obtained from the best fit parameters of Ref. [1] for each GC. First we select all the evolutionary equivalent points of the isochrone for the magnitude range considered in this work. Then we interpolate all the computed tracks on the same magnitude interval. Finally we compare the tracks and the isochrone at each EEPs magnitude and do a least square fit for $\alpha_{\rm MLT}$. This yields for each cluster a "best match" $\alpha_{\rm MLT}$ since it

is obtained by comparing two different models (track to isochrone). For the combination of all the clusters within a metallicity sample, since a best fit isochrone is not available we do not compare tracks to the best fit isochrone, instead we perform a fit to all the stars in the CMD for the full sample following the same fitting procedure as in Ref. [1] but using tracks as the theoretical model instead of isochrones and varying only $\alpha_{\rm MLT}$. We refer to this as best fit $\alpha_{\rm MLT}$ since it is obtained via a model to data comparison.

To compute the scatter for each cluster, each star in the RGB is assigned a value of the mixing length parameter, $\alpha^{\rm i}_{\rm MLT}$, obtained by linear interpolation of the values corresponding to the two closest tracks at the same magnitude, and a corresponding shift $S^{\rm i}$ as the difference between the interpolated $\alpha^{\rm i}_{\rm MLT}$ and the corresponding best match $\alpha_{\rm MLT}$.

The dispersion in $\alpha_{\rm MLT}$ is then given by

$$\sigma_\alpha = \sqrt{\frac{1}{\rm N}\sum_{\rm i=1}^{\rm N}({\rm S^i})^2}\,. \tag{3.2}$$

For each sample we take the mean of the scatters of the individual clusters in the sample. The results can be seen in in Table 3, but more detailed results on a cluster by cluster basis are reported in Appendix C, Table 4.

4 Results

The considerations of Sec. 3.1 indicate that the adopted fiducial value for $\alpha_{\rm MLT}$ adopted by Ref. [1] is not biased. The findings of Sec. 3.3 and Fig. 5 yield an estimate for $\Delta_\alpha/\Delta_{\rm [Fe/H]} = -0.4$ (the change in $\alpha_{\rm MLT}$ required to compensate a change in metallicity in order to keep the color of the RBG unchanged) around the fiducial value for $\alpha_{\rm MLT}$ and for the effective value of [Fe/H] and magnitude cut. In Sec. 3.1 the scatter between spectroscopic and CMD-estimated metallicity is estimated to be $\sigma_{\rm [Fe/H]} = 0.093$. If this is attributed solely to cluster to cluster (or star to star) changes in mixing length parameter, we obtain an upper limit of $\sigma_\alpha^{\rm spec.met} = 0.04$ (the superscrip stresses that this is computed resorting to spectroscopic metallicity data).

Without resorting to external data sets, we can proceed empirically. The spread in color (color scatter) of the RGB for each GC, is generated by a combination of effects, the dominant one being measurement and photometric errors, as well as all other stellar parameters variations, which are subdominant. If the color scatter is attributed solely to changes in mixing length parameter it can be used to provide a conservative estimate of star to star variations in $\alpha_{\rm MLT}$. This statement assumes that measurement and photometric errors and variations of stellar parameters are all random and uncorrelated. In principle, if different sources of scatter are suitably (anti) correlated, this would not necessarily be conservative estimate. We deem this possibility very unlikely. Combining GC of similar metallicity, the scatter around the RGB also accounts for possible cluster-to-cluster variations as RGBs of clusters of similar metallicities are mostly affected by $\alpha_{\rm MLT}$. In this case there is an additional contribution to the scatter arising from the fact that to convert the observed CMD to the absolute one we have used the best-fit values of absorption and distance, which may be affected by their own measurement errors.

Results are reported in table 4. First note that the scatter in color ~ 0.02 is much smaller than the initial color cut of $\Delta{\rm C} = 0.06$, which clips only the tails of the color distribution beyond 3σs and thus confirming that the initial cut does not affect the estimate of the

[Fe/H] < -2.0, 12 clusters				
Metallicity	$\alpha(\mathcal{M}_1)$ best fit	$\alpha(\mathcal{M}_1)$ best match	$\sigma_\alpha(\mathcal{M}_1)$	$\sigma_\alpha(\mathcal{M}_2)$
$Z = 0.00005$	1.9	1.89	0.17	0.08
$Z = 0.00010$	1.9	1.95	0.17	0.1
$Z = 0.00015$ **	2.0	1.98	0.17	0.08
$Z = 0.00020$	2.0	2.03	0.17	0.08
$-2.0 <$ [Fe/H] < -1.75, 11 clusters				
Metallicity	$\alpha(\mathcal{M}_1)$ best fit	$\alpha(\mathcal{M}_1)$ best match	$\sigma_\alpha(\mathcal{M}_1)$	$\sigma_\alpha(\mathcal{M}_2)$
$Z = 0.00015$	1.8	1.81	0.14	0.07
$Z = 0.00020$**	1.9	1.85	0.14	0.08
$Z = 0.00025$**	1.9	1.89	0.14	0.07
$Z = 0.00030$	1.9	1.93	0.13	0.08
$-1.75 <$ [Fe/H] < -1.50, 15 clusters				
Metallicity	$\alpha(\mathcal{M}_1)$ best fit	$\alpha(\mathcal{M}_1)$ best match	$\sigma_\alpha(\mathcal{M}_1)$	$\sigma_\alpha(\mathcal{M}_2)$
$Z = 0.00025$	1.8	1.81	0.14	0.07
$Z = 0.00030$**	1.8	1.85	0.14	0.08
$Z = 0.00035$	1.9	1.89	0.13	0.07
$Z = 0.00040$	1.9	1.91	0.13	0.07

Table 3. Summary of the mixing length best fit and best match for the $\mathcal{M}_1$ cut and dispersion for each of the metallicity samples (full information for individual clusters is available in appendix C). Each sample spans a range in metallicities, and we report results for several fiducial metallicity values covering the range. The values closer to the effective [Fe/H] metallicity of the sample are flagged by the asterisks. The best fit value for $\alpha_{\rm MLT}$ depends very weekly on metallicity (both the metallicity of the sample and the adopted fiducial metallicity), the scatter does not show any significant dependence on metallicity.

scatter. In Appendix C we report the results for the dispersion in color and in mixing length parameter for each cluster and for each of our three sub-samples combined. We note that all GCs of similar metallicity have a similar value of the dispersion. Finally, Table 3 reports the mixing length best fit and dispersion for each of the metallicity samples. The best fit value for $\alpha_{\rm MLT}$ depends very weekly on metallicity (both the metallicity of the sample and the adopted fiducial metallicity), the scatter does not show any significant dependence on metallicity. The scatter for each metallicity sample (which include $\gtrsim 10$ clusters) is comparable with the individual cluster scatter indicating that there is not additional cluster-to-cluster variation. We adopt a, suitably weighted combined scatter across the three metallicity samples of $\sigma_\alpha^{\rm CMD} = 0.15$ as a conservative estimate of the $\alpha_{\rm MLT}$ scatter estimated from the CMD of the clusters in the sample. Recall that we have attributed the full color scatter of the RGB to $\alpha_{\rm MLT}$, when the color scatter include contributions from measurement errors, photometric errors as well as variations of all other model parameters.

A suite of tests ensuring the robustness of these results to several commonly adopted assumptions is presented in the appendices. In particular Appendix A discusses the impact of chosen fiducial values of mass and metallicity; Appendix B compares different stellar codes and Appendix D tests the effects of microphysics modelling. In summary, there is no indication that stars in old GCs have values for the depth of the convection envelope different from those obtained for the Sun. For the 38 GC considered here we find that the preferred value for the mixing length parameter is $\alpha_{\rm MLT} = 1.90 \pm 0.04\,(\text{or} \pm 0.15)$ with (without) resorting to spectroscopic metallicity determinations, where the reported error is estimated conservatively.

5 Conclusions and implications for the age of the Universe

An estimate of the age of the Universe from the age of the oldest globular clusters was presented in Ref. [1]: the age of the oldest clusters being $t_{\rm GC} = 13.32 \pm 0.10({\rm stat.}) \pm 0.5({\rm sys.})$ Gyr, and the inferred age of the Universe $t_{\rm U} = 13.5^{+0.16}_{-0.14}({\rm stat.}) \pm 0.5({\rm sys.})$ Gyr. The dominant contribution to the error on this quantity is due to the systematic uncertainty in the depth of the convention envelope (the mixing length parameter) accounting for 0.3 (i.e. 60%) of the 0.5 systematic error budget. Ref. [1] adopted a range in $\alpha_{\rm MLT}$ corresponding to the full range considered in Ref. [2] which in the convention of this paper corresponds to $2\Delta_\alpha = 0.7$.

Here we have studied the dependence of the morphology of the RGB in the GCs CMD on changes in $\alpha_{\rm MLT}$, in order to provide a more realistic estimate of the uncertainty on this parameter. We have shown that the range used in Ref. [1] include values that do not fit the observed properties of the GCs in our sample. After studying the degeneracy between $\alpha_{\rm MLT}$ and metallicity, we have estimated an upper limit for the uncertainty of $\alpha_{\rm MLT}$ for our sample: $\sigma_\alpha^{\rm spec.met} = 0.04$ or $\sigma_\alpha^{\rm CMD} = 0.15$ (depending whether using external spectroscopic metallicity determinations or not). It is interesting to note that recently, Ref. [11] performed a Bayesian calibration of the mixing length parameter α using mock and real data of the Hyades open cluster and found an average value $\langle\alpha\rangle = 2.01 \pm 0.05$. This result is in good agreement with our findings.

With this reduction of the dominant systematic contribution to the age determination (from 0.3 to 0.13 or 0.034 Gyr), the mixing length parameter cease to be the dominant contribution to the uncertainty; now the leading systematic uncertainties are due to nuclear reaction rates and opacities.

Thanks to the reduction in the systematic error budget achieved in this work, we conclude[6] that the age of the oldest globular clusters is $t_{\rm GC} = 13.32 \pm 0.10({\rm stat.}) \pm 0.23(0.33)({\rm sys.})$ Gyr, which corresponds to an age of the Universe of $t_{\rm U} = 13.5^{+0.16}_{-0.14}({\rm stat.}) \pm 0.23(0.33)({\rm sys.})$ Gyr., an uncertainty of 0.27(0.36) Gyr if statistical and systematic errors are added in quadrature. This determination of the age of the Universe is cosmological-model agnostic, in the sense that it does not depend in any significant way on the cosmological model adopted, and is in good agreement with the cosmological model-dependent determination of $t_{\rm U} = 13.8 \pm 0.02$ Gyr inferred from the Planck mission from observations of the Universe at $z \sim 1100$, assuming the standard ΛCDM model. The implications for cosmology of this consideration are explored in a companion paper [20].

Acknowledgments

We thank the stellar modelers for making their stellar models publicly available. This work is supported by MINECO grant PGC2018-098866-B-I00 FEDER, UE. LV acknowledges support by European Union's Horizon 2020 research and innovation program ERC (BePreSySe, grant agreement 725327). JLB is supported by the Allan C. and Dorothy H. Davis Fellowship. The work of BDW is supported by the Labex ILP (reference ANR-10-LABX-63) part of the Idex SUPER, received financial state aid managed by the Agence Nationale de la Recherche, as part of the programme Investissements d'avenir under the reference ANR-11-IDEX-0004-02; and by the ANR BIG4 project, grant ANR-16-CE23-0002 of the French Agence Nationale

[6] To propagate exactly an error in $\alpha_{\rm MLT}$ into an error in age one would have to reproduce the full calculations of Ref. [2], which goes well beyond the scope of this paper. Ref. [2] shows that $\Delta_\alpha = \pm 0.35$ yields a $\Delta_{\rm age} = \pm 0.3$. Here we simply rescale the age uncertainty according to our newly determined $\alpha_{\rm MLT}$ uncertainty.

de la Recherche. The Center for Computational Astrophysics is supported by the Simons Foundation.

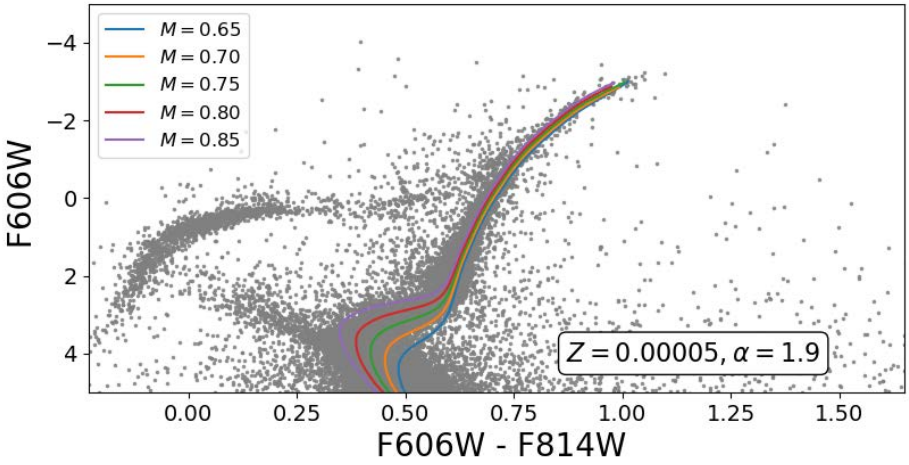

Figure 7. Effect of varying mass for a star with a fixed metallicity and mixing length. The grey points represent the CMD of all the clusters in the low metallicity sample. The lines are stellar tracks for an age of 13.32 Gyr corresponding to different initial masses. If the tracks are interpreted as isochrones such a spread in mass would correspond to a (widely unrealistic) range in age from 11 to 30 Gyr. Note that the RGB morphology is very insensitive to mass (and age). The $\alpha_{\rm MLT}$ value adopted here is 1.9 as it is the closest in our grid to the `DSED` code solar value.

A Impact of mass, metallicity and $\alpha_{\rm MLT}$ on the RGB

As mentioned in section 3.2.2, mass and metallicity are key parameters for our purpose of constraining the mixing length parameter. It is possible to compare the effect of mass (for a track) to the effect of age (for an isochrone). The initial mass of the star influences the time spent on the main sequence but affects very little the red giant branch. In figure 7 we explore a range of masses from $M = 0.65$ to 0.85 $M_{\odot}$ with $\Delta_M = 0.05$.

Metallicity affects the color of the RGB: an increase in metallicity will result in a tilt of the RGB towards higher C. In Figure 8 we show the effect of varying metallicity for a track with a fixed mass and mixing length, compared to a change in mixing length for fixed mass. This figure illustrates that for a metallicity interval comparable with that of each of our samples, the mixing length is the determining parameter in the color of the RGB.

The value of the $\alpha_{\rm MLT}$ parameter is stellar code dependent. The conversion between different code-conventions is just a shift, while the relevant quantity for our argument here is the interval or range adopted which is convention-independent. In Ref. [1] we used the isochrones from the `DSED` model for a solar value for $\alpha_{\rm MLT}$ and here stellar tracks from an independent code. An even slightly incorrect conversion would result into adopting an incorrect fiducial $\alpha_{\rm MLT}$ value and possibly an over-estimate of the color scatter. To map the response of the RGB to changes in mixing length parameter values, we compute tracks for discrete values of $\alpha_{\rm MLT}$ (from 1.2 to 2.8 in steps of 0.1) as illustrated in Figure 9 where the tracks are centered around $\alpha_{\rm MLT} = 2$.

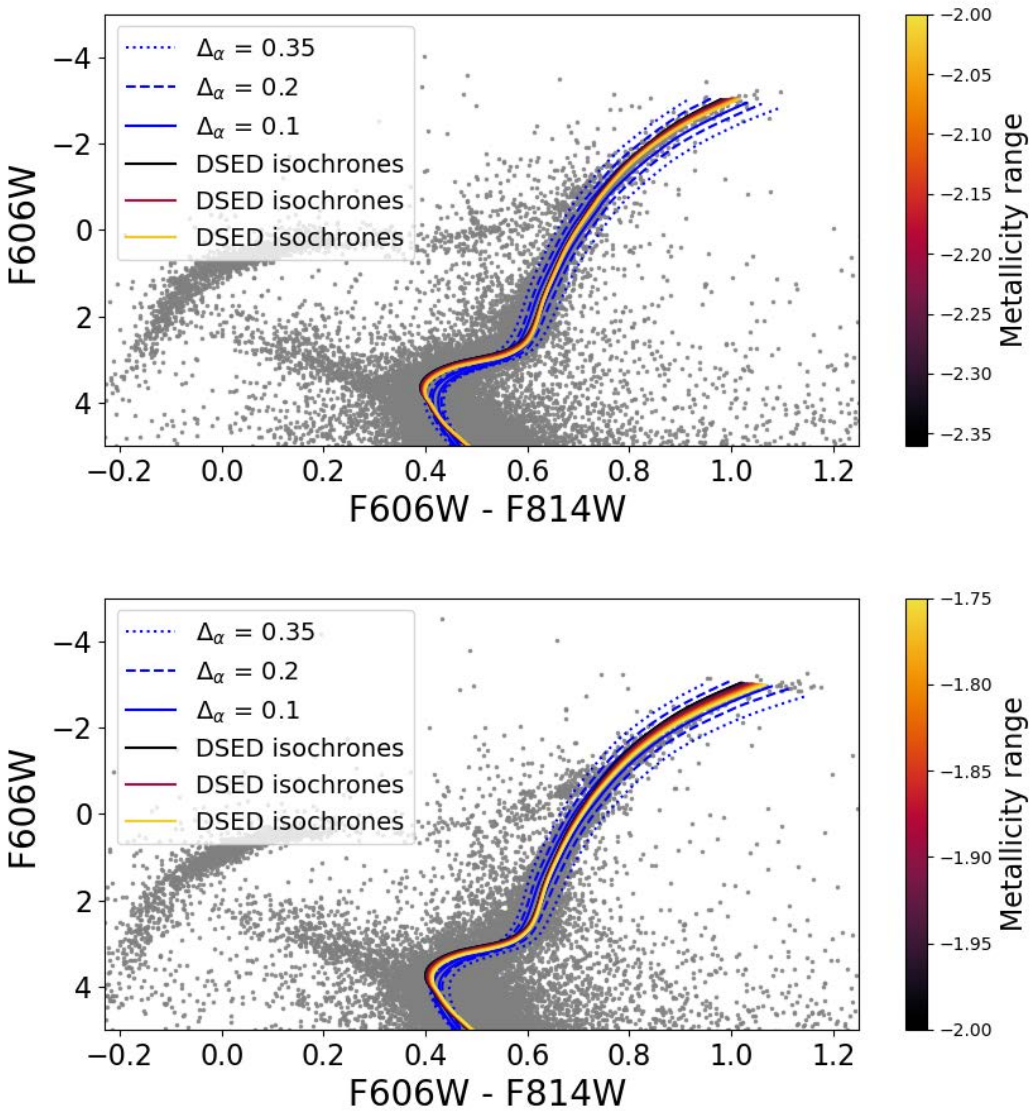

Figure 8. Effect of varying metallicity for a track with a fixed mass and mixing length, compared to a change in mixing length for fixed mass. Top panel: Grey points: the combined CMD of the sample of 12 clusters with metallicity Fe/H< -2. Solid lines tracks color-coded by metallicity for a range spanning the low metallicity sample. Blue lines: effects of changes in $\alpha_{\rm MLT}$. Bottom pane: as for top panel but for the intermediate metallicity sample.

Bolometric corrections are used to transform from observed colors to theoretical effective temperature and viceversa. These corrections, if not accurate enough, can lead to an additional systematic uncertainty. To quentify this effect, we use two different sets of bolometric corrections [9, 10]. As it is shown in Fig. 9 both lead to the same transformation of colors to effective temperature. We therefore do not propagate any additional uncertainty due to bolometric corrections.

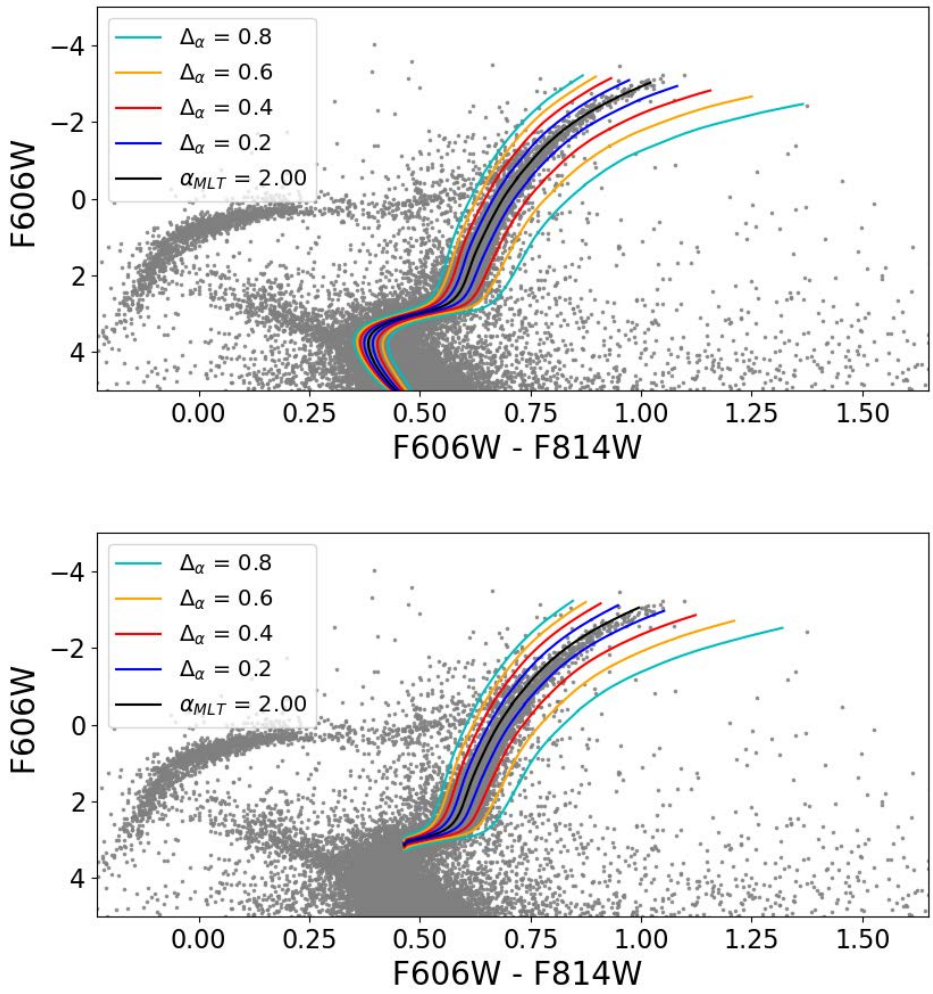

Figure 9. Stellar tracks are shown for a star with initial mass 0.80 $M_{\odot}$ and $Z = 0.0002$ for the MESA code and several values of the mixing length around $\alpha = 2$. The spread of the RGB roughly corresponds to $\Delta_{\alpha} \sim 0.1$. Top panel: Using the Casagrande & VandenBerg [10] bolometric correction, Bottom panel: Using bolometric correction computed from the Castelli & Kurucz 2003 [9] atmospheric spectra. on the relevant part of the RGB the two plots are virtually indistinguishable.

B Effect of opacities and nuclear reaction rates

Uncertainties in opacities and nuclear reaction rates also contribute to the systematic error budget on age determinations, but are expected to be sub-dominant compared to the effect of the mixing length parameter. Here we illustrate this by resorting to available outputs of a different stellar code where these quantities are different from those assumed in `MESA`. In this case we chose the old version (1996) of the `JimMacD` code and stellar tracks [6], which uses very different stellar opacities, boundary conditions and mixing-length formulation. `JimMacD` tracks are available for initial mass 0.8 $M_{\odot}$ (hence we compare directly with `MESA` for this value of the mass) and for a coarse grid of $\alpha_{\rm MLT}$ values (recall that the solar value for $\alpha_{\rm MLT}$ for `JimMacD` is 1.4, which is however not available on the provided grid). This is shown in

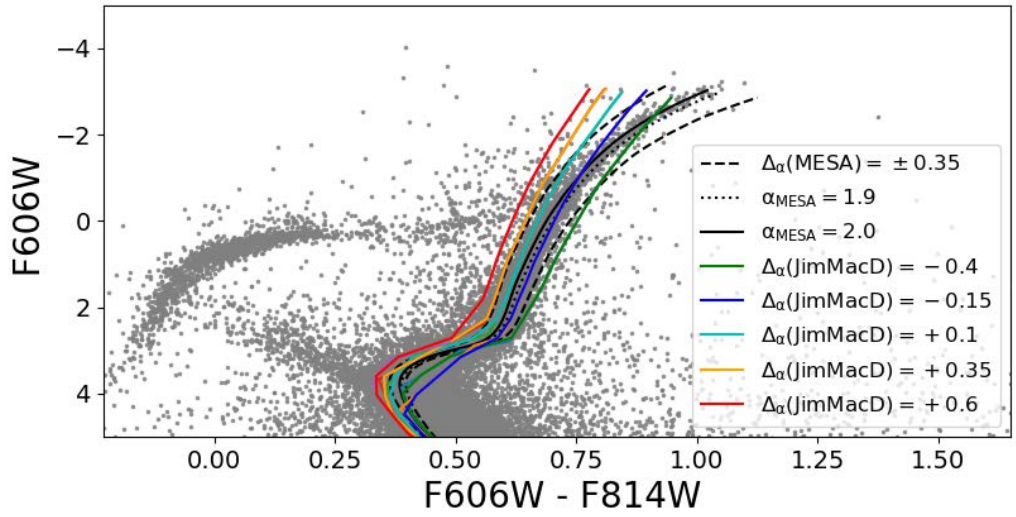

Figure 10. Response of the RGB to changes in $\alpha_{\rm MLT}$ across different codes. As before, the gray points correspond to all the stars in the CMD of the 12 clusters in the low metallicity sample. The black solid line corresponds to `MESA` track for $\alpha_{\rm MLT} = 2$, $M = 0.8 M_{\odot}$, $Z = 0.00002$, the dotted line to $\alpha_{\rm MLT} = 1.9$ for reference, and the dashed lines illustrate a change $\Delta_{\alpha} = \pm 0.35$ around the solar value. The solid lines in colors correspond to `JimMcD` tracks for the same mass and metallicities and for shifts from the solar value as indicated in the legend. The poor fit at the very tip of the RGB is due to the lack of cool opacities in the code unlike the modern `MESA` stellar code.

Fig. 10. Note that the `JimMacD` code fails to fit the tip of the RGB because of the lack of cold opacities, not available at that time. Where this is not a relevant effect, tracks for solar values of the mixing langth parameters agree well, and the response of the RGB color to changes in $\alpha_{\rm MLT}$ is very similar across the two codes: we find that for $\mathcal{M} = 0$ and for the same mass 0.8 $M_{\odot}$, metallicity and $\alpha_{\rm MLT}$ step sampled by `JimMacD` tracks, $\Delta {\rm C}/\Delta\alpha_{\rm MLT} = -0.12$ and -0.13 for `MESA` and `JimMacD` respectively. We therefore conclude that the differences do not significantly bias the RGB color or consequently the recovery of an $\alpha_{\rm MLT}$ value consistent with solar, further supporting the robustness of the results reported in the main text.

C Parameter constrains for all GCs

We double check that the $\alpha_{\rm MLT}$ that best fits the RGB is consistent with the adopted fiducial value of Ref. [1] and consequently the fiducial adopted here too. An incorrect fiducial $\alpha_{\rm MLT}$ value would yield to biases and possibly an over-estimate of the color scatter. Table 4 reports for each cluster the color scatter as a function of magnitude cut, the best match $\alpha_{\rm MLT}$, the scatter in this quantity as a function of magnitude cut and fiducial assumed metallicity. The table also report the best fit $\alpha_{\rm MLT}$ for the combination of the GC in each sample and the recomputed scatter with respect to this quantity rather than the best match $\alpha_{\rm MLT}$. The differences, however are unimportant.

The tables presented here compement Table 3 in the main text. The best fit $\alpha_{\rm MLT}$ is well consistent with the solar value adopted by `DSED` ($\alpha_{\rm MLT} = 1.938$), validating this choice for the fiducial value assumed with no evidence for any bias.

Sample 1, 12 clusters with [Fe/H] <2.0

			$Z = 0.00005$				$Z = 0.00010$				$Z = 0.00015$				$Z = 0.00020$			
GC name	$\sigma_{color}(\mathcal{M}_0)$	$\sigma_{color}(\mathcal{M}_1)$	α best match	$\sigma_\alpha(\mathcal{M}_0)$	$\sigma_\alpha(\mathcal{M}_1)$	$\sigma_\alpha(\mathcal{M}_2)$	α best match	$\sigma_\alpha(\mathcal{M}_0)$	$\sigma_\alpha(\mathcal{M}_1)$	$\sigma_\alpha(\mathcal{M}_2)$	α best match	$\sigma_\alpha(\mathcal{M}_0)$	$\sigma_\alpha(\mathcal{M}_1)$	$\sigma_\alpha(\mathcal{M}_2)$	α best match	$\sigma_\alpha(\mathcal{M}_0)$	$\sigma_\alpha(\mathcal{M}_1)$	$\sigma_\alpha(\mathcal{M}_2)$
NGC 2298	0.0231	0.0236	1.8	0.22	0.19	N/A	1.9	0.22	0.16	N/A	1.9	0.22	0.17	N/A	2	0.21	0.16	N/A
NGC 4590	0.0198	0.0158	1.9	0.21	0.14	N/A	2	0.19	0.13	N/A	2	0.2	0.13	N/A	2.1	0.18	0.14	N/A
NGC 4833	0.018	0.0196	1.8	0.16	0.15	0.09	1.9	0.15	0.14	0.08	1.9	0.16	0.14	0.09	2	0.16	0.14	0.08
NGC 5053	0.0155	0.0195	1.9	0.15	0.14	N/A	2	0.18	0.16	N/A	2	0.16	0.15	N/A	2.1	0.21	0.18	N/A
NGC 6341	0.0172	0.0175	1.9	0.17	0.15	0.05	2	0.16	0.16	0.08	2	0.16	0.15	0.04	2	0.16	0.15	0.04
NGC 6397	0.0254	0.0277	1.9	0.21	0.2	N/A	1.9	0.22	0.22	N/A	1.9	0.24	0.24	N/A	2	0.22	0.2	N/A
NGC 6426	0.0239	0.0287	1.9	0.23	0.24	N/A	2	0.22	0.21	N/A	2	0.22	0.22	N/A	2.1	0.21	0.2	N/A
NGC 6779	0.0241	0.0258	1.9	0.21	0.18	0.09	1.9	0.22	0.19	0.11	2	0.2	0.17	0.09	2	0.21	0.18	0.1
NGC 7078	0.0219	0.0204	2	0.19	0.15	0.08	2	0.2	0.16	0.08	2.1	0.18	0.15	0.08	2.1	0.18	0.15	0.07
NGC 7099	0.0268	0.0211	1.9	0.25	0.16	0.11	1.9	0.27	0.18	0.14	2	0.22	0.14	0.09	2	0.23	0.14	0.12
Palomar 15	0.0285	0.0284	1.9	0.27	0.21	N/A	2	0.24	0.17	N/A	2	0.25	0.18	N/A	2	0.26	0.2	N/A
Terzan 8	0.0169	0.0189	1.9	0.17	0.14	N/A	1.9	0.17	0.14	N/A	2	0.18	0.15	N/A	2	0.17	0.14	N/A
All 12 GCs	0.0226	0.0223	1.89	0.2	0.17	0.08	1.95	0.2	0.17	0.1	1.98	0.2	0.17	0.08	2.03	0.2	0.17	0.08

GC name	$\sigma_{color}(\mathcal{M}_0)$	$\sigma_{color}(\mathcal{M}_1)$	α best fit	$\sigma_\alpha(\mathcal{M}_0)$	$\sigma_\alpha(\mathcal{M}_1)$	$\sigma_\alpha(\mathcal{M}_2)$	α best fit	$\sigma_\alpha(\mathcal{M}_0)$	$\sigma_\alpha(\mathcal{M}_1)$	$\sigma_\alpha(\mathcal{M}_2)$	α best fit	$\sigma_\alpha(\mathcal{M}_0)$	$\sigma_\alpha(\mathcal{M}_1)$	$\sigma_\alpha(\mathcal{M}_2)$	α best fit	$\sigma_\alpha(\mathcal{M}_0)$	$\sigma_\alpha(\mathcal{M}_1)$	$\sigma_\alpha(\mathcal{M}_2)$
All 12 GCs	0.0226	0.0223	1.9	0.21	0.17	0.1	1.9	0.22	0.19	0.13	2	0.2	0.16	0.1	2	0.2	0.17	0.12

Sample 2, 11 clusters with -2.0 <[Fe/H] <-1.75

			$Z = 0.00015$				$Z = 0.00020$				$Z = 0.00025$				$Z = 0.00030$			
GC name	$\sigma_{color}(\mathcal{M}_0)$	$\sigma_{color}(\mathcal{M}_1)$	α best match	$\sigma_\alpha(\mathcal{M}_0)$	$\sigma_\alpha(\mathcal{M}_1)$	$\sigma_\alpha(\mathcal{M}_2)$	α best match	$\sigma_\alpha(\mathcal{M}_0)$	$\sigma_\alpha(\mathcal{M}_1)$	$\sigma_\alpha(\mathcal{M}_2)$	α best match	$\sigma_\alpha(\mathcal{M}_0)$	$\sigma_\alpha(\mathcal{M}_1)$	$\sigma_\alpha(\mathcal{M}_2)$	α best match	$\sigma_\alpha(\mathcal{M}_0)$	$\sigma_\alpha(\mathcal{M}_1)$	$\sigma_\alpha(\mathcal{M}_2)$
Arp 2	0.0164	0.0156	1.8	0.16	0.13	N/A	1.9	0.15	0.11	N/A	1.9	0.15	0.11	N/A	2	0.16	0.12	N/A
NGC 4147	0.0155	0.0151	1.8	0.14	0.12	N/A	1.8	0.14	0.12	N/A	1.9	0.16	0.11	N/A	1.9	0.15	0.11	N/A
NGC 5024	0.0173	0.0193	1.8	0.17	0.16	0.07	1.9	0.16	0.14	0.05	1.9	0.16	0.14	0.06	2	0.16	0.14	0.06
NGC 5466	0.0154	0.0159	1.8	0.14	0.12	N/A	1.9	0.14	0.11	N/A	1.9	0.13	0.11	N/A	1.9	0.13	0.11	N/A
NGC 6093	0.0212	0.022	1.8	0.21	0.16	0.08	1.8	0.21	0.16	0.1	1.9	0.2	0.14	0.08	1.9	0.2	0.15	0.09
NGC 6101	0.0181	0.0215	1.8	0.15	0.15	0.07	1.8	0.16	0.16	0.1	1.9	0.16	0.14	0.06	1.9	0.16	0.14	0.08
NGC 6144	0.027	0.0308	1.8	0.24	0.21	N/A	1.8	0.25	0.22	N/A	1.8	0.26	0.24	N/A	1.9	0.22	0.19	N/A
NGC 6254	0.0226	0.0219	1.8	0.24	0.15	0.08	1.9	0.21	0.14	0.09	1.9	0.22	0.14	0.08	1.9	0.22	0.14	0.08
NGC 6535	0.0201	0.0155	1.8	0.21	0.09	N/A	1.9	0.17	0.07	N/A	1.9	0.17	0.07	N/A	1.9	0.18	0.08	N/A
NGC 6541	0.0216	0.0208	1.9	0.19	0.14	0.07	1.9	0.2	0.14	0.07	2	0.18	0.14	0.08	2	0.18	0.13	0.07
NGC 6809	0.0177	0.02	1.8	0.15	0.15	N/A	1.8	0.15	0.15	N/A	1.8	0.15	0.15	N/A	1.9	0.17	0.14	N/A
All 11 GCs	0.0205	0.0217	1.81	0.18	0.14	0.07	1.85	0.18	0.14	0.08	1.89	0.18	0.14	0.07	1.93	0.18	0.13	0.08

GC name	$\sigma_{color}(\mathcal{M}_0)$	$\sigma_{color}(\mathcal{M}_1)$	α best fit	$\sigma_\alpha(\mathcal{M}_0)$	$\sigma_\alpha(\mathcal{M}_1)$	$\sigma_\alpha(\mathcal{M}_2)$	α best fit	$\sigma_\alpha(\mathcal{M}_0)$	$\sigma_\alpha(\mathcal{M}_1)$	$\sigma_\alpha(\mathcal{M}_2)$	α best fit	$\sigma_\alpha(\mathcal{M}_0)$	$\sigma_\alpha(\mathcal{M}_1)$	$\sigma_\alpha(\mathcal{M}_2)$	α best fit	$\sigma_\alpha(\mathcal{M}_0)$	$\sigma_\alpha(\mathcal{M}_1)$	$\sigma_\alpha(\mathcal{M}_2)$
All 11 GCs	0.0205	0.0217	1.8	0.2	0.16	0.09	1.9	0.19	0.14	0.07	1.9	0.19	0.14	0.07	1.9	0.19	0.15	0.09

Sample 3, 15 clusters with -1.75 <[Fe/H] <-1.5

			$Z = 0.00025$				$Z = 0.00030$				$Z = 0.00035$				$Z = 0.00040$			
GC name	$\sigma_{color}(\mathcal{M}_0)$	$\sigma_{color}(\mathcal{M}_1)$	α best match	$\sigma_\alpha(\mathcal{M}_0)$	$\sigma_\alpha(\mathcal{M}_1)$	$\sigma_\alpha(\mathcal{M}_2)$	α best match	$\sigma_\alpha(\mathcal{M}_0)$	$\sigma_\alpha(\mathcal{M}_1)$	$\sigma_\alpha(\mathcal{M}_2)$	α best match	$\sigma_\alpha(\mathcal{M}_0)$	$\sigma_\alpha(\mathcal{M}_1)$	$\sigma_\alpha(\mathcal{M}_2)$	α best match	$\sigma_\alpha(\mathcal{M}_0)$	$\sigma_\alpha(\mathcal{M}_1)$	$\sigma_\alpha(\mathcal{M}_2)$
IC4499	0.0186	0.0215	1.9	0.16	0.14	N/A	1.9	0.16	0.14	N/A	1.9	0.16	0.15	N/A	2	0.16	0.13	N/A
NGC 3201	0.0241	0.0248	1.8	0.18	0.14	0.08	1.8	0.17	0.13	0.06	1.8	0.18	0.13	0.07	1.9	0.2	0.14	0.08
NGC 5139	0.0192	0.0211	1.9	0.17	0.14	0.06	1.9	0.17	0.14	0.07	1.9	0.17	0.14	0.09	2	0.18	0.14	0.06
NGC 5272	0.0157	0.0202	1.7	0.15	0.14	0.08	1.8	0.13	0.13	0.05	1.8	0.13	0.13	0.06	1.8	0.14	0.13	0.07
NGC 5286	0.0221	0.0228	1.9	0.2	0.16	0.07	1.9	0.21	0.17	0.09	2	0.18	0.15	0.06	2	0.18	0.15	0.07
NGC 5986	0.0268	0.0285	1.8	0.23	0.17	0.07	1.8	0.23	0.19	0.08	1.9	0.22	0.16	0.08	1.9	0.22	0.16	0.07
NGC 6218	0.0161	0.0141	1.7	0.15	0.07	N/A	1.7	0.15	0.07	N/A	1.8	0.12	0.08	N/A	1.8	0.12	0.07	N/A
NGC 6584	0.0173	0.0194	1.8	0.16	0.14	0.05	1.8	0.17	0.15	0.06	1.9	0.14	0.13	0.06	1.9	0.14	0.13	0.05
NGC 6656	0.0233	0.0243	1.9	0.19	0.14	0.07	1.9	0.2	0.15	0.1	2	0.17	0.13	0.05	2	0.17	0.13	0.07
NGC 6681	0.0206	0.0214	1.8	0.19	0.15	0.09	1.9	0.18	0.14	0.1	1.9	0.18	0.13	0.09	1.9	0.18	0.14	0.09
NGC 6752	0.0174	0.0204	1.7	0.17	0.12	0.11	1.8	0.14	0.11	0.08	1.8	0.14	0.11	0.09	1.8	0.15	0.11	0.11
NGC 6934	0.017	0.0211	1.8	0.15	0.14	0.08	1.8	0.15	0.14	0.06	1.8	0.16	0.14	0.06	1.9	0.14	0.13	0.08
NGC 7006	0.0197	0.0258	1.8	0.17	0.18	0.09	1.9	0.17	0.17	0.1	1.9	0.17	0.17	0.09	1.9	0.17	0.17	0.09
NGC 7089	0.0176	0.0184	1.8	0.18	0.14	0.05	1.9	0.16	0.13	0.06	1.9	0.16	0.13	0.05	1.9	0.16	0.13	0.05
Ruprecht 106	0.0223	0.0202	1.9	0.22	0.13	N/A	1.9	0.23	0.14	N/A	2	0.18	0.11	N/A	2	0.19	0.11	N/A
All 15 GCs	0.021	0.0251	1.81	0.18	0.14	0.07	1.85	0.17	0.14	0.08	1.89	0.16	0.13	0.07	1.91	0.17	0.13	0.07

GC name	$\sigma_{color}(\mathcal{M}_0)$	$\sigma_{color}(\mathcal{M}_1)$	α best fit	$\sigma_\alpha(\mathcal{M}_0)$	$\sigma_\alpha(\mathcal{M}_1)$	$\sigma_\alpha(\mathcal{M}_2)$	α best fit	$\sigma_\alpha(\mathcal{M}_0)$	$\sigma_\alpha(\mathcal{M}_1)$	$\sigma_\alpha(\mathcal{M}_2)$	α best fit	$\sigma_\alpha(\mathcal{M}_0)$	$\sigma_\alpha(\mathcal{M}_1)$	$\sigma_\alpha(\mathcal{M}_2)$	α best fit	$\sigma_\alpha(\mathcal{M}_0)$	$\sigma_\alpha(\mathcal{M}_1)$	$\sigma_\alpha(\mathcal{M}_2)$
All 15 GCs	0.021	0.0251	1.8	0.19	0.16	0.1	1.8	0.19	0.17	0.12	1.9	0.18	0.15	0.1	1.9	0.18	0.15	0.1

Table 4. Dispersion in color and mixing length for the 4 fiducial adopted metallicity values. The results are given for each cluster in each of the sub-samples and all combined. For the combined sample we report both the means of the best match $\alpha_{\rm MLT}$ values and the best-fit $\alpha_{\rm MLT}$. For magnitude bins with less than 10 stars, the dispersion α is not computed (N/A). The color dispersion is not affected by the choice of initial metallicity.

D Assessing robustness: Tests of microphysics

Throughout this work, we have assumed a fixed $\alpha_{\rm MLT}$ through the stellar tracks: this value does not change in itself the duration of the lifetime of the star. The lifetime of low-mass stars to helium flash is mostly dependent on mass and metallicity. In fact, the lifetime in Gyr to the He flash can be fitted with 5% precision by the formula (adopting a helium mass fraction $Y = 0.24$)

$$\log t = -0.207 - 3.691 \log(M/M_\odot) + 11.327 \log(1.76 - Z) + 0.870 \log(0.0086 + Z) \quad \text{(D.1)}$$

Beside the mixing length and the metallicity, which, as we have seen, determine the color of the RGB to leading and next-to-leading order, other parameters can also affect the

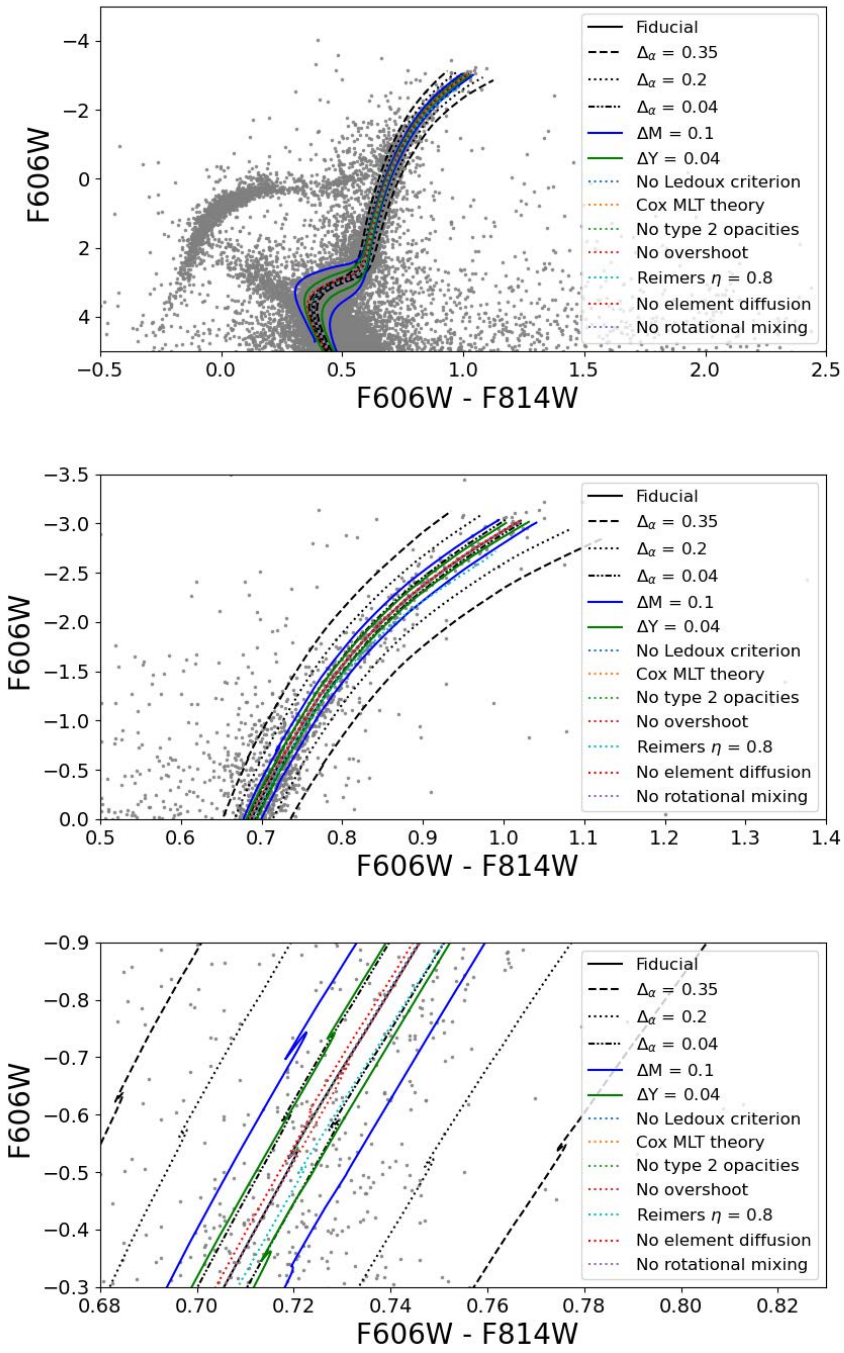

Figure 11. The effect on the RGB of (extreme) changes of other microphysics parameters besides the mixing length. The three panels are subsequent zoom ins in the relevant part of the CMD. Note that the effect is much smaller than that of $\alpha_{\rm MLT}$, and well below the intrinsic broadening of the RGB (gray points) and thus below star-to-star color variations.

color of the RGB, although with a weaker dependence: initial mass, initial helium mass fraction, overshooting of the convection depth, mass loss, rotational mixing and element

diffusion. These are kept fixed at their fiducial values in our main analysis, here we quantify their effect. We also explore changing the mixing length theory to the Cox formulation [17] . We compute stellar tracks by varying a single parameter at the time while keeping the other parameters fixed to the fiducial configuration (see section 3.2.2) with a mixing length value $\alpha = 1.9$ being this the closest in our grid to the solar value 1.938.

This is illustrated in Figure 11 where the top panel shows the full RGB and the bottom panel is a zoom-in on the Helium flash region, to make visible the (small) effect of some of the parameters we consider. Variations of initial mass, initial helium mass fraction and diffusion, which alters the lifetime of the star, affect the main sequence more severely than the RGB. The rest of the parameters influence the more advanced life stages of the star. Type 2 opacities are important to compute the helium burning rate and a variation of the mass loss parameter cause the tracks to deviate towards the end of the RGB. It is well known that a shift in mass of $\Delta M = 0.1$ or a shift in Helium of $\Delta Y = 0.04$, are heavily disfavoured by the data as these parameters also change the main sequence and the MSTO and with such shifts models do not fit this part of the CMD. We also test different models of convection (Henyey and Cox [17, 18]), the implementation or not of overshoot, and with or without Ledoux criterion (for more information see Ref. [6] and references therein). The value for the mass loss Reimers parameter $\eta = 0.8$ is an extreme value motivated by the morphology the horizontal branch of the CMD of globular clusters (e.g., [8, 19]). For completeness, we also show rotational mixing, even though it mainly affects massive stars. This is the motivation for the adopted choices in the Figure. Most of the parameters tested have little to no impact for low mass stars or will affect the horizontal or asymptotic branch which are not of interest for this paper.

Changes in the initial mass ΔM and in the initial helium mass fraction ΔY have a much bigger effect than all other changes, which are much more subtle, and small compared to the intrinsic broadening of the RGB. Unlike $\alpha_{\rm LMT}$, the other parameters of the mixing length theory do modify the stellar tracks but maintaining the color of the RGB unaltered. We also illustrate the effect of $\Delta_\alpha = 0.35$, the value very conservatively adopted by [1], and $\Delta_\alpha = 0.2$ and 0.04 as estimated by the two approaches presented in the main text. These considerations indicate that the results reported are robust to any possible changes in key stellar parameters.

References

[1] D. Valcin, J. L. Bernal, R. Jimenez, L. Verde and B. D. Wandelt, JCAP **12** (2020), 002 doi:10.1088/1475-7516/2020/12/002 [arXiv:2007.06594 [astro-ph.CO]].

[2] E. M. O'Malley, C. Gilligan and B. Chaboyer, *Absolute Ages and Distances of 22 GCs Using Monte Carlo Main-sequence Fitting*, *ApJ* **838** (2017) 162 [1703.01915].

[3] R. Wagner-Kaiser, A. Sarajedini, T. von Hippel, D. C. Stenning, D. A. van Dyk, E. Jeffery et al., *The ACS survey of Galactic globular clusters - XIV. Bayesian single-population analysis of 69 globular clusters*, *MNRAS* **468** (2017) 1038 [1702.08856].

[4] R. Jimenez, A. Cimatti, L. Verde, M. Moresco and B. Wandelt, *The local and distant Universe: stellar ages and H_0*, *JCAP* **2019** (2019) 043 [1902.07081].

[5] Paxton, B., Bildsten, L., Dotter, A., et al.,*Modules for Experiments in Stellar Astrophysics (MESA)*, *Apjs* **192** (2011) 3

[6] R. Jimenez and J. MacDonald, *Stellar evolutionary tracks for low-mass stars*, *MNRAS* **283** (1996) 721.

[7] J. Choi, A. Dotter, C. Conroy, M. Cantiello, B. Paxton and B. D. Johnson, *Mesa Isochrones and Stellar Tracks (MIST). I. Solar-scaled Models*, *ApJ* **823** (2016) 102 [1604.08592].

[8] R. Jimenez, P. Thejll, U. G. Jorgensen, J. MacDonald and B. Pagel, *Ages of globular clusters: a new approach*, *MNRAS* **282** (1996) 926 [astro-ph/9602132].

[9] Castelli, F. & Kurucz, R. L. 2003,*Modelling of Stellar Atmospheres* , 210, A20

[10] Casagrande, L. & VandenBerg, D. A.,*Synthetic stellar photometry - I. General considerations and new transformations for broad-band systems*, *MNRAS* **444** (2014) 392

[11] Tognelli, E., Dell'Omodarme, M., Valle, G., et al.,*Bayesian calibration of the mixing length parameter α_{ML} and of the helium-to-metal enrichment ratio $\Delta Y/\Delta Z$ with open clusters: the Hyades test-bed*, *mnras* **501** (2021) 383

[12] A. Dotter, B. Chaboyer, D. Jevremović, V. Kostov, E. Baron and J. W. Ferguson, *The Dartmouth Stellar Evolution Database*, *ApJS* **178** (2008) 89 [0804.4473].

[13] Mosumgaard, J. R., Jørgensen, A. C. S., Weiss, A., et al. 2019, arXiv:1910.10163

[14] W. E. Harris, *A Catalog of Parameters for Globular Clusters in the Milky Way*, *AJ* **112** (1996) 1487.

[15] W. E. Harris, *A Catalog of Parameters for Globular Clusters in the Milky Way*, 2010, arXiv:1012.3224

[16] R. Kippenhahn and A. Weigert, *Stellar Structure and Evolution*. 1990.

[17] Cox, J. P. & Giuli, R. T. 1968, Principles of stellar structure, by J.P. Cox and R. T. Giuli. New York: Gordon and Breach, 1968

[18] Henyey, L., Vardya, M. S., & Bodenheimer, P., 1965, ApJ, 142, 841.

[19] McDonald I., Zijlstra A. A., 2015, MNRAS, 448, 502. doi:10.1093/mnras/stv007

[20] Bernal, J.L., et al. in preparation.

[21] Hauschildt, P. H., Allard, F., & Baron, E.*The NextGen Model Atmosphere Grid for 3000¡=T_{eff}¡=10,000 K*, 1999, Apj, 512, 377.

[22] Hauschildt, P. H., Allard, F., Ferguson, J., et al., *The NEXTGEN Model Atmosphere Grid. II. Spherically Symmetric Model Atmospheres for Giant Stars with Effective Temperatures between 3000 and 6800 K*, 1999, Apj, 525, 871.

FIGURE 3.1: The Messier 80 globular cluster in the constellation Scorpius by NASA, The Hubble Heritage Team, STScI, AURA. Public domain

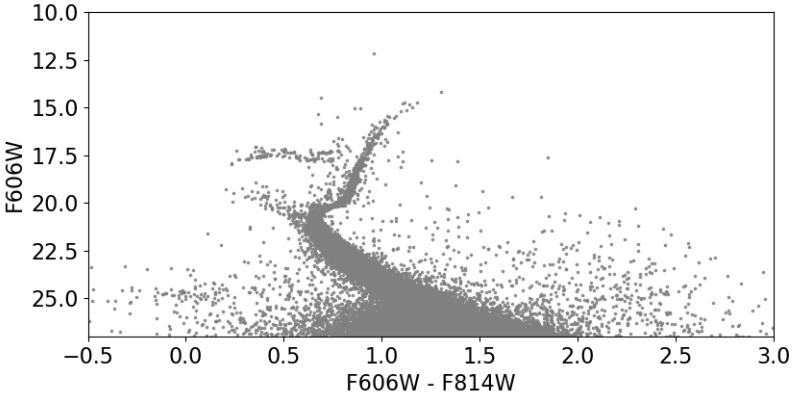

FIGURE 3.2: CMD of the globular cluster IC4499 made with data from the HST-ACS survey (Sarajedini et al., 2007).

3.5 Cosmic chronometers and standard clocks

In section 1.2, I presented the tension which exists between the direct and indirect measurements of the rate of expansion of the universe today, H_0. On one side as these measurements seem to indicate that the expansion rate at early times is different from that at late times, various solutions modifying the physics beyond the standard model have been proposed. On the other side as it is not necessary to assume a cosmological model for direct determinations, systematic errors and new ways of measuring the constant are sought in order to achieve a convergence of the results.

Since the velocity can be determined from the redshift, the quantity to constrain should be related to the redshift and H_0. As the expansion describes the evolution of the scale factor as a function of time, we can derive a relationship between time t and redshift z.

$$\left.\begin{aligned} H(z) &\equiv \frac{\dot{a}}{a} \equiv \frac{da}{dt}\frac{1}{a} \\ a &= \frac{1}{1+z} \\ da &= -\frac{1}{(1+z)^2}dz \end{aligned}\right\} \quad dt = -\frac{dz}{H(z)(1+z)} \tag{3.1}$$

Cosmic chronometers (Jimenez and Loeb, 2002; Stern et al., 2010) use the differential-age technique where the quantity measured is the change in the age of the universe as a function of redshift dt/dz. This method is based on the calibration of old stellar populations. To be qualified as *standard clocks*, celestial objects must fulfill two requirements:

1. The stellar populations must be found in bound systems in order to assume a common formation history.
2. Even though the objects have experienced several periods of stellar formation, their light must be dominated by an old stellar population.

In their articles Jimenez and Loeb 2002; Stern et al. 2010 used passively–evolving red-envelope galaxies with little to no stellar formation because the models at the time were less prone to systematic errors. However, globular clusters can also be used as standard clocks.

3.6 The trouble beyond H_0 and the new cosmic triangles

It is generally easier to measure with precision the relative age of standard clocks than their absolute age because assumptions on the time of formation need to be made, but a measurement of the absolute age with sufficiently small errors would bring a new perspective to the H_0 tension and may even allow to discriminate between the models. If we integrate the relationship given by the equation 3.1,

$$\int_{t_1}^{t_2} dt = -\int_{z1}^{z2} \frac{dz}{(1+z)H(z)} \tag{3.2}$$

the age of the universe t_U can be expressed as a function of the Hubble constant:

$$t_U = \int_0^{t_0} dt = \frac{1}{H_0}\int_0^{\infty} \frac{dz}{(1+z)E(z)} \tag{3.3}$$

with

$$E(z)^2 = \frac{H^2(z)}{H_0^2} = \left[\Omega_{r,0}(1+z)^4 + \Omega_{m,0}(1+z)^3 + \Omega_{k,0}(1+z)^2 + \Omega_{\Lambda,0}\right] \tag{3.4}$$

where $E(z)$ is a function depending on the assumed cosmological model and the inferred value of the various cosmological parameters (Ω_m, Ω_Λ etc.). As can be seen from Equation 3.3, a determination of t_U independent of a cosmological model would make it possible to constrain some of the parameters.

Editors' Suggestion

Trouble beyond H_0 and the new cosmic triangles

José Luis Bernal,[1] Licia Verde,[2,3] Raul Jimenez,[2,3] Marc Kamionkowski,[1]
David Valcin,[2] and Benjamin D. Wandelt[4,5,6]

[1]*Department of Physics and Astronomy, Johns Hopkins University, 3400 North Charles Street, Baltimore, Maryland 21218, USA*
[2]*ICC, University of Barcelona, Martí i Franquès, 1, E-08028 Barcelona, Spain*
[3]*ICREA, Passeig Lluis Companys 23, Barcelona 08010, Spain*
[4]*Sorbonne Université, CNRS, UMR 7095, Institut d'Astrophysique de Paris, 98 bis bd Arago, 75014 Paris, France*
[5]*Sorbonne Université, Institut Lagrange de Paris (ILP), 98 bis bd Arago, 75014 Paris, France*
[6]*Center for Computational Astrophysics, Flatiron Institute, 162 5th Avenue, New York, New York 10010, USA*

(Received 15 February 2021; accepted 8 April 2021; published 26 May 2021)

The distance ladder using supernovae yields higher values of the Hubble constant H_0 than those inferred from measurements of the cosmic microwave background (CMB) and galaxy surveys, a discrepancy that has come to be known as the "Hubble tension". This has motivated the exploration of extensions to the standard cosmological model in which higher values of H_0 can be obtained from CMB measurements and galaxy surveys. The trouble, however, goes beyond H_0; such modifications affect other quantities, too. In particular, their effects on cosmic times are usually neglected. We explore here the implications that measurements of the age t_U of the Universe, such as a recent inference from the age of the oldest globular clusters, can have for potential solutions to the H_0 tension. The value of H_0 inferred from the CMB and galaxy surveys is related to the sound horizon at CMB decoupling (or at radiation drag), but it is also related to the matter density and to t_U. Given this observation, we show how model-independent measurements may support or disfavor proposed new-physics solutions to the Hubble tension. Finally, we argue that cosmological measurements today provide constraints that, within a given cosmological model, represent an overconstrained system, offering a powerful diagnostic tool of consistency. We propose the use of ternary plots to simultaneously visualize independent constraints on key quantities related to H_0 like t_U, the sound horizon at radiation drag, and the matter density parameter. We envision that this representation will help find a solution to the trouble of and beyond H_0.

DOI: 10.1103/PhysRevD.103.103533

I. INTRODUCTION

The standard, ΛCDM, cosmological model, has successfully passed increased scrutiny, as observations of the cosmic microwave background (CMB) [1–3], type-Ia supernovae (SNeIa) [4] and large-scale structure [5–8] have improved drastically over recent years. Nonetheless, tensions have arisen for specific parameters when their values are inferred, within the ΛCDM, from different probes and observables. The biggest tension is related to determinations of the Hubble constant $H_0 \equiv 100h$ km/s/Mpc, and has increased in the last decade to be in the $4-5\sigma$ [9,10].

The current state of the H_0 tension is illustrated in Fig. 1, where we show marginalized posteriors for measurements depending on early-times physics (like *Planck* [1] or baryon acoustic oscillations with a big bang nucleosynthesis (BBN) prior on the physical density of baryons [11,12]), late-time expansion history (using strong lensing time delays from TDCOSMO [13–17][1] and cosmic chronometers [19,20]), and local measurements, independent of cosmology, from SH0ES [21] and CCHP [22]. Except for cosmic chronometers, all competitive H_0 constraints considered here rely on distance measurements.[2]

The two determinations yielding the largest tension are obtained from the CMB power spectra and the SH0ES distance ladders using SNeIa calibrated by Cepheids. CCHP calibrates the SNeIa instead with the tip of the red giant branch (TRGB) and finds a lower value of H_0 [22] (see also [26–28]).

[1]There are ongoing efforts to relax the dependence of strong lensing time delays H_0 inference on the assumed expansion rate [18].

[2]Some H_0 constraints related with large-scale structure do not depend on the sound horizon, but still depend on distance scales, such as the size of the horizon at matter-radiation equality [23,24].

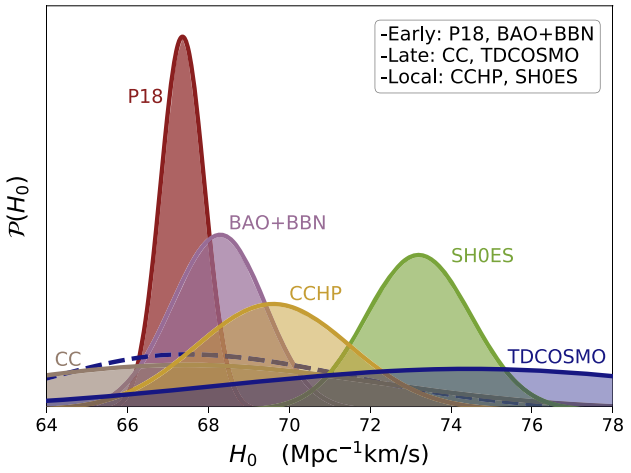

FIG. 1. Summary of constraints on H_0 from cosmic chronometers (CC) [20], *Planck* (P18) [1], baryon acoustic oscillations with a BBN prior on the baryon abundance (BAO + BBN) [12], CCHP [22], SH0ES [25], and strong-lensing time delays (TDCOSMO) [17]. We also show (dashed line) the TDCOSMO constraint including resolved kinematics from SLACS galaxies, which assumes both samples belong to the same parent population. Note that the results shown in this figure are subject to different model assumptions.

Given the strong constraints imposed by available data on the product of the sound horizon r_d at radiation drag and h, r_d has been targeted as the critical quantity to be modified in order to solve the H_0 tension. Baryon acoustic oscillations (BAO) and SNeIa disfavor any strong deviation from the evolution of the expansion rate predicted ΛCDM, while strongly constraining $r_d h$ [29–31]. In light of current constraints, the modifications of ΛCDM best poised to reduce the H_0 tension involve altering prerecombination physics as to lower the value of r_d, as it is discussed in Ref. [32], where it is argued that other possibilities, both before and after recombination are disfavored by observations or theoretically unlikely. There is a plethora of proposed models to do so and those showing more promise involve boosts of the expansion history between matter-radiation equality and recombination (see e.g., [33–48]).

Despite the fact that most of the attention has been focused on modifying distance scales across cosmic history, the expansion rate, thus H_0, also determines the age-redshift relation. Measuring cosmic ages can provide a constraint on H_0 completely independent from r_d, other standard scales, or distance measurements (see e.g., [49] for a study regarding the presence of a cosmological constant). Cosmic chronometers measure directly the expansion rate using differential ages [19]; this approach is limited to relatively low redshifts, covering a range that overlaps with distance measurements. On the other hand, since relative changes in the expansion history at early times do not significantly modify the age of the Universe, independent inferences of absolute lookback times, such as the age of the Universe, may weigh in on the H_0 tension.

In this work, we discuss how the age of the Universe inferred from a recent determination of the age of the oldest globular clusters [50–52] can offer an additional perspective on the H_0 controversy. Our results suggest that an accurate and precise measurement of the age of the Universe provides an important test of the hypothesis that the H_0 tension suggests new early-Universe physics but standard late-Universe physics. In the process, we also update constraints on the low-redshift expansion rate using recent relative distance redshift measurements.

In the same way as the H_0 tension was reframed as the inconsistency between r_d, h, and their product $r_d h$ (inferred independently in a model-agnostic way from low redshifts observations) [29–31], the same can be said about other sets of quantities that can be constrained independently, albeit assuming a cosmological model. One is the combination of the matter density parameter Ω_M today, h^2, and their product, the physical matter density $\Omega_M h^2$. The other set is the age t_U of the Universe and h, and their combination $t_U h$, which is completely determined by the shape of the expansion history and measured independently.

This is reminiscent of the "cosmic triangle" proposed in Ref. [53] two decades ago, where the matter, cosmological constant, and curvature density parameters are related to one another because they sum to unity. The original cosmic triangle is a ternary plot which served to visualize cosmological constraints that led to favor the (now standard) flat ΛCDM model. Here, in full analogy, we propose the use of ternary plots as diagnosis diagrams to examine the tension between cosmological quantities independently measured from different observations. Ternary plots are specially suited for this purpose, as we show for the cases of r_d, Ω_M, and t_U listed above.

This article is organized as follows. We present updated constraints on the late-Universe expansion rate as a function of redshift in Sec. II; discuss the role cosmic ages play in the H_0 tension in Sec. III; present the new cosmic triangles in Sec. IV; and finally conclude in Sec. V.

II. UPDATED EXPANSION RATE CONSTRAINTS

We begin by presenting updated model-agnostic constraints on the expansion rate as a function of redshift, $E(z) \equiv H(z)/H_0$, using the latest, state-of-the-art data. These constraints on $E(z)$ are a key input for the results of Secs. III, IV, and our conclusions.

We use SNeIa observations from Pantheon [4] and BAO measurements from 6dFGRS [54], SDSS DR7 [55], BOSS [5], and eBOSS, including galaxies, quasars, and Lyman-α

forest [56–60] as relative distance indicators.[3] Note that although BAO-only analyses assume a fiducial cosmology, their results are robust to be applied to other cosmologies (see e.g., [61,63]).

Two models for $E(z)$ are examined: ΛCDM, and a parametrization using natural cubic splines, the nodes of which have a varying position, without imposing flatness, which we refer to as "generic" expansion and as such falls under what we here refer to as "model-agnostic" approach. Given its flexibility, the generic expansion shall be understood as a marginalization over cosmological models predicting a smooth $E(z)$. Other uses of this parametrization, known as flexknot, can be found in e.g., Refs. [64,65].

The free parameters for the ΛCDM case are $\{\Omega_M, r_d, h, M_{SN}\}$, where M_{SN} is the absolute magnitude of SNeIa; on the other hand, the generic expansion needs $\{z_{knot}^{(1,N-1)}, \boldsymbol{E}_{knot}^{(1,N)}, \Omega_k, r_d, h, M_{SN}\}$ as free parameters, where $\boldsymbol{E}_{knot}$ are the values of $E(z)$ at the knots of the splines, located at z_{knot}, and Ω_k is the density parameter associated with curvature. The first and last knot are fixed at $z = 0$ and $z = 2.4$, respectively, and $E(0) = 1$ by definition. Although our results do not significantly depend on the number of knots used, we find $N = 4$ provides the best performance, allowing for as much freedom as possible but avoiding overfitting and dE/dz changing sign too many times, and report the results obtained under this choice. We use uniform priors in all cases.

We use the public code MABEL[4] [67], to run Monte Carlo Markov chains with the sampler ZEUS [68,69][5] to constrain the shape of the expansion rate in the late-time Universe ($z \leq 2.4$) and the quantity $r_d h$ with uncalibrated distance measurements from BAO and SNeIa measurements. Note that, with the data included in the analysis, h and r_d individually are completely unconstrained; only their product is constrained.

The new BAO and SNeIa data allow the constraints on the generic $E(z)$ to be extended up to $z = 2.4$, as shown in Fig. 2. The generic reconstruction yields an $E(z)$ which is consistent with the prediction of a ΛCDM model from *Planck* and BAO + SNeIa. Allowed deviations from *Planck*'s ΛCDM best fit are $\lesssim$3–4% at $z \lesssim 0.8$; this bound weakens slightly $\lesssim$10% at $0.8 \lesssim z \lesssim 2.4$, due to the degradation in the constraining power of SNeIa observations. While still being consistent with the ΛCDM prediction, the reconstructed posterior allows for a boost of the expansion rate (∼15% larger than *Planck*'s ΛCDM best fit) at $1.5 \lesssim z \lesssim 2.4$, this can be seen as an "excess wiggle" in the plot; however, it is not significant and we should remark that there are no measurements in that redshift range corresponding to the gap between the redshift covered by Supernovae data/eBOSS quasars and the Lyman-α forest data. Note also that those expansion histories showing an excess expansion rate at these redshifts need a lower $E(z)$ than ΛCDM at low redshifts. These results extend and improve previous constraints from agnostic reconstructions of $E(z)$ (see e.g., Ref. [29], where reported 68% confidence level limits of the deviations are 5% at $z \lesssim 0.6$ but grow significantly at higher redshift).

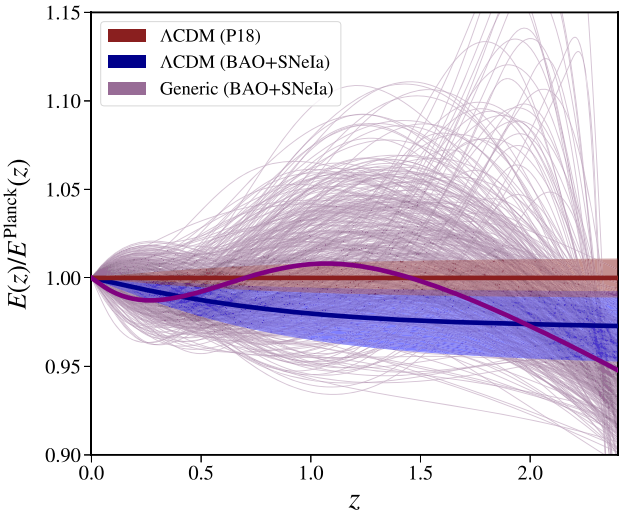

FIG. 2. Best fit evolution of the expansion rate with redshift (thick lines) normalized by *Planck*'s ΛCDM best fit $[E(z)/E^{\rm Planck}(z)]$ and 68% confidence level uncertainties (shaded regions, thin lines). *Planck*'s ΛCDM results are reported in red and BAO + SNeIa constraints assuming ΛCDM are in blue. In purple, the reconstruction from BAO + SNeIa assuming a generic expansion; thin lines are a sample of 500 flexknot splines reconstruction from the 68% cases with highest posterior.

Moreover, we find $\Omega_k = -0.02 \pm 0.10$ and $r_d h = 100.3 \pm 1.2$ Mpc which represent, respectively, a factor of 6 and factor of 2 improvement compared to the results reported in Ref. [71] [although the parametrization of $E(z)$ is different, so this comparison is more qualitative than strictly quantitative; the improvement is driven by the new data gathered over the past five years]. These constraints can be compared to those obtained also from BAO + SNeIa when assuming a flat ΛCDM model: $r_d h = 100.6 \pm 1.1$ Mpc and $\Omega_M = 0.297 \pm 0.013$. As can be seen, the generic reconstruction, despite having five extra model parameters, does not degrade the ΛCDM $r_d h$ constraints. Furthermore, it returns constraints on $r_d h$ comparable to *Planck* results assuming ΛCDM ($r_d h = 99.1 \pm 0.9$ Mpc), without relying on early-time physics or observations.

[3]Standard BAO analyses adopt a prior on r_d to break the $r_d h$ degeneracy and calibrate the distance measurements, following the approach known as inverse cosmic distance ladder. Not using that prior and marginalizing over r_d removes any dependence on prerecombination physics, since the BAO measurements are robust to modifications of the prerecombination physics of ΛCDM [61]. We use measurements from BAO-only analyses, following the eBOSS likelihoods and criterion to combine with BOSS measurements from [62].

[4]See Ref. [66].

[5]See Ref. [70].

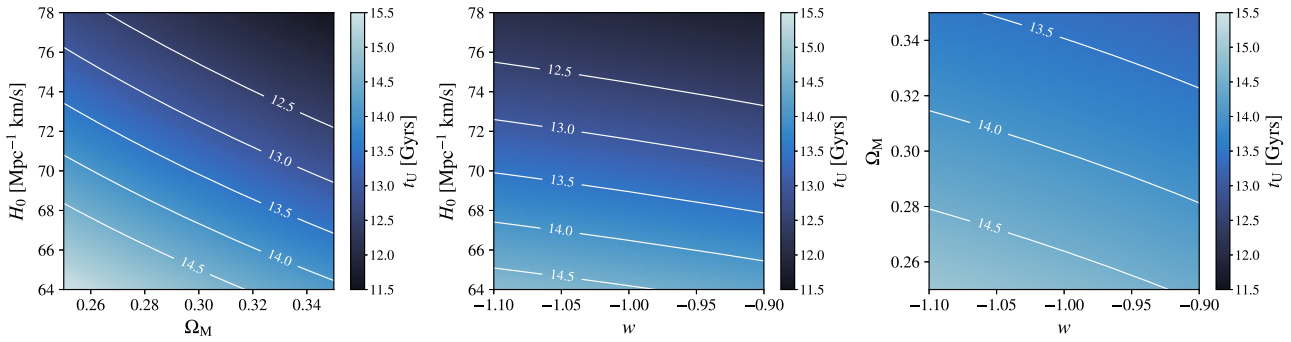

FIG. 3. Age of the Universe (in Gyr) as function of H_0 and Ω_M for $w = -1$ (left panel), H_0 and w for $\Omega_M = 0.3138$ (central panel), and Ω_M and w for $h = 0.6736$ (right panel). When a parameter is not varied, it is fixed to *Planck* ΛCDM best-fit value. White lines mark contours with constant value of t_U.

III. COSMIC AGES AND H_0

In addition to cosmic distances, the expansion rate of the Universe determines the lookback time. This opens up the possibility to use time (or age) measurements to weigh in on the H_0 tension. The cosmic chronometers method uses relative ages to determine $H(z)$, but ages can also be used in a complementary way. The lookback time t as function of redshift is given by

$$t(z) = \frac{977.8}{H_0}\int_0^z \frac{dz'}{(1+z')E(z')}\text{Gyr}, \tag{1}$$

with $H(z)$ in km s^{-1} Mpc^{-1}. Following Eq. (1), the age of the Universe is $t_U \equiv t(\infty)$. We show the dependence of t_U on H_0, Ω_M, and a constant equation of state parameter w for dark energy in a wCDM model in Fig. 3. It is evident that the strongest dependence is on H_0, while Ω_M and w have less influence.

The integral in Eq. (1) is dominated by contributions from redshifts below few tens, decreasing as z grows. Therefore, any exotic prerecombination physics does not significantly affect the age of the Universe. On the other hand, $E(z)$ is bound to be very close to that of a CMB-calibrated ΛCDM model at $z \lesssim 2.4$, as shown in the previous section. Hence, a precise and robust determination of t_U which does not significantly rely on a cosmological model, in combination with BAO and SNeIa, may weigh in on proposed solutions to the H_0 tension. If an independent (and model-agnostic) determination of t_U were to coincide with *Planck*'s inferred value assuming ΛCDM, ∼13.8 Gyrs, alternative models involving exotic physics relevant only in the early Universe would need to invoke additional modifications also of the late-Universe expansion history to reproduce all observations with a high value of H_0 as their prediction for t_U would be too low. This is because the value of the integral in Eq. (1) assuming standard physics after recombination cannot be too different from ΛCDM's prediction once BAO and SNeIa are considered, and then $t_U \propto H_0^{-1}$. As we will see below, current measurements of t_U are just precise enough to hint at this scenario.

Recently, a value of the age of Universe, $t_U = 13.5 \pm 0.15(\text{stat.}) \pm 0.23(\text{syst.})$ (± 0.27 when adding statistical and systematic uncertainties in quadrature) was inferred from a sample of old globular clusters (GCs) in Refs. [51,52].[6] This study involves a Bayesian analysis of the properties of 38 GCs, including their age, distance, metallicity, reddening, and abundance of α-enhanced elements. t_U is inferred from the age of the oldest of these GCs (marginalized over all other parameters and including systematic errors) estimating and correcting for the age of the Universe at the moment of GCs formation, and generously marginalizing over the small residual dependence on cosmology.

We can confront local H_0 measurements with the t_U inferred from GCs, since they are related by $H_0 t_U$, which can be obtained using Eq. (1) and a constraint on $E(z)$ for all the redshifts that contribute significantly to the integral. Redshifts below 2.4 [where the generic $E(z)$ reconstruction is available] only cover about 75% of the age of the Universe. If we assume that deviations from a ΛCDM expansion history are driven by the poorly known dark energy component, then $E(z)$ at $z > 2$ is effectively that of an Einstein de Sitter Universe. In this case the reconstructed $E(z)$ is perfectly consistent with ΛCDM and only relatively small deviations are allowed. If we consider more extreme deviations from ΛCDM, additional data probing the expansion history at higher redshifts would be needed to extend the constraints on the generic $E(z)$ to cover a larger fraction of t_U.

[6]This systematic uncertainty was determined using external metallicity spectroscopic measurements of the GCs. We refer the interested reader to Ref. [52] for more details and an alternative estimate based only on the color-magnitude diagrams of the globular clusters.

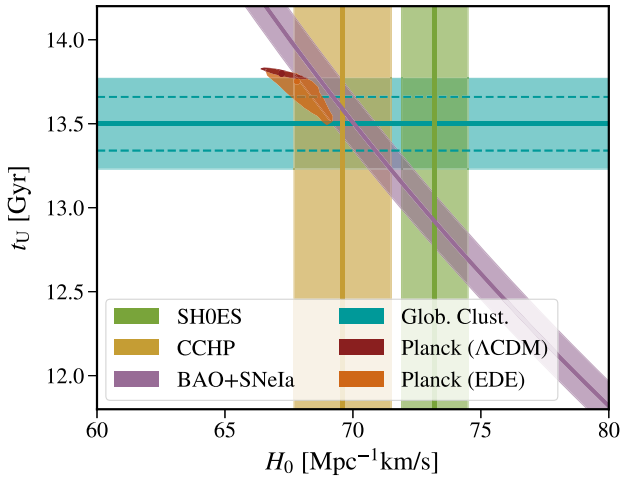

FIG. 4. 68% confidence level marginalized constraints in the H_0–t_U plane, from independent measurements, as indicated in the legend. Dashed cyan lines denote the size of the statistical 1σ errors from globular clusters, while the shaded region also includes systematic uncertainties. BAO + SNeIa constraints assume a ΛCDM cosmology. We show *Planck* results assuming ΛCDM (red) and EDE (orange).

Hence, we assume for this study a ΛCDM expansion rate $E(z)$, using the value of Ω_M inferred from BAO and SNeIa and its error.[7] Note that exotic models modifying only prerecombination cosmology do not affect directly the late-time $E(z)$ (which remains that of a ΛCDM model); hence, our inferred $H_0 t_U$ also applies to these models. As an example, we consider early dark energy (EDE) models. In particular, we use the EDE model posterior obtained in Refs. [72,73] for the *Planck* data; the model features three additional cosmological parameters compared to ΛCDM.

We show 68% confidence level marginalized constraints on the H_0–t_U plane from SH0ES, CCHP, GCs, BAO + SNeIa, and *Planck* in Fig. 4. We find $H_0 t_U = 945 \pm 11$ Gyr Mpc^{-1} km/s from BAO + SNeIa assuming ΛCDM, while $H_0 t_U = 928 \pm 7$ and 932 ± 7 Gyr Mpc^{-1} km/s from *Planck* assuming ΛCDM and EDE, respectively. As a reference, combining BAO + SNeIa with SH0ES and TRGB returns $t_U = 12.93 \pm 0.29$ and $t_U = 13.62 \pm 0.42$ Gyr, respectively, while *Planck*'s inferred values are 13.80 ± 0.02 Gyr (ΛCDM) and $13.76^{+0.06}_{-0.16}$ Gyr (EDE).

These results show that for SH0ES to be compatible with BAO + SNeIa the Universe must be significantly younger than inferred by *Planck*, no matter whether ΛCDM or EDE are assumed; this statement is robust to early-time physics assumptions. The age of the Universe inferred from GCs weakly favors older Universes than SH0ES combined with BAO + SNeIa, but the current systematic error budget is too large to firmly distinguish. There are ongoing efforts to reduce the impact of systematic errors (see e.g., [52]), so that GCs constraints on t_U have the potential to discriminate among different scenarios proposed to solve the H_0 tension (statistical errors are indicated with dashed lines).

[7]The expected effect of adopting the reconstructed $E(z)$ where available and a ΛCDM one at higher z is a possible increase of the error bars on $t_U H_0$ of $\lesssim 10\%$.

IV. THE NEW COSMIC TRIANGLES

The H_0 tension was reframed as a consistency test between r_d (an early-time quantity) and H_0 (a late-time quantity), which can be done using a model-agnostic approach, in Ref [29]. Similarly, assuming a cosmological model, allows for a similar consistency test between Ω_M and H_0 to be performed, as proposed in Ref. [74]. With the updated constraints on $E(z)$, $r_d h$, and Ω_M obtained in Sec. II, we can revisit these consistency checks. Moreover, the H_0, t_U, and $H_0 t_U$ constraints obtained with the Ω_M values inferred from BAO + SNeIa, adds a third consistency test related with H_0.

These three cases are three triads of two cosmological quantities and their product determined independently. These triads are $\{t_U, H_0, H_0 t_U\}$, $\{r_d, h, r_d h\}$, $\{\Omega_M, h^2, \Omega_M h^2\}$. Within a given cosmological model (although some of the constraints can be obtained model independently), and in the absence of systematic errors, a generic triad $\{a, b, ab\}$ of parameters determined by independent experiments i, j, and k, respectively, is an overconstrained system which must fulfill $a_i \times b_j = (ab)_k$ within statistical uncertainty. This is what makes these triads a powerful diagnostic tool of consistency, especially in the context of the H_0 tension. Therefore, the cosmological model(s) yielding agreement of all these triads are favored by the data.

Cosmology faced a similar situation in 1999, when information from CMB anisotropies, SNeIa, and clusters observations was combined to determine whether the Universe is flat and if there was evidence for a nonzero cosmological constant [53]. In that case, the triad was $\{\Omega_M, \Omega_k, \Omega_\Lambda\}$, where $\Omega_\Lambda = 1 - \Omega_M - \Omega_k$ is the density parameter associated to the cosmological constant today.

These triads may be represented in a plane (as done e.g., in Fig. 4), but due to the relation between their components, they can be more efficiently represented in a ternary plot. Taking the logarithm of each quantity in the triads of the form $\{a, b, ab\}$ [which fulfills $\log_{10}(a) + \log_{10}(b) - \log_{10}(ab) = 0$], we can build ternary plots; every point on these ternary plots sums up to 0. This representation provides an intuitive and illustrative simultaneous look at independent cosmological constraints. We use them to illustrate the state of the H_0 tension in each of the three complementary frames that have been discussed. We refer to these ternary plots as the new cosmic triangles.

Each of the triads discussed in this work involves quantities directly related to H_0 and provides different angles to study the H_0 tension: in terms of times, distances, and the

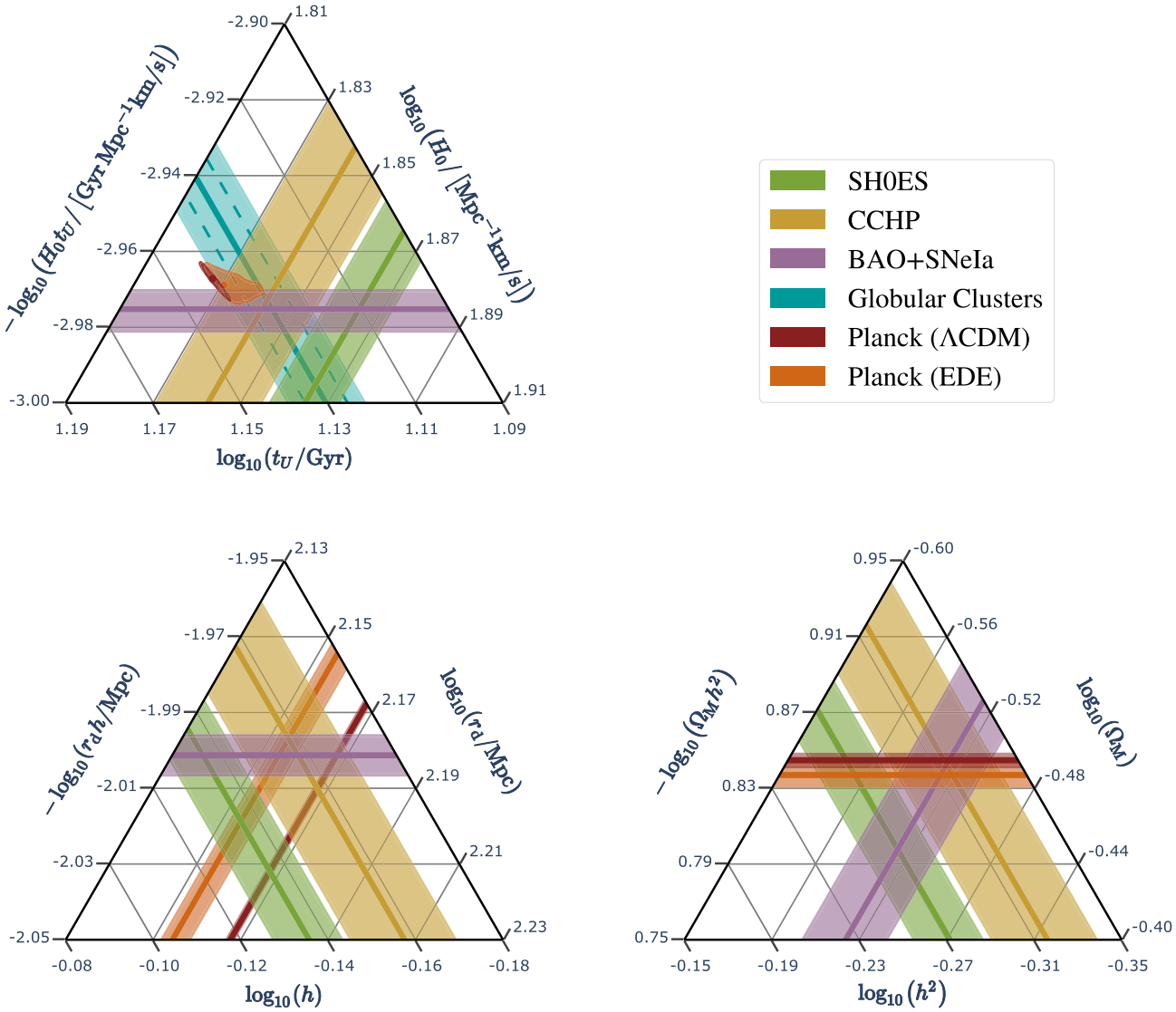

FIG. 5. 68% confidence level marginalized constraints on the new cosmic triangles: we show the triad corresponding to the age of the Universe and the Hubble constant (upper left), to the sound horizon at radiation drag and the reduced Hubble constant (bottom left), and to the total matter density parameter today and the square of the reduced Hubble constant (bottom right). Note that all points in each figure sum up to 0, while the ticks in the axes determine the direction of equal values for each axis.

abundance of matter. In interpreting the observational constraints, we can distinguish between early-time, late-time, and local observations, which in turn may depend on early-time (prerecombination), late-time (low redshift), or fully local physics. In all cases, we can use BAO + SNeIa results to link local and early-Universe measurements. Note that the triad corresponding to h and r_d is the only one that is agnostic with respect to the choice of a cosmological model for the low-redshift expansion history.[8]

We show the new cosmic triangles in Fig. 5; the interpretation of the ternary plots can be eased by comparing this figure with Fig. 4. Each side of the triangle corresponds to the logarithm of one of the quantities involved, or their product, and the direction of the ticks in the axes determine the lines of equal value for each quantity. All the constraints shown in these plots (with the exception of the contours corresponding to *Planck* in the upper panel) are bands that refer only to the axis with aligned ticks. The preferred region in the parameter space will be the one with constraints from where the three axes overlap. On the other hand, if there is no point in which the constraints referring to all three axes overlap, the measurements are in tension. We can appreciate the tension within

[8] r_d inferred values from *Planck* are largely independent of standard postrecombination physics, as we can see comparing results from standard analyses [1] with those using only early-Universe information [71].

ΛCDM in the triangles corresponding to $r_d h$ and $\Omega_M h^2$. As expected, considering the region favored by BAO + SNeIa, *Planck* constraints obtained within ΛCDM are consistent with CCHP, but show some tension with SH0ES. The tensions are always smaller in the case of EDE, but not enough for this model to be preferred over ΛCDM.

Figure 5 clearly shows the synergies of considering the three triads at the same time. The most studied so far has been the one involving r_d and h, since it was argued that the most promising way to solve the H_0 tension was to reduce the value r_d while keeping a standard evolution of the low-redshift expansion rate [29,32]. We can also see that this triangle is the one showing the largest tension between *Planck* assuming ΛCDM, SH0ES, and BAO + SNeIa, and the one for which models like EDE show promise. The triangle including Ω_M shows a smaller tension: combining BAO + SNeIa with SH0ES (CCHP) we find $\Omega_M = 0.159 \pm 0.009$ ($\Omega_M = 0.144 \pm 0.01$), which is in 1.8σ (0.1σ) tension with *Planck*'s constraint assuming ΛCDM. The tension reduces to 1.5σ when compared to the *Planck* results assuming EDE. Since BAO + SNeIa constrain $E(z)$ at low redshift to be very similar to (and fully consistent with) the best fit of *Planck* assuming ΛCDM, this tension is fully sourced by the H_0 tension, no matter the cosmological model under consideration.

However, the situation for the triad involving the age of the Universe is different. As argued above, modifications of the early-Universe cosmology do not directly change the age of the Universe. This is why *Planck* EDE posteriors overlap with those assuming ΛCDM (extending along the direction of constant Ω_M, i.e., the constraint on $H_0 t_U$ from BAO + SNeIa). In this representation, the region of overlap of *Planck*, BAO + SNeIa, and GCs posteriors is in large tension with SH0ES. However, current determinations of t_U alone are not precise enough to definitively disfavor the combination of SH0ES with BAO + SNeIa.

Finally, Fig. 5 clearly indicates that if GCs were to still return a high value of t_U but with reduced error-bars, deviations from ΛCDM that only affect prerecombination physics will not be enough to reconcile all the measurements. If this will turn out to be the case, a combination of both high and low redshift modifications to the ΛCDM model may be required to solve the H_0 tension. Alternatively one would have to look into much more local effects, such as those affecting the distance ladder calibration and in particular effects or processes which may be responsible for the mismatch between CCHP and SH0ES.

V. CONCLUSIONS

The discrepancies between model-independent measurements and model-dependent inferred values of H_0 from different experiments (each of them sensitive to different physics and systematic errors) might be a hint for the need of modifying the standard ΛCDM model. The most promising deviations from ΛCDM proposed to solve such tensions involve a boost in the expansion rate before recombination, as to lower the value of r_d and reconcile the direct and the inverse distance ladder. However, we argue in this work, there is a more varied phenomenology, that goes well beyond r_d, to be matched by any new physics put forward to solve the H_0 tension, especially regarding cosmic ages: the trouble goes beyond H_0.

We update agnostic reconstructions of the evolution of the expansion rate of the late-time Universe with recent BAO and SNeIa measurements, extending the reconstruction up to $z \sim 2.4$. We find that BAO and SNeIa constrain the evolution of $H(z)$ to be fully consistent with the one from ΛCDM *Planck*'s best-fit prediction: any possible deviation must be well below the 5%(10%) level at $z < 0.8$ ($z < 2.4$). This further supports previous claims that modifications of the expansion rate at low redshifts are disfavored by the data (see e.g., [29,30,32]). In the coming years, line-intensity mapping [75–79], quasar observations [80,81], and strong lensing systems [67] will probe significantly higher redshifts, allowing for agnostic analyses like this one to be extended up to $z \sim 10$–20 (covering effectively $> 90\%$ of the Universe's history).

We discuss the impact of a recent, almost cosmology-independent, inference of the age of the Universe from the age of the oldest globular clusters. While the relation between H_0 and r_d can be addressed with modifications of the early-time physics, t_U is dominated by the expansion rate at $z \lesssim 30$, hence insensitive to high-redshift cosmology. The t_U determination is also insensitive to effects such as cosmological dimming (e.g., violations of the Etherington relation), cosmological screening, deviations from general relativity at large scales affecting growth of structures, and any phenomenology affecting cosmological distance measures. Therefore, if a high t_U were to be measured reliably and with small enough error bars, it would disfavor models with high H_0 and standard low-redshift physics. In this case then both, pre- and post-recombination modifications to ΛCDM, may be required to reconcile all measurements. Alternatively one would have to invoke much more local effects (be these cosmological, see e.g., [82–85], or astrophysical, in particular effects or processes which may be responsible for the mismatch between CCHP and SH0ES) affecting the local H_0 determination only, while leaving all other cosmological observations unchanged.

In such case, viable solutions to the H_0 trouble will fall in either of two classes of very different nature: local and global. Global solutions, would have to invoke new physics beyond ΛCDM which affect the entire Universe history from before recombination all the way to the low-redshift, late-time Universe. Modifying only early-time physics will not be enough. Because of their global nature,

such solutions affect quantities well beyond H_0, but would be highly constrained by the wealth of high-precision cosmological observations available. Local solutions on the other hand, leave unaffected the global properties of cosmology; as such either do not require new physics beyond ΛCDM (and thus fall in the realm of astrophysics), or include new physics which only affect very local observations.

A program to improve the inference of t_U and reduce the systematic uncertainties, may give this measurement enough power to discriminate between these two different kinds of viable solutions for the H_0 tension.

Finally we identify three triads of independently measured quantities, relating H_0 with t_U, r_d, Ω_M, respectively. Each of these triads is an overconstrained system, hence we propose the use of ternary figures (the new cosmic triangles) to report and visualize the constraints. These new cosmic triangles allow for a simultaneous and easy-to-interpret visual representation of constraints on different yet related quantities. We hope that this representation will help to guide further efforts to find a solution to the trouble of (and beyond) H_0.

ACKNOWLEDGMENTS

The authors thank Tristan L. Smith, Vivian Poulin, and Geoff C.-F. Chen for comments on last versions of this manuscript. J. L. B. is supported by the Allan C. and Dorothy H. Davis Fellowship. This work is supported in part by MINECO Grant No. PGC2018-098866-B-I00 FEDER, UE. L. V. acknowledges support by European Union's Horizon 2020 research and innovation program ERC (BePreSySe, Grant Agreement 725327). ICC researchers acknowledge "Center of Excellence Maria de Maeztu" award to the ICCUB (CEX2019-000918-M). This work was supported at Johns Hopkins by NSF Grant No. 1818899 and the Simons Foundation. The work of B. D. W. is supported by the Labex ILP (reference ANR-10-LABX-63) part of the Idex SUPER, received financial state aid managed by the Agence Nationale de la Recherche, as part of the programme Investissements d'avenir under the reference ANR-11-IDEX-0004-02; and by the ANR BIG4 project, Grant No. ANR-16-CE23-0002 of the French Agence Nationale de la Recherche. The Center for Computational Astrophysics is supported by the Simons Foundation.

[1] N. Aghanim *et al.* (Planck Collaboration), Planck 2018 results. VI. Cosmological parameters, Astron. Astrophys. **641**, A6 (2020).
[2] J. W. Henning *et al.*, Measurements of the temperature and E-mode polarization of the CMB from 500 square degrees of SPTpol data, Astrophys. J. **852**, 97 (2018).
[3] S. Aiola, E. Calabrese, L. Maurin, S. Naess, B. L. Schmitt *et al.*, The atacama cosmology telescope: DR4 maps and cosmological parameters, arXiv:2007.07288.
[4] D. M. Scolnic, D. O. Jones, A. Rest, Y. C. Pan *et al.*, The complete light-curve sample of spectroscopically confirmed SNe Ia from pan-STARRS1 and cosmological constraints from the combined pantheon sample, Astrophys. J. **859**, 101 (2018).
[5] S. Alam and *et al.* (SDSS-III BOSS Collaboration), The clustering of galaxies in the completed SDSS-III baryon oscillation spectroscopic survey: Cosmological analysis of the DR12 galaxy sample, Mon. Not. R. Astron. Soc. **470**, 2617 (2017).
[6] T. M. C. Abbott, F. B. Abdalla, A. Alarcon, J. Aleksić, S. Allam, S. Allen *et al.*, Dark Energy Survey year 1 results: Cosmological constraints from galaxy clustering and weak lensing, Phys. Rev. D **98**, 043526 (2018).
[7] C. Heymans, T. Tröster, M. Asgari, C. Blake, H. Hildebrandt, B. Joachimi *et al.*, KiDS-1000 Cosmology: Multi-probe weak gravitational lensing and spectroscopic galaxy clustering constraints, arXiv:2007.15632.
[8] S. Alam *et al.* (eBOSS Collaboration), The completed SDSS-IV extended baryon oscillation spectroscopic survey: Cosmological implications from two decades of spectroscopic surveys at the apache point observatory, Phys. Rev. D **103**, 083533 (2021).
[9] L. Verde, P. Protopapas, and R. Jimenez, Planck and the local Universe: Quantifying the tension, Phys. Dark Universe **2**, 166 (2013).
[10] L. Verde, T. Treu, and A. G. Riess, Tensions between the early and late Universe, Nat. Astron. **3**, 891 (2019).
[11] G. E. Addison, D. J. Watts, C. L. Bennett, M. Halpern, G. Hinshaw, and J. L. Weiland, Elucidating ΛCDM: Impact of baryon acoustic oscillation measurements on the Hubble constant discrepancy, Astrophys. J. **853**, 119 (2018).
[12] N. Schöneberg, J. Lesgourgues, and D. C. Hooper, The BAO + BBN take on the Hubble tension, J. Cosmol. Astropart. Phys. 10 (2019) 029.
[13] G. C. F. Chen, C. D. Fassnacht, S. H. Suyu, C. E. Rusu, J. H. H. Chan, K. C. Wong *et al.*, A SHARP view of H0LiCOW: H_0 from three time-delay gravitational lens systems with adaptive optics imaging, Mon. Not. R. Astron. Soc. **490**, 1743 (2019).
[14] K. C. Wong, S. H. Suyu, G. C. F. Chen, C. E. Rusu, M. Millon, D. Sluse *et al.*, H0LiCOW—XIII. A 2.4 per cent measurement of H_0 from lensed quasars: 5.3σ tension between early- and late-Universe probes, Mon. Not. R. Astron. Soc. **498**, 1420 (2020).
[15] A. J. Shajib, S. Birrer, T. Treu, A. Agnello, E. J. Buckley-Geer, J. H. H. Chan *et al.*, STRIDES: A 3.9 per cent measurement of the Hubble constant from the strong lens system DES J0408-5354, Mon. Not. R. Astron. Soc. **494**, 6072 (2020).

[16] M. Millon, A. Galan, F. Courbin, T. Treu, S. H. Suyu, X. Ding *et al.*, TDCOSMO. I. An exploration of systematic uncertainties in the inference of H_0 from time-delay cosmography, Astron. Astrophys. **639**, A101 (2020).

[17] S. Birrer, A. J. Shajib, A. Galan, M. Millon, T. Treu *et al.*, TDCOSMO IV: Hierarchical time-delay cosmography—joint inference of the Hubble constant and galaxy density profiles, arXiv:2007.02941.

[18] G. C. F. Chen, C. D. Fassnacht, S. H. Suyu, A. Yıldırım, E. Komatsu, and J. L. Bernal, TDCOSMO VI: Distance measurements in time-delay cosmography under the mass-sheet transformation, arXiv:2011.06002.

[19] R. Jimenez and A. Loeb, Constraining cosmological parameters based on relative galaxy ages, Astrophys. J. **573**, 37 (2002).

[20] B. S. Haridasu, V. V. Luković, M. Moresco, and N. Vittorio, An improved model-independent assessment of the late-time cosmic expansion, J. Cosmol. Astropart. Phys. 10 (2018) 015.

[21] A. G. Riess, S. Casertano, W. Yuan, L. M. Macri, and D. Scolnic, Large magellanic cloud cepheid standards provide a 1% foundation for the determination of the Hubble constant and stronger evidence for physics beyond ΛCDM, Astrophys. J. **876**, 85 (2019).

[22] W. L. Freedman, B. F. Madore, T. Hoyt, I. S. Jang, R. Beaton, M. G. Lee, A. Monson, J. Neeley, and J. Rich, Calibration of the tip of the red giant branch, Astrophys. J. **891**, 57 (2020).

[23] E. J. Baxter and B. D. Sherwin, Determining the Hubble constant without the sound horizon scale: Measurements from CMB lensing, Mon. Not. R. Astron. Soc. **501**, 1823 (2020).

[24] O. H. E. Philcox, B. D. Sherwin, G. S. Farren, and E. J. Baxter, Determining the Hubble constant without the sound horizon: Measurements from galaxy surveys, Phys. Rev. D **103**, 023538 (2021).

[25] A. G. Riess, S. Casertano, W. Yuan, J. B. Bowers, L. Macri, J. C. Zinn, and D. Scolnic, Cosmic distances calibrated to 1% precision with Gaia EDR3 parallaxes and Hubble space telescope photometry of 75 Milky Way cepheids confirm tension with LambdaCDM, Astrophys. J. Lett. **908**, L6 (2021).

[26] W. Yuan, A. G. Riess, L. M. Macri, S. Casertano, and D. M. Scolnic, Consistent calibration of the tip of the red giant branch in the large magellanic cloud on the hubble space telescope photometric system and a redetermination of the Hubble constant, Astrophys. J. **886**, 61 (2019).

[27] M. J. Reid, D. W. Pesce, and A. G. Riess, An improved distance to NGC 4258 and its implications for the Hubble constant, Astrophys. J. Lett. **886**, L27 (2019).

[28] D. M. Nataf, S. Cassisi, L. Casagrande, and A. G. Riess, On the color-metallicity relation of the red clump and the reddening toward the magellanic clouds, Astrophys. J. **910**, 121 (2021).

[29] J. L. Bernal, L. Verde, and A. G. Riess, The trouble with H_0, J. Cosmol. Astropart. Phys. 10 (2016) 019.

[30] V. Poulin, K. K. Boddy, S. Bird, and M. Kamionkowski, Implications of an extended dark energy cosmology with massive neutrinos for cosmological tensions, Phys. Rev. D **97**, 123504 (2018).

[31] K. Aylor, M. Joy, L. Knox, M. Millea, S. Raghunathan, and W. L. Kimmy Wu, Sounds discordant: Classical distance ladder and ΛCDM-based determinations of the cosmological sound horizon, Astrophys. J. **874**, 4 (2019).

[32] L. Knox and M. Millea, Hubble constant hunter's guide, Phys. Rev. D **101**, 043533 (2020).

[33] T. Karwal and M. Kamionkowski, Dark energy at early times, the Hubble parameter, and the string axiverse, Phys. Rev. D **94**, 103523 (2016).

[34] V. Poulin, T. L. Smith, T. Karwal, and M. Kamionkowski, Early Dark Energy can Resolve the Hubble Tension, Phys. Rev. Lett. **122**, 221301 (2019).

[35] T. L. Smith, V. Poulin, and M. A. Amin, Oscillating scalar fields and the Hubble tension: A resolution with novel signatures, Phys. Rev. D **101**, 063523 (2020).

[36] M.-X. Lin, G. Benevento, W. Hu, and M. Raveri, Acoustic dark energy: Potential conversion of the Hubble tension, Phys. Rev. D **100**, 063542 (2019).

[37] P. Agrawal, F.-Y. Cyr-Racine, D. Pinner, and L. Randall, Rock 'n' roll solutions to the Hubble tension, arXiv:1904.01016.

[38] K. V. Berghaus and T. Karwal, Thermal friction as a solution to the Hubble tension, Phys. Rev. D **101**, 083537 (2020).

[39] J. Sakstein and M. Trodden, Early Dark Energy from Massive Neutrinos as a Natural Resolution of the Hubble Tension, Phys. Rev. Lett. **124**, 161301 (2020).

[40] F. Niedermann and M. S. Sloth, New early dark energy, Phys. Rev. D **103**, L041303 (2021).

[41] M. Zumalacárregui, Gravity in the era of equality: Towards solutions to the Hubble problem without fine-tuned initial conditions, Phys. Rev. D **102**, 023523 (2020).

[42] M. Braglia, M. Ballardini, W. T. Emond, F. Finelli, A. E. Gümrükçüoğlu, K. Koyama, and D. Paoletti, Larger value for H_0 by an evolving gravitational constant, Phys. Rev. D **102**, 023529 (2020).

[43] M. Ballardini, M. Braglia, F. Finelli, D. Paoletti, A. A. Starobinsky, and C. Umiltà, Scalar-tensor theories of gravity, neutrino physics, and the H_0 tension, J. Cosmol. Astropart. Phys. 10 (2020) 044.

[44] M. Braglia, W. T. Emond, F. Finelli, A. E. Gumrukcuoglu, and K. Koyama, Unified framework for early dark energy from α-attractors, Phys. Rev. D **102**, 083513 (2020).

[45] G. Ballesteros, A. Notari, and F. Rompineve, The H_0 tension: ΔG_N vs $\Delta N_{\rm eff}$, J. Cosmol. Astropart. Phys. 11 (2020) 024.

[46] F. Niedermann and M. S. Sloth, Resolving the Hubble tension with new early dark energy, Phys. Rev. D **102**, 063527 (2020).

[47] M. Braglia, M. Ballardini, F. Finelli, and K. Koyama, Early modified gravity in light of the H_0 tension and LSS data, Phys. Rev. D **103**, 043528 (2021).

[48] T. Abadi and E. D. Kovetz, Can conformally invariant modified gravity solve the Hubble tension? Phys. Rev. D **103**, 023530 (2021).

[49] A. Jaffe, H 0 and odds on cosmology, Astrophys. J. **471**, 24 (1996).

[50] R. Jimenez, A. Cimatti, L. Verde, M. Moresco, and B. Wandelt, The local and distant Universe: Stellar ages and H_0, J. Cosmol. Astropart. Phys. 03 (2019) 043.

[51] D. Valcin, J. L. Bernal, R. Jimenez, L. Verde, and B. D. Wandelt, Inferring the age of the universe with globular clusters, J. Cosmol. Astropart. Phys. 12 (2020) 002.
[52] D. Valcin, R. Jimenez, L. Verde, J. L. Bernal, and B. D. Wandelt, The age of the universe with globular clusters: Reducing systematic uncertainties, arXiv:2102.04486.
[53] N. A. Bahcall, J. P. Ostriker, S. Perlmutter, and P. J. Steinhardt, The cosmic triangle: Revealing the state of the universe, Science **284**, 1481 (1999).
[54] F. Beutler, C. Blake, M. Colless, D. H. Jones, L. Staveley-Smith, L. Campbell, Q. Parker, W. Saunders, and F. Watson, The 6dF galaxy survey: Baryon acoustic oscillations and the local Hubble constant, Mon. Not. R. Astron. Soc. **416**, 3017 (2011).
[55] A. J. Ross, L. Samushia, C. Howlett, W. J. Percival, A. Burden, and M. Manera, The clustering of the SDSS DR7 main Galaxy sample—I. A 4 per cent distance measure at $z = 0.15$, Mon. Not. R. Astron. Soc. **449**, 835 (2015).
[56] H. Gil-Marín, J. E. Bautista, R. Paviot, M. Vargas-Magaña, S. de la Torre, S. Fromenteau *et al.*, The completed SDSS-IV extended baryon oscillation spectroscopic survey: Measurement of the BAO and growth rate of structure of the luminous red galaxy sample from the anisotropic power spectrum between redshifts 0.6 and 1.0, Mon. Not. R. Astron. Soc. **498**, 2492 (2020).
[57] A. Raichoor, A. de Mattia, A. J. Ross, C. Zhao, S. Alam, S. Avila *et al.*, The completed SDSS-IV extended baryon oscillation spectroscopic survey: Large-scale structure catalogues and measurement of the isotropic BAO between redshift 0.6 and 1.1 for the emission line galaxy sample, Mon. Not. R. Astron. Soc. **500**, 3254 (2020).
[58] J. Hou, A. G. Sánchez, A. J. Ross, A. Smith, R. Neveux, J. Bautista *et al.*, The completed SDSS-IV extended baryon oscillation spectroscopic survey: BAO and RSD measurements from anisotropic clustering analysis of the Quasar Sample in configuration space between redshift 0.8 and 2.2, Mon. Not. R. Astron. Soc. **500**, 1201 (2021).
[59] R. Neveux, E. Burtin, A. de Mattia, A. Smith, A. J. Ross, J. Hou *et al.*, The completed SDSS-IV extended baryon oscillation spectroscopic survey: BAO and RSD measurements from the anisotropic power spectrum of the Quasar sample between redshift 0.8 and 2.2, Mon. Not. R. Astron. Soc. **499**, 210 (2020).
[60] H. du Mas des Bourboux, J. Rich, A. Font-Ribera, V. de Sainte Agathe, J. Farr, T. Etourneau *et al.*, The completed SDSS-IV extended baryon oscillation spectroscopic survey: Baryon acoustic oscillations with Lyman-α forests, Astrophys. J. **901**, 153 (2020).
[61] J. L. Bernal, T. L. Smith, K. K. Boddy, and M. Kamionkowski, Robustness of baryon acoustic oscillations constraints to beyond-ΛCDM cosmologies, Phys. Rev. D **102**, 123515 (2020).
[62] https://svn.sdss.org/public/data/eboss/DR16cosmo/tags/v1_0_0/likelihoods/BAO-only/.
[63] P. Carter, F. Beutler, W. J. Percival, J. DeRose, R. H. Wechsler, and C. Zhao, The impact of the fiducial cosmology assumption on BAO distance scale measurements, Mon. Not. R. Astron. Soc. **494**, 2076 (2020).
[64] J. A. Vázquez, M. Bridges, M. P. Hobson, and A. N. Lasenby, Model selection applied to reconstruction of the primordial power spectrum, J. Cosmol. Astropart. Phys. 06 (2012) 006.
[65] M. Millea and F. Bouchet, Cosmic microwave background constraints in light of priors over reionization histories, Astron. Astrophys. **617**, A96 (2018).
[66] https://github.com/jl-bernal/MABEL.
[67] G. C.-F. Chen and J. L. Bernal (to be published).
[68] M. Karamanis and F. Beutler, zeus: A Python implementation of the ensemble slice sampling method (to be published).
[69] M. Karamanis and F. Beutler, Ensemble slice sampling, arXiv:2002.06212.
[70] https://zeus-mcmc.readthedocs.io/.
[71] L. Verde, J. L. Bernal, A. F. Heavens, and R. Jimenez, The length of the low-redshift standard ruler, Mon. Not. R. Astron. Soc. **467**, 731 (2017).
[72] R. Murgia, G. F. Abellán, and V. Poulin, The early dark energy resolution to the Hubble tension in light of weak lensing surveys and lensing anomalies, Phys. Rev. D **103**, 063502 (2021).
[73] T. L. Smith, V. Poulin, J. L. Bernal, K. K. Boddy, M. Kamionkowski, and R. Murgia, Early dark energy is not excluded by current large-scale structure data, arXiv:2009.10740.
[74] W. Lin, K. J. Mack, and L. Hou, Investigating the Hubble constant tension: Two numbers in the standard cosmological model, Astrophys. J. Lett. **904**, L22 (2020).
[75] K. S. Karkare and S. Bird, Constraining the expansion history and early dark energy with line intensity mapping, Phys. Rev. D **98**, 043529 (2018).
[76] J. B. Muñoz, A Standard Ruler at Cosmic Dawn, Phys. Rev. Lett. **123**, 131301 (2019).
[77] J. L. Bernal, P. C. Breysse, H. Gil-Marín, and E. D. Kovetz, User's guide to extracting cosmological information from line-intensity maps, Phys. Rev. D **100**, 123522 (2019).
[78] J. L. Bernal, P. C. Breysse, and E. D. Kovetz, Cosmic Expansion History from Line-Intensity Mapping, Phys. Rev. Lett. **123**, 251301 (2019).
[79] M. B. Silva, E. D. Kovetz, G. K. Keating, A. Moradinezhad Dizgah, M. Bethermin, P. Breysse *et al.*, Mapping large-scale-structure evolution over cosmic times, arXiv:1908.07533.
[80] G. Risaliti and E. Lusso, A Hubble diagram for quasars, Astrophys. J. **815**, 33 (2015).
[81] G. Risaliti and E. Lusso, Cosmological constraints from the Hubble diagram of quasars at high redshifts, Nat. Astron. **3**, 272 (2019).
[82] H. Desmond, B. Jain, and J. Sakstein, Local resolution of the Hubble tension: The impact of screened fifth forces on the cosmic distance ladder, Phys. Rev. D **100**, 043537 (2019).
[83] H. Desmond, B. Jain, and J. Sakstein, Erratum: Local resolution of the Hubble tension: The impact of screened fifth forces on the cosmic distance ladder [Phys. Rev. D **100**, 043537 (2019)], Phys. Rev. D **101**, 069904 (2020).
[84] H. Desmond, B. Jain, and J. Sakstein, Erratum: Local resolution of the Hubble tension: The impact of screened fifth forces on the cosmic distance ladder [Phys. Rev. D **100**, 043537 (2019)], Phys. Rev. D **101**, 129901 (2020).
[85] H. Desmond and J. Sakstein, Screened fifth forces lower the TRGB-calibrated Hubble constant too, Phys. Rev. D **102**, 023007 (2020).

Chapter 4

Conclusion

The objective of this thesis was to demonstrate "How cosmology can help and benefit from other areas of physics" and I hope that after the presentation of the work carried out during the doctorate, the reader will be a little more convinced.

4.1 Non linear bias and neutrino mass

In the first part of this thesis I devoted myself to the study of the clustering of dark matter in the presence of massive neutrinos. The goal of the project was to measure the extent to which massive neutrinos impact the bias of dark matter halos and to find an easy way to implement the corrections for future analyzes. At the beginning the idea was simply to use a phenomenological model in order to calibrate the bias of halos produced by numerical simulations but the discovery of the `FAST-PT` (McEwen et al., 2016) software pushed us to extend our methodology to perturbation theory. This project gave rise to very interesting results such as the fact that it was possible to rescale the amplitude of the power spectrum as a function of the mass of neutrinos or that the prescriptions that we have proposed, using perturbation theory, still held in non-linear scales.

It also enabled the creation of an emulator `BE-HaPPy`. There are a few bias emulators in the literature (Tinker et al., 2010; McClintock et al., 2019; Muñoz and Dvorkin, 2018) but either they often rely on analytical formulas which tend to break at non-linear scales or they don't really take into account the impact of massive neutrinos. The innovation of `BE-HaPPy` is that the bias calibration has been carried out up to non-linear scales on simulations with and without massive neutrinos. In addition, the fact that most of the perturbative terms and the rescaling coefficients are calculated beforehand makes the code less computationally expensive.

As seen in Chapter 2, the power suppression caused by neutrinos mostly affects small scales. However in the past, the modeling of the power spectrum at these scales was not precise enough for the fact of neglecting massive neutrinos to have a real impact. In this new era of precision cosmology, incorrect processing of neutrinos can lead to a systematic shift in the inference of cosmological parameters (Raccanelli, Verde, and Villaescusa-Navarro, 2019). A good treatment of the power spectrum at non-linear scales increases the chances of obtaining good constraints on the cosmological model and therefore on the mass of neutrinos. It's a win-win situation.

4.2 Age of the universe and H_0 tension

The second part of my thesis was devoted to the study of globular clusters. As seen in the previous section, these objects are very valuable for astronomy but also for cosmology. Not being an astronomer by training, I was able to approach the analysis of globular clusters with a fresh pair of eyes. However, it is difficult to navigate between astronomy and cosmology because at the same time I wanted the cosmological community to understand the value of my research so I didn't want to make things too technical and at the same time I wanted to provide quality work with a solid theoretical and experimental basis so that my work was acknowledged by astronomers.

Usually the determination of the characteristics of globular clusters is done by methods such as main sequence fitting where the calibration is performed by measuring the difference in luminosity at the main sequence turn-off point between apparent and absolute magnitude. The introduction of a Bayesian method in the analysis of our sample gave us a greater freedom in the choice of independent parameters, whether it was the quantity or the different priors. The choice to use the full shape of the color magnitude diagram also made it possible to reduce the degeneracies between the different parameters. With this new methodology we obtained the most precise estimate of the age of the universe ever using globular clusters. If we compare our final result ($t_{\rm U} = 13.5^{+0.16}_{-0.14}(\text{stat.}) \pm 0.23(0.33)(\text{sys.})$ at 68% confidence level) with recent estimates (Chaboyer et al. 2017 using 9 clusters and O'Malley, Gilligan, and Chaboyer 2017 using 22 GCs), we see that the errors have been reduced by $\simeq 2$. As our results in Valcin et al. 2020 were dominated by systematic errors, the next step was to find a way to reduce them. Systematic errors come from uncertainties in the treatment of the physics which governs the evolution of stars but also from the calibration mismatch between the stellar model and the data. As it would have been time consuming to deal with each and everyone of them, we focused on the mixing length theory which allowed us to reduce the systematic error by half.

Once put in the context of the H_0 tension, our estimate of the age of the universe can provide new perspectives and ultimately help constrain the value of H_0. It is a very good example of interplay between different areas of physics where we applied principles more familiar to cosmology to an open problem of astronomy and in return we obtained an estimate of the age of globular clusters and by extension of the universe (assuming a time of galaxy formation), almost independent of a cosmological model.

4.3 Prospects

In this section I chose to classify the prospects from the different publications into two categories according to the two different aspects of my work. One specific to cosmology itself and the other more technical, specific to computational methods.

4.3.1 Cosmology oriented prospects

Extension of `BE-HaPPy`

Although very useful, emulators are often overlooked in favor of analytical formulas. This can be explained by the fact that the analytical formulas are more versatile while

the emulators are dependent on the cosmology used during their calibration. One solution to override the limitation of cosmology dependency would be to calibrate the emulator with different base cosmologies.

`BE-HaPPy` has been calibrated with different redshifts, neutrino masses, mass ranges etc., so that the user has the freedom to interpolate the parameters to the value of her/his choice but unfortunately it is only available for a single cosmology close to Planck (Planck Collaboration et al., 2016). To model the bias of the dark matter halos, I used the `HADES` numerical simulations developed by Francisco Villaescusa-Navarro, Arka Banerjee, Emanuele Castorina and Matteo Viel. `HADES` is available for several masses of neutrinos and different cosmologies where σ_8 is varied, however the realizations having sufficient resolution for the completion of our project all have the same cosmology. Recently the successor to `HADES`, `Quijote` simulations (Villaescusa-Navarro et al., 2020), was made public and simulations were created for Planck and 17 other cosmologies. This would make it possible to extend `BE-HaPPy`.

Another long-term possibility for extending `BE-HaPPy` would be to provide an emulator for the bias of galaxies. It is easier to model the clustering of halos because it just represents a virialization of dark matter while the bias of galaxies on the other hand requires the addition of HOD models which describe the occupation of halos by galaxies according to their properties.

Constraining cosmological model with GCs

One of the conclusions of the publication "The trouble beyond H_0 and the new cosmic triangles" (Bernal et al., 2021) is that despite the reduction by half of the errors in the estimated age of the universe, it is not yet possible to discredit certain values of the Hubble constant, in particular the ones at odds namely those obtained with the CMB and type Ia supernovae. Two possibilities are available to us to improve the estimation of the age of clusters: either by reducing statistical errors or by reducing systematic errors.

Assuming that the dispersion around the most likely age follows a Gaussian distribution (which is almost already the case see Figure 6 and 7 of Valcin et al. 2020), increasing the size of the sample would reduce statistical errors. We used 68 clusters from the HST-ACS catalog (Sarajedini et al., 2007), a number already greater than that of previous analyzes. Increasing the number of clusters would mean resorting to other catalogs. The problem is that astronomical surveys generally use different filters and magnitude cuts. It would therefore be necessary to convert everything into a common system. Another way to improve statistical errors would be to reduce the degeneracies between the different parameters. For our analysis we have limited ourselves to the main sequence stars and the red giant branch. Adding the stars of the horizontal branch would be a great asset. Its particular position in the color magnitude diagram would allow to anchor the distance and thus considerably reduce the degeneracy with the absorption.

Systematic errors, on the other hand, depend on the stellar model used. When it is simply a question of a difference in calibration between the model and the data, it is possible to measure the shift occasioned. This is what we did in the manuscript (Valcin et al., 2021). But when the error comes from the treatment of a physical phenomenon, it becomes more complicated. Either because it requires a modification of the stellar

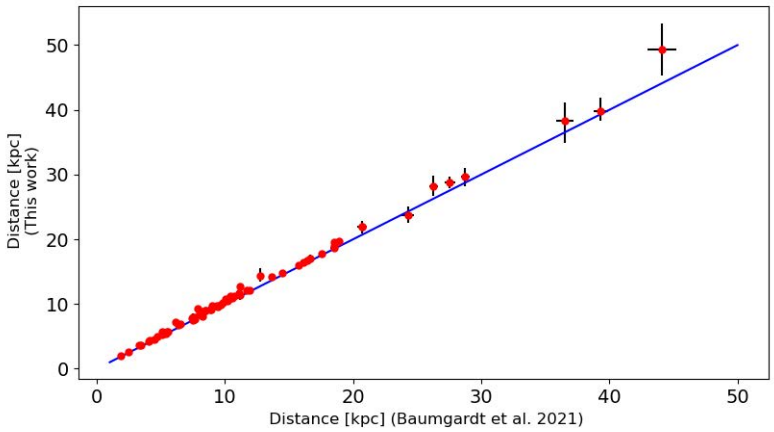

FIGURE 4.1: Figure made with the distance estimates of Valcin et al. 2020 and Baumgardt and Vasiliev 2021.

code (which in turn requires a good understanding of the theory) or because the theory is not yet sufficiently developed.

Another possible development of this project would be to reanalyse the catalog of clusters but this time using GAIA distances as prior. Indeed in Valcin et al. 2020 we compared our estimates of the distance to the ones of O'Malley, Gilligan, and Chaboyer 2017 and found that our distances were a bit different and attributed the difference to the degeneracy of the distance with other parameters. Recently we compared our distances to GAIA EDR3 latest release (Baumgardt and Vasiliev, 2021) and found a remarkable agreement, especially at smaller distances (see Figure 4.1). It would therefore be very interesting to see the effect on the age determination since GAIA distances have very small errors bars.

4.3.2 Code oriented prospects

Application of `BE-HaPPy` to data or mocks

Complex modeling of the effects at non-linear scales tend to lengthen the computation time. This can be detrimental for Monte Carlo samplers such `Emcee` (Foreman-Mackey et al., 2013) or `Montepython` (Brinckmann and Lesgourgues, 2019), where it is necessary to recalculate the same quantity thousands of times. For example an addition of one second per calculation results in an increase of nearly three hours after 10,000 iterations. For this reason when the data of large-scale surveys are analyzed, power spectra are modeled using a fixed template, i.e formulas whose coefficients are calibrated beforehand according to an assumed cosmological model. Corrections are then applied to account for the effects of an incorrect cosmological model. These prescriptions are intended to make analyses more efficient and less computationally expensive.

The combination of `BE-HaPPy` and `FAST-PT` (McEwen et al., 2016) makes the calculation of the different power spectra very efficient. Thus the increase in computation time is compensated by the increase in precision. It is an acceptable compromise. A new idea for the analysis of surveys would be to implement the modifications that I made to `FAST-PT` as well as the coefficients calibrated from the numerical simulations in a

Monte Carlo sampler. It would therefore be possible to vary the cosmological model at each iteration of the chains, which would provide a more agnostic inference of the cosmological parameters.

Using machine learning to bypass stellar grids

Currently state of the art stellar grids (`DSED` Dotter et al. 2008, `MIST` Dotter 2016, `BASTI` Pietrinferni et al. 2004, `PARSEC` Bressan et al. 2012 etc.) can only produce one dimensional theoretical isochrones. However if we look at the CMD of a globular cluster (see Figure 3.2) it is clear that not all features can be reproduced simply by applying a photometric Gaussian dispersion around a true underlying isochrone. The origin of this dispersion is not well understood, although it could be partly explained by the presence of multiple populations.

A more efficient way to compare the CMD diagram of GCs would be to use a theoretical model consisting of a 2D distribution rather than a 1D distribution. By accessing Monte Carlo softwares such as `MOCCA` (Giersz et al., 2013; Giersz et al., 2014) or N-Body codes like `Dragon` (Wang et al., 2016), which follow the dynamical history and evolution of stars, binaries and clusters, it is possible to generate theoretical CMDs and then compare them to data which is equivalent to measuring the distance between two histograms. Machine learning has several algorithms perfectly suited to carry out this task e.g. Earth Mover.

Cosmology is very good at reproducing and interpreting well understood phenomena (see CMB) but it may come to a point where we need to model, subtract or marginalize quantities that we do not understand to access the substance of the signal. In this regard machine learning turns out to be a real asset. By providing a set of initial conditions, it should be possible to produce color-magnitude diagrams without resorting to stellar grids. E.g. Green et al. (2021) designed a new methodology to map stellar parameters to broad-band stellar photometry.

Bibliography

Abbott, B. P. et al. (Feb. 2016). **?**Observation of Gravitational Waves from a Binary Black Hole Merger**?** In: 116.6, 061102, p. 061102. DOI: 10.1103/PhysRevLett.116.061102. arXiv: 1602.03837 [gr-qc].

Alpher, R. A., H. Bethe, and G. Gamow (Apr. 1948). **?**The Origin of Chemical Elements**?** In: *Physical Review* 73.7, pp. 803–804. DOI: 10.1103/PhysRev.73.803.

Baade, W. (Feb. 1956). **?**The Period-Luminosity Relation of the Cepheids**?** In: 68.400, p. 5. DOI: 10.1086/126870.

Bahcall, John N. and Raymond Davis (1976). **?**Solar Neutrinos: A Scientific Puzzle**?** In: *Science* 191.4224, pp. 264–267. ISSN: 0036-8075. DOI: 10.1126/science.191.4224.264. eprint: https://science.sciencemag.org/content/191/4224/264.full.pdf. URL: https://science.sciencemag.org/content/191/4224/264.

Baumgardt, Holger and Eugene Vasiliev (May 2021). **?**Accurate distances to Galactic globular clusters through a combination of Gaia EDR3, HST and literature data**?** In: *arXiv e-prints*, arXiv:2105.09526, arXiv:2105.09526. arXiv: 2105.09526 [astro-ph.GA].

Bernal, José Luis et al. (May 2021). **?**Trouble beyond H_0 and the new cosmic triangles**?** In: *PRD* 103.10, 103533, p. 103533. DOI: 10.1103/PhysRevD.103.103533. arXiv: 2102.05066 [astro-ph.CO].

Boggess, N. W. et al. (Oct. 1992). **?**The COBE Mission: Its Design and Performance Two Years after Launch**?** In: 397, p. 420. DOI: 10.1086/171797.

Bressan, Alessandro et al. (Nov. 2012). **?**PARSEC: stellar tracks and isochrones with the PAdova and TRieste Stellar Evolution Code**?** In: 427.1, pp. 127–145. DOI: 10.1111/j.1365-2966.2012.21948.x. arXiv: 1208.4498 [astro-ph.SR].

Brinckmann, Thejs and Julien Lesgourgues (Mar. 2019). **?**MontePython 3: Boosted MCMC sampler and other features**?** In: *Physics of the Dark Universe* 24, 100260, p. 100260. DOI: 10.1016/j.dark.2018.100260. arXiv: 1804.07261 [astro-ph.CO].

Caldwell, R. R., Rahul Dave, and Paul J. Steinhardt (Feb. 1998). **?**Cosmological Imprint of an Energy Component with General Equation of State**?** In: 80.8, pp. 1582–1585. DOI: 10.1103/PhysRevLett.80.1582. arXiv: astro-ph/9708069 [astro-ph].

Chaboyer, B. et al. (Feb. 2017). **?**Testing Metal-Poor Stellar Models and Isochrones with HST Parallaxes of Metal-Poor Stars**?** In: 835.2, 152, p. 152. DOI: 10.3847/1538-4357/835/2/152. arXiv: 1702.00803 [astro-ph.SR].

Cowan C. L., Jr. et al. (July 1956). **?**Detection of the Free Neutrino: A Confirmation**?** In: *Science* 124.3212, pp. 103–104. DOI: 10.1126/science.124.3212.103.

Davis, Raymond, Don S. Harmer, and Kenneth C. Hoffman (May 1968). **?**Search for Neutrinos from the Sun**?** In: 20.21, pp. 1205–1209. DOI: 10.1103/PhysRevLett.20.1205.

Del Popolo, Antonino and Morgan Le Delliou (Feb. 2017). **?**Small Scale Problems of the ΛCDM Model: A Short Review**?** In: *Galaxies* 5.1, p. 17. DOI: 10.3390/galaxies5010017. arXiv: 1606.07790 [astro-ph.CO].

Dotter, Aaron (Jan. 2016). **?**MESA Isochrones and Stellar Tracks (MIST) 0: Methods for the Construction of Stellar Isochrones**?** In: 222.1, 8, p. 8. DOI: 10.3847/0067-0049/222/1/8. arXiv: 1601.05144 [astro-ph.SR].

Dotter, Aaron et al. (Sept. 2008). **?**The Dartmouth Stellar Evolution Database**?** In: 178.1, pp. 89–101. DOI: 10.1086/589654. arXiv: 0804.4473 [astro-ph].

Efstathiou, George (Mar. 2021). **?**To H0 or not to H0?**?** In: *arXiv e-prints*, arXiv:2103.08723, arXiv:2103.08723. arXiv: 2103.08723 [astro-ph.CO].

Einstein, A. (Jan. 1916). **?**Die Grundlage der allgemeinen Relativitätstheorie**?** In: *Annalen der Physik* 354.7, pp. 769–822. DOI: 10.1002/andp.19163540702.

Foreman-Mackey, Daniel et al. (Mar. 2013). **?**emcee: The MCMC Hammer**?** In: 125.925, p. 306. DOI: 10.1086/670067. arXiv: 1202.3665 [astro-ph.IM].

Friedmann, A. (Jan. 1922). **?**Über die Krümmung des Raumes**?** In: *Zeitschrift fur Physik* 10, pp. 377–386. DOI: 10.1007/BF01332580.

Fukuda, Y. et al. (Aug. 1998). **?**Evidence for Oscillation of Atmospheric Neutrinos**?** In: 81.8, pp. 1562–1567. DOI: 10.1103/PhysRevLett.81.1562. arXiv: hep-ex/9807003 [hep-ex].

Giersz, Mirek et al. (May 2013). **?**MOCCA code for star cluster simulations - II. Comparison with N-body simulations**?** In: 431.3, pp. 2184–2199. DOI: 10.1093/mnras/stt307. arXiv: 1112.6246 [astro-ph.GA].

Giersz, Mirek et al. (Nov. 2014). **?**Monte Carlo modelling of globular star clusters - many primordial binaries, IMBH formation**?** In: *arXiv e-prints*, arXiv:1411.7603, arXiv:1411.7603. arXiv: 1411.7603 [astro-ph.GA].

Green, Gregory M. et al. (Jan. 2021). **?**Data-driven Stellar Models**?** In: 907.1, 57, p. 57. DOI: 10.3847/1538-4357/abd1dd. arXiv: 2006.16258 [astro-ph.GA].

Hinshaw, G. et al. (June 2007). **?**Three-Year Wilkinson Microwave Anisotropy Probe (WMAP) Observations: Temperature Analysis**?** In: 170.2, pp. 288–334. DOI: 10.1086/513698. arXiv: astro-ph/0603451 [astro-ph].

Hubble, E. P. (Mar. 1929a). **?**A spiral nebula as a stellar system, Messier 31.**?** In: 69, pp. 103–158. DOI: 10.1086/143167.

Hubble, Edwin (Mar. 1929b). **?**A Relation between Distance and Radial Velocity among Extra-Galactic Nebulae**?** In: *Proceedings of the National Academy of Science* 15.3, pp. 168–173. DOI: 10.1073/pnas.15.3.168.

Jackson, J. C. (Jan. 1972). **?**A critique of Rees's theory of primordial gravitational radiation**?** In: 156, 1P. DOI: 10.1093/mnras/156.1.1P. arXiv: 0810.3908 [astro-ph].

Jimenez, Raul and Abraham Loeb (July 2002). **?**Constraining Cosmological Parameters Based on Relative Galaxy Ages**?** In: 573.1, pp. 37–42. DOI: 10.1086/340549. arXiv: astro-ph/0106145 [astro-ph].

Jimenez, Raul et al. (May 2019). **?**Measuring the homogeneity of the universe using polarization drift**?** In: 2019.5, 048, p. 048. DOI: 10.1088/1475-7516/2019/05/048. arXiv: 1902.11298 [astro-ph.CO].

Kaiser, Nick (July 1987). **?**Clustering in real space and in redshift space**?** In: 227, pp. 1–21. DOI: 10.1093/mnras/227.1.1.

Kovac, J. M. et al. (Dec. 2002). **?**Detection of polarization in the cosmic microwave background using DASI**?** In: 420.6917, pp. 772–787. DOI: 10.1038/nature01269. arXiv: astro-ph/0209478 [astro-ph].

Leavitt, Henrietta S. (Jan. 1908). **?**1777 variables in the Magellanic Clouds**?** In: *Annals of Harvard College Observatory* 60, pp. 87–108.3.

Leavitt, Henrietta S. and Edward C. Pickering (Mar. 1912). **?**Periods of 25 Variable Stars in the Small Magellanic Cloud.**?** In: *Harvard College Observatory Circular* 173, pp. 1–3.

Lemaître, Abbé G. (Oct. 1931). **?**Contributions to a British Association Discussion on the Evolution of the Universe.**?** In: 128.3234, pp. 704–706. DOI: 10.1038/128704a0.

Lemaître, G. (Jan. 1927). **?**Un Univers homogène de masse constante et de rayon croissant rendant compte de la vitesse radiale des nébuleuses extra-galactiques**?** In: *Annales de la Société Scientifique de Bruxelles* 47, pp. 49–59.

Lesgourgues, Julien (Apr. 2011). **?**The Cosmic Linear Anisotropy Solving System (CLASS) I: Overview**?** In: *arXiv e-prints*, arXiv:1104.2932, arXiv:1104.2932. arXiv: 1104.2932 [astro-ph.IM].

McClintock, Thomas et al. (July 2019). **?**The Aemulus Project IV: Emulating Halo Bias**?** In: *arXiv e-prints*, arXiv:1907.13167, arXiv:1907.13167. arXiv: 1907.13167 [astro-ph.CO].

McEwen, Joseph E. et al. (Sept. 2016). **?**FAST-PT: a novel algorithm to calculate convolution integrals in cosmological perturbation theory**?** In: 2016.9, 015, p. 015. DOI: 10.1088/1475-7516/2016/09/015. arXiv: 1603.04826 [astro-ph.CO].

Monfardini, A. et al. (Apr. 2006). **?**The microcalorimeter arrays for a rhenium experiment (MARE): A next-generation calorimetric neutrino mass experiment**?** In: *Nuclear Instruments and Methods in Physics Research A* 559.2, pp. 346–348. DOI: 10.1016/j.nima.2005.12.006. arXiv: hep-ex/0509038 [hep-ex].

Muñoz, Julian B. and Cora Dvorkin (Aug. 2018). **?**Efficient computation of galaxy bias with neutrinos and other relics**?** In: 98.4, 043503, p. 043503. DOI: 10.1103/PhysRevD.98.043503. arXiv: 1805.11623 [astro-ph.CO].

O'Malley, Erin M., Christina Gilligan, and Brian Chaboyer (Apr. 2017). **?**Absolute Ages and Distances of 22 GCs Using Monte Carlo Main-sequence Fitting**?** In: 838.2, 162, p. 162. DOI: 10.3847/1538-4357/aa6574. arXiv: 1703.01915 [astro-ph.SR].

Paxton, Bill et al. (Jan. 2011). **?**Modules for Experiments in Stellar Astrophysics (MESA)**?** In: 192.1, 3, p. 3. DOI: 10.1088/0067-0049/192/1/3. arXiv: 1009.1622 [astro-ph.SR].

Penzias, A. A. and R. W. Wilson (July 1965). **?**A Measurement of Excess Antenna Temperature at 4080 Mc/s.**?** In: 142, pp. 419–421. DOI: 10.1086/148307.

Perlmutter, S. et al. (June 1999). **?**Measurements of Ω and Λ from 42 High-Redshift Supernovae**?** In: 517.2, pp. 565–586. DOI: 10.1086/307221. arXiv: astro-ph/9812133 [astro-ph].

Pietrinferni, Adriano et al. (Sept. 2004). **?**A Large Stellar Evolution Database for Population Synthesis Studies. I. Scaled Solar Models and Isochrones**?** In: 612.1, pp. 168–190. DOI: 10.1086/422498. arXiv: astro-ph/0405193 [astro-ph].

Planck Collaboration et al. (Sept. 2016). **?**Planck 2015 results. XIII. Cosmological parameters**?** In: 594, A13, A13. DOI: 10.1051/0004-6361/201525830. arXiv: 1502.01589 [astro-ph.CO].

Planck Collaboration et al. (Sept. 2020). **?**Planck 2018 results. VI. Cosmological parameters**?** In: 641, A6, A6. DOI: 10.1051/0004-6361/201833910. arXiv: 1807.06209 [astro-ph.CO].

Pontecorvo, B. (1957). **?**Mesonium and anti-mesonium**?** In: *Sov. Phys. JETP* 6, p. 429.

— (1967). **?**Neutrino Experiments and the Problem of Conservation of Leptonic Charge**?** In: *Zh. Eksp. Teor. Fiz.* 53, pp. 1717–1725.

Raccanelli, Alvise, Licia Verde, and Francisco Villaescusa-Navarro (Feb. 2019). **?**Biases from neutrino bias: to worry or not to worry?**?** In: 483.1, pp. 734–743. DOI: 10.1093/mnras/sty2162. arXiv: 1704.07837 [astro-ph.CO].

Ratra, Bharat and P. J. E. Peebles (June 1988). **?**Cosmological consequences of a rolling homogeneous scalar field**?** In: 37.12, pp. 3406–3427. DOI: 10.1103/PhysRevD.37.3406.

Riess, Adam G. et al. (Sept. 1998). **?**Observational Evidence from Supernovae for an Accelerating Universe and a Cosmological Constant**?** In: 116.3, pp. 1009–1038. DOI: 10.1086/300499. arXiv: astro-ph/9805201 [astro-ph].

Riess, Adam G. et al. (July 2016). **?**A 2.4% Determination of the Local Value of the Hubble Constant**?** In: 826.1, 56, p. 56. DOI: 10.3847/0004-637X/826/1/56. arXiv: 1604.01424 [astro-ph.CO].

Riess, Adam G. et al. (Feb. 2021). **?**Cosmic Distances Calibrated to 1% Precision with Gaia EDR3 Parallaxes and Hubble Space Telescope Photometry of 75 Milky Way Cepheids Confirm Tension with ΛCDM**?** In: 908.1, L6, p. L6. DOI: 10.3847/2041-8213/abdbaf. arXiv: 2012.08534 [astro-ph.CO].

Sarajedini, Ata et al. (Apr. 2007). **?**The ACS Survey of Galactic Globular Clusters. I. Overview and Clusters without Previous Hubble Space Telescope Photometry**?** In: 133.4, pp. 1658–1672. DOI: 10.1086/511979. arXiv: astro-ph/0612598 [astro-ph].

Smoot, G. F. et al. (Sept. 1992). **?**Structure in the COBE Differential Microwave Radiometer First-Year Maps**?** In: 396, p. L1. DOI: 10.1086/186504.

Stern, Daniel et al. (Feb. 2010). **?**Cosmic chronometers: constraining the equation of state of dark energy. I: H(z) measurements**?** In: 2010.2, 008, p. 008. DOI: 10.1088/1475-7516/2010/02/008. arXiv: 0907.3149 [astro-ph.CO].

Tinker, Jeremy L. et al. (Dec. 2010). **?**The Large-scale Bias of Dark Matter Halos: Numerical Calibration and Model Tests**?** In: 724.2, pp. 878–886. DOI: 10.1088/0004-637X/724/2/878. arXiv: 1001.3162 [astro-ph.CO].

Valcin, David et al. (Dec. 2019). **?**BE-HaPPY: bias emulator for halo power spectrum including massive neutrinos**?** In: 2019.12, 057, p. 057. DOI: 10.1088/1475-7516/2019/12/057. arXiv: 1901.06045 [astro-ph.CO].

Valcin, David et al. (Dec. 2020). **?**Inferring the age of the universe with globular clusters**?** In: 2020.12, 002, p. 002. DOI: 10.1088/1475-7516/2020/12/002. arXiv: 2007.06594 [astro-ph.CO].

Valcin, David et al. (Feb. 2021). **?**The Age of the Universe with Globular Clusters: Reducing Systematic Uncertainties**?** In: *arXiv e-prints*, arXiv:2102.04486, arXiv:2102.04486. arXiv: 2102.04486 [astro-ph.GA].

Villaescusa-Navarro, Francisco et al. (Sept. 2020). **?**The Quijote Simulations**?** In: 250.1, 2, p. 2. DOI: 10.3847/1538-4365/ab9d82. arXiv: 1909.05273 [astro-ph.CO].

Wang, Long et al. (May 2016). **?**The DRAGON simulations: globular cluster evolution with a million stars**?** In: 458.2, pp. 1450–1465. DOI: 10.1093/mnras/stw274. arXiv: 1602.00759 [astro-ph.SR].

Weinheimer, Ch. (2002). **?**KATRIN, a next generation tritium decay experiment in search for the absolute neutrino mass scale**?** In: *Progress in Particle and Nuclear Physics* 48.1, pp. 141–150. ISSN: 0146-6410. DOI: https://doi.org/10.1016/S0146-6410(02)00120-5. URL: https://www.sciencedirect.com/science/article/pii/S0146641002001205.